

PROCESSING-STRUCTURE-PROPERTY CORRELATION IN ULTRAFINE GRAINED 6061 ALUMINIUM ALLOY

Ph.D. THESIS

by

P.NAGESWARA RAO



DEPARTMENT OF METALLURGICAL AND MATERIALS ENGINEERING
INDIAN INSTITUTE OF TECHNOLOGY ROORKEE
ROORKEE-247667, INDIA
JANUARY, 2015

PROCESSING-STRUCTURE-PROPERTY CORRELATION IN ULTRAFINE GRAINED 6061 ALUMINIUM ALLOY

A THESIS

*Submitted in partial fulfilment of the
requirements for the award of the degree
of*

DOCTOR OF PHILOSOPHY

in

METALLURGICAL AND MATERIALS ENGINEERING

by

P.NAGESWARA RAO



DEPARTMENT OF METALLURGICAL AND MATERIALS ENGINEERING
INDIAN INSTITUTE OF TECHNOLOGY ROORKEE
ROORKEE-247 667, INDIA
JANUARY, 2015



INDIAN INSTITUTE OF TECHNOLOGY ROORKEE ROORKEE

CANDIDATE'S DECLARATION

I hereby certify that the work which is being presented in the thesis entitled **“PROCESSING-STRUCTURE-PROPERTY CORRELATION IN ULTRAFINE GRAINED 6061 ALUMINIUM ALLOY”** in partial fulfilment of the requirements for the award of the Degree of Doctor of Philosophy and submitted in the Department of Metallurgical and Materials Engineering of the Indian Institute of Technology Roorkee is an authentic record of my own work carried out during a period from December, 2009 to January, 2015 under the supervision of Dr. R. Jayaganthan, Professor, Metallurgical and Materials Engineering Department, Indian Institute of Technology Roorkee, Roorkee.

The matter presented in this thesis has not been submitted by me for the award of any other degree of this or any other institute.

(P.NAGESWARA RAO)

This is to certify that the above statement made by the candidate is correct to the best of my knowledge.

Date: _____

(R.JAYAGANTHAN)
(Supervisor)

ABSTRACT

The thesis presents the processing-structure-property correlation in ultrafine grained Al 6061 alloy. The coarse grained alloy with grain size in several microns is processed through various thermo mechanical routes to develop ultrafine grained (UFG) structure in it. To ensure the UFG structure in thermo mechanically processed alloy, electron back scattered diffraction (EBSD), Transmission electron microscopy (TEM), X-ray diffraction (XRD) techniques are employed. The mechanical properties of UFG material are evaluated through hardness and tensile testing at room temperature and compared with its coarse grained counterpart. In the course of grain refinement, the precipitates with nanoscale features imparting strengthening effect to the coarse grained matrix undergo several physical and chemical changes. Ultimately, it influences the mechanical properties of the UFG alloy. The precipitation evolution in UFG material is monitored through differential scanning calorimetry (DSC) and TEM. The main objective of the present study is to understand the effect of microstructure developed through various thermomechanical routes on enhancement of strength and ductility of Al 6061 alloy.

Al-6061 alloy was processed through cryorolling (CR) up to ~92% thickness reduction. Effect of low temperature ageing and annealing at high temperatures on microstructure and mechanical properties was investigated. The results evidenced that low temperature ageing has resulted simultaneous increment in the strength and ductility of the UFG Al 6061 alloy. EBSD and TEM investigations on microstructure show the UFG structure in the Al alloy is stable up to annealing temperature, 250 °C. The role of second phase particles on retaining the microstructural stability is emphasized. The TEM studies revealed that second phase Mg₂Si particles are effectively pinning the grain boundaries due to the Zener drag effect. Owing to the presence of heterogeneities in the material, a duplex structure was observed upon annealing at temperatures, 150 to 200°C. At high temperatures, annealing leads to coarsening of the second phase particles, which reduces Zener drag effect by precipitate particles. Abnormal grain growth was observed after annealing at high temperatures (300°C).

To investigate the effect of dynamic ageing along with cryorolling on the mechanical properties and microstructural evolution of Al 6061 alloy, the alloy was subjected to cryorolling followed by warm rolling at 145 °C (WR- Cryorolling+Warm rolling). It was found that the combination of cryorolling and warm rolling is more effective than cryorolling alone. The WR samples showed a significant improvement in tensile strength (376 MPa) and partial

improvement in ductility (5%) as measured from tensile testing. The DSC, XRD and TEM investigations have shown that the superior properties of the alloy obtained through WR were attributed to formation of fine precipitates during warm rolling. DSC results of WR material have revealed that WR material undergoes low temperature ageing to enhance the strength further. The effect of ageing on WR samples was investigated and the optimum ageing condition was found to be 125 °C for 45 hours, which results in improved tensile strength of (406 MPa) and good tensile ductility (10%). The tensile strength of WR + peak aged (WR + PA) sample (406 MPa) was found to be 11% more than that of cryorolled + peak aged (CR + PA) sample (365 MPa). During peak ageing treatment, the strength has been retained by pinning of dislocations through nanosized precipitates generated during warm rolling and it has been improved further by precipitation of the remnant dissolved second phase in the matrix. The thermal and microstructural stability of the WR alloy is found to be better than CR alloy. It was also observed that, by performing warm rolling at high temperatures (~ 200 °), a good combination of strength and ductility in Al 6061 can be obtained.

To obtain maximum strengthening contribution from precipitation strengthening in UFG precipitation hardenable Al 6061 alloy, it is essential to understand the evolution and kinetics of precipitates. Hence, a detailed investigation has been made on the effect of CR and WR on precipitation evolution by using DSC and TEM. Hardness measurements were made to substantiate the TEM and DSC results. A significant change has been observed in precipitation sequence even at very low percentage of deformation (5%). The sequence of nanoclusters and major strengthening precipitate phases (β''/β') were altered with increasing deformation. At low temperatures (<150 °C), two distinct cluster peaks were observed upon cryogenic deformation. At high temperatures (>150 °C), the deformed alloy has shown the absence of β' formation as compared to undeformed coarse grained material. TEM investigation of the deformed alloy revealed bimodal distribution of precipitates with both very fine and coarse structures. Pre-deformation of the alloy led to the simultaneous formation of β'' and β' precipitates in both CR and WR materials. Activation energies of the different precipitates in deformed alloys were calculated by adopting Kissinger analysis. It is observed that the activation energy for the formation of various precipitates the alloy with very low percentage of deformation (5%) is decreased as compared to undeformed bulk alloy. However, with increasing percentage of deformation beyond the 5%, the activation energies are significantly higher as compared to the undeformed bulk alloy. With increasing degree of deformation, the diffusivity of the solute

species gets decelerated and therefore reaction rate becomes sluggish as evident from the microstructural changes observed in the alloy. The solute atoms are trapped by the tangled dislocations.

To understand the effect of microstructure on precipitation behaviour and mechanical properties of the Al 6061 alloy deformed up to larger strains under cryogenic temperature, multidirectional forging (MDF) at liquid nitrogen temperature has been conducted. The solution treated and water quenched alloy was subjected to cryoforging up to cumulative strains of 1.8, 3.6 and 5.4. The evolution of UFG structure with increasing cumulative strains was investigated through EBSD and TEM. The results indicate that microstructure with an ultrafine grain morphology (average size 250 nm) was achieved through cryogenic forging up to cumulative strain of 5.4. Tensile strength has increased from 180 MPa to 388 MPa with 4.5% percentage of elongation to failure. Tensile test results revealed that MDFed material after ageing led to significant improvement in work hardening and its tensile ductility. Strengthening of the matrix through various mechanisms has been quantified with the existing models to estimate the yield strength of the as forged and peak aged material. The precipitation hardening response in UFG material is found to be 35% lower than that of the coarse grained material as observed in the present work. The reasons could be; i) the presence of high dislocation densities has reduced the coherency of the precipitates with the Al matrix, ii) deformation led to transformation of β'' (fine needle shaped phase) to β' (rod shaped phase). With increasing MDF strain at liquid nitrogen temperature up to 6, evolution of new UFGs through dynamic recrystallization was observed through EBSD. However, due to non-uniform distribution of the strain in the MDF samples, structural inhomogeneity from center to the outer edges of the sample was observed. The structural inhomogeneity in the samples was investigated through hardness measurements at various cumulative strains such as 1.8, 3.6 and 6. The results suggest that with increasing strain, the degree of inhomogeneity can be reduced.

Acknowledgments

I am using this opportunity to thank my supervisor Prof. **R. Jayaganthan** for assigning this work to me, his inspiring guidance, and for giving his expertise to this thesis. I am sincerely grateful to him for being patiently with me during the research work and the extra care shown on me. It was pleasure to work under him.

I express my sincere gratitude to Prof. S. K. Nath (Head - MMED, Chairman-SRC), Dr. Mukesh Bhardwaj (Internal member, SRC), Dr. I.V. Singh (External member, SRC), Prof. Anjan Sil (Chairman, DRC) for their valuable suggestions to improve this thesis.

I would like to give my special thanks to Prof. Ramesh Chandra (Head, IIC) for providing the TEM and EBSD facilities, which are very essential to carry out this work. I also thank to Prof. Gautama, Dr. Mani Krishna and Dr. Vishwanadh for their great support I received in all the matters during my Ph.D specially in operating TEM.

I would like to express my sincere thanks to Mr. T.K. Sharma, Mr. B.D. Sharma, Mr. Shakthi Guptha, Mr. Rajendra Sharma and Mr. R.K. Sharma Technical staff of MMED for their great support during the research period.

Furthermore my heartiest thanks to Dr.Sushantha Kumar Panigrahi, Dr. Dharmendra Singh and Dr. S. Pradeep for their help at difficult times and friendly advices and inspiring technical inputs. The time I spent with them is memorable. Without their support completing this thesis would have been impossible.

I would like to express my gratitude to all the friends who are supported directly or indirectly to complete this thesis.

My sincere thanks to my wife **Vani** for her great patience, love and support during my thesis work. I cannot appreciate her in terms of words. My heartiest thank goes to my brothers Suresh and Prasad, and sisters Parvathi, Bhargavi and Lavanya and to my sweet Ammi (Roshni). I also thank to my Uncle G.Viswanatha Naidu and Auntie G. Krishnamma for their great support from the beginning of Ph.D.

I am deeply grateful to Dr. Rayapati Subramanyam Naidu and Dr. Rayapti Venkat for the inspiration given to do Ph.D. Without them I would not have thought about doing Ph.D.

At last, my gratitude to goes to my parents **P. Durvasulu Naidu** and **P. Jamuna**, who supported me always and looking forward patiently for me to complete my thesis work. I dedicate this work to them.

(P.Nageswara rao)

Table of Contents

	Page No.
Candidate declaration-----	i
Abstract -----	ii
Acknowledgements-----	v
Contents-----	vi
List of Figures-----	xii
List of Tables-----	xxii
Definitions and Abbreviations-----	xxiii
List of Publications-----	xxvi
	1
Chapter 1 Introduction	
	5
Chapter 2: Literature Review	
2.1 Introduction-----	5
2.2 Principle of Severe Plastic Deformation-----	5
2.3 SPD techniques-----	6
2.3.1 Equal channel angular pressing-----	6
2.3.2 High pressure torsion (HPT) -----	12
2.3.3 Multi directional forging (MDF)-----	13
2.3.4 Accumulative roll bonding (ARB) -----	14
2.3.5 Asymmetric rolling -----	15
2.4 Cryorolling-----	16
2.5 Homogeneity evolution in SPD processed materials -----	17
2.6 Hybrid materials-----	18
2.7 Thermal stability-----	19
2.8 Applications of UFG material-----	20
2.9 Aluminium alloys-----	22
2.9.1 Aluminium alloys in Modern life-----	22
2.9.2 Properties of Aluminium and its alloys-----	23
2.9.3 Aluminium alloys in automotive and aerospace industry-----	24

2.9.4 Precipitation phenomenon in 6xxx Series Alloys-----	25
2.9.5 Clusters and Negative Strength Response-----	26
2.9.6 Mechanical properties of Al 6061 alloy processed through various SPD techniques.-----	27
2.9.7 Microstructural elements in SPD processed Al alloys	29
2.9.8 Strengthening mechanisms in Aluminium alloys-----	31
2.9.9 Strategies to enhance the ductility in Al alloys-----	35
2.10 Problem formulation-----	38
2.10.1 Current Literature on Bulk ultrafine grained & nanostructured materials -----	38
2.10.2 Motivation-----	39
2.10.3 Objectives-----	39
2.10.4 Work plan and Layout of the thesis-----	40
Chapter 3: Experimental Procedure	42
3.1 Introduction-----	42
3.2 Materials-----	42
3.3 Experimental setup-----	43
3.3.1 Cryorolling-----	43
3.3.2 Warm rolling-----	44
3.3.3 Cryoforging-----	44
3.4 Heat Treatments-----	45
3.4.1 Solid Solution Heat Treatment (ST) and Quenching-----	45
3.4.2 Short annealing and longtime annealing-----	45
3.4.3 Artificial ageing and Natural ageing-----	46
3.5 Mechanical Characterization-----	46
3.5.1 Vickers hardness-----	46
3.5.2 Tensile testing-----	47
3.6 Microstructural Characterization-----	48
3.6.1 Optical microscopy (OM)-----	48
3.6.2. Scanning Electron Microscopy (SEM)/EBSD-----	49

3.6.3. Transmission Electron Microscopy (TEM)-----	49
3.7 Sample preparation-----	49
3.7.1 Mechanical grinding/polishing-----	49
3.7.2 Etching-----	50
3.7.3 Electro polishing-----	50
3.7.4 Twin jet electro polishing-----	50
3.8 Differential Scanning Calorimetry (DSC)-----	50

Chapter 4: Cryorolling 53

4.1 Introduction-----	53
4.2 Experimental-----	54
4.3 Results -----	56
4.3.1 Effect of cryorolling on microstructural and mechanical properties--	56
4.3.1.1 Microstructure-----	56
4.3.1.2 DSC studies-----	60
4.3.1.3 Mechanical properties-----	61
4.3.2 Effect of low temperature ageing on microstructure and mechanical properties of CR Al 6061 alloy-----	62
4.3.2.1 Mechanical properties-----	62
4.3.2.2 Microstructure-----	64
4.3.3 Microstructural and Thermal stability studies of CR92% Al 6061 alloy --	64
4.3.3.1 TEM studies-----	64
4.3.3.2 EBSD studies-----	72
4.3.3.3 DSC studies-----	72
4.3.3.4 XRD Results-----	76
4.3.4 Mechanical Properties-----	77

4.4 Discussions-----	78
4.4.1 Effect of Annealing on Mechanical properties-----	78

4.4.2 Role of Second phase in evolution of microstructure during annealing-	80
4.5 Conclusions-----	81

82

Chapter 5 :Warm rolling

5.1 Effect of Cryorolling followed by Warm rolling on Microstructure and Mechanical Properties of Al 6061 alloy -----	83
5.1.1 Introduction-----	83
5.1.2 Experimental-----	83
5.1.3 Results-----	85
5.1.3.1 Effect of warm rolling and ageing on microstructure and mechanical properties-----	85
5.1.3.1.1 Hardness-----	85
5.1.3.1.2 XRD Analysis-----	87
5.1.3.1.3 DSC-----	88
5.1.3.1.4 Microstructure-----	90
5.1.3.1.5 Tensile properties-----	94
5.1.3.2 Microstructure and thermal stability of CR+WR alloy -----	97
5.1.4 Discussions-----	99
5.1.5 Conclusions-----	103
5.2 Effect of post cryorolling treatments on microstructure and mechanical properties of Al 6061 alloy-----	105
5.2.1 Introduction -----	105
5.2.2 Experimental Details-----	106
5.2.3 Results-----	106
5.2.3.1 Hardness-----	106
5.2.3.2 DSC Study-----	107
5.2.3.3 XRD analysis-----	108
5.2.3.4 Microstructure-----	110
5.2.3.5 Tensile properties-----	112
5.2.4 Discussion-----	115
5.2.5 Conclusions-----	118

Chapter 6: Precipitation behaviour	119
6.1 Precipitation behavior of cryorolled and warm rolled Al 6061 alloy-----	120
6.1.1 Introduction-----	120
6.1.2 Experimental-----	121
6.1.3 Results and discussions-----	122
6.1.3.1 DSC studies-----	122
6.1.3.2 Hardness evolution-----	130
6.1.3.3 TEM studies-----	133
6.1.4 Conclusions-----	140
6.2 Effect of deformation strain on precipitation behavior of Al 6061 alloy---	142
6.2.1 Introduction-----	142
6.2.2 Experimental details-----	143
6.2.3 Results-----	144
6.2.3.1 Effect of strain-----	144
6.2.3.1.1 Cluster peaks evolution-----	144
6.2.3.1.2 β''/β' phase formation-----	147
6.2.3.2 Natural ageing behavior of ST and CR material-----	148
6.2.3.3 Effect of strain on activation energy-----	151
6.2.4 Discussions-----	156
6.2.4.1 Cluster formation and Natural ageing behavior-----	156
6.2.4.2 Activation energy-----	158
6.2.4.3 Effect of quenching temperature-----	159
6.2.5 Conclusions-----	159
Chapter 7: Cryoforging	161
7.1 Effect of cryoforging followed by low temperature ageing on microstructure and mechanical properties of Al 6061 alloy-----	162
7.1.1 Introduction-----	162
7.1.2 Experimental procedures-----	163
7.1.3 Results-----	166

7.1.3.1 Microstructure (before ageing)-----	166
7.1.3.2 Mechanical properties-----	174
7.1.3.3 Fractography-----	177
7.1.3.4 Mechanical Behavior (After Ageing)-----	178
7.1.3.5 Microstructure-----	181
7.1.3.6 Fractography-----	185
7.1.4 Discussions-----	185
7.1.4.1 Yield Strength-----	190
7.1.4.2 Work hardening rate and Ductility-----	198
7.1.5 Conclusions-----	199
7.2 Evolution of microstructural homogeneity in cyoforged Al 6061 alloy-----	200
7.2.1 Introduction-----	200
7.2.2 Experimental details-----	201
7.2.3 Results -----	204
7.2.3.1 Variation in Hardness-----	204
7.2.3.2 Evolution of Microstructure-----	206
7.2.3.3DSC studies-----	220
7.2.4 Discussions-----	220
7.2.4.1 Homogeneity after MDF -----	224
7.2.5 Conclusions-----	225
 Chapter 8: Suggestions for Future Work	 226
References	227

List of Figures

No.	Title	Page No.
Figure 2.1:	Schematic representation showing the principle of ECAP processing	12
Figure 2.2:	Schematic representation of Bridgman apparatus[48]-----	13
Figure 2.3:	Schematic representation of multi directional forging.....	14
Figure 2.4:	Schematic representation of ARB process [56].....	15
Figure 2.5:	Schematic representation of asymmetric rolling due to (a) Non-unity roll radius ratio, (b) Non-unity roll speed ratio and (c) Single roll drive rolling [33]-----	16
Figure 2.6:	Microstructure of initially ECAP deformed material (two ECAP passes in Route Bc) after annealing at 320 °C under the influence of an additional stress of 1.25 MPa (a), 5 MPa (b) and 15 MPa (c).....	20
Figure 2.7:	a) SEM micrograph of top surface of hot embossed UFG Al 1050 alloy; b) Optical micrograph of top surface of hot embossed coarse grained Al 1050 alloy[126].....	22
Figure 2.8:	Consumption of Aluminium in various sectors (Data plotted based on 2013 reports)-----	23
Figure 2.9:	Usage of Al in various forms in Audi A8 [135]-----	25
Figure 2.10:	Hardness and DSC plots of AA 6111 alloy obtained through isochronal heating [137]-----	26
Figure 2.11:	TEM micrographs of Al–3% Mg alloy sample after HPT at room temperature; a) UFG grains with non-equilibrium grain boundaries, b) HRTEM image taken at location ‘A’ shown in Figure 3(a), c) HRTEM image taken at location B shown in Figure 3(b) [158]-----	30
Figure 2.12:	The Hall-Petch relation for the Al alloys: AA 1100, Al-3% Mg, AA 1570 and AA 7475 [115][164]-----	32
Figure 2.13:	Alloy grain structure in the HPT processed AA7075 (scale bar: 50 nm) [168]-----	33
Figure 2.14:	Typical tensile engineering stress-strain curves of the as-processed Al-Cu-Sc (short-dash curve), Al-Cu (dash curve), and artificially aged Al-Cu-Sc (solid curve), Al-Cu (dash-dot curve) UFG alloys [193]-----	37

Figure 2.15:	Flow diagram showing the plan of the present work-----	41
Figure 3.1:	Two high rolling mill used for cryorolling-----	43
Figure 3.2:	Friction screw forging press used for Multi axial forging-----	45
Figure 3.3:	Computerized Vickers Hardness Tester (FIE-Model:VM 50 PC)-----	46
Figure 3.4:	S-Series, H25K-S tensile testing machine-----	47
Figure 3.5:	Schematic diagram of a tensile specimen; a) ASTM E8 sub size specimen, b) Nonstandard size specimen-----	47
Figure 3.6:	LEICA DMI5000 M- Optical microscopy used in the present work--	48
Figure 3.7:	Perkin Elmer's DSC 8000 series machine-----	51
Figure 3.8:	Punch and die used to prepare DSC samples-----	52
Figure 4.1:	Flow chart of experimental procedure adopted in this chapter-----	55
Figure 4.1:	Optical micrographs of ST Al 6061 alloy obtained through: a) using polarized light mode, b) using bright field mode, c) using dark field mode-----	56
Figure 4.3:	Optical micrographs of solution treated (ST) and cryorolled (CR) Al 6061 alloy samples at different % of reductions such as: (a) 35%, (b) 50%, (c) 70%, (d) 92%-----	57
Figure 4.4:	TEM micrographs of Al 6061 alloy after cryorolling; a) Bright filed image, b) SAED micrograph-----	58
Figure 4.5:	EBSD microstructures of CR92% Al 6061 alloy; a) Orientation image micrograph shown with high angle grain boundaries, b) Orientation image micrograph shown with low angle grain boundaries, c) Image quality map, d) Magnified view of area cropped area from Figure 4.5 (b)-----	59
Figure 4.6:	DSC heat flow curves of Al 6061 alloy; ST and CR material-----	60
Figure 4.7:	Variation in mechanical properties of CR 6061 alloy with increasing deformation at cryogenic temperature; a) Vickers hardness, b) Tensile test results-----	62
Figure 4.8:	Ageing behaviour of CR Al 6061 alloy at 100°C, 125°C and 145 °C-	63
Figure 4.9:	Comparison of tensile properties of Al 6061 alloy processed through various conditions; ST, (ST+PA) T6, CR92%, CR+PA-----	63

Figure 4.10:	Representative TEM images of CR92% Al 6061 alloy; a) shows partially recovered grains after peak ageing treatment (PA), b) shows nanosized precipitates observed in CR92%+PA samples-----	65
Figure 4.11:	TEM micrographs of CR92% Al 6061 alloy annealed at different temperatures for 1 hour: a) 150 °C, b) 200 °C, c) 250 °C-----	66
Figure 4.12:	TEM micrographs of CR92% Al 6061 alloy annealed at 150 °C for 1 hour; a) Evolution of very fine grains at the periphery of coarse particles (CP), b) Enlarged view of the area indicated with arrow in Figure 4.12(a)-----	68
Figure 4.13:	TEM micrographs of CR92% Al 6061 alloy annealed at 200 °C for 1 hour; Evolution of very fine grains at the periphery of big second phase particle (particle stimulated nucleation)-----.	69
Figure 4.14:	TEM micrographs of CR92% Al 6061 alloy annealed at 250 °C for 1 hour; Pinning of second phase particles at the grain boundaries and grain faces-----	70
Figure 4.15:	TEM micrographs of CR92% Al 6061 alloy annealed at 300 °C for 1 hour: a) Interaction of second phase particles at the grain boundaries and individual dislocations inside the grain, b) ‘ β ’ phase rod shaped stable precipitates oriented in particular direction-----	71
Figure 4.16:	EBSD data of CR Al 6061 alloy; a) and b) are OIM micrographs of the alloy annealed at 150 °C, c) and d) are OIM micrographs of the alloy annealed at 200 °C. b) and d) are magnified view of cropped areas from (a) and (c) respectively-----	73
Figure 4.17:	EBSD microstructures of CR Al 6061 alloy annealed at 250 °C for 1 hour; a) OIM shown with high angle grain boundaries, b) OIM shown with low angle grain boundaries, c) IQ map, d) Magnified view of area cropped from Figure 4.17(a), e) Grain orientation spread (GOS) map of Figure 4.17(d), f) GOS data-----	74
Figure 4.18:	EBSD microstructures of CR Al 6061 alloy annealed at 300 °C for 1 hour; a) OIM showing distribution of low angle grain boundaries, b) IQ map, c) Recrystallized area portioned from Figure 4.18(a), d) Portioned area with grain size less than 5 μm -----	75
Figure 4.19:	DSC heat flow curves of CR 92% Al 6061 alloy annealed at various temperatures-----	76
Figure 4.20:	XRD patterns of CR 92% Al 6061 alloy sample annealed at different temperatures for 1 hour: A) 0 °C, B) 150 °C, C) 200 °C, D) 250 °C,	77

E) 300 °C, F) 350 °C-----

Figure 4.21:	Variation in Mechanical properties of CR 92% Al 6061 alloy with annealing temperature. a) Evolution of micro hardness and % of recrystallization with annealing temperature, b) Variation in tensile strength and ductility with annealing temperature-----	79
Figure 5.1:	Process flow diagram.-----	84
Figure 5.2:	Effect of cryorolling and warm rolling on hardness behavior of Al 6061 alloy-----	86
Figure 5.3:	Vickers hardness of the WR sample after ageing at 100°C, 125°C, 145 °C as function of ageing time-----	86
Figure 5.4:	Vickers Hardness of ST, CR, WR of Al 6061 alloy aged at 125 °C as a function of ageing time-----	88
Figure 5.5:	XRD patterns of ST, CR, WR, WR + PA and CR + PA Al 6061 alloy-----	89
Figure 5.6:	DSC thermograms of Al 6061 alloy; CR, WR, CR+PA, WR+PA-----	89
Figure 5. 7:	Optical microstructure of coarse grained material after solid solution treatment (ST)-----	91
Figure 5.8:	EBSD micrographs of ST material on rolling plane; a) Inverse pole figure map, b) Image quality map with grain boundaries	92
Figure 5.9:	EBSD micrographs of Al 6061 alloy after CR and WR; a) & b) OIM maps with larger area, c) &d) are IQ maps of a) & b), e) & f) OIM maps representing small area with LAGBs and HAGBs of CR and WR materials.....	93
Figure 5.10:	Misorientation angle distribution Al 6061 alloy; a) CR, b) WR-----	94
Figure 5.11:	TEM micrographs of Al 6061 alloy; a) CR, b) WR-----	95
Figure 5.12:	TEM micrographs of Al 6061 alloy (a) CR + PA, (b) WR + PA-----	95
Figure 5.13:	Engineering stress– engineering strain curves of various heat treated conditions of Al 6061 alloy (a) ST, (b) T6, (c) CR, (d) CR + PA, (e) CR + WR, (f) WR + PA-----	96
Figure 5.14:	Variation in hardness of Al 6061 alloy with different thermo mechanical processing; CR and WR-----	98
Figure 5.15:	DSC heat flow curves of WR Al 6061 alloy after annealing for 1 hour at different temperatures-----	99
Figure 5.16:	EBSD micrographs of WR Al 6061 alloy after annealing at different temperatures; 150 °C, 200 °C and 250 °C-----	101

Figure 5.17:	EBSD micrographs of CR Al 6061 alloy annealed at 250 °C for 1 hour-----	102
Figure 5.18:	EBSD micrographs of Al 6061 alloy annealed at 300 °C for 1 hour; (a) and (b) Orientation image micrograph and Image quality maps of WR Al 6061 alloy, (c) and (d) Orientation image micrograph and Image quality maps of CR Al 6061 alloy-----	102
Figure 5.19:	Hardness behaviour of Al 6061 alloy at various heat treated conditions; ST, CR, CR+SA, WR1-----	107
Figure 5.20:	Variation in Vickers hardness of the CR + SA and WR1 sample after ageing at 100 °C (a), 125 °C (b), and 150 °C (c) as function of ageing time-----	108
Figure 5.21:	DSC thermograms of Al 6061 alloy; a) CR+SA, b) WR1	109
Figure 5.22:	XRD patterns of Al 6061 alloy processed through various conditions: CR + SA, WR1, SA + PA, WR + PA-----	110
Figure 5.23:	TEM micrographs of Al 6061 alloy processed through various conditions: (a) CR, (b) CR + SA, (c) WR1-----	111
Figure 5.24:	TEM micrographs of CR + SA and WR1 Al 6061 alloy after peak ageing treatment: (a) SA + PA, (b) WR1 + PA-----	112
Figure 5.25:	TEM image of precipitates in SA + PA sample: (a) dark field image of precipitates at lower magnification, (b) bright field image of precipitates at lower magnification, (c) bright field image of spherical and needle shaped precipitates at higher magnification, (d) SAED pattern of image shown in Figure 5.25 (a) -----	113
Figure 5.26:	TEM image of precipitates in WR + PA sample: (a) bright field image of precipitates at lower magnification, (b) bright field image of needle shaped precipitates at higher magnification, (c) SAED pattern of image shown in Figure 5.26(a)-----	114
Figure 5.27:	Variation in UTS, YS and % elongation values of Al 6061 alloy processed through various conditions; ST, T6, CR, CR+SA, WR1, SA+PA, WR1+PA-----	115
Figure 6.1:	Process flow charts of ST, CR and WR-----	121
Figure 6.2:	Typical DSC thermograms of Al 6061 alloy at various heat treated conditions: (a) ST, CR and WR and (b) close up view of image (a) showing only low temperature peaks-----	123
Figure 6.3:	DSC thermograms of Al 6061 alloy at various heat treated conditions with various heating rates: (a) ST, (b) CR, and (c) WR-----	125

Figure 6.2:	Kissinger plots for the various exothermic peaks in ST, CR and WR material-----	128
Figure 6.5:	DSC thermograms obtained with 20 °C/min heating rate along with the hardness plots of Al 6061 alloy: (a) ST, (b) CR, and (c) WR-----	131
Figure 6.6:	Bright field TEM micrograph of ST material isochronally heated up to end of the major exothermic peaks: (a) peak B and (b) peak C----	134
Figure 6.7:	Dark field TEM micrographs and (B ¹ / ₄ [001]Al) SAED for CR material heated to 238 °C (half reaction temperature) with 20 °C/min heating rate: (a) needle shaped β'' precipitates at lower magnification, (b) β'' precipitates at higher magnification observed at different location and (B ¹ / ₄ [001]Al) SAED micrograph-----	135
Figure 6.8:	TEM micrograph of CR material heated to 238 °C (half reaction temperature) with 20 °C/min heating rate: (a) Bright field TEM micrograph rod shaped β' precipitates, (b) Dark field TEM micrograph of rod shaped β' precipitates observed at different location and (B ¹ / ₄ [111]Al) SAED micrograph.-----	136
Figure 6.9:	Dark field TEM images of CR material heated to 275 °C (end reaction temperature) with 20 °C/min heating rate. Co-existence of very fine and coarse precipitates corresponding to β'' and β' precipitates at (a) lower magnification and (b) higher magnification--	137
Figure 6.10:	Dark field TEM micrographs of WR material heated to 236 °C (half reaction temperature) with 20 °C/min heating rate: (a) needle shaped β'' precipitates at lower magnification, (b) magnified view of figure (a), (c) existence rod shaped β' precipitates in the same sample and (d) (B=[011]Al) SAED micrograph for Figure 6.10 (a)-----	138
Figure 6. 11:	Dark field TEM micrographs of WR material heated to 295 °C (end reaction temperature) with 20 °C/min heating rate, showing fine β'-rod shaped precipitates-----	139
Figure 6. 3:	Dark filed TEM micrograph along with SAED patterns of CR and WR material heated to 365 °C with 20 °C/min heating rate: (a) CR and (b) WR-----	139
Figure: 6.13:	Process flow chart of various conditions in the present work-----	143
Figure: 6.14:	DSC heat flow curve of the Al 6061 alloy after ST for 2 hour followed by ice water quenching-----	145
Figure 6.15:	DSC heat flow curves in the range 10°C – 150 °C of CR material with different strain-----	146

Figure 6.16:	Effect of chemical composition on cluster peak formation in Al alloy deformed at cryogenic temperature up to true strain of 2.9-----	146
Figure 6.17:	DSC heat flow curves in the range 200 °C – 350 °C of CR material with different strain-----	148
Figure 6.18:	Effect of cryorolling on thermal behavior of Al 6061 alloy; a) ST, b) T6-----	149
Figure 6.19:	Effect of cryorolling on thermal behavior of Al 6061 alloy; a) OA, b) Pure Aluminum-----	150
Figure 6.20:	Natural ageing (NA) behavior of ST material; a) NA time up to 20 min, b) Magnified view of cluster peaks in Figure 6.20(a)-----	152
Figure 6.21:	Natural ageing (NA) behavior of ST material for longer hours-----	153
Figure 6.22:	Natural ageing (NA) behavior of CR material; a) NA time up to 1 hour, b) Natural ageing (NA) behavior of CR material for longer hours-----	154
Figure 6.23:	NA behavior of ST and CR material for 19 days-----	155
Figure 6.24:	Ageing behavior of CR material at -20 °C-----	155
Figure 7.1:	Schematic representation for sampling of hardness measurements microstructural characterization and tensile testing-----	165
Figure 7.2:	Optical micrograph of as-received material after solution treatment. Images were taken under polarized light-----	166
Figure 7.3:	Optical micrograph of Al 6061 alloy along the RD-TD plane after MDF at 77 K; a) after 3 cycles ($\sum \Delta\varepsilon=1.8$), b) after 6 cycles ($\sum \Delta\varepsilon=3.6$), c) after 9 cycles ($\sum \Delta\varepsilon= 5.4$), d) after 9 cycles showing deformation bands-----	167
Figure 7.4:	TEM Microstructures of MDF at 77 K, along with corresponding SAED pattern in inset: a) after 3 cycles ($\sum \Delta\varepsilon=1.8$), b) after 6 cycles ($\sum \Delta\varepsilon=3.6$)-----	169
Figure 7.5:	TEM Microstructures of MDF at 77 K, after 3 cycles ($\sum \Delta\varepsilon=1.8$). Area between dotted lines shows deformation bands with lamellar structure-----	170
Figure 7.6:	TEM Microstructures of MDF at 77 K, after 6 cycles ($\sum \Delta\varepsilon=3.6$). a) Microstructure at the deformation band .b), c), d) magnified view of encircled area shown in Figure 7.6a-----	171
Figure 7.7:	TEM Microstructures of MDF at 77 K, after 9 cycles ($\sum \Delta\varepsilon=5.4$). a) Bright field with SAED pattern , b), Bright field image showing recovered sub grain structure, c) Hand drawn sketch of sub grain	172

boundaries of Figure 7.7(b) ,d) Magnified view of subgrain seen in Figure 7.7(b) , arrow mark indicates array of dislocations at the boundary-----

Figure 7.8:	TEM Microstructures of MDF at 77 K, after 9 cycles ($\sum \Delta\varepsilon=5.4$)-----	173
Figure 7.9:	Mechanical properties of MDFed Al 6061 alloy; a) Variation in Vickers hardness with increasing MDF strain at 77K, b) Engineering stress Vs Engineering strain plots of Al 6061 alloy, Starting solution treated condition, MDFed conditions at 77 K up to different cumulative strains $\sum \Delta\varepsilon=1.8$ (3 cycles), $\sum \Delta\varepsilon=3.6$ (6 cycles), $\sum \Delta\varepsilon=5.4$ (9 cycles)-----	175
Figure 7.10:	SEM fractographs of tensile samples; a) Solution treated condition ($\sum \Delta\varepsilon=0$), (b) after 3 cycles ($\sum \Delta\varepsilon=1.8$), c) after 6 cycles ($\sum \Delta\varepsilon=3.6$), d) after 9 cycles ($\sum \Delta\varepsilon= 5.4$)-----	178
Figure 7.11:	Vickers hardness behavior of bulk coarse grained solution treated material (ST) and MDFed material, ageing at 125 °C; a) Variation in hardness versus ageing time plot, b) Variation in hardness of ST and MDFed material before and after ageing treatment-----	179
Figure 7.12:	Tensile testing plots of Al 6061 coarse grained alloy and MDF alloy with and without ageing; a) Engineering stress versus Engineering strain, b) True stress versus True strain-----	180
Figure 7.13:	Inverse pole figure maps of Al 6061 alloy after MDF up to 9 cycles; a) without ageing, b) with ageing-----	183
Figure 7.14:	Grain average Misorientation (GAM) profiles of 9 cycles MDF material before and after ageing treatment-----	184
Figure 7.15:	TEM microstructure of Al 6061 alloy after MDF up to 3 cycles followed by peak ageing treatment-----	186
Figure 7.16:	TEM microstructures of Al 6061 alloy after MDF with peak ageing treatment; a) 6 cycles, b) 9 cycles (Bright field micrograph), c) 9 cycles (Dark field micrograph)-----	187
Figure 7.17:	Various kind of precipitates that are observed in MDF 3 cycles after peak ageing treatment; a) Bright filed image of spherical shaped precipitates, b) Dark field image of precipitates, c) Bright filed image of needle shaped precipitates-----	188
Figure 7.18 :	Various type of precipitates in MDF 6 cycles after peak ageing treatment; a) Bright field image of spherical shaped precipitates, b) Bright filed image of fine needle shaped-----	189
Figure 7.19:	Various type of precipitates in MDF 9 cycles after peak ageing	192

treatment; a) Bright filed image of spherical shaped precipitates, b) Bright filed image of needle shaped precipitates, c) Bright filed image of needle shaped precipitates with higher magnification, d) Bright filed image of area marked with square box in Figure 7.19(c)--

Figure 7.20:	Fractured surface of Al 6061 alloy after MDF up to 3, 6 and 9 cycles followed by peak ageing; a) SEM image of 3 cycles b) SEM image of 6 cycles c) SEM of 9 cycles d) Back scattered electron image (BSE) of image shown in Figure 7.20(c), e) EDS spectrum obtained from the point indicated in the Figure 7.20(d), f) Elemental composition of EDS spectrum shown in Figure 7.20 (e)-----	193
Figure 7.21:	TEM micrograph of 9 cycles MDF material after peak ageing treatment, shows fragmentation of coarse second phase particles-----	195
Figure 7.22:	Schematic representation of sampling for mechanical and microstructural studies in MDF sample. (a) Sectioning of MDF sample, (b) Location of hardness measurements, (c) A – D represents location of EBSD scans-----	203
Figure 7.23:	Vickers hardness distribution plots on central plane of MDF material with various MDF cycles-----	205
Figure 7.24:	EBSD micrograph of 3 cycles MDF; a) Orientation image micrograph, b) Image quality map, c) Area marked with square box in the image (a), d) - f) Misorientation profiles along the line T1,T2 and T3-----	207
Figure 7.25:	EBSD micrograph of 6 cycles MDF; a) Orientation image micrograph, b) Image quality map, c) Free hand sketch of MSB developed in 6 cycles MDF; d)-f) Misorientation profiles along the line T1, T2 and T3-----	209
Figure 7.26:	EBSD map (Image quality (IQ) map) of 10 cycles MDF Al 6061 alloy at location A shown in Figure 7.22(C)-----	211
Figure 7.27:	EBSD maps of cropped area from image shown in Figure 7.27; a) Inverse pole figure map, b) IQ map overlaid with high angle grain boundaries (green color); c) IQ map overlaid with low angle grain boundaries (red color)-----	212
Figure 7.28:	EBSD data of 10 cycles MDF Al 6061 alloy at location A as shown in Figure 7.22 (c); a) Dynamically recrystallized grains partitioned using criteria, GOS <1; b) Grain size distribution plot of the partitioned area shown in Figure 7.28(a)-----	213

Figure 7.29:	EBSD map (Image quality (IQ) map)) of 10 cycles MDF Al 6061 alloy at location B shown in Figure 7.22 (C)-----	214
Figure 7.30:	EBSD maps of cropped area from image shown in Figure 7.29; a) Inverse pole figure map, b) IQ map overlaid with high angle grain boundaries (green color); c) IQ map overlaid with low angle grain boundaries (red color)-----	215
Figure 7.31:	EBSD data of 10 cycles MDF Al 6061 alloy at location B; a) Dynamically recrystallized grains partitioned using criteria, GOS <1; b) Grain size distribution plot of the partitioned area shown in Figure 7.30(a)-----	216
Figure 7.32:	EBSD Maps of 10 cycles MDF Al 6061 alloy at location C as shown in Figure 7.22(C); a) Inverse pole figure map, b) IQ map; c) Grain size map; d) Grain size distribution plot-----	217
Figure 7.33:	EBSD maps along with local misorientation profiles of location indicated with boxes in Figure 7.32(a); a), b) and c) are inverse pole figure maps of the areas indicated in boxes a, b and c respectively, d), e), f) Misorientation profiles along the lines indicated in Figure 7.33. a), b) and c) respectively-----	218
Figure 7.34:	EBSD micrograph at near to edge (at location ‘D’ in Figure 7.22(c) in central plane of 10 cycles MDF sample-----	219
Figure 7.35:	(a) Misorientation plots of microstructure observed at various strain levels; b) Misorientation plots of microstructure at various locations on central plane of 10 cycles MDF sample; A,B,C and D-----	221
Figure 7.36:	DSC curves of MDF sample after 3,6,10 MDF cycles.-----	222

List of Tables

No.	Title	Page
Table 2.1:	List of various techniques based on SPD principle used to produce UFG materials-----	7
Table 2.2:	Properties of Al 6061 alloy processed through various SPD routes-	28
Table 3.1:	Chemical composition of the Al 6061 alloy-----	42
Table 5.1:	Variation in UTS, YS and elongation values of (a) ST, (b) T6, (c) CR, (d) CR + PA, (e) WR, (f) WR + PA-----	96
Table 6.1:	Peak temperatures and activation energies of various processed conditions-----	129
Table 7.1	Mechanical properties of Al 6061 alloy after MDF followed by peak ageing treatment-----	181
Table 7.2	Values of parameters used in the equation's (7.2), (7.3), (7.4), (7.5), (7.6) and (7.8)-----	197

Definitions and Abbreviations

A	Constant
AATCP	Solid solution treated, artificially aged in 473° K for 20 min and then TCPed
APFIM	Atom probe field ion microscopy
APT	Atom probe tomography
ARB	Accumulative roll bonding
b	Burgers vector
B	Constant
C	Solute content
CG	Coarse grained
CR	Cryorolling
DB	Grain boundary spacing
DSC	Differential scanning calorimetry
EBSA	Equal channel angular pressing
ECAP	Equal channel angular pressing
EDS	Energy dispersive spectroscopy
f	Fraction of HAGBs
FCC	Face centered cubic
FSP	Friction stir processing
FSP	Friction stir processing
G	Shear modulus
GB	Grain boundaries
GBS	Grain boundary strengthening
GNB	Geometrically necessary boundaries
GND	Geometrically necessary dislocations
GOS	Grain orientation spread

HAGBs	High angle grain boundaries
HPT	High pressure torsion
IPF	Inverse pole figure
IQ	Image Quality
k	constant
LAGBs	Low angle grain boundaries
M	Taylor's factor
MAF	Multi axial forging
MDF	Multi directional forging
MEMS	Microelectromechanical systems
MMC	Metal matrix composites
NATCP	Solid solution treated, naturally aged for 21 days and then TCPed.
OA	Overaged
OIM	Orientation image micrograph
OM	Optical microscopy
PA	Peak ageing
SA	Short annealing
SEM	Scanning electron microscopy
SPD	Severe plastic deformation
SSSS	Super saturated solid solution
SSTCP	Solid solution treated then TCPed
TCP	Tube channel pressing
TCPAA	Solid solution treated, TCPed and then artificially aged in 473 K for 20 min.
TCPNA	Solid solution treated, TCPed and then naturally aged for 21 days
TE	Twist extrusion

TSL	Tex SEM Laboratories
UTS	Ultimate tensile strength
WR	Cryorolling 70% + Warm rolling 66% at 145 °C
WR1	Cryorolling 80%+ Warm rolling 50% at 200 °C
XRD	X-ray diffraction
YS	Yield strength
α	Material dependent constant
β	Constant
γ	Constant
θ_{LAGB}	Average value of LAGB misorientations
ν	Poisson ratio
σ_0	Peierls-Nabarro stress

Chapter 1

Introduction

Aluminum alloys are known for their high specific strength, good ductility and better corrosion resistance for various structural applications in aerospace, automobile and construction engineering sectors [1]. The conventional mechanisms that are used to enhance strength of the aluminium alloys are solid solution strengthening, strain hardening and precipitation hardening. The thermal treatments and especially the precipitation hardening arising from ageing treatment is well suited for the manufacturing of cost-effective final products using Al alloys. Therefore, precipitation hardenable Al alloys are widely used structural materials in aerospace and transportation industries. In precipitation hardenable alloys, the strength is achieved through impeding the motion of dislocations by precipitates. The precipitation strengthening can be achieved through natural ageing or artificial ageing of solid solution treated material. During the process of ageing, the redundant alloying elements as solutes in the supersaturated solution evolve out in the form of nano clusters, followed by formation of different intermediate metastable phases, which subsequently transform in to stable phases. The coherent and semi coherent nature of the metastable phases with matrix leads to strengthening of the alloy during straining. The nature, size, volume fraction and distribution of the precipitates determine their contribution for strengthening of the precipitation hardenable Al alloys. Al 6061 is a medium strength age hardenable alloy, has been used for the fabrication of food containers as well as various structural components of aircraft.

An ever growing demand for better performance of materials in aerospace and automotive industries and the urgent need to reduce fuel cost motivates engineers and scientists to develop new materials with superior mechanical and corrosion resistance properties. The excellent mechanical properties of nanostructured (microstructural features less than 100 nm) and ultrafine grained (grain size less than 1000 nm) materials as compared to coarse grained materials has attracted the attention of materials scientists, worlds wide. The major challenges to the scientific community lie in producing the nano or ultrafine grain morphology in bulk products so as to be exploitable in fabricating the structural components in heavy engineering applications. Severe plastic deformation techniques (SPD) have been identified as potential routes for producing bulk nanostructured Al alloys. SPD techniques involve large plastic strain during deformation to

achieve significant grain refinement [2]. The unique features of SPD techniques are [2]; i) the high strain is imposed without any significant change in the overall dimensions of the work piece, and ii) the shape is retained by using special tool geometries that prevent free flow of the material and thereby produce a significant hydrostatic pressure, which is essential to achieve better grain refinement through generation of high densities of lattice defects in the bulk materials. The various SPD processes used to produce UFG structure in Al alloys are; equal channel angular pressing (ECAP) [3], high pressure torsion (HPT) [4], multi axial forging (MAF), hydrostatic extrusion (HE), twist extrusion (TE) [5] [6], accumulative roll bonding (ARB) [7] [8], friction stir processing (FSP) [9] and severe cold rolling [10] [11] [12]. According to the definition of SPD process, techniques such as ECAP, HPT, MAF, TE, and HE produce UFG structures in the materials without significant changes in initial dimensions of the samples. Along with the deformation strain, process type and temperature also play an important role in achieving homogeneous grain refinement. It is well known fact that the mechanism of grain refinement involves continuous generation and multiplication of dislocations in the coarse grains during deformation and their subsequent rearrangement through migration leads to the formation of sub grains with dense dislocation walls. The another mechanism commonly observed is formation and intersection of micro shear bands, which results in the formation and transformation of low angle grain boundaries to high angle grain boundaries. The shear band formation is commonly observed at lower deformation temperature due to strain localization, where the mobility of dislocations is restricted and also it depends on the materials and its alloying elements.

By subjecting material to severe plastic deformation (SPD), grain size gets reduced and its yield strength increases as per Hall-Petch effect. Along with grain boundary strengthening in ultrafine grained materials (UFG), nano precipitation achieved through suitable thermo mechanical treatment would enhance the strength of UFG materials as reported in the literature [13] [14]. The other important structural features such as dislocations, subgrain boundaries, nano-twins and solute atoms are found to be vital for strengthening of the material in addition to the above two strengthening factors. The substantial improvement in strength of the UFG material with the above discussed structural features is due to the sum of all the individual factors contributing to strengthening mechanisms.

The strength and ductility are important primary properties for the materials used in structural applications, which can be achieved by microstructural engineering. Materials after

SPD show high strength but low ductility due to poor work hardenability. In last two decades, a special focus is given to develop the strategies to increase strength of the ultrafine grained materials without loss of their ductility. In pure metals with UFG structure, the ductility of the material is increased by slight compromise on strength. Ductility in Al alloys can be improved by subjecting it to SPD below the artificial ageing temperatures followed by low temperature ageing. During this SPD processing, the drop in strength due to recovery during ageing is compensated by precipitation hardening effect to the matrix during straining. The increase in ductility in the alloy is due to its ability to accumulate dislocations surrounding the precipitates during SPD processing.

In precipitation hardenable ultrafine grained/nanostructured aluminium alloys, the strengthening mechanisms are due to grain size strengthening (σ_{GS}), precipitation strengthening (σ_{PS}), solid solution strengthening (σ_{SS}), and dislocation strengthening (σ_{DS}). All these mechanisms do not work in unison for improving the strength. Exploiting maximum contribution from each efficient strengthening mechanism is a viable option for realizing the improved strength in the alloys with the reduction in ductility. In coarse grained aluminum alloys, precipitation hardening is found to be most efficient strengthening mechanism. SPD processing of alloy generates several structural defects in the material and these defects influence the precipitation sequence significantly and its coherency with the matrix. To realize the cost effective and more efficient method of production of high strength materials through SPD processing, the improvement in mechanical properties achieved through this route should be significantly higher than the conventional processing routes. The precipitation behavior of UFG Al alloys is found to be different from its coarse grain counterpart. Therefore, a thorough investigation is necessary to understand the precipitation behavior in UFG Al alloys. In most of the SPD techniques (ECAP, HPT, ARB, HE, FSP) the materials undergo severe plastic deformation either at room temperature or elevated temperature. This leads to continuous phase transformation due to uncontrolled precipitation process, which is complex to understand in UFG Al alloys [15] [16] [17] [18]. However, the process, such as involving deformation at cryogenic temperatures allows controlling the precipitation phenomena by suppressing diffusion during the deformation process. Cryorolling and cryoforging are low temperature deformation techniques, are well known in the literature. .

Cryorolling is one of the ideal deformation processing techniques used to produce UFG structure in Al alloy sheets. The total strain required to produce UFG structure is reduced substantially due to the suppression of dynamic recovery during cryorolling. Multi directional forging (MAF) is an established SPD processing technique to produce UFG structures in the bulk metals and alloys. It enables to impart very large strain (higher than 6.0) to the materials and the processability at wide range of temperature during deformation. MAF at cryogenic temperature exploits the combined effect of very low temperature and very high plastic strain induced during processing for the efficient production of UFG structure in the alloys.

The literature on precipitation kinetics and its influence on mechanical properties of Al 6061 processed by cryorolling, warm rolling, and cryoforging is very limited. Therefore, the present work has been focused mainly on production of ultrafine grained Al alloy (Al 6061) from its bulk alloy by adopting various thermo mechanical routes such as cryorolling, combination of cryorolling followed by warm rolling and cryoforging and investigate the influence of these deformation routes on microstructural evolution and mechanical behavior. A novel method to produce high strength Al 6061 aluminum alloy has been proposed based on the present work.

Chapter 2

Literature review

2.1 Introduction

In this chapter, the principles of production of bulk ultrafine grained (UFG)/ Nano structured materials by various SPD techniques are discussed in section 2.2. The properties of UFG/Nanostructured materials are discussed in section 2.3

2.2 Principle of Severe Plastic Deformation

In the polycrystalline metals, grain size plays a crucial role in deciding its mechanical properties such as strength, ductility, fracture toughness etc. In conventional coarse grained material, the grain size falls in several microns. The physical and mechanical properties of coarse grained materials are well understood. It is well known that the materials with ultrafine/nanosized grains exhibit excellent physical, mechanical and chemical properties over bulk coarse grain materials. The term “Ultrafine grained materials (UFG)” is used for the materials with grain size within the range of 100-1000 nm [4] [3] [19]. “Nanostructured materials (NS)” is the term used for the material where the microstructural features are within the size range of 1-100 nm at least in one dimension [20].

The methods to produce UFG/NS materials can be broadly classified in to two approaches. First is the “Bottom up” approach in which the UFG/NS materials are developed through assembling individual atoms, or from nanoscale building blocks such as nano particles [20]. The bottom-up methods are inert gas condensation [21], high energy ball milling [22], electro deposition and chemical and physical deposition technique [23].

In “top-down” approach, bulk materials with coarse grain size are processed through the techniques where the material undergo severe plastic straining or shock loading to develop fine structural features. Under sever plastic straining, high density of dislocations is generated inside the coarse grains and they rearrange themselves into grain boundaries network to evolve a new grains. Usually, the material processed through SPD techniques possesses structural features with less than 1000 nm. Most of the SPD techniques are designed in such a way that the cross-

sectional dimensions of the work piece are not affected. This feature is necessary for SPD techniques in order to induce high strains. There are several advantages with top down approach (SPD techniques over bottom up approaches as given below.

- i) SPD techniques enable to produce UFG/NS materials in bulk
- ii) A fully dense, porous free structure is possible to achieve in the bulk nanostructured materials.
- iii) SPD techniques are derived from classical metal forming techniques, which can be easily implemented in industry for bulk production.

2.3 SPD techniques

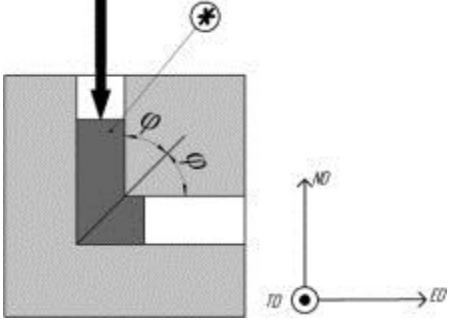
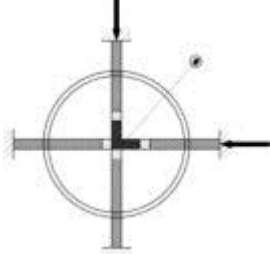
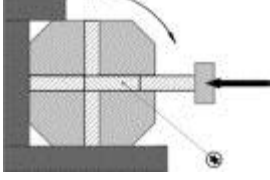
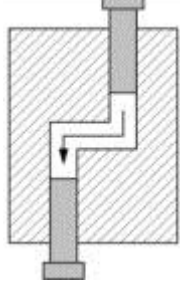
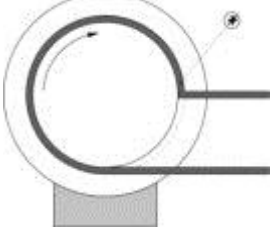
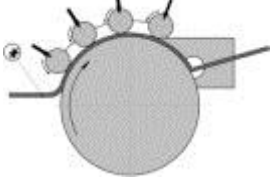
The most popular and widely investigated SPD techniques are ECAP, HPT and MDF. Feasibility of processing bulk materials using MDF and ECAP at high temperatures made them popular for producing nanostructures in brittle materials also. The other popular SPD techniques are accumulative roll bonding, continuous confined strip shearing, twist extrusion and constrained groove pressing, etc. Among conventional sheet metal forming techniques, cryorolling and asymmetric rolling have been widely used to develop UFG/Nano grain structure in the material. There are several other techniques developed recently using the basic principle of SPD and they are listed in *Table 2.1*

2.3.1 Equal channel angular pressing

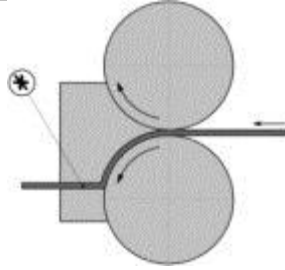
ECAP principle

ECAP for the production of ultrafine grain/nanostructured materials was first developed by Segal and his co-workers in 1981 [24]. After their work, interest in the production of UFG/NS materials through SPD has been ever growing. In this technique, a material with uniform cross section is forced through a intersecting channels of the same cross section (*Figure 2.1*) under minimum friction conditions [25] [26]. During this process, material undergoes shear localization along a fixed plane under steady state [24] . This process is repeated by rotating orientation of the material blank along the length direction after every pass. The amount of imposed strain can be increased by applying back pressure at the end of the sample and by increasing number of passes. The grain refinement takes place through simple shear. With increasing number of passes, the average misorientation of the grain boundaries increases, which leads to formation of high angle grain boundaries in the material [27] [28] [29] [30] .

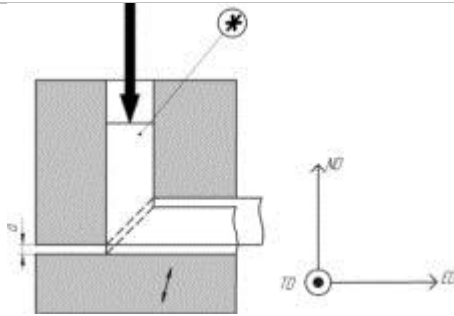
Table 2.1: List of various techniques based on SPD principle used to produce UFG materials

Process	Schematic representation
1) Equal-channel angular pressing (ECAP) [31]	
i) Repetitive side extrusion [31]	
ii) Rotary-die ECAP [31]	
iii) Parallel channel ECAP (PC-ECAP) [31]	
iv) ECAP- Conform [31]	
v) Con-shearing [31]	

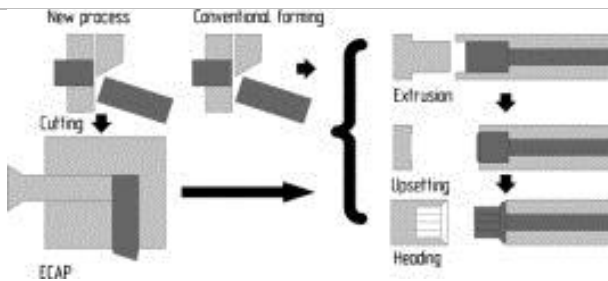
vi) Continuous confined strip shearing (C2S2) [31]



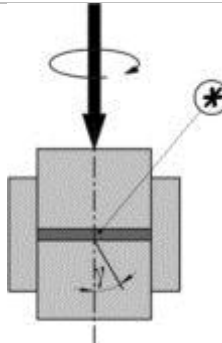
vii) Incremental ECAP (I-ECAP) [31]



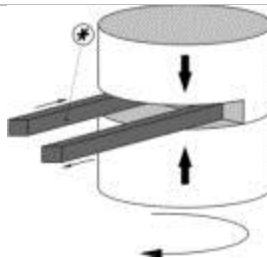
viii) Continuous manufacturing of bolts [31]



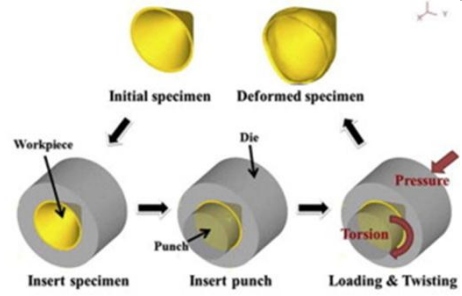
2) High-pressure torsion (HPT) [31]



i) Continuous high-pressure torsion [31]

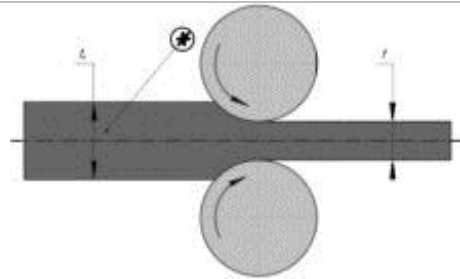


ii) Hollow Cone -HPT process
[32]

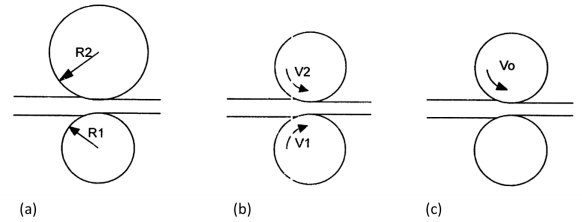


3) Rolling based techniques

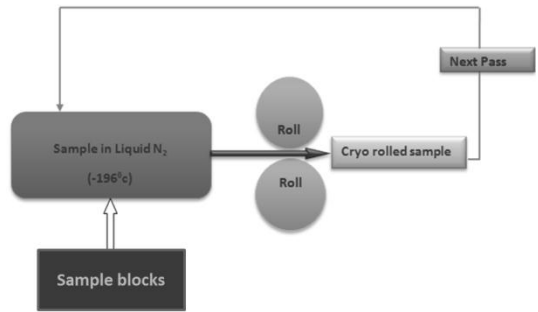
i) Accumulative roll bonding
(ARB) [31]



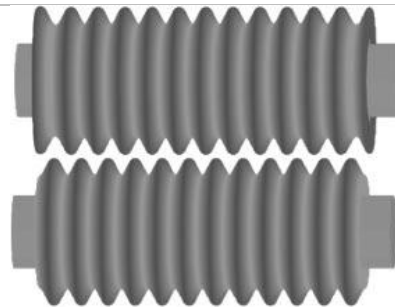
ii) Asymmetric rolling [33]



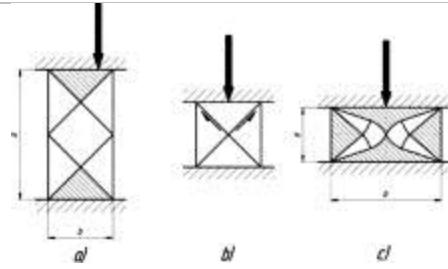
iii) Cryorolling [34]



iv) Wavy rolling [35] [36]

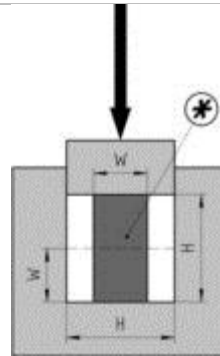


4) Multi-axial forging [31]



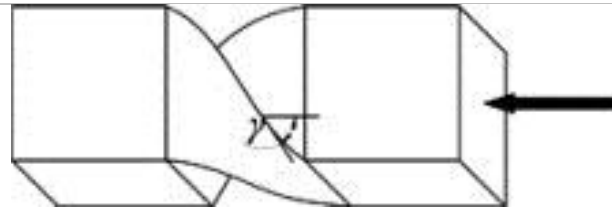
i) Channel die forging

ii) Cyclic close-die forging (CCDF) [31]

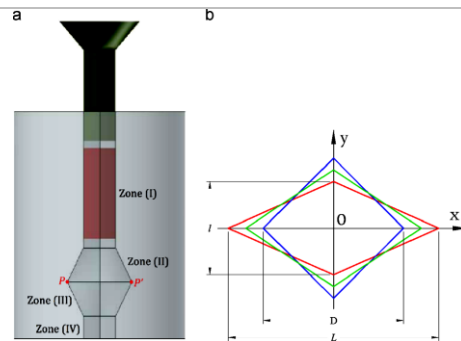


5) Extrusion based techniques

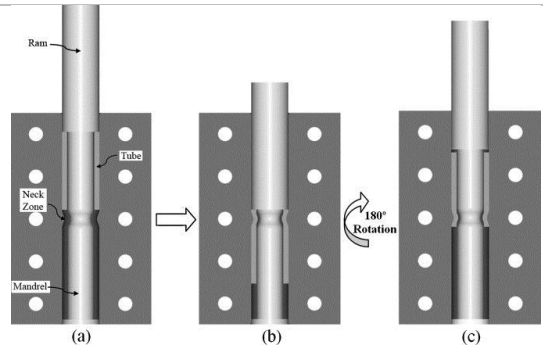
i) Twist extrusion [31]



ii) Pure shear Extrusion [37]

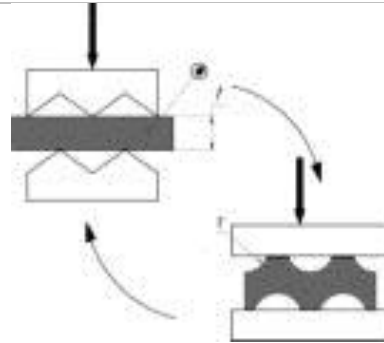


iii) Tube Channel Pressing (TCP)
[38]

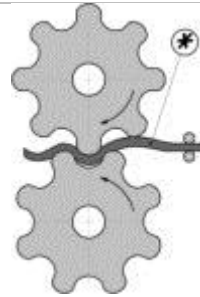


6) Other techniques

i) Repetitive corrugation and straightening (RCS) [31]



ii) Continuous repetitive corrugating and straightening (RCS) [31]



ECAP has become very popular technique to produce UFG structure in various metals such as Al [27] [28] , Cu [39], Mg [40] and Ti [41], and their alloys [30] [42] and intermetallics [43]. In the last decade, rapid progress in modifying the basic ECAP process has been made in order to develop effective processing procedure for continuous production, which would be suitable for industrial applications [44] .

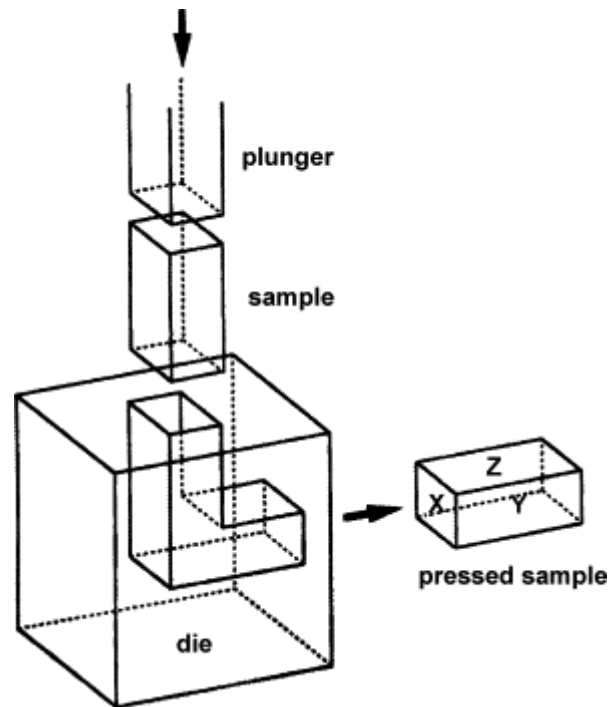


Figure 2.1: Schematic representation showing the principle of ECAP processing ([26]

2.3.2 High pressure torsion (HPT)

HPT technique is derived from Bridgman technique which was used to increase the torsional strength of the samples by applying compressive and torsional forces simultaneously (*Figure 2.2*) [45]. The typical shape of the samples that can be produced through this technique is in disc form. Improved mechanical properties have been realized through this process [39]. The major advantages of HPT process is due to its ability to produce materials with exceptionally small grains sizes, often lying in the lower sub micrometer or nanometer range [46]. It often produces grain boundaries with high fraction of high angle grain boundaries [46] [47].

The limitations of the HPT are as follows; i) The microstructure and property in the samples processed through HPT is not homogeneous due to inhomogeneous strain distribution in the samples, ii) It is limited to produce small scale samples only, iii) The tooling and equipment cost is relatively high.

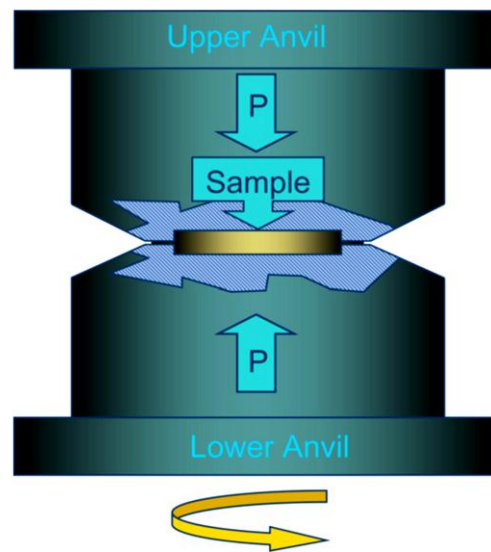
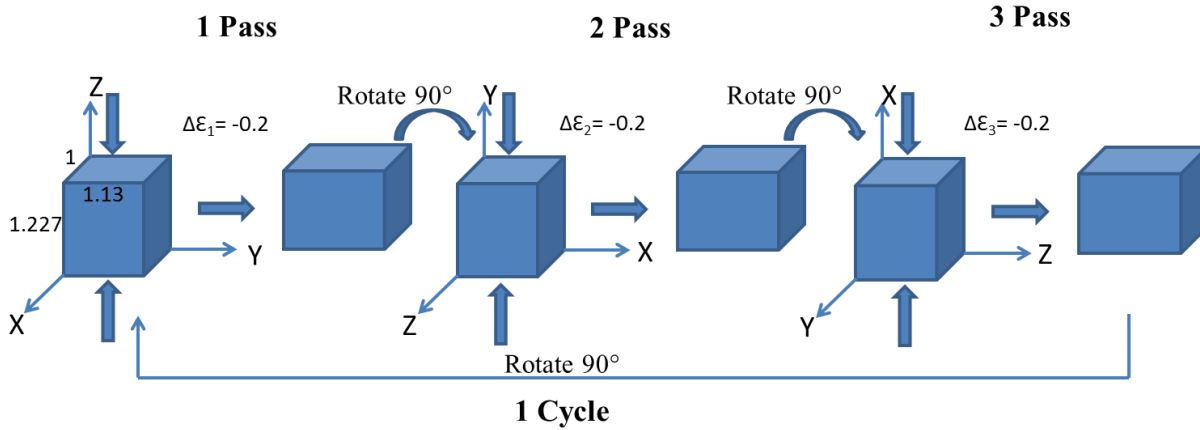


Figure 2.2: Schematic representation of Bridgman apparatus [48]

2.3.3 Multi directional forging (MDF)

Multiple forging also known as multidirectional forging, developed in the year 1990, has been used to refine the microstructures of bulk billets of titanium alloys, magnesium alloys and high strength nickel base alloys [49]. It is the simplest method to achieve larger strains with minimum distraction from its original shape and allows processing of bulk products [50]. Multidirectional forging involves repeated setting-drawing in three orthogonal directions. Along with deformation strain, deformation temperature also plays a critical role in refining the grain structure. MDF with high processing temperature is used to produce fine grain structure in brittle materials. Magnesium and its alloys have been successfully MDFed at room temperature to elevated temperatures [51] [52] [53] [54]. Cherukuri et al. [55] have performed multi-axial

forging (MAF) on Al 6061 alloy and reported that MAFed material has shown similar trends in mechanical properties with ECAPed material. It has also been reported that non-uniform distribution of micro hardness observed at initial deformations, has decreased with increasing accumulated strain [55]. *Figure 2.3* shows the principle of MDF.



Equivalent strain in one pass : $\Delta\epsilon_i = \ln(1/1.227) = -0.2$
 Cumulative strain in one cycle: $\Delta\epsilon_{n=1} = |\Delta\epsilon_1 + \Delta\epsilon_2 + \Delta\epsilon_3| = 0.6$

Figure 2.3: Schematic representation of multi directional forging.

2.3.4 Accumulative roll bonding (ARB)

At first Saito et al., [56] have proposed this technique to produce UFG structure in the various metals and alloys. The process involves stacking of two strips one above another and subjected to conventional rolling process with reduction per pass by ~50%. Here, conventional rolling process is used to produce bond between two layers. For a sound bonding between two layers, the surface of the strips was properly surface treated. The obtained sheet after rolling is cut into two halves in length direction. The sectioned pieces are stacked again after surface treatment and rolled again. The whole process is repeated again and again to induce severe strain in the material. The grain refinement takes place in the material through pure shear [56]. *Figure 2.4* shows the schematic representation of the ARB process. Later this process has been successfully used to produce metallic multi layered composites by performing roll bonding between dissimilar metals and alloys [57] [58] [59] [60] [61]. In addition, ARB is also applied for the production of metal matrix composites by sheathing mixed powders and subjecting them to a roll-bonding process [31] [62]. The advantages of this process are simplicity, cheap

manufacturing, capability of mass production and easy adoptability in industrial process [63]. Despite of several advantages, the disadvantages are lengthy process, poor ductility due to breakage of bond between layers.

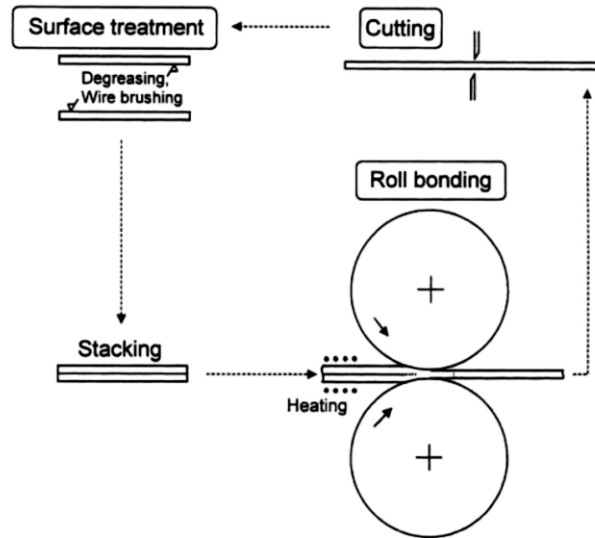


Figure 2.4: Schematic representation of ARB process [56]

2.3.5 Asymmetric rolling

Asymmetric rolling (ASR) process was developed by Kim and Lee [64] to produce shear texture in the material through shear deformation. Later Jin and Lloyd [65], Cui and Ohori [66] have applied ASR at room temperature to develop fine grained structure in the AA 5754 alloy and pure Al respectively. Grain sizes with 1-2 μm were obtained in pure Al alloy due to dynamic continuous recrystallization and in AA 5754 after static recrystallization. ASR also known as differential speed rolling (DSR) in which the diameter of the rolls is different or the rotating speeds of the upper and lower rolls are different from each other (*Figure 2.5*). It can employ additional shear strain to the material in addition to compressive force [65] [66]. It has been successfully used for various metals and alloys for grain refinement and texture modifications [33][67] [68] [69] [70]. The advantages of ASR over symmetric rolling are [71]; i) It can introduce much more redundant shear deformation, ii) Promotes the deformation to extend to the center regions of the rolled sheets.

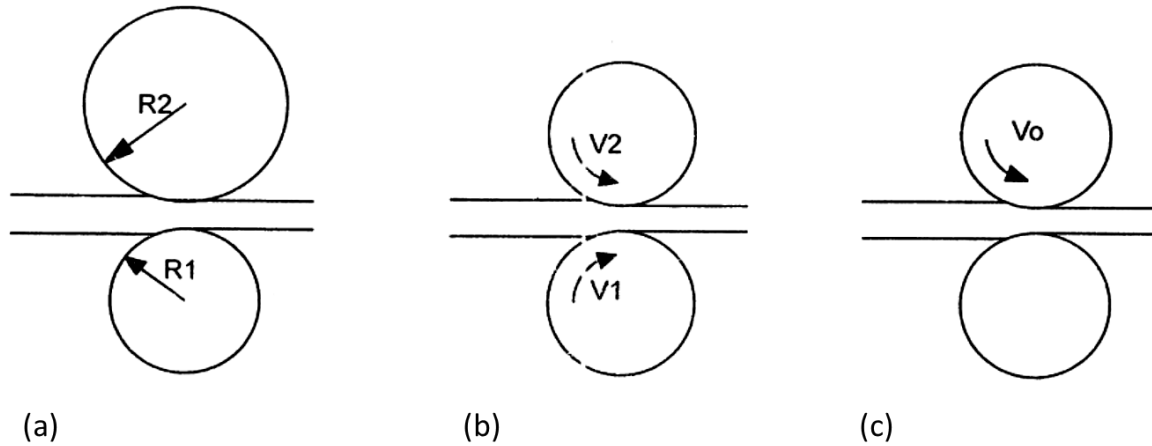


Figure 2.5: Schematic representation of asymmetric rolling due to (a) Non-unity roll radius ratio, (b) Non-unity roll speed ratio and (c) Single roll drive rolling [33].

2.4 Cryorolling

Cryorolling has been used as a popular technique to produce UFG structure in various metals and alloys due to various advantages over other SPD techniques. Grain refinement mechanism is dependent on various factors such as amount of strain imposed and processing temperature. The amount of strain required to produce UFG structure is reduced by decreasing the processing temperature. The major advantage of cryogenic deformation process over other SPD techniques is due to its ability to produce UFG structure with less induced strain. The starting material should be in sheet form to produce sheet metal products for high strength applications. Cryorolling process can be used easily to produce lengthy sheets and it is viable for industrial scale production without significantly affecting the existing production process. The cryorolling process can be accomplished by using conventional rolling mill and by using liquid nitrogen. During the process, samples were dipped in liquid nitrogen and sufficient time is given to attain the samples temperature to liquid nitrogen temperature and then rolling is performed. Rolling at very low temperature (near to liquid nitrogen temperature) suppresses dynamic recovery, which results in accumulation of dislocation.

The effect of cryogenic deformation on stored energy and recrystallization behavior of Al alloys (Al 3004(Al-Mn) and Al 5083 (Al-Mg)) was first reported by Furui et al., [72] in 1999. They have reported that the stored energy and work hardening imparted by two-directional rolling at cryogenic temperature were larger than of the two directional rolling at room temperature. The grain size after recrystallization was found to be lower than that of the materials

processed at room temperature conditions [73]. It is attributed to increased stored energy due to cryogenic deformation. The stored energy and its release rate during recovery and recrystallization process of Aluminium alloys rolled to 90% reduction at cryogenic temperature have also been reported [74]. DSC measurements have shown that in the cryorolled materials, the stored strain energy is released at 173 K and it has increased with increasing temperature up to 573 K. The released amount of stored strain energy is largest in pure Al than the alloys.

Noda et al., [75] have reported improvement in mechanical properties of Al 3004 alloy by heavily working at cryogenic temperature. Heavily deformed material has been subjected to short annealing to produce fine grains. With decreasing short annealing time, better improvement in mechanical properties by smaller grain size has been achieved. However, the formation of UFG/NS was not reported as the minimum grain size was found to be above 2-3 micrometers in their work [75]. It is attributed to complete restoration of heavily deformed structure with ultrafine subgrains during recovery and recrystallization at high temperatures. Later, in the course of investigation of development of UFG/NS material with high strength and good ductility, Wang et al. [76] have observed the UFG structure with grain size below 200 nm in cryorolled Cu. Since then, cryorolling has become a very popular technique to produce UFG/NS in the metals and alloys. Several metals and alloys have been successfully processed through cryorolling.

2.5 Homogeneity evolution in SPD processed materials

Even though the production of UFG/NG structured materials through SPD processing of bulk materials is an established technique, there are issues which limit the application of UFG/NG structured materials. One of the issues is microstructural inhomogeneity in the SPD processed samples. There are several published reports on homogeneity evolution studies through hardness measurements in various SPD techniques [46] [77] [78] [79] [80] [81] [82] [83] [84] [85] [86] [87] [88] . The degree of homogeneity can be easily tracked by measuring hardness with increasing degree of deformation. SPD processing has both positive and negative effects on homogeneity of microstructural features. In certain cases, SPD leads to homogeneous microstructure with UFG formation. Starting materials with as cast structure possesses lot of second phase segregations at the grain boundaries and dendritic structures. SPD leads to break down of cast structures and distribution of coarse particles enhances microstructural homogeneity and mechanical properties [88] [89]. Whereas, in the starting alloys with wrought structures and in pure metals, inhomogeneity can be clearly seen. In principle, the shear strain imposed in ECAP

process is homogeneous [90] [91]. However, in practice, there are several factors that affect homogeneity such as; die angle, frictional forces between the die wall and billet walls, presence of dead zone in the corners, and end sections [92] [93] [94]. It was reported that by increasing number of passes, applying back pressure [95] and with proper lubrication between die wall and billet wall, inhomogeneity can be minimized.

In HPT, the measured hardness values at the center are less as compared to the periphery. However, it was observed that with increasing number of turns and applied pressure, the extent of inhomogeneity decreases [46], which is not consistent. The different views of homogeneity evolution of various metals processed through HPT are attributed to the different stacking fault energy of the materials [47] [96] [97] [98] [99]. Lee et al., [84] have studied the homogeneity evolution in ARB processed Al 6061 alloy through hardness measurements along the thickness direction. It was reported that, the inhomogeneous distribution in hardness through the thickness is due to the redundant shear strain near the surface and the wire-brushing before the roll-bonding [84]. Cherukuri and Srinivasan [55] have observed the non-uniform hardness distribution in MDF at the initial deformation steps, but with increasing strain, the difference in hardness has been reduced.

2.6 Hybrid materials

SPD has been successfully used to produce the materials with superior physical and mechanical properties over conventional coarse grained materials through nanostructuring. However, achieving multi-functional properties through a single material is difficult. For this, hybrid material may be the solution. The scope of UFG material applications can be widened by combining two or more materials to develop hybrid material with desired properties. SPD techniques could be used to produce hybrid materials. Processing of hybrid materials through SPD has dual benefits as i) it allows production of final product with hybrid materials; ii) it is possible to produce hybrid materials with fine grained structure. SPD techniques enables production of composites and hybrid materials, particularly multi layered metal matrix composites, bi-material tubes and other combinations of materials [100]. The SPD methods that are suitable for the production of hybrid materials are ARB, HPT, Torsion and Extrusion.

2.7 Thermal stability

It is essential to ensure thermal stability of UFG materials besides achieving superior mechanical properties of SPD processed material at room temperature. The stored energy of the metal increases when it is subjected to cold working. It is the characteristic of the process of cold working and the energy stored by the metal is an essential feature of the cold worked state [101]. The stored energy makes the metal unstable and under favorable conditions, metal will undergo restoration process. Hot working is the process where the metal undergoes plastic deformation above critical temperatures, thus no energy is stored during the process [101]. The essential characteristic of the stored energy of cold work is that remains in the metal until it is released during a restoration process [101]. In UFG production, materials processed through cryogenic deformation, often subjected to post processing annealing to reduce the stored energy. Most of the SPD processes are carried out at room temperature, or below critical temperature. The objective of SPD processing is to enhance the mechanical properties of the materials. The enhancement in strength of materials is realized through grain refinement by severe plastic deformation. The microstructure that develops through SPD is observed to be sensitive to the elevated temperature [102]. For instance, SPD processed pure oxygen free copper is found to be sensitive even to room temperature [31]. SPD processed Cu through ECAP has shown poor thermal stability than cold rolled Cu with same strain [103]. This is attributed to lower activation energy for discontinuous recrystallization with increasing ECAP passes. In cryorolling process, rolling at near to the liquid nitrogen temperature is used to induce large cold work energy even with lower strains and controlled annealing process allows developing material with desired properties [76]. Severely deformed Cu through cryorolling has shown formation of coarse grains in the micron size with just 3 min of annealing at 200 °C [76]. The loss of stability depends on the amount of strain imposed, temperature, and purity of the material.

To increase the applications of UFG materials for elevated temperature applications, its thermal stability has to be enhanced. Several strategies have been followed to enhance the thermal stability of the UFG materials. Bhaumik et al., [104] have demonstrated the effect of additional mechanical stress during annealing of SPD AA 3103 alloy. Additional stress during annealing results in retardation of recrystallization and led to stable microstructure (shown in *Figure 2.6*). However, the recovery rate is faster under external load.

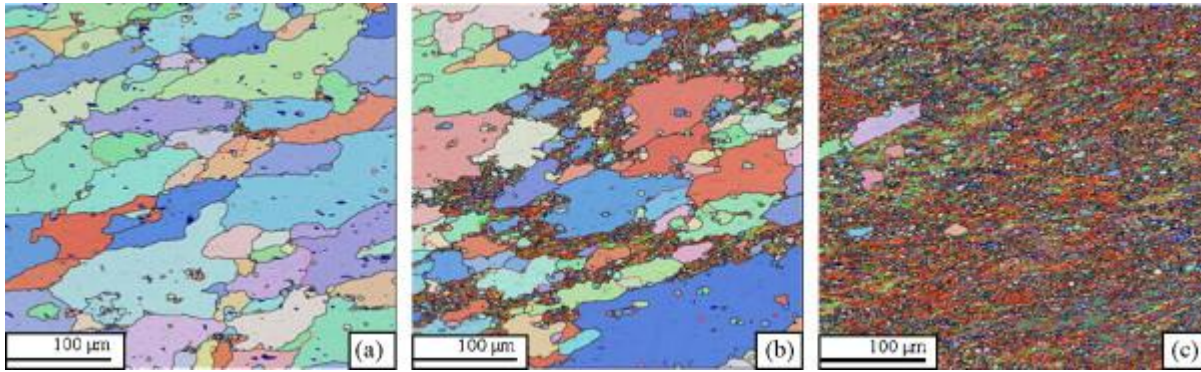


Figure 2.6: Microstructure of initially ECAP deformed material (two ECAP passes in Route Bc) after annealing at 320 °C under the influence of an additional stress of 1.25 MPa (a), 5 MPa (b) and 15 MPa (c) [104].

Addition of scandium to the aluminium alloy has significantly increased the thermal stability of the fine grained structure formed during SPD [105] [106] [107]. Similarly, addition of Cr and Zr to the Cu has increased stability of the UFG structure under elevated temperatures at 500 °C [108]. The strategies applied to improve other properties such as strength, ductility, and fracture toughness could also help to enhance the thermal stability of the microstructure. The selection of apt thermo mechanical process will also help to optimize the multi-functional properties such as thermal, mechanical, and electrical properties. For example, in precipitation hardenable Al alloys, post ageing at low temperature, after cryorolling, leads to relieve the internal stresses, increases ductility by reducing dislocation density, increases strength by precipitation hardening and reduces grain coarsening through pinning of grain boundaries by precipitates [109] [110] [111] [112] [113].

2.8 Applications of UFG material

UFG/NS materials could serve as potential materials for structural and functional applications in various engineering sectors such as aerospace, constructions, automotive, defense, electronics, biomedical, etc. [114] [115]. The process of commercialization of UFG/NS materials is hindered due to small size of SPD processed material and their cost of production [115]. However, the recent developments in SPD techniques, allowed scaling up of the processing up to industry production level.

A) Biomedical applications

The metals such as Fe, Mg, and Ti are widely used for biomedical applications as body implants. The field of biomaterials is significantly growing due to ever increasing demand for bio implants. The physical properties that are generally considered for biomaterials includes hardness, tensile strength, modulus, elongation, fatigue strength, impact properties, wear, dimension stability, biodegradability, biocompatibility [116]. Materials for permanent implants such as bone and tooth replacements should possess inert behavior in body fluids, whereas for temporary implants, material must degrade at a suitable rate for the targeted application [31]. Titanium alloys are widely using as permanent body implants due to its excellent combination of physical and electrochemical properties. Implants with pure Fe and Mg are highly biodegradable. Recent studies have proven that UFG materials processed through SPD can be used as suitable candidates for biomedical applications [117] [118] [119] [120] [121] [122] [123]. The reported literature shows that the commercial pure Ti with UFG structure developed through SPD will be better replacement for Ti alloys. By nanosizing the microstructure of CP Ti, the mechanical behavior and biocompatibility have increased [122] [123]. The materials processed through SPD have shown better corrosion resistance in body fluids over coarse grained materials. Fine grained Mg has shown significant enhancement of fatigue life and endurance limit as well as reduction in corrosion rate in Hanks solution [124]. In particular biomedical applications, high dissolution rate of materials might require. Instance UFG Copper processed through ECAP, with grain size 380 nm has shown higher corrosion current than coarse grained Cu in Hanks's solution [118]. Fine grained Cu is excellent material for contraception applications [118],

B) Microelectromechanical systems (MEMS)

In order to have a better mechanical strength of the micro parts in MEMS, the average grain size should be less than the part dimension. UFG/NS materials are suitable candidates for these applications. Latest developments in SPD by miniaturizing the processing technique allows to produce micron scale products with desired grain size to enhance the strength and fracture toughness of the material [125]. For instance, UFG AA 1050 produced through ECAP has shown better surface smoothness and thermal conductivity as compared to coarse grained material in micro heat exchanger applications [126] [127]. *Figure 2.7* shows the surface morphology of hot embossed UFG Al-1050 and coarse grained Al 1050 alloy. The top surface of micro channels of the coarse grained alloy is rougher than UFG alloy [126].

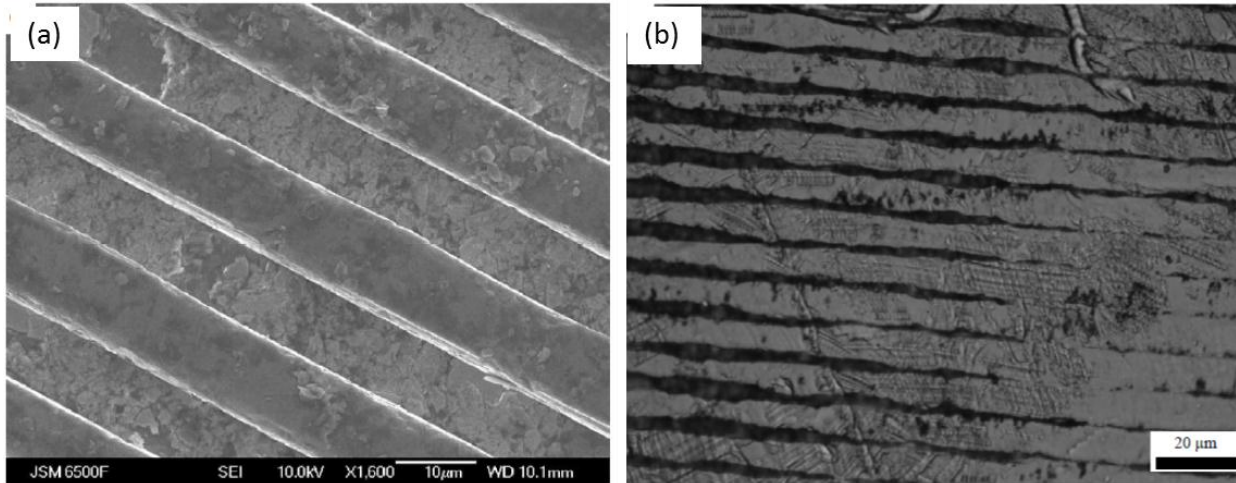


Figure 2.7: a) SEM micrograph of top surface of hot embossed UFG Al 1050 alloy; b) Optical micrograph of top surface of hot embossed coarse grained Al 1050 alloy [126].

2.9 Aluminium alloys

Aluminium is the second most used metal [128] and third most common element on the earth [129]. As compared to other common metals, it is new comer owing to difficulty of its extraction from its ores. Aluminium in the high pure form is very soft and light and it exhibits yield strength of only 7-11 MPa. In its pure form, it has limited applications, like packaging materials and electrical applications because of its light weight, soft and good thermal conductivity, respectively. In annealed condition, the strength of the Al can be increased only through alloying to provide solid solution strengthening. Based on the alloying elements and its processing routes, Al alloys are broadly classified in to cast alloys and wrought alloys with different series.

2.9.1 Aluminium in Modern life

Aluminium has become essential element in the modern life due to its light weight, durability and infinite recyclability. Without Aluminium, many of the conveniences would not have existed today. In fact, people use more aluminum today than at any point in the 125-year history of the metal's commercial production [130]. Some of the facts of Aluminium and its usage in the modern life are [130]

- i) Every person in the most of the world uses aluminium in every single day.

- ii) The world is striving for more fuel efficient future, where the aluminium is playing a big role.
- iii) Aluminum is an essential element to this country's energy and manufacturing future.
- iv) In the United States, the Aluminium industry today supports 672,000 jobs and \$152 billion in economic output, which is nearly 1 percent of GDP.

According to 2013 statistics, the consumption of Aluminium in US is shown in below *Figure 2.8*.

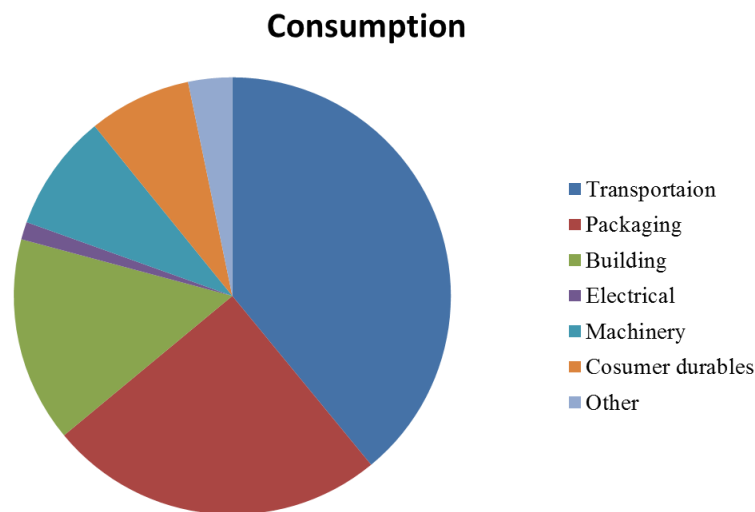


Figure 2.8 : Consumption of Aluminium in various sectors (Data plotted based on 2013 reports)

2.9.2 Properties of Aluminium and its alloys

1. High specific strength with good formability and good weldability makes this aluminium alloys important materials for aerospace and automobile applications.
2. Good corrosion resistance by forming thin oxide layer which is adherent to the surface and possible to enhance the corrosion resistance by anodizing the surface allowed aluminium alloys as potential candidates for naval applications.
3. High thermal and electrical conductivity allowed their use in electrical and heat exchanger applications.
4. Nonmagnetic property makes arc welding of Aluminium and its alloys easier.
5. High toughness at very low temperatures enables its usage in cryogenic applications.

6. Low melting point and high yield in recycling reduces the cost of recycling processes.
7. Light weight, softness of the material with non-poisonous and colorless oxide layer over the surface facilitated extensive use in packing industry.
8. High modulus of elasticity makes it useful for load bearing application.

2.9.3 Aluminium alloys in automotive and aerospace industry

There is a huge demand for Aluminium alloys in automobile industries due to increasing customer requirements for economic fuel consumption. Several modified or new Aluminium alloys have been developed in the last decades for the construction of light weighing automobiles [131] [132]. The aerospace and sports industry have been benefitting from the utilization of aluminum alloys for decades in terms of significant weight savings and enhanced performance [133]. In Europe, the usage of Aluminium in passenger cars has been doubled in the last decade [134]. With the synergic efforts from automotive industry and aluminum industry has led to development of several aluminum alloys for the designing of light weight cars [131]. The advantage of Aluminium is easy availability in huge variety of semi-finished forms which suits for mass production in cost efficient manner. Aluminium is used in variety of forms as castings, extrusions and sheets in engine blocks, power train parts, space frames, sheet structures, hang on parts and in other structural components in various commercial cars models (Audi A2, A8, BMW Z8, Lotus Elise, Honda NSX, Jaguar, DC-E-class, Renault, Peugeot etc.) [132]. For automotive sheet applications the main classes of aluminum alloys are heat treatable Al-Mg-Si (6xxx) alloys and non-heat treatable Al-Mg-Mn (5xxx) alloys [135]. The Al-Mg-Si alloys possess good formability, surface finish, corrosion resistance and good age hardening response. The frequently used various Al-Mg-Si alloys in automotive industry are AA6009, AA6010, AA6016, AA6111, AA 6181A [134] [135]. Whereas the 5xxx alloys are used in inner body panel applications due their good combination strength and formability [135].

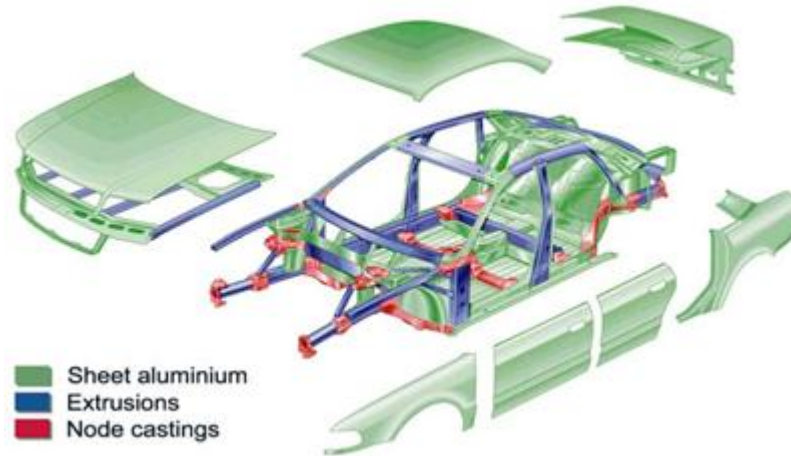
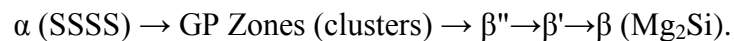


Figure 2.9: Usage of Al in various forms in Audi A8 [135]

2.9.4 Precipitation phenomenon in 6xxx Series Alloys

In 6xxx series Al alloys, the optimized heat treatment condition to obtain maximum precipitation hardening response involves, annealing at high temperature (520-560 °C) to dissolve second phase in the Al matrix followed by water quenching at faster rate to room temperature to retain the solute in Al matrix and then immediately subjecting to artificial ageing at temperatures between 160 -180 °C for few hours. This process is denoted as “T6” condition. The generally accepted precipitation sequence in 6xxx alloys is as follows [136]:



T6 treated condition possess β'' precipitates, which is considered to be primary strengthening phase to the Al matrix. However in actual manufacturing process of car body panels, in automotive industries involves warm and cold rolling of Al alloys sheets to final thickness followed by annealing treatment at 520-560 °C. During this process the deformed sheets undergo two processes, i) recovery and recrystallization, which facilitates for further easy press forming. ii) Solid solution treatment by dissolving solutes into the Al matrix. After sufficient time of annealing the sheets are quenched to room temperature at faster rate to obtain sheets in the state of super saturated solid solution. Now this alloy sheets are stored at room temperature and transported to automotive body manufacturers. This alloy is then further deformed into the required shape and assembled in to the body frame and subjected to paint baking process. Paint baking is the final stage of car body manufacturing process which carries out at 180-210 °C for few minutes. During this process the alloy undergo artificial ageing process

and the strength of the alloy sheets increases. The increase in strength is mainly due to formation of β'' precipitates.

2.9.5 Clusters and Negative strength response

The precipitation evolution process in Al-Mg-Si alloys begins with formation of clusters/G.P zones at early stages. It can be proved through increase in hardness of the sample or through observing exothermic peak (peak A) in DSC heat flow curve. *Figure 2.10* shows the hardness and DSC plots of AA 6111 alloy obtained through isochronal heating [137].

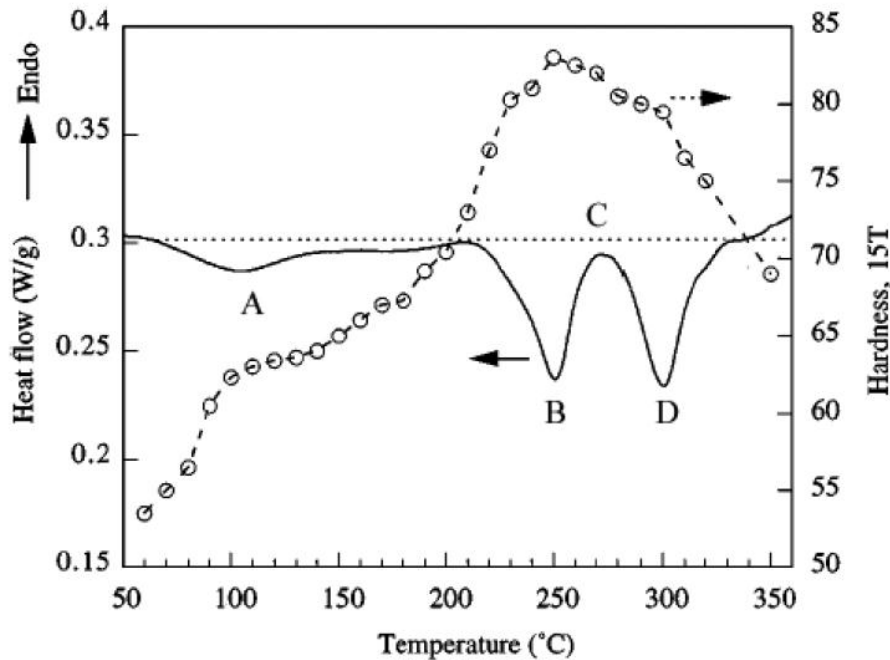
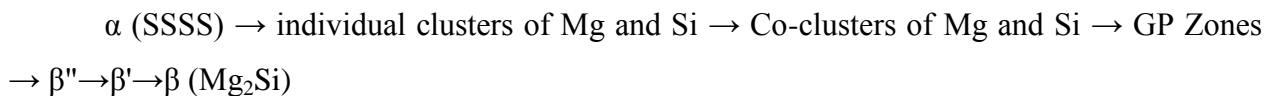


Figure 2.10 Hardness and DSC plots of AA 6111 alloy obtained through isochronal heating [137].

Edwards et al., [138] have reported that the peak A in the *Figure 2.10* is actually of two overlapping peaks corresponding to clusters and GP-zone formation. The suggested precipitation sequence as follows:



The clusters are very small and are difficult to observe through conventional TEM. Advanced characterization techniques such as HRTEM and 3D atom probe topographies are used to characterize the clusters. Clusters that forms at initial stages of ageing are found to be have

significant influence on β'' precipitates that forms at medium stages of ageing. Ultimately the properties after peak aged treatment is depends up on size, number density, distribution and characteristic of β'' precipitates. It was reported that the SSSS alloy subjected to NA has shown slower hardening response and poor hardness than the alloy without NA, after artificial ageing during baking treatment [139]. This negative strengthening response is due to the clusters that form during NA results less availability of solute content to form β'' precipitates during subsequent artificial ageing [139]. In automotive body manufacturing process, the delay at room temperature after solid solution treatment is unavoidable. So the negative strengthening response due to NA has become critical issue from several years. Due to difficulty in characterization of clusters through conventional TEM resulted poor understanding of clusters. However by employing advanced characterization techniques such as ATP significant progress has been achieved in understanding of cluster formation. Several strategies have been made to overcome this problem. One of those is giving pre-ageing (PA) treatment immediately after solid solution treatment [140]. It was observed that the precipitates that forms at PA treatment are relatively stable at room temperature and act as nucleation sites or they can be directly transform in to primary strengthening phase β'' during later artificial ageing [141] [142]. PA has resulted increased ageing kinetics and hardening response in 6xxx series Al alloys [143] [144].

Precipitation in 6xxx series alloys is complicated as it is influenced by many factors such as temperature, alloying elements, etc. In order to further study negative strength response, an understanding of the precipitation sequence is required.

2.9.6 Mechanical properties of Al 6061 alloy processed through various SPD techniques.

Al 6061 alloy has been processed through several SPD techniques to enhance its mechanical properties through achieving UFG structure. *Table 2.2* lists mechanical properties (strength and ductility) of Al 6061 alloy achieved through various SPD techniques reported in literature. Kim et al., [145] have achieved better mechanical properties in the material Pre-ECAP solid-solution treatment combined with post-ECAP aging treatment. Terada et al., [146] have investigated the effect of ageing behaviour in room temperature of ARBed alloy and reported that low temperature (100 °C) ageing is best suitable for enhancing mechanical properties through cluster formation. High temperature (170 °C) ageing has resulted precipitate coarsening. HPT at room temperature followed by low temperature ageing has resulted drop in strength, however increase in ductility is observed. The higher strength observed in HPT Al 6061 alloy is attributed

to massive segregation of alloying elements along grain boundaries [147]. Cai et. al., have reported that dynamic ageing using ECAE is efficient approach to achieve superior mechanical properties in Al–Mg–Si alloys [148]. Even though there are several reports on mechanical behaviour of UFG Al 6061 alloy, a detailed investigation on precipitation evolution and its influence on mechanical properties are lacking.

Table 2.2. Properties of Al 6061 alloy processed through various SPD routes.

Technique	Mater	Ref	Processing	$\sigma_{0.2}$	σ_{UTS}	δ
ECAP	Al 6061	2000 [149]	ECAP at RT up to 6 pass ($\epsilon=6$)	~280	~310	15
ECAP	Al 6061	2001 ([145])	ECAP at 125 °C up to an equivalent strain 4	~385	~420	~22
			ECAP at 125 °C up to an equivalent strain 4 +static ageing at 100 °C/48 h	~415	~459	~18
ARB	AL 6061	2002([150])	ARB at RT		363	5
			T6		310	17
ECAE	Al 6061	2004 [148]	One ECAE pass at 100 °C followed by two ECAE passes at 170 °C to gain total strain 2	~295	370	~ 11
ECAP	Al 6061	2007 ([151])				
HPT	Al 6061	2008 ([152])	HPT at RT	660+21	690+28	5.5+0.3
			HPT+ Ageing	565+17	585+20	13.5+1.1
			T6	276+14	365+16	14+1.0
			ST+WQ	150+7	275+10	23+1.0
ARB	Al6061	2011 [153]	ARB up to 5 cycles	-	~360	~4.2
			ARB up to 5 cycles + Aged at 100 °C	-	~450	~6.2
			ARB up to 5 cycles + Aged at 160 °C	-	~370	~8
TCP	Al 6061	2013 ([154])	SSTCP	~325	~385	~4.2
			NATCP	~350	~390	~3.7
			AATCP	~352	~378	~4.2
			TCPNA	~305	~350	~5.5
			TCPAA	~310	~350	~11
HPT	AA 6060	2014 ([155])	T6	158+-2	183+-4	13.2+-1
			HPT at RT, 6 GPa, n=10	475+20	525+10	6+0.5
			HPT at 100 °C, 6 GPa, n = 10	427 ± 20	478 ± 10	6.2 ± 0.5
			HPT at 180 °C, 6 GPa, n = 10	291 ± 17	324 ± 10	8.3 ± 0.5

2. 9.7 Microstructural elements in SPD processed Al alloys

i) Dislocations: In SPD process, dislocations are the building blocks for the evolution of new grains. Dislocations induced during deformation facilitate evolution of new grains. They may exist in the form of tangles zones or rather random structures [156]. In high stacking fault energy materials, faster dynamic recovery will takes place through annihilation of dissimilar type dislocation. Dislocation accumulation can be enhanced by performing cryogenic deformation. A material deformed at cryogenic temperatures possesses high dislocation tangled zones due to reduced dynamic recovery.

ii) Dislocation cells or sub grains: Dislocation cell or subgrain boundary is the primary element in the evolution of new ultrafine grain through plastic deformation. These are the smallest volume elements in the deformed microstructure [156]. The boundaries of dislocation cell or subgrain forms through the rearrangement of similar type dislocations. Materials that undergo deformation at very low temperature possess thick dislocation walls with dislocation tangled zones. The interior of the dislocation possess relatively lower dislocation density than the boundaries.

iii) Geometrically necessary dislocations (GND): Huajian and Yonggang [157] have defined geometrically necessary dislocations as, “An extra storage of dislocations that are required to accommodate the lattice curvature that arises whenever there is a non-uniform plastic deformation.” These dislocations will contribute for work hardening by acting as an obstacle to the motion of statically stored dislocations. GND densities are estimated by using EBSD technique.

iv) Non-equilibrium grain boundaries: The evolution of UFG/NS in SPD process involves generation of high densities of dislocations followed by formation of cellular structure and its continuous transformation to granular structure by the interaction of generated dislocations with cell walls and grain boundaries [158]. The grain boundaries that form in SPD process contain very high density of extrinsic dislocations, which results in high energies and high internal stresses. These boundaries are called non-equilibrium grain boundaries. *Figure 2.11* shows the TEM micrograph of Al Al–3% Mg alloy sample after HPT at room temperature. It is evident from the image that presence of distorted and diluted grain boundaries with the presence of high densities of extrinsic dislocations makes the grain boundaries non-equilibrium [158]. The extrinsic dislocations present in the grain boundaries in SPD processed material influence the mechanical properties. These can easily move in the grain boundaries leading to negative Hall-Petch effect [115] [159] [160]. From the ductility point of view, non-equilibrium grain

boundaries might be favorable to achieve decent elongations in UFG/NS materials processed through SPD.

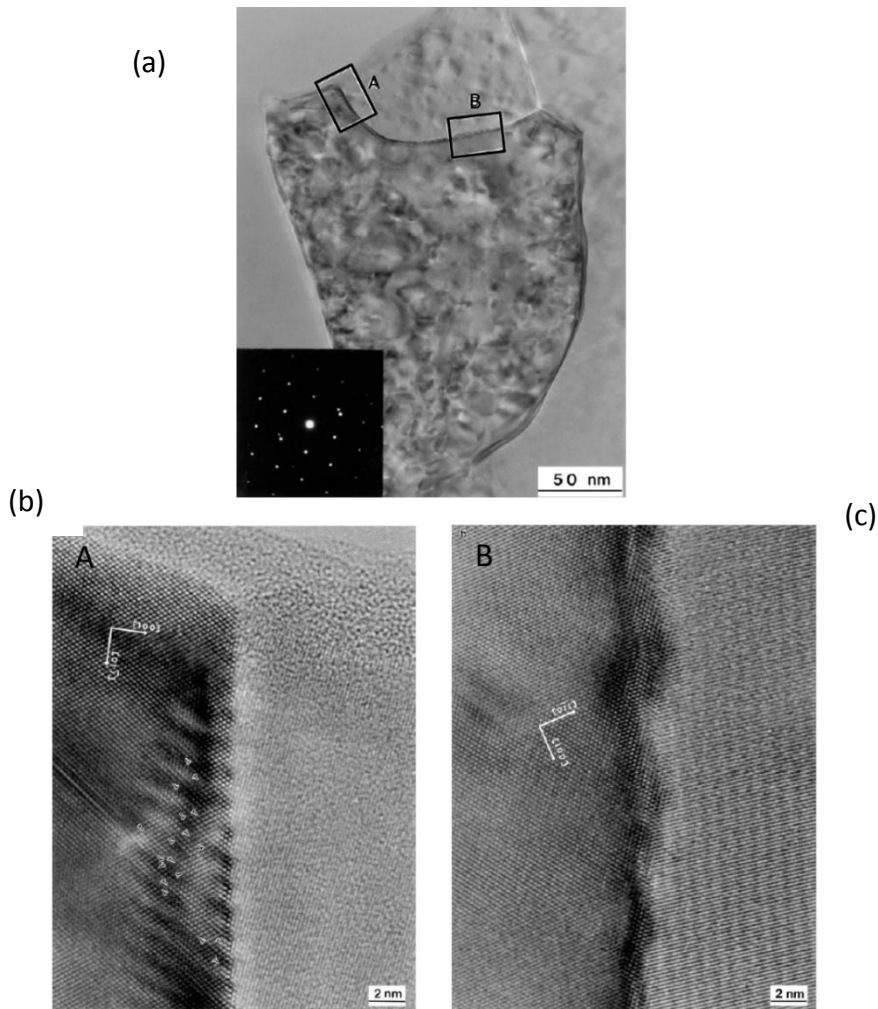


Figure 2.11: TEM micrographs of Al-3% Mg alloy sample after HPT at room temperature; a) UFG grains with non-equilibrium grain boundaries, b) HRTEM image taken at location 'A' shown in **Figure 2.11(a)**, c) HRTEM image taken at location B shown in **Figure 2.11(b)**. This image is taken from the reference [158].

2.9.8 Strengthening mechanisms in Aluminium alloys

i) Grain boundary strengthening

Grain boundary is the area where the lot of lattice perturbation exists. When the dislocation faces grain boundary, its motion gets hindered. It leads to pile up of dislocations at the grain boundaries. Therefore, the distance travelled by a glissile dislocation before reaching grain boundary decreases with decreasing size resulting in higher strength [115]. This effect is called as grain boundary strengthening. In coarse grained aluminium alloy, the grain size is in the range of few microns to several microns (three digits). Coarse grained aluminium alloys shows normal yielding and work hardening behavior, whereas UFG materials shows sharp yield point [161]. In the early 1950s, Hall and Petch have proposed a relation between yield stress (σ_y) to the grain size (d) of the undeformed material [162] [163].

$$\sigma_y = \sigma_0 + Kd^{-m} \text{ -----(2.1)}$$

where σ_0 is the Peierls or frictional stress, 'K' a coefficient and an exponent 'm' is 1/2. It was observed from (Figure 2.12), that this relation is also well valid for UFG (grain size 100-1000 nm) in Al alloys [164]. However, in the materials developed through severe plastic deformation, microstructure contains grain boundaries with different misorientation angle. The resistance provided to the dislocation pileup by grain boundary depends on its nature, and the nature of the grain boundaries depends on method of synthesis [165]. A grain boundary with low angle misorientation provides less resistance to the dislocation motion as compared to the grain boundaries with high angle misorientation. Later, the Hall-Petch relation has been modified to include the grain boundary character, and the proposed modified Hall-Petch relation by Niels Hansen [165] is

$$\begin{aligned} \sigma_f &= \sigma_0 + \left[M\alpha G\sqrt{3b\theta LAGB(1-f)} + k_1\sqrt{f} \right] D_B^{-\frac{1}{2}} \\ &= \sigma_0 + k_2 D_B^{-\frac{1}{2}} \end{aligned} \quad (2.2)$$

Where σ_f – is flow stress, M- Taylor's factor, α - Material dependent constant, G- Shear modulus, b- Burgers vector, D_B - Grain boundary spacing, k_1 - constant, f- Fraction of HAGB. In micro crystalline and UFG materials, the pile-up of dislocations at grain boundaries is a key

mechanistic process underlying an enhanced resistance to plastic flow from grain refinement [166].

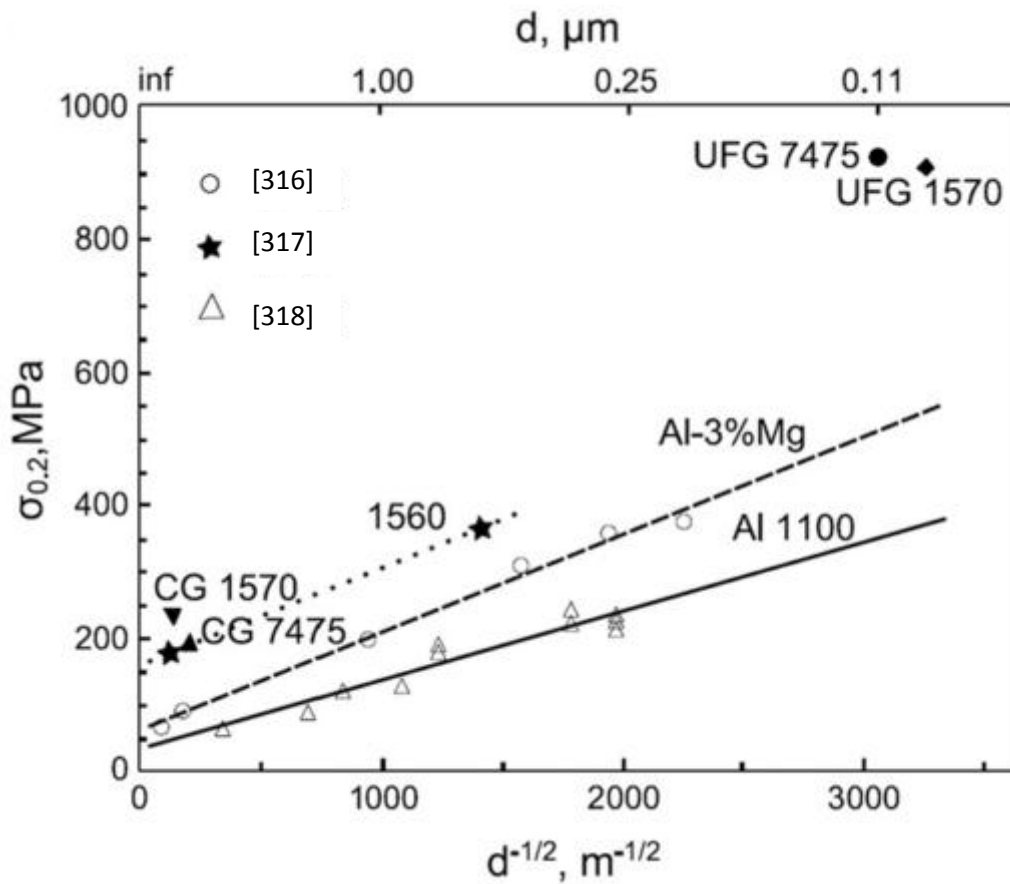


Figure 2.12: The Hall-Petch relation for the Al alloys: AA 1100, Al-3% Mg, AA 1570 and AA 7475 [115] [164].

ii) Solid solution strengthening

In the category of non-heat treatable Aluminium alloys, the strengthening mainly comes from solid solution strengthening and grain boundary strengthening. Al 1xxx (Al- small amounts of Fe and Si), 3xxx (Al-Mn) and the 5xxx (Al-Mg) alloys comes under this category. These alloys are widely used in the range of applications where a low to medium strength, a good formability, and a good corrosion resistance are desirable [167]. A systematic work has been carried out on the effect of solid solution on strengthening of the matrix in coarse grained Al alloys. It has been observed that the strength by solid solution is directly proportional to the concentration (C) of solute in the matrix.

The relation is

$$\sigma_{SS} = HC^n \text{ -----2.3}$$

Where H and n are constants. The value of n can be in the range of 0.5-0.75 [167]. This is very much valid for coarse grained Al alloys. However, the recent observation in UFG/NS Al alloys, produced by SPD indicates the breakdown of the relationship shown in equation (2.3) due to solute atom segregations at the grain boundaries. The atom probe tomography analysis of Al 6061 alloy processed through HPT [147] has shown segregation of Mg, Si, and Cu along the new grain boundaries. In the similar way, Al 7075 processed through HPT has shown solute segregations at the grain boundaries (*Figure 2.13*) [168].

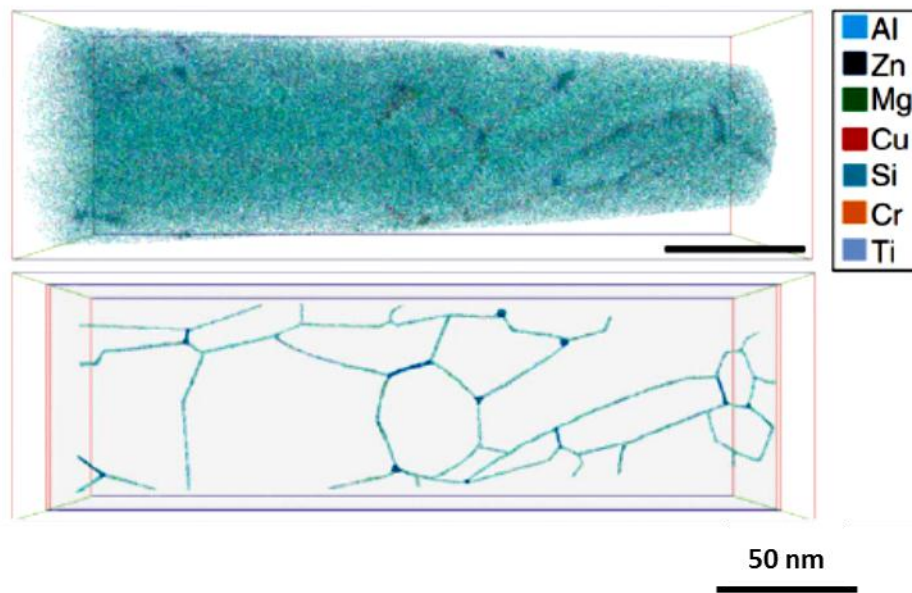


Figure 2.13: Alloy grain structure in the HPT processed AA7075 (scale bar: 50 nm).

UFG/NS material possesses large volume fraction of grain boundaries. This may lead to segregation of large fraction of solute at the grain boundaries, which is a different phenomenon as compared to coarse grained material [169]. Solute segregations in UFG/NS Al alloys are due to increased diffusion coefficient of the material by increasing dislocation densities and vacancy concentrations. Solute segregation also depends on the grain boundary character. Non equilibrium grain boundaries are often observed in UFG/NS material developed through SPD. These boundaries possess increased excess energy and act as sinks for solute atoms [170]. Due to solute segregations, the estimated strength from the grain boundaries in nanostructured material

processed through HPT is less than the experimentally obtained value [147]. It is attributed to retardation of dislocation initiation at the grain boundaries [164] [171].

iii) Precipitation hardening

A German metallurgist, Alfred Wilm (1869-1937), has invented the new Aluminium alloy known as “Duraluminium”, which has extensive applications in air crafts [172]. He has published an article on age hardening in Aluminium alloys in 1911 by mentioning “*My studies of aluminum alloys at the central office for scientific-technical investigations in Neubabelberg, which I have been conducting since 1903, have shown that even a small amount of magnesium added to aluminum enables hardening by a thermal treatment.*” [173] [174]. This phenomenon has brought revolution in the Aluminium alloys and led to development of several age hardenable aluminium alloys with medium strength to high strength. There are several studies in conventional coarse grained aluminium alloys on precipitation hardening effect. Coming to UFG/NS Al alloys, the precipitation hardening response is different as compared to the coarse grained counterparts [115]. Overlapping of two strengthening mechanisms makes it difficult in UFG/NS Al alloys to understand the actual hardening effect through precipitation. Different strategies have been implemented to optimize the precipitation hardening effect in UFG/NS Al alloys. It includes SPD processing i) At elevated temperatures after solid solution treatment, ii) At room temperatures after solid solution treatment, followed by low temperature ageing, iii) After solid solution treatment followed by various ageing conditions viz., natural ageing, artificial ageing and over ageing.

The selection of strategy depends on the feasibility of processing. cryorolling and cryomilling processes facilitate to perform deformation at desired heat treated condition. Whereas in other SPD processes (ECAP, HPT, ARB, FSP, HE), design of the technique makes it necessary to perform processing at room temperature or above room temperature. UFG structure evolution through SPD processing involves continuous generation of dislocations and its transformation to UFG. SPD processing at room temperature or above room temperature of solid solution treated material leads to simultaneous evolution of precipitates and UFGs. The process involves complex phase transformations such as nucleation, growth, fragmentation and segregation of second phase precipitates [16] [18] [48] [175] [176] [177] [178] [179] [180] [181]. This makes it very difficult to understand the precipitation evolution in UFG/NS aluminium alloys. Due to poor ductility, alloys after SPD processing are subjected to post heat treatment

processes. However, the alloys which are SPD processed at elevated temperatures have shown poor mechanical properties after post SPD ageing treatments. This is attributed to coarsening of precipitates, which are already formed during SPD processing. Whereas, the alloys which are deformed under cryogenic temperature or at room temperature have shown significant improvement in strength and ductility as compared to as deformed alloys after post SPD ageing at low temperatures. Hence, that it can be considered as an effective approach to enhance the strength and ductility.

2.9.9 Strategies to enhance the ductility in UFG Al alloys

i) Bimodal Grain size distribution

Wang et al., [76] have reported the effect of bimodal structure on ductility without affecting the strength of nanostructured Cu produced by cryorolling. The applied recipe is “developing UFG/NS structure which renders high strength to the material, by heavily deforming at cryogenic temperature followed by annealing for a short time. Annealing leads to formation of micron sized grains in matrix of UFG/NS, which attributes for increased tensile ductility. Since then, there are several attempts made on different metals to achieve the similar effect. However, the improvement in ductility was observed with the expense of strength. Whereas, Panigrahi and Jayagnathan [182] have successfully developed UFG Al 6063 alloy with enhanced strength and ductility. The proposed strategy is “Solid solution treatment followed by water quenching to room temperature → Cryorolling → short annealing at 155 °C for 5 minutes → low temperature (125 °C) ageing for 12 hours. Cryorolling after solid solution treatment results in improved strength by accumulation of high density of dislocations and formation of subgrain boundaries in the material. Short annealing leads to formation of recovered or partially recrystallized grains, which would act as empty rooms for newly generate dislocations to accommodate plastic deformation. Further, low temperature ageing leads to increase in strength by precipitation hardening effect. The selection of short annealing temperature and time is critical to observe the enhanced ductility without affecting strength. However, it is obvious that by performing short annealing results in restoration process through recovery and recrystallization. It will have definite negative influence on strength. In precipitation hardenable alloys, it is not observable due to nullifying effect by cluster strengthening effect. There are several other reports where bimodal or inhomogeneous grain structure synthesized by consolidation of mixture of various range of

sized powders has shown improved tensile ductility [183] [184] [185] [186] [187]. During extrusion, the coarse grains elongate along the extrusion direction. It was reported that presence of duplex or bimodal structure of elongated coarse and fine grains have both advantages and disadvantages [187]. The advantages are, presence of coarse grained regions may contribute in enhancing the ductility and fracture toughness by interfering with the crack and shear banding. The disadvantage is, due to elongated structures, the material possesses anisotropy in its properties. When the stress is applied normal to extrusion direction, both the strength and ductility are reduced in engineered bimodal extrusions. Apart from increase in ductility with the presence of coarse grain structure in the microstructure, the coarser grains possess lower strength compared to fine grains. It can be noted that the increase in ductility through this route is with the cost of ductility.

ii) Introducing nanosized precipitates

Introducing nanosized precipitates in to the matrix is found to be an effective approach to enhance the ductility of the UFG Aluminium alloys. Firstly Zhao et al., [188] have reported significant improvement in the ductility of UFG Al 7075 alloy without the expense of ductility. The recipe is (i) Allowing second phase particles to dissolve in to the matrix in coarse grained material; ii) Producing UFG structure through deformation at supersaturated solid solution state, and (iii) Proper ageing treatments to form nanosized precipitates in the UFG microstructure. Generation of nano precipitates alone will not help to enhance the ductility of the material. During ageing process, the microstructure undergo recovery process, thus the dislocation density will be reduced. The annihilation of dislocations during recovery process will leave a space for dislocations that generate during deformation. Thus, ductility of the material is increased. To enable the material to undergo stable plastic flow, the nanosized precipitates play a major role and also they accumulate more dislocations; thus the work hardening rate of the material gets increased. The drop in strength due to annihilated dislocations is compensated by the nano sized precipitates, but it also enhances the strength further. The simultaneous improvement in strength and ductility has not been achieved earlier [145] [189] [190]. Later Cheng et al., [191] have slightly modified the strategy proposed by Zhao et al., [188] approach and successfully achieved improvement in both strength and ductility in Al 2014 alloy. It indicates that to achieve simultaneous strength and ductility in the Al alloys, effective control of precipitation process is required. Compared to room temperature or elevated temperature SPD processing, cryogenic

deformation after solid solution treatment of the alloy facilitates no phase transformation during the process, due to suppressed diffusion of solute atoms. Nucleation and growth of the precipitates can be effectively controlled by post deformation heat treatments. However, there are some issues with the above said approach. As discussed in the previous section (Non-equilibrium grain boundaries), SPD processed material contains non-equilibrium grain boundaries, which are at high energy state. In Al alloys which are more prone to intergranular precipitation such as Al-Cu, Al-Cu-Zn, during post SPD precipitation process, these non-equilibrium grain boundaries promote intergranular precipitation, which leads to intergranular fracture with poor ductility [192]. In recent studies by Jiang et al., [193], they have observed enhanced ductility in micro alloyed- Al-Cu material after ECAP followed by artificial ageing. *Figure 2.14* shows the stress strain diagram of UFG Al-Cu-Sc alloy by micro alloying. Addition of Sc in Al-Cu alloy has suppressed the intergranular precipitation of θ -Al₂Cu phase and by promoting intragranular precipitation of θ' -Al₂Cu phase.

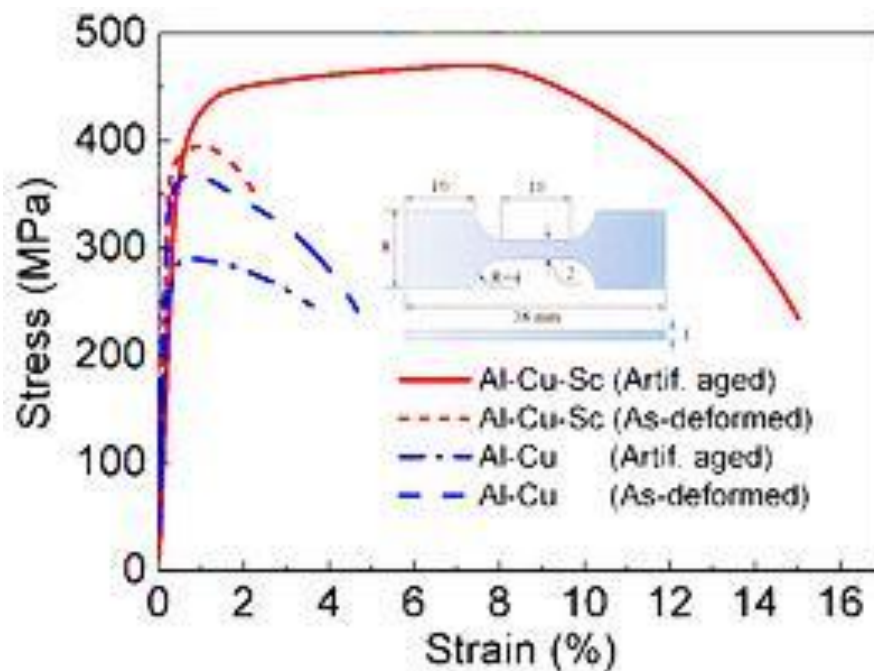


Figure 2.14: Typical tensile engineering stress-strain curves of the as-processed Al-Cu-Sc (short-dash curve), Al-Cu (dash curve), and artificially aged Al-Cu-Sc (solid curve), Al-Cu (dash-dot curve) UFG alloys [193].

iii) Modifying Grain boundary characters

The microstructure that develops during SPD generally is characterized by nature of the grain boundaries. If the misorientation with the neighbor grains is less than 15° , then it is called as low angle grain boundaries (LAGB). If it is more than 15° , then it is called high angle grain boundaries (HAGB). It has been observed that the misorientation of the adjacent grains directly influences the mechanical properties [194] [195]. Grain boundaries render strength to the material by acting as an obstacle to the gliding of mobile dislocations. However, the amount of strength that can be imparted to the material is dependent on the grain boundary character. In the material with HAGBs, activation of slip between the adjacent grains is difficult and it requires more energy [194]. Thus, the strength of the material increases. Increase in strength with the expense of ductility is not desirable as high strength with reasonable ductility of materials is essential for engineering applications. In contrast to HAGB, LAGBs shows poor resistance to the gliding of mobile dislocations [194]. This property can be utilized to enhance the ability of plastic deformation in UFG/NS materials. Hu et al., [194] have recently reported increased ductility and uniform elongation while retaining high strength by engineering the relative proportion of LAGBS in the Al alloys.

2.10 Problem formulation

2.10.1 Current Literature on Bulk ultrafine grained & nanostructured materials

A thorough literature survey has been made on the development of high strength Al alloys processed through SPD techniques. The important findings from the literature are as given below.

- Bulk SPD processing techniques have been found to be attractive for the development of advanced materials with significant improvement in mechanical properties.
- In addition to grain boundary strengthening, SPD processing also causes the strengthening to bulk ultrafine grained and nanostructured materials due to other structural features such as non-equilibrium grain boundaries, grain boundary segregation of solute atoms, nano twins, and nano particles.
- A new development in SPD techniques, especially in high pressure torsion, facilitates to produce functional nanomaterials with significant improvement in their magnetic, optical properties compared to bulk materials.

- The problem of poor tensile ductility in ultrafine grained (UFG) Al alloys has been resolved by introducing nanosized precipitates in to the UFG structure, which has led to improvement in both strength and ductility.

2.10.2 Motivation

Apart from the several advantages of SPD techniques to produce UFG structure in the metals and alloys, the difficulties associated scale up from laboratory to industrial applications for producing large sized structural components still persists. For the large scale production, cryorolling and cryoforging could be potential techniques for producing ultrafine and nanostructures in the bulk materials. In precipitation hardenable Al alloys, strengthening through precipitation is an efficient method, which has received significant attention for several years. The literature on precipitation kinetics of UFG Al alloys is very scarce. Grain boundary strengthening as well as precipitation plays a vital role in imparting tensile strength and ductility to Al alloy. A thorough understanding of precipitation phenomenon in UFG Al alloys is essential to maximize its strengthening contribution for simultaneous improvement in strength and ductility. Therefore, the present research work has been focused t to develop ultrafine grained precipitation hardenable Al alloy sheets (Al 6061 Alloy) from their bulk Al alloy by using cryorolling technique and cryoforging technique. The effect of deformation on the precipitation evolution in the Al alloys has been given due importance in the present work for tailoring mechanical properties of UFG Al alloys.

2.10.2 Objectives

The following objectives in Al 6061 alloys were formulated based on the current literature in UFG Al alloys

- (i) To produce ultrafine grained Al 6061 alloy from its bulk alloy by cryorolling and to study its ageing behaviour, microstructural stability and thermal stability.
- (ii) To investigate the effect of cryorolling followed by warm rolling on strength and ductility of Al 6061 alloy.
- (iii) To study the microstructural and thermal stability of warm rolled material and to investigate the scope of warm rolling to enhance the ductility of Al 6061 alloy.
- (iv) To investigate the precipitation evolution in cryorolled and warm rolled Al 6061 alloy.
- (v) To study the effect of cryorolling strain on precipitation behavior of Al 6061 alloy.

- (vi) To investigate the evolution of ultrafine grain structures and its homogeneity developed in the alloy at high strain and low temperature.

2.10.3 Work plan and Layout of the thesis

To fulfill the above objectives, a systematic work plan has been made and executed. The layout of the proposed work is shown in *Figure 2.15*. The layout of the thesis is as follows;

The **Chapter 1** gives a brief introduction about Aluminium alloys, various SPD processes and various strengthening mechanisms in UFG Aluminium alloys. It is followed by literature survey of Aluminium alloys, its applications in various sectors and various SPD techniques used to produce UFG structure in Al alloys and its principles are discussed in the **Chapter 2**. In **Chapter 3**, materials and experimental procedures are described. **Chapter 4** presents the effect of cryorolling on microstructure and mechanical properties of Al 6061 alloy. Besides that, the microstructural stability of UFG Al 6061 alloy is also discussed. A special attention is given to investigate the influence of precipitates on thermal stability of cryorolled Al 6061 alloy. The effect of cryorolling followed by warm rolling in Al 6061 is described in **Chapter 5**. In **Chapter 6**, a detailed investigation of the precipitation evolution in cryorolled and warm rolled material is made. Also, the effect of deformation strain on precipitation evolution in Al 6061 alloy is discussed. **Chapter 7** investigates the effect of cryoforging on microstructural evolution, ageing behaviour, and mechanical properties in Al 6061 alloy. The scope of future work is given in **Chapter 8**.

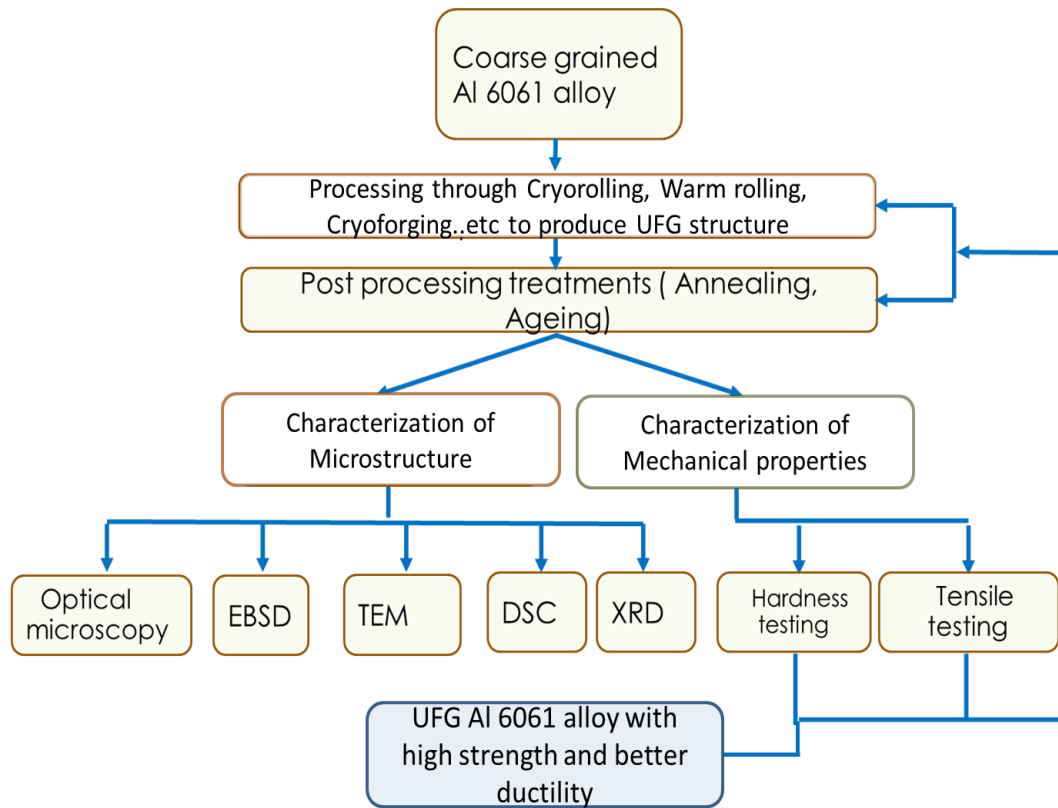


Figure 2.15: Flow diagram showing the plan of the present work

Chapter 3

Experimental Procedure

3.1 Introduction

The experimental investigations were made to understand the effect of cryorolling, cryorolling followed by warm rolling and cryoforging on the microstructure and mechanical properties of heat-treatable AA 6061 alloy. Mechanical properties are investigated by Vickers hardness tests and tensile tests at room temperature. The recommended, ASTM E8 sub size specimen standards are used for tensile testing in rolled conditions. The nonstandard samples are used to test the cryoforged sample. Microstructural characterizations of the samples subjected to different deformation processing are performed through Optical microscopy (OM), Scanning electron microscopy (SEM)/EBSD and Transmission electron microscopy (TEM). Differential scanning calorimetry is used along with TEM to examine the precipitation behaviour of deformed and bulk materials.

3.2 Materials

Material used in the present investigation was medium strength precipitation hardenable Al 6061 alloy. The major alloying elements are Mg and Si. The preliminary experiments for cryorolling studies made on the alloy was received from Hindustan Aeronautics limited (HAL), Bangalore, India, in the as cast form. The rest of the experiments are carried out with the alloy received from Hindalco Industries Pvt. Ltd. India, in the wrought form (1 inch thick plate). The chemical compositions of the alloys are listed in *Table 3.1*. The difference in wt. percentages of Mg and Si of both the alloys is very little. Before performing experiments, sample with required dimensions are machined from the as received material and subjected to solid solution treatment.

Table 3.1 Chemical composition of the Al 6061 alloy

Initial condition	Elements	Mg	Si	Fe	Cu	Mn	Cr	Zn	Al
Material in the as cast form	Wt.%	1.2	0.7	0.22	0.3	0.02	0.19	0.014	Balance
Material in the wrought form	Wt.%	1.01	0.67	0.28	0.2	0.04	0.05	0.06	Balance

3.3 Experimental setup

3.3.1 Cryorolling

Rolling at or near to liquid nitrogen temperature is known as cryorolling. Cryorolling is widely used to produce ultrafine grained metals and alloys in bulk sheets. Deformation processing at liquid nitrogen temperature suppresses the dynamic recovery and therefore accumulates high density of dislocations, which subsequently rearrange themselves to form ultrafine grained/nanostructures in the bulk materials. In the present study for cryorolling, a simple conventional laboratory two high rolling mill was used. The diameter of the rolls was 110 mm, and the operational speed is 8 rpm.



Figure 3.1: Two high rolling mill used for cryorolling

The experimental set up is shown in *Figure 3.1*:

The procedure of cryorolling involves;

- Samples are machined with desired dimensions and proper heat treatment is given before cryorolling.
- Samples are held in sample holders and dipped in the liquid nitrogen cans and allowed it for 15 min to attain equilibrium temperature with the liquid nitrogen.

- Samples are taken out from the liquid nitrogen and then immediately rolled, followed by immediate immersion of samples in liquid nitrogen. This process takes approximately 10-15 seconds.
- After first rolling pass, the successive passes are given within an interval of 5-10 minutes.
- Several passes are given to achieve final thickness of the samples. Limited reduction per pass is given to avoid more heat generation in the sample.

3.3.2 Warm rolling

In the present study along with cryorolling (CR), a combination of cryorolling and warm rolling experiments were also carried out. For this, samples were partially rolled through cryorolling and subsequently processed by warm rolling at various temperatures to achieve final thickness. Here, rolling above room temperature is termed as warm rolling. In the warm rolling process, samples after cryorolling were kept in electrical muffle furnace at desired temperature and allowed to get equilibrated by giving sufficient soaking time before every pass. The reduction per pass was given constant throughout warm rolling.

3.3.3 Cryoforging

Rectangular samples with $27 \times 30.5 \times 33 \text{ mm}^3$ were machined from the as received plate and solution treated at $520 \text{ }^\circ\text{C}$ for 2 hours and water quenched at room temperature. The samples were then subjected to multi directional forging (MDF) at 77 K using friction screw forging machine at an approximate strain rate of 10 s^{-1} . The first forging axis was parallel to the rolling direction of the starting sample. The direction of the sample is changed for every pass at an angle of 90° . The sample dimension ratio 1:1.13:1.22 was maintained constant throughout the processing. MDF at cryogenic temperature was performed by filling the die with liquid nitrogen and its level was maintained up to sample height during forging. After every pass, the sample is allowed to attain thermal equilibrium with liquid nitrogen by giving 5-10 min soaking time. *Figure 3.2* shows the schematic diagram of MDF for a single cycle. Strain per pass is fixed as $\Delta\epsilon_i = 0.2$ (where 'i' number of passes) and maintained constant throughout all passes. The cumulative strain after one cycle of MDF was $\sum\Delta\epsilon_{n=1} = 0.6$ (where 'n' is number of cycles). In the present study, MDF was carried out to cumulative strains of 1.8, 3.6, 5.4 and 6 i.e., 3, 6, 9 and 10 cycles, respectively. After 4 cycles, the samples are reshaped by maintaining sample dimension ratio constant. Samples were successfully forged up to 9 cycles without any cracking.

After MDF, samples were prepared by sectioning along the plane perpendicular to the last forging axis i.e., the highest dimension side.



Figure 3.2: Friction screw forging press used for Multi axial forging

3.4 Heat Treatments

3.4.1 Solid Solution Heat Treatment (ST) and Quenching: The starting material in the present investigation is from ST condition. ST was performed in a muffle furnace at 520 ± 5 °C. The samples were solutionized for 2 hours at atmosphere and quenching is performed by using cold water at room temperature and iced water.

3.4.2 Short annealing and longtime annealing: Short annealing is the process commonly used to develop bimodal grain structure in the ultrafine grained materials. Processed material is kept at annealing temperatures for short time and immediately quenched in to cold water at room

temperature. The short annealing temperature, used in the present investigation was 200 °C for 10 minutes.

3.4.3 Artificial ageing and Natural ageing: Artificial ageing is performed by keeping the samples at above room temperature in the furnace. The artificial ageing temperatures used in this study are 100 °C, 125°C, 145°C, 150 °C. Natural ageing is performed by keeping the samples at room temperature.

3.5 Mechanical Characterization

3.5.1 Vickers hardness

The samples were tested for hardness. In case of rolled samples, hardness was measured on the rolling plane, whereas for forged samples, measurements were taken on the plane perpendicular to the last forging axis. Prior to performing hardness testing, samples were grinded up to 1200 grit size emery papers followed by rough (blazer cloth) cloth polishing to obtain scratch free surface. The samples were properly dried and then the hardness was measured by using (FIE 500) Vickers hardness machine with test load of 5 kg and as dwell time of 15s. In case of rolled samples to obtain the hardness of each condition, minimum 6 reading were taken and averaged them. For MDF samples, the forging strain is inhomogeneous from center to surface. Therefore, the hardness was measured on the plane perpendicular to the last forging axis as the grid shown in *Figure 3.3*.



Figure 3.3: Computerized Vickers Hardness Tester (FIE-Model:VM 50 PC)

3.5.2 Tensile testing



Figure 3.4: S-Series, H25K-S tensile testing machine.

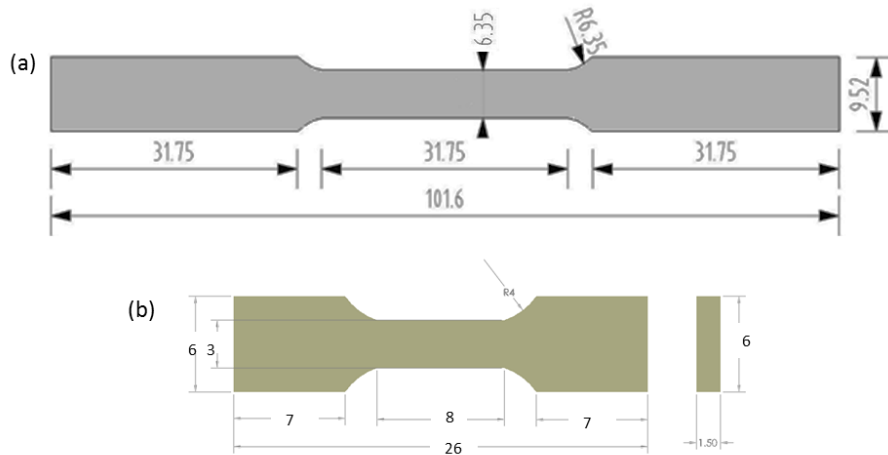


Figure 3.5: Schematic diagram of a tensile specimen; a) ASTM E8 sub size specimen, b) Nonstandard size specimen.

Tensile tests were carried out at room temperature to evaluate the strength and ductility of coarse grained and UFG materials with different heat treated conditions. In case of rolled samples, tensile samples were prepared according to ASTM E8 sub-size specimen (*Figure 3.5 (a)*) standards. Whereas in MDF, tensile testing was performed on samples with nonstandard dimensions as shown in *Figure 3.5(b)*. To maintain accuracy in the dimensions, samples were cut

through electro discharge machining. All the samples were tested by using Tinius Olsen 25 KN machine (S-Series, H25K-S, (*Figure 3.4*)) with crosshead speed of 1 mm/minute. Before testing, samples edges were properly polished to ensure scratch free surface and uniform gauge length. In each condition, at least four samples were tested to ensure the repeatability. The reported values are the average values of four test results.

3.6 Microstructural Characterization

3.6.1 Optical microscopy (OM)

OM was used to investigate the starting microstructures of bulk material after solid solution treatment and the effect of rolling and forging strain on the initial microstructure. Leica optical microscopy (LEICA DMI5000 M) with magnification lenses range from x5 to x100 and a digital video camera connected to computer was used (*Figure 3.6*). To obtain the microstructure with distinguished grains, polarized light is used. Dark field mode is used to observe the second phase particle, segregation and distribution in starting material. The procedures for sample preparation for optical microscopy involves mechanical grinding followed by cloth polishing with MgO (heavy) powder to obtain mirror like surface. Samples were properly dried and etched with Poulton's reagent and rinsed with distilled water. These samples are investigated under OM.



Figure 3.6: LEICA DMI5000 M- Optical microscopy used in the present work.

3.6.2. Scanning Electron Microscopy (SEM)/EBSD

FEI Quanta scanning electron microscopy equipped with energy dispersive spectroscopy and electron beam diffraction (EBSD) facility has been used to investigate the microstructural characteristics in the bulk coarse grained and UFG materials. EBSD analysis facilitates to investigate the evolution of subgrains through recovery and recrystallization, changes in grain orientations, changes in misorientation distributions and grain boundary spacing in the material. The samples were prepared with the area of interest for the EBSD investigation. Proper care was taken to avoid damage to the surface of the investigation while sectioning sample. While cutting bulk samples, cold water was used to prevent heat generation, which causes microstructural changes on the sectioned surface. After sectioning, the samples were mechanically grinded followed by cloth polishing to obtain scratch free mirror like surface. The final steps of the polishing involve electro polishing followed by polishing with colloidal silica medium containing 0.05 micron size colloidal silica for 10 to 15 minutes. This procedure gives an excellent polished surface, which gives high quality diffraction patterns.

3.6.3. Transmission Electron Microscopy (TEM)

TECHNAI 200 KV TEM with double tilt holder and equipped with energy dispersive X-ray (EDX) analysis was used to examine the microstructure evolution in UFG materials and precipitation studies in bulk and UFG materials. For TEM characterization of samples, thin foils were prepared from the area of interest in the alloy and polished through twin jet electro polisher. The detailed procedure for TEM sample preparation is discussed in section 3.7.4.

3.7 Sample preparation

3.7.1 Mechanical grinding/polishing

As a first step in the sample preparation for microstructural characterization, samples are mechanically grinded by using 320-, 600-, 800-, 1200- grit silicon carbide papers by using kerosene as a lubricant cum coolant. With increasing grit size, the force applied over the sample was reduced and grinding time is increased. After 1200 grit paper grinding, polishing is done by using two types of cloths with magnesium oxide (heavy) abrasive powder. At first, billiards cloth (wool fabric) is used for rough polishing and then short napped synthetic cloth for fine polishing.

3.7.2 Etching

Samples were etched before investigating under optical microscopy. Poultons reagent was selected to obtain the microstructure in bulk coarse grained and deformed material. The etchant solution was prepared by adding 50ml Poultons reagent with 25ml HNO₃, 1ml HF, and 1ml H₂O. Few drops of etchant was dropped on the sample surface and allowed it for 30-40 sec, rinsed with distilled water and dried under cold air blower.

3.7.3 Electro polishing

For EBSD characterization, sample preparation involves electro polishing. Sample surface contains deformed layer that came from mechanical grinding followed by cloth polishing. Mirror like surface polished samples have been dried completely with air blower before conducting electro polishing. Solution with 20:80 perchloric acid to methanol was used as electro polishing solution at -15 °C. Sample was used as an anode and a piece of stainless steel was used as a cathode in the circuit and constant potential of 11 V was applied to the electrode. After 90-120 s, samples were immediately removed from solution and rinsed with pure water followed by drying with cold air stream.

3.7.4 Twin jet electro-polishing

For TEM characterization, the following procedures were adopted for sample preparation; Samples were mechanically grinded up to 80 -100 μm thickness by using 320, 600, 1000, 1200 grit size emery papers. Discs with 3 mm diameter were punched by using GATAN TEM sample punching machine. Fischione model 110 twin-jet electro-polisher with low temperature container was used to electro polish the thin discs using solution 20: 80 perchloric acid to methanol ratio at - 30 °C and DC voltage of 40 V. Solution with 30: 70 nitric acid to methanol at -25 °C and 20V is also suitable for Al samples. Usually the solution temperature varies ± 5 °C during polishing. Liquid nitrogen was used to reduce the solution temperature. After thinning, samples were cleaned twice in the pure methanol before drying. Tablet capsules were used to preserve the samples.

3.8 Differential Scanning Calorimetry (DSC)

In Al-Mg-Si alloys, precipitation process involves several exothermic and endothermic reactions. DSC is an indirect method to investigate the precipitation process. DSC is used to examine the thermal behavior of bulk and deformed materials. In this study, two types of DSC machines were used. Preliminary studies on effect of warm rolling are carried out by using Perkin

Elmers Paris diamond which runs from room temperature (20 °C) to high temperature (1200 °C). The rest of the samples are tested through low temperature differential scanning calorimetry, which belongs to Perkin Elmer's 8000 model (*Figure 3.7*) and it comes under power compensation type DSCs. The starting scanning temperature is -5 °C. Before running the scan, samples were allowed to get thermal equilibrium with sample pans. Instrument is properly calibrated by performing several runs with standard samples. The sample preparation for DSC testing involves punching of 5mm diameter disc shape samples from 0.6 mm thick sheet. *Figure 3.8* shows the punch and die used for sample preparation from the bulk alloy and rolled sheets. The mass of the samples is maintained as 30 mg. In ST condition, to avoid the deformation effect due to punching, samples were first punched prior to ST. Pure aluminium samples with same weight as alloy samples were prepared by punching and annealing at 450 °C for 2 hours followed by furnace cooling. The base line corrections for each measurement of alloy are done by using pure aluminium scan. High pure Nitrogen gas is used as a purging gas with 20 ml/min flow rate.



Figure 3.7: Perkin Elmer's DSC 8000 series machine.

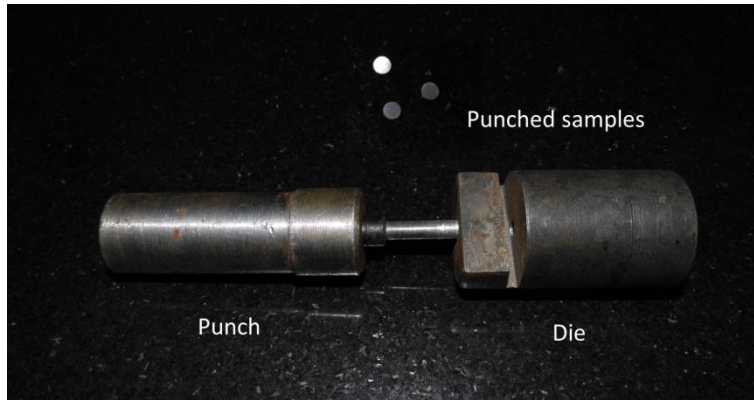


Figure 3.8: Punch and die used to prepare DSC samples.

4.1 Introduction

Cryorolling is one of the potential techniques to produce UFG structure in various metals and alloys in the form of bulk sheets. It can be adopted in industries for commercial production. Especially in materials like Al alloys, it is difficult to produce UFG structure through conventional rolling process, owing to its high stacking fault energy [196] [197] [198]. However, cryorolling has been successfully employed to develop UFG structure in pure Al and its alloys [11] [199] [200] [201] [202]. Improved mechanical and corrosion properties of the UFG Al alloys have been observed over its coarse grained counter parts. Al 6061 alloy is mostly used in transportation sector for light weight body constructions where there is a great demand for materials with high specific strength. There are no experimental studies on development of UFG structure and thermal stability in Al 6061 alloy processed through cryorolling. Therefore in the present study, cryorolling process is chosen to produce high strength Al 6061 alloy sheets. In heat treatable Al alloys, selection of proper heat treatment is necessary for starting material to produce high strength crack free sheets after cryorolling. Literature suggests that, in precipitation hardenable alloys, T0 heat treated condition is best suitable for cryorolling [13] [14] [202]. It facilitates ease in deformation and, presence of Mg in solid solution state will reduce the recovery rate of dislocations along with cryogenic deformation, which helps to achieve steady state in dislocation accumulation. However, low ductility after cryorolling is often reported due to poor work hardenability and therefore early stage of necking occurs during tensile testing as reported in the literature [13] [14]. Also, UFG materials produced through plastic deformation techniques possess high density of crystal lattice defects which makes them thermally unstable due to excessive energy [49] [203]. It drives them to equilibrium state at elevated temperatures [49]. It has been reported that the driving force available for grain growth in fine grain structured material, where the grain size $\sim 0.1\mu\text{m}$, is 10^3 times higher than for the material with grain size of $100\mu\text{m}$, and it may lead to some solid state transformations [204].

There are several studies reported on the UFG/NS evolution in Al alloys during heating of the severely deformed materials by employing TEM [200], X-ray methods, EBSD [110],

electrical resistance, DSC [110] and dilatometry techniques [205]. It was reported that the UFG/NS is not stable and grain growth occurs even at 0.5 Tm. In the alloys the second phase particles play a crucial role in retaining the fine grain structure during high temperature annealing [206] [207] [208] [209]. Since Al 6061 alloy is precipitation hardenable, where the Mg₂Si precipitates play a major role in strengthening of the matrix in coarse grained alloy, it is necessary to understand its role in enhancing strength and ductility as well as thermal stability of the alloy at elevated temperatures.

In the present work, Al 6061 alloy is processed through cryorolling up to true strain 2.6 followed by low temperature ageing. The microstructure evolution and mechanical properties of the alloy before and after ageing is investigated through optical microscopy, EBSD, TEM, hardness testing and tensile testing. Furthermore, the cryorolled material is subjected to annealing at various temperatures ranging from 150 °C to 300 °C to observe the thermal stability of the alloy. Effect of annealing on microstructural evolution and precipitation has been investigated through detailed EBSD, TEM and DSC analysis.

4.2 Experimental

Al 6061 alloy samples with dimensions 12 × 30 × 40 mm³ were machined from the as received material, solution treated (ST) and then water quenched to room temperature. The ST samples were then CR up to a true strain ~2.6. The CR 92% samples were further subjected to low temperature ageing at 100°C, 125°C and 140 °C for long hours. To study the effect of annealing on microstructure evolution and mechanical properties, all the rolled sheets were annealed at various temperatures ranging from 150 °C to 350 °C with 50 °C interval for 1 hr. To evaluate the mechanical properties of ST, CR92%, CR92%+ aged and CR92%+ annealed samples, hardness and tensile tests were carried out at room temperature. Vickers hardness was measured on the surface plane parallel to the rolling direction, an average of at least eight readings were taken to obtain hardness. The tensile samples were machined according to ASTM E8 standard, minimum four samples were tested. The coarse grained microstructure with increasing cryorolling strain was examined by employing optical microscopy. To examine the UFG structure evolution EBSD, TEM is employed. To study the precipitate evolution after annealing at different temperatures of cryorolled samples, XRD and DSC were used. The flow chart of experimentation is shown in *Figure 4.1*

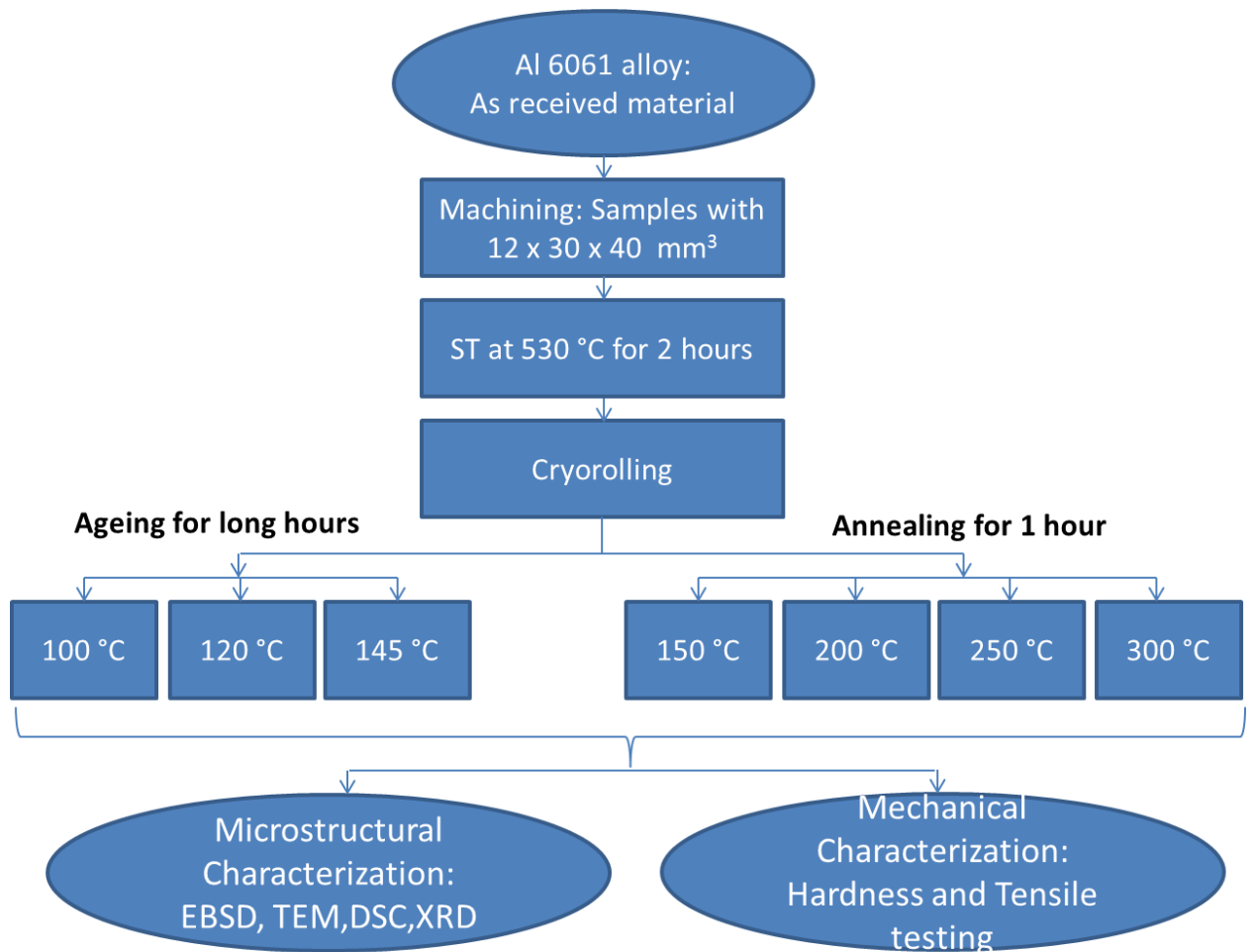


Figure 4. 1: Flow chart of experimental procedure adopted in this chapter.

4.3 Results

4.3.1 Effect of cryorolling on microstructural and mechanical properties

4.3.1.1 Microstructure

The optical microstructure of coarse grained Al 6061 alloy after solid solution treatment is shown in *Figure 4.2*. The alloy exhibits equiaxed structure with an average grain size of 80 μm .

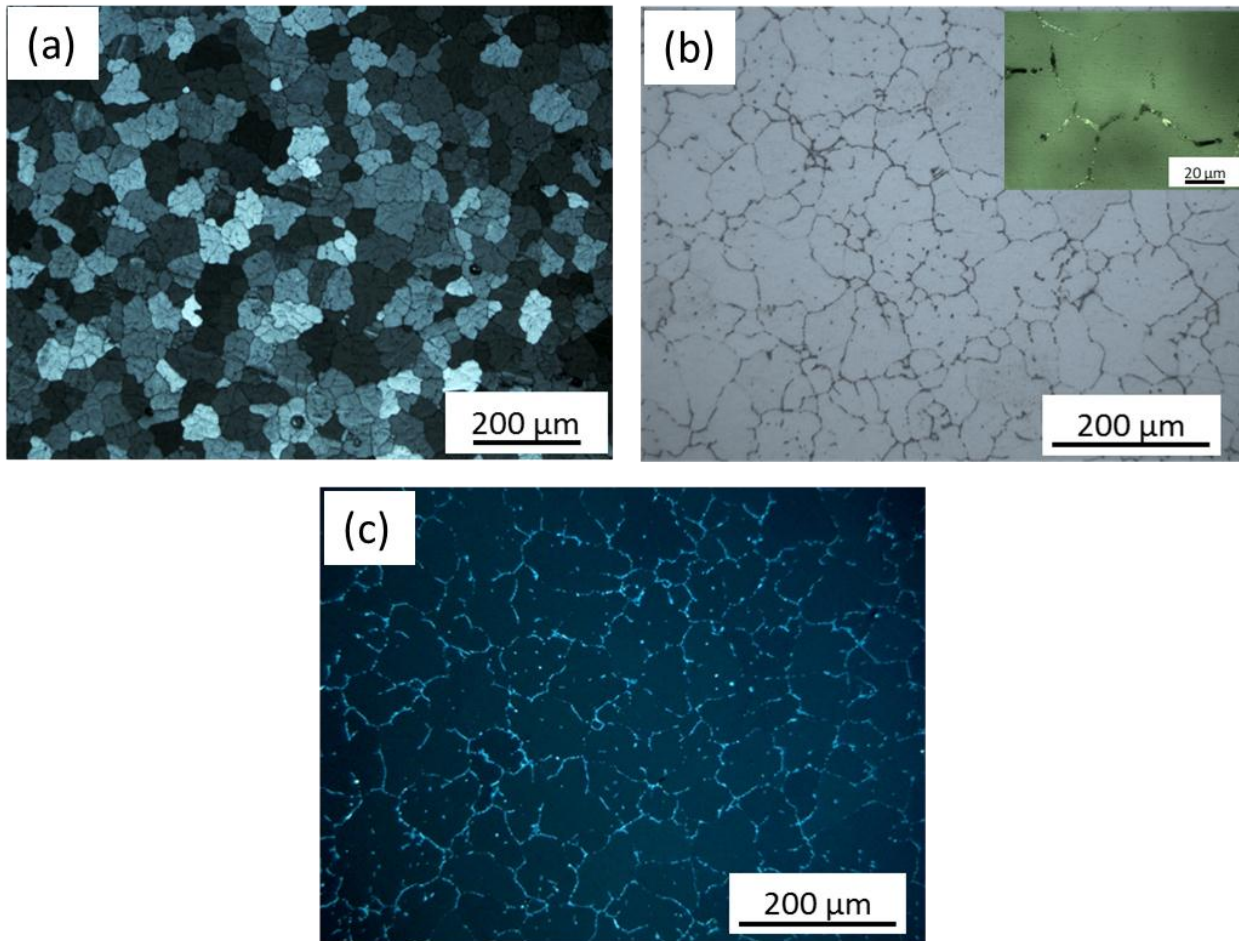


Figure 4.2: Optical micrographs of ST Al 6061 alloy obtained through: a) using polarized light mode, b) using bright field mode, c) using dark field mode.

Figure 4.2 (a) is obtained through observation under polarized light. *Figure 4.2(b)* shows bright field light image, with dendritic structure. In inset, it is shown that second phase particles are segregated at the grain boundaries which is typical characteristic of as cast material. *Figure 4.2 (c)* shows a dark field light image of *Figure 4.2 (b)*. Particles segregated at grain boundaries are highlighted in white color. *Figure 4.3* shows the optical microstructure of the material with

increasing cryorolling strain. Elongated grain structure along the rolling direction and fragmentation of chain like coarse constituent particles along the grain boundaries are seen (*Figure 4.3(c)*). With increasing strain to true strain of 2.6, the original grain boundaries got perturbed and the evolution of dislocation cell boundaries and its transformation to ultrafine grains is difficult to characterize under optical microscopy. High resolution microscopy techniques (TEM and EBSD) are employed to characterize the UFG structure evolution in high strained samples, during annealing.

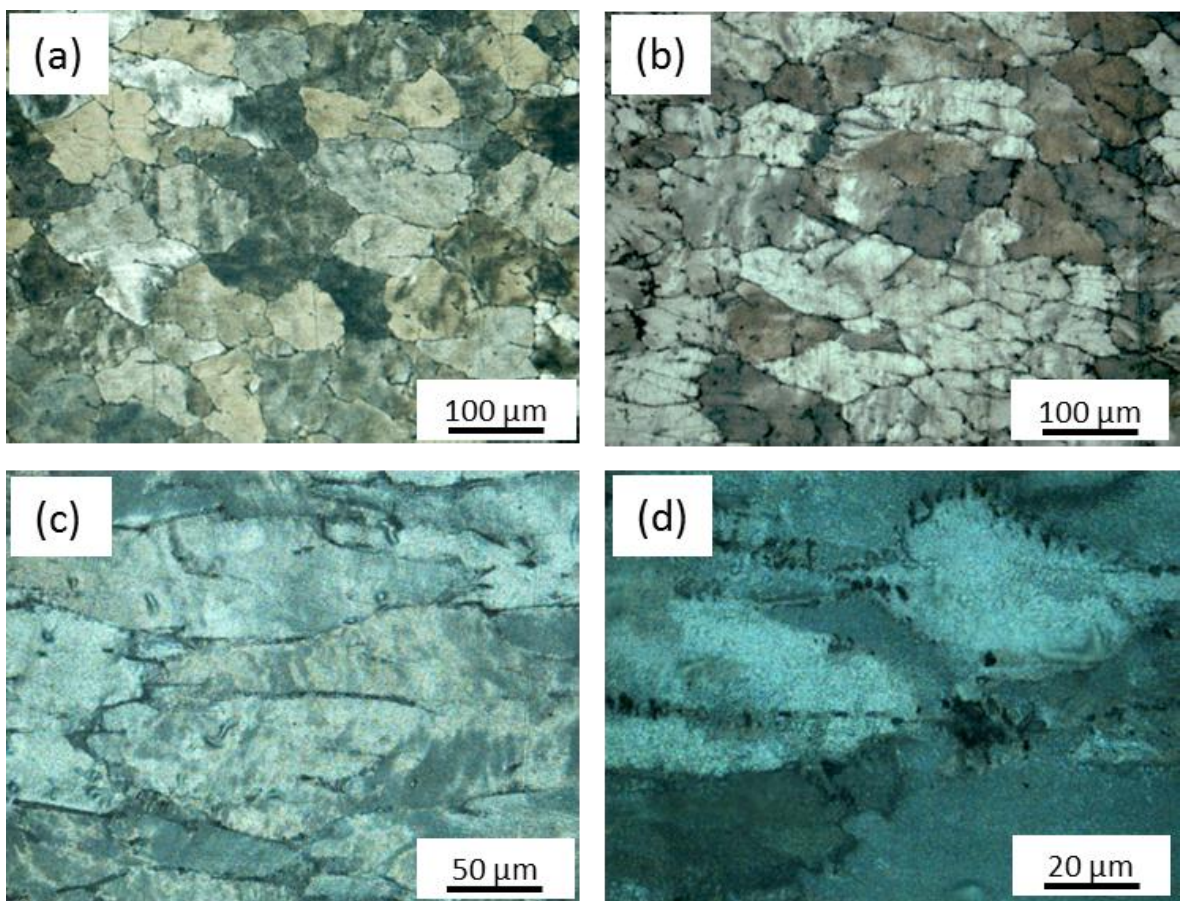


Figure 4.3: Optical micrographs of solution treated (ST) and cryorolled (CR) Al 6061 alloy samples at different % of reductions such as: (a) 35%, (b) 50%, (c) 70%, (d) 92%.

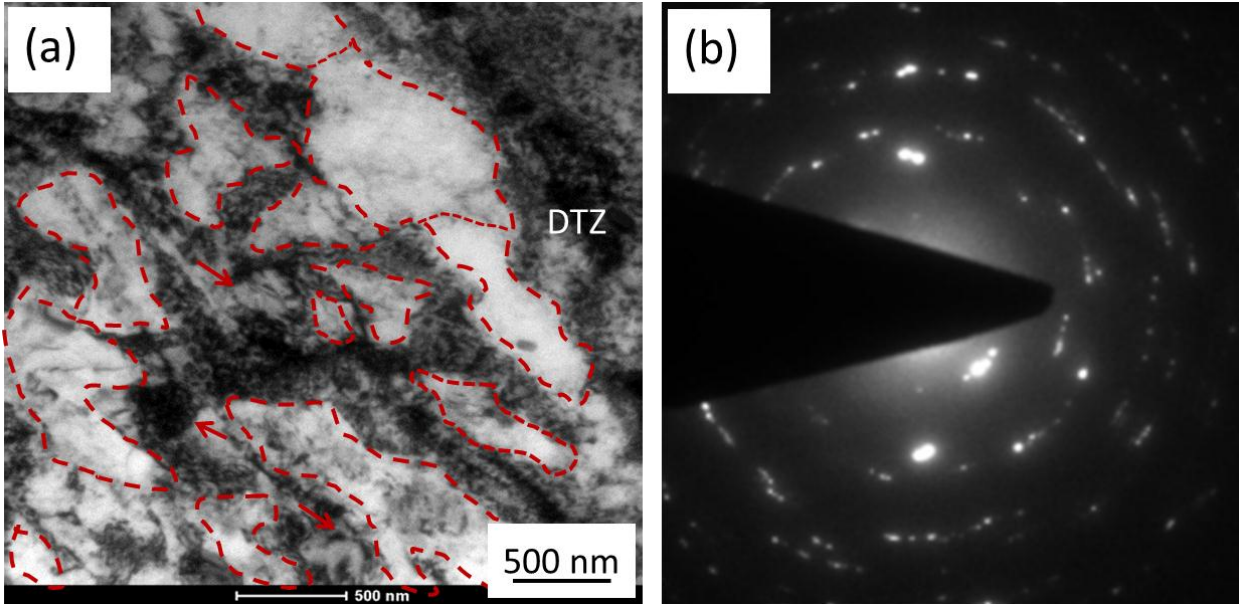


Figure 4.4 TEM micrographs of Al 6061 alloy after cryorolling; a) Bright field image, b) SAED micrograph

Figure 4.4 shows the TEM micrographs of Al 6061 alloy after CR up to true strain 2.6. Figure 4.4 (a) shows the typical as cryorolled material possesses microstructural features with few equiaxed ultrafine grains (shown with arrow mark), often elongated UFGs and dislocation tangled zones (DTZ) with high density of dislocations. The width and length of the elongated subgrains are 200 - 400 nm and 200 - 1000 nm, respectively. Areas outlined with dotted red lines in Figure 4.4 (a) are the interiors of the subgrains with reduced dislocation densities. The selected area electron diffraction pattern of CR92% material shown in Figure 4.4(b) indicates formation of randomly oriented polycrystalline structure.

To obtain more information from the larger area of the samples corresponding to CR 92% condition, EBSD technique is adopted. Figure 4.5 shows orientation image micrographs (OIM) along with image quality map (IQ Map) obtained through EBSD for CR 92% material. In the orientation image maps, the black area indicates un-partitioned area. Coarse constituent particles are observed along the grain boundaries as evident from optical micrographs of ST material and CR materials (Figure 4.2 and Figure 4.3). Figure 4.5(a) shows OIM with high angle grain boundaries (misorientation $> 15^\circ$). Figure 4.5 (b) shows a closed network of grey lines which represents low angle grain boundaries ($2^\circ < \text{Misorientation} < 15^\circ$). Figure 4.5 (c) represents IQ map and Figure 4.5(d) represents OIM of small area ($12 \times 12 \mu\text{m}^2$) cropped from Figure 4.5(b). From the EBSD data, it is clear that after CR92%, material possesses several grains under sub

micrometer size with low angle misorientation grain boundaries. High strained zones are formed along the grain boundaries, due to the presence of second phase coarse particles led to evolution of UFG with high angle grain boundaries. It is in agreement with TEM observations. However, the density of the subgrain boundaries has varied with respect to grain orientation.

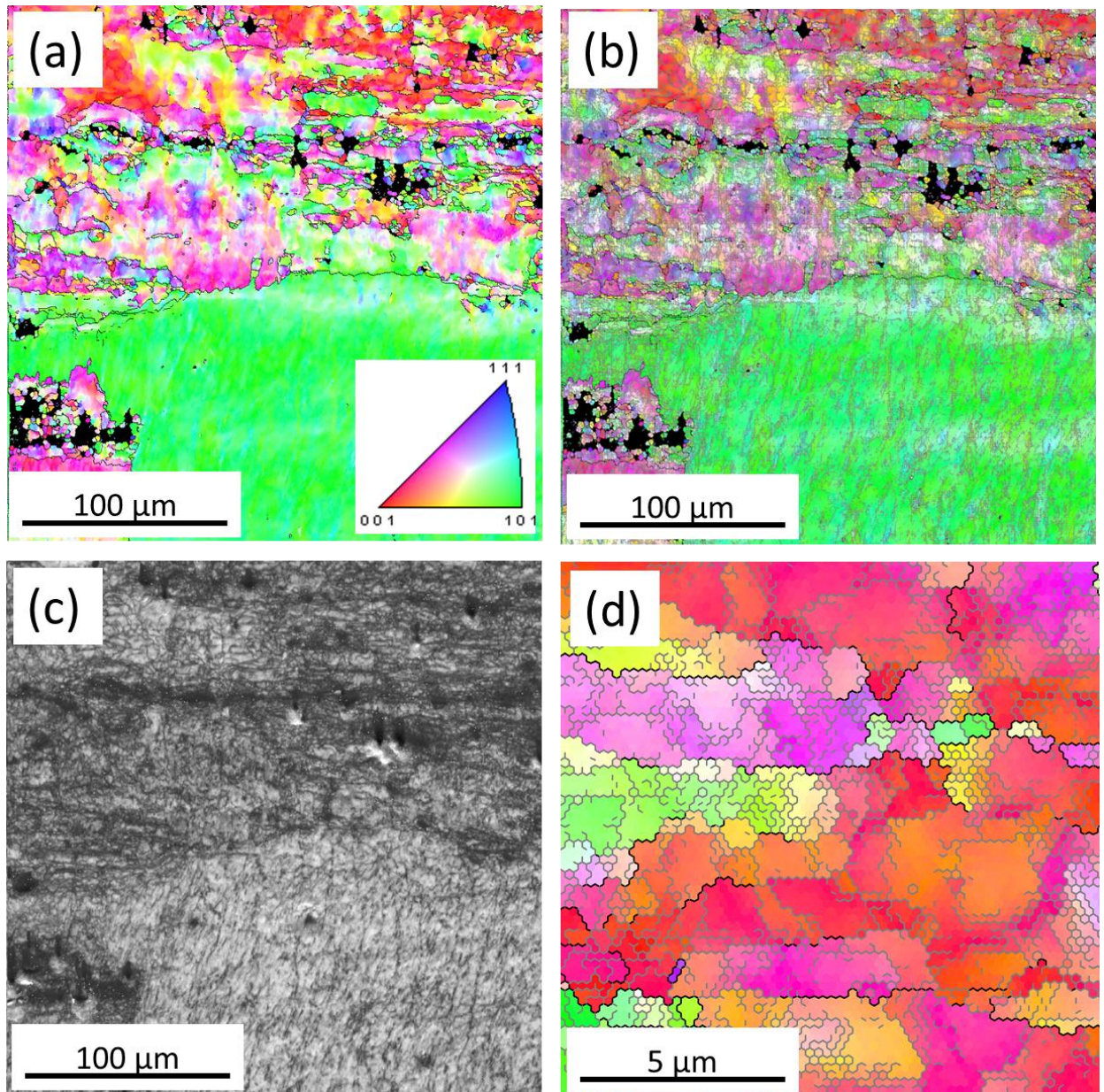


Figure 4.5 EBSD microstructures of CR92% Al 6061 alloy; a) Orientation image micrograph shown with high angle grain boundaries, b) Orientation image micrograph shown with low angle grain boundaries, c) Image quality map, d) Magnified view of area cropped area from **Figure 4.5 (b)**.

Grains oriented along $\langle 101 \rangle$ have shown poor refinement as compared to the rest. Orientation gradients in *Figure 4.5(d)* indicate the presence of high dislocation densities in the material. It is also evident from *Figure 4.5(d)* that, the transformation of low angle grain boundaries to high angle grain boundaries.

4.3.1.2 DSC studies

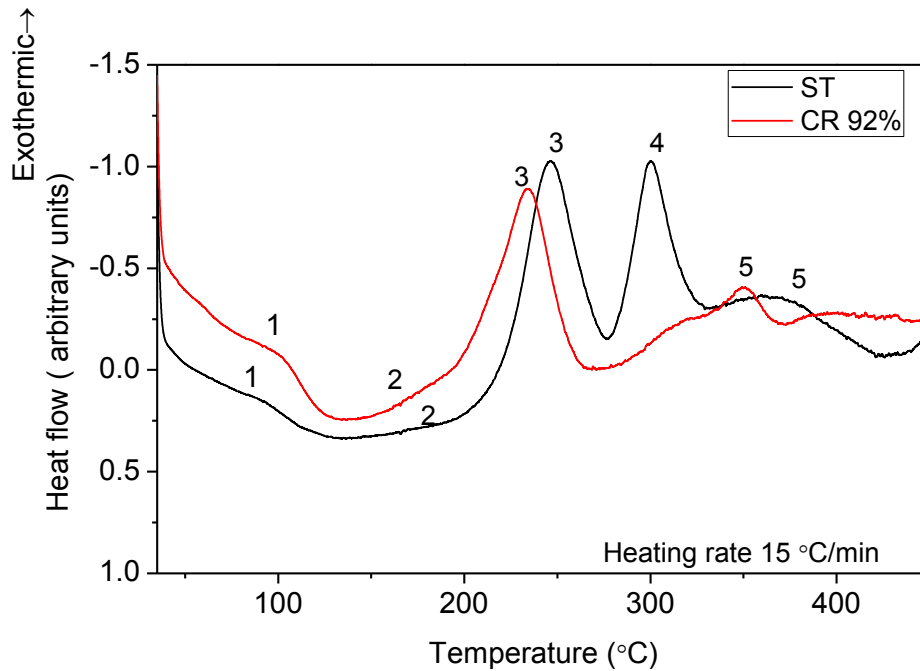


Figure 4.6: DSC heat flow curves of Al 6061 alloy; ST and CR material

To study the influence of CR on precipitation behavior of ST Al 6061 alloy, the material was subjected to DSC testing with 15°C/min scan rate under nitrogen atmosphere. The starting temperature of the DSC scan was at room temperature. Typical DSC plots of ST, CR are shown in *Figure 4.6*. The peaks obtained for ST sample with heating rate of 15 °C/min are identical with the precipitation sequence of Al 6061 alloy reported in the literature [138] [210] [211] [212] [213]. In the *Figure 4.6* the DSC plot of ST sample shows five exothermic reaction peaks marked as 1 to 5 at temperatures around 80, 190, 242, 290, 350 °C, respectively. The first two broad low intensity peaks at 80 °C and 190 °C are believed to be associated with the formation of Mg/Si co-clusters, and formation of G.P Zones. The next two major exothermic peaks 3 and 4 at temperatures 242 °C and 290 °C correspond to precipitation of β'' phase and its transformation to β' phase. The observed small hump at 350 °C (Peak 5) was similar to the one reported in the

literature [12] [136] [213]. It was observed that peak 5 corresponds to the precipitation of β - Mg_2Si or Si, which are not in agreement with the results reported in the literature [138] [212]. CR has resulted significant changes in the number and the position of exothermic peaks corresponding to precipitation formation in the alloy. In the CR sample, the exothermic reaction peak ranging from 195 -260 °C, which is believed to be the peak corresponding to β'' and it has shifted to low temperature (about 10 °C) as compared to that of ST sample. However there was no significant shift in the peaks corresponding to the cluster formation and G.P Zones formation peaks. The DSC results have shown that β' formation peak (peak 4) is suppressed in the cryorolled alloy. Only a single peak with a slight shift towards left is observed in CR sample due to the effect of deformation by cryorolling, which accelerates aging kinetics [12]. The suppression of β' peak in Al 6061 alloy was also observed in the deformed monolithic and composites by Appendino et al., Birol, and Song et.al., [212] [213] [214]. It may be due to, the most of the solutes precipitate out as needle shaped and this would suppress the formation of peak 4, corresponding to β' formation as reported in their work. Another possibility could be simultaneous formation of β'' and its transformation to β' may occur without any sensible heat effect due to acceleration in ageing kinetics of precipitation by cryorolling.

4.3.1.3 Mechanical properties

Figure 4.7 shows the variation in mechanical properties of CR Al 6061 alloy with increasing percentage of deformation. The starting material with coarse grain structure after solution treatment has shown hardness as 54 Hv (*Figure 4.7 (a)*). By performing cryorolling up to 92 % thickness reduction, hardness has raised to 101 Hv. The hardness profile shows that, the increase in hardness after 70% has become sluggish. *Figure 4.7 (b)* shows the variation in tensile test properties of CR 6061 alloy with different % of reductions. The trend observed in UTS, YS and percentage of elongation of various thickness reduction samples at cryogenic temperature indicates typical cold rolled material behavior. The raise in UTS and YS of CR 92% alloy as compared to its coarse grained counterpart is 63% and 440% respectively. However the % of elongation has reduced from 30% to 4%.

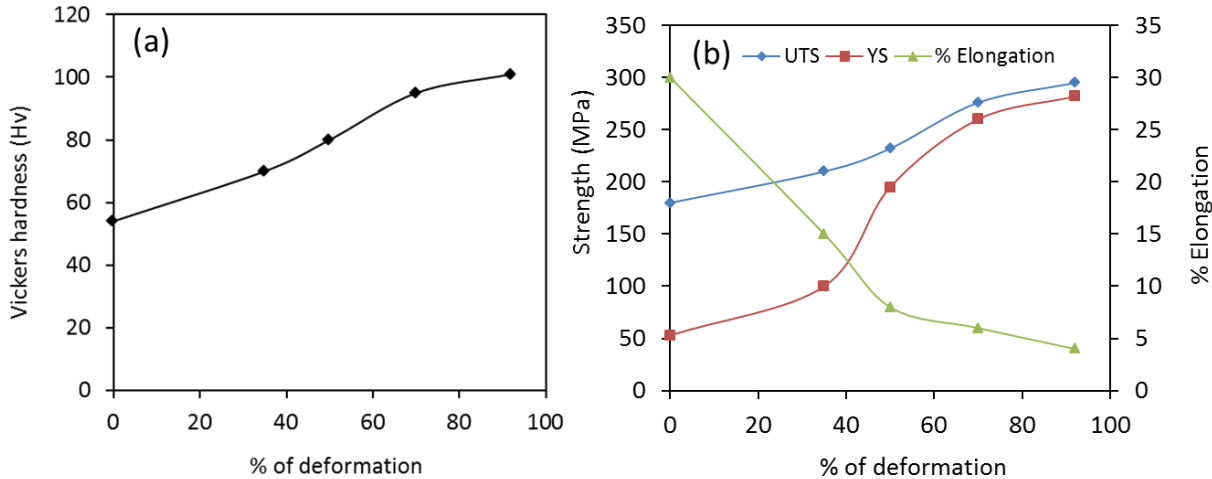


Figure 4.7: Variation in mechanical properties of CR 6061 alloy with increasing deformation at cryogenic temperature; a) Vickers hardness, b) Tensile test results.

4.3.2 Effect of low temperature ageing on microstructure and mechanical properties of CR Al 6061 alloy.

4.3.2.1 Mechanical properties

a) Hardness

Figure 4.8 shows the variation in Vickers hardness in CR 92% Al 6061 alloy with increasing ageing time at various ageing temperatures 100°C, 125°C and 145 °C. With increasing ageing time increase in hardness is observed in all temperatures. However ageing at 125 °C has resulted maximum hardness. The maximum hardness observed at 125 °C, is 117 Hv. It is nearly 16 % increment as compared to as CR material. Ageing at 145 °C has resulted sharp rise in hardness at the beginning, however it drops with increasing ageing time due to faster recovery of microstructure by annihilation of dislocations.

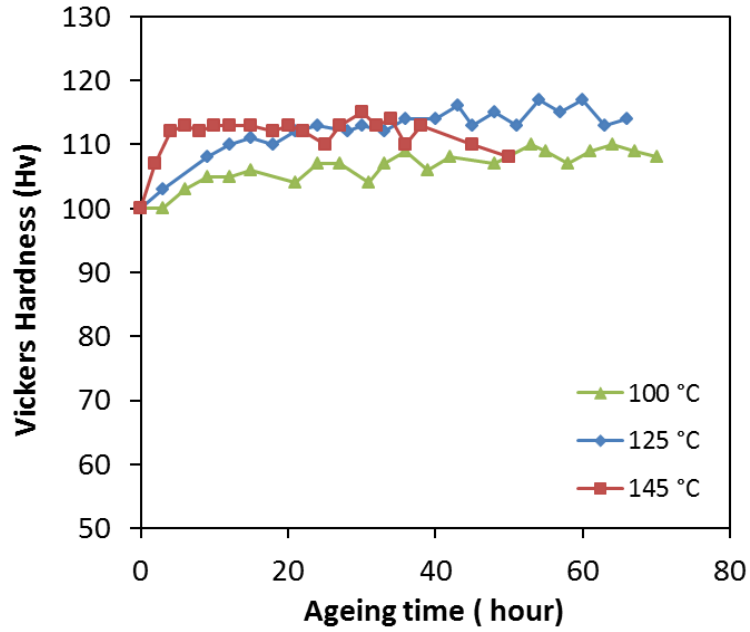


Figure 4.8: Ageing behaviour of CR Al 6061 alloy at 100°C, 125°C and 145 °C

b) Tensile properties

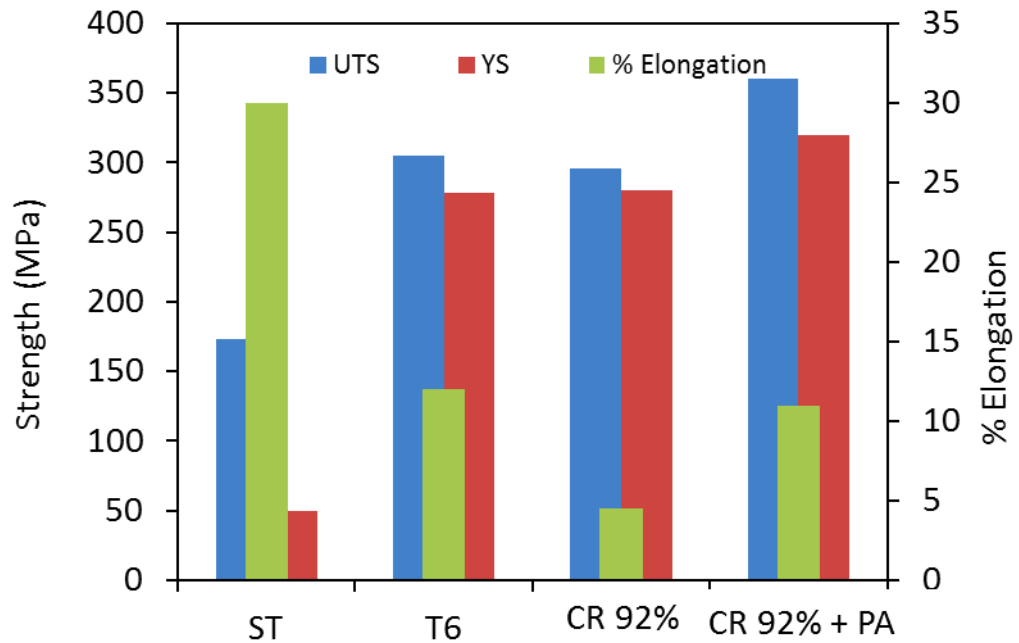


Figure 4.9: Comparison of tensile properties of Al 6061 alloy processed through various conditions; ST, (ST+PA) T6, CR 92%, CR 92%+PA.

Figure 4.9 shows the variation in tensile properties of CR92% material after low temperature ageing. Tensile properties of coarse grained material after ST and ST+PA (T6) heat treatments are also shown in the *Figure 4.9*. Low temperature ageing has resulted simultaneous improvement in UTS, YS and % of elongation of the CR92% material. The % elongation observed in CR92%+PA material is much higher than that of CR92% material. The improvement in tensile properties of CR92%+PA material is attributed to formation fine nanosized precipitates which contributes for further strengthening of the CR 92% material and reduction of dislocation densities through recovery process while under low temperature ageing which contributes for increase in % elongation.

4.3.2.2 Microstructure

Figure 4.10 displays the bright field TEM micrograph of CR 92% material after peak ageing treatment (125 °C for 55 hours). Low temperature ageing has resulted formation of UFGs with well-defined grain boundaries along with deformed microstructure retained from CR, processing non-equilibrium grain boundaries (*Figure 4.10 (a)*) [215]. The size of the UFGs is found to be in the range of 200 to 400 nm. The reasonable contrast difference between UFG to neighboring area indicates, increase in misorientation of the subgrain boundaries. *Figure 4.10 (b)* depicts very fine nanosized precipitates distributed throughout the matrix (shown with arrows) which are formed during ageing. These are believed to be the end sections of needle shaped precipitates of β'' precipitates. The poor visibility of precipitates in the matrix is due to presence of dislocations.

4.3.3 Microstructural and Thermal stability studies of CR92% Al 6061 alloy

4.3.3.1 TEM studies

To investigate the microstructural and thermal stability of CR 92% Al 6061 alloy, the material is subjected to annealing at different temperatures ranging from 150 °C to 300 °C with an interval of 50 °C. *Figure 4.11* shows the TEM micrographs of annealed alloy at 150 °C, 200 °C and 250 °C for 1 hour. After annealing (*Figure 4.11*) significant changes were observed in the CR92% material.

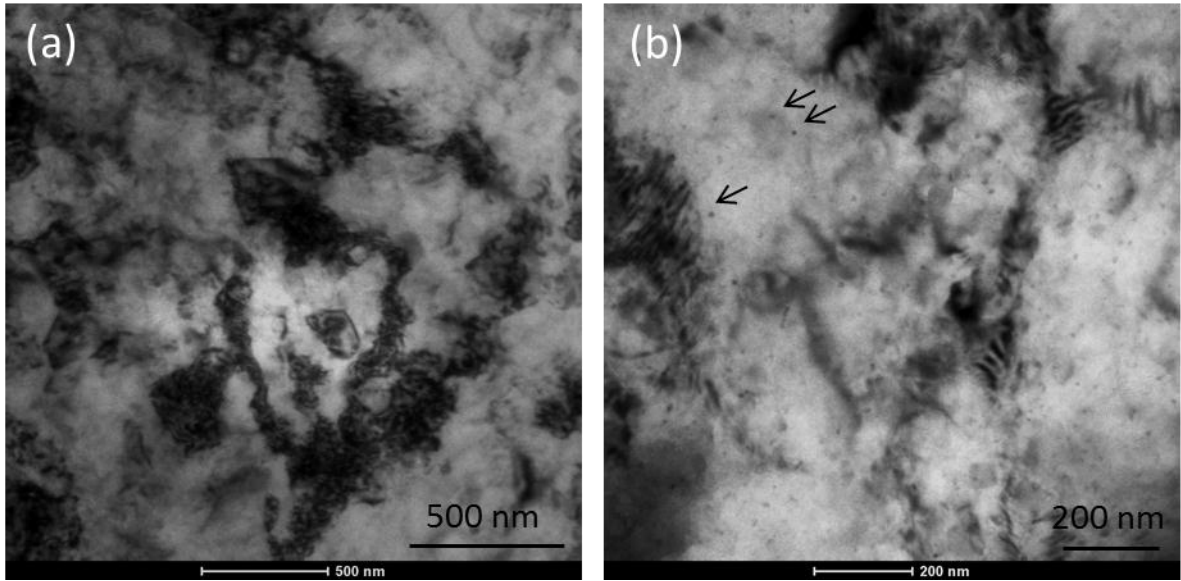


Figure 4.10: Representative TEM images of CR 92% Al 6061 alloy; a) shows partially recovered grains after peak ageing treatment (PA), b) shows nanosized precipitates observed in CR92%+PA samples.

Formations of UFGs with an average size of 300 nm are observed in 150 °C annealed sample. Upon annealing, dislocation density has been reduced by annihilation during the process of rearrangement of dislocations into sharp grain boundaries (*Figure 4.11 (a)*). Precipitates are indicated with red color circles in *Figure 4.11(a)*. At 150 °C annealing, along with recovery, precipitation also takes place. *Figure 4.11 (b)* represents the microstructure after annealing at 200 °C for 1 hour with homogenous distribution of UFGs. The average grain size is observed to be 350 nm. Few grains with sharp grain boundaries and relatively free from dislocations at inside are evident from the *Figure 4.11 (b)*. Still some grains with fuzzy grain boundaries are observed. With further increasing annealing temperature to 250 °C, the UFG size has slightly increased to 400 nm (*Figure 4.11 (c)*). The fraction of UFGs with sharp grain boundaries and dislocation free interiors has increased. TEM investigation is further extended to observe the roll of coarse particles corresponding to second phase and undissolved constituent particles in the grain refinement. Several micrographs were taken and montage them to represent large area.

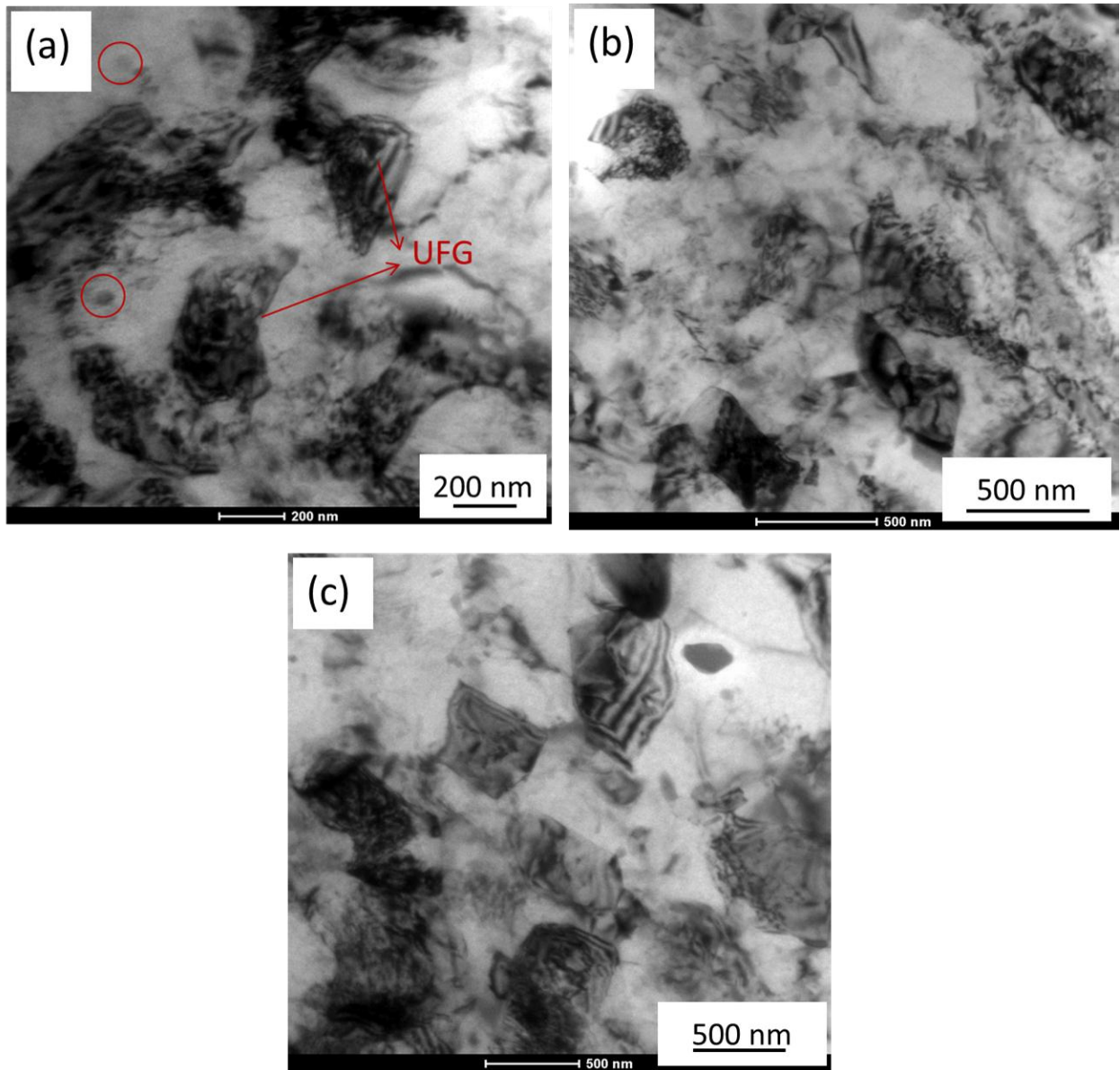


Figure 4.11: TEM micrographs of CR92% Al 6061 alloy annealed at different temperatures for 1 hour: a) 150 °C, b) 200 °C, c) 250 °C.

Figure 4.12 shows coarse particle (CP) surrounded with several very fine grains (size from 70 nm to 200 nm) at its boundary along with dislocations networks in the CR material annealed at 150 °C for 1 hour. These fine grains (marked with arrows in *Figure 4.12 (a)*) are evolved with sharp grain boundaries and dislocation free interiors with clear contrast with the neighboring areas. *Figure 4.12(b)* shows a small area in *Figure 4.12(a)* in enlarged view. The visible fringe in *Figure 4.12(b)* is corresponding to moiré patterns. Fine grains with an average

size of 200 nm are evident in *Figure 4.12(b)*. However, the contrast with the back ground matrix indicates low angle grain boundaries. *Figure 4.13* shows a montage of TEM micrographs obtained from the CR92% material after annealing at 200 °C for 1 hr. Several fine grains were sticking along the surface of coarse particle (CP). Fine circular shaped particle are observed which are corresponding to the Mg₂Si phase. During CR process, the second phase remains as a solute in the matrix and it imparts solid solute strengthening to the matrix. During deformation, it leads to enhancement of dislocation density.

With increasing annealing temperature, grain coarsening taken place. Simultaneously, precipitates became coarser and it pins the grain boundaries (*Figure 4.14*). Grain coarsening has occurred and duplex microstructure was observed with grain sizes ranging from 500 nm to 1µm. *Figure 4.15* shows alloy annealed at 300 °C, where the fully coarse grains with ~ 4 µm sizes are seen. It also shows a reasonably uniform distribution of second phase within the grains and at the grain boundary. After annealing at high temperatures (300 °C), these particles were grown and strongly interact with the grain boundaries, and the residual dislocations within these grains as shown in *Figure 4.15(a)*. The interaction of second phase particles with grain faces, grain edges and residual dislocation inside the grain were clearly represented in the *Figure 4.15 (a)*. *Figure 4.15(b)* shows the presence of spherical and rod shaped precipitates oriented in specific direction in another location of the same sample annealed at 300 °C for 1 hr.

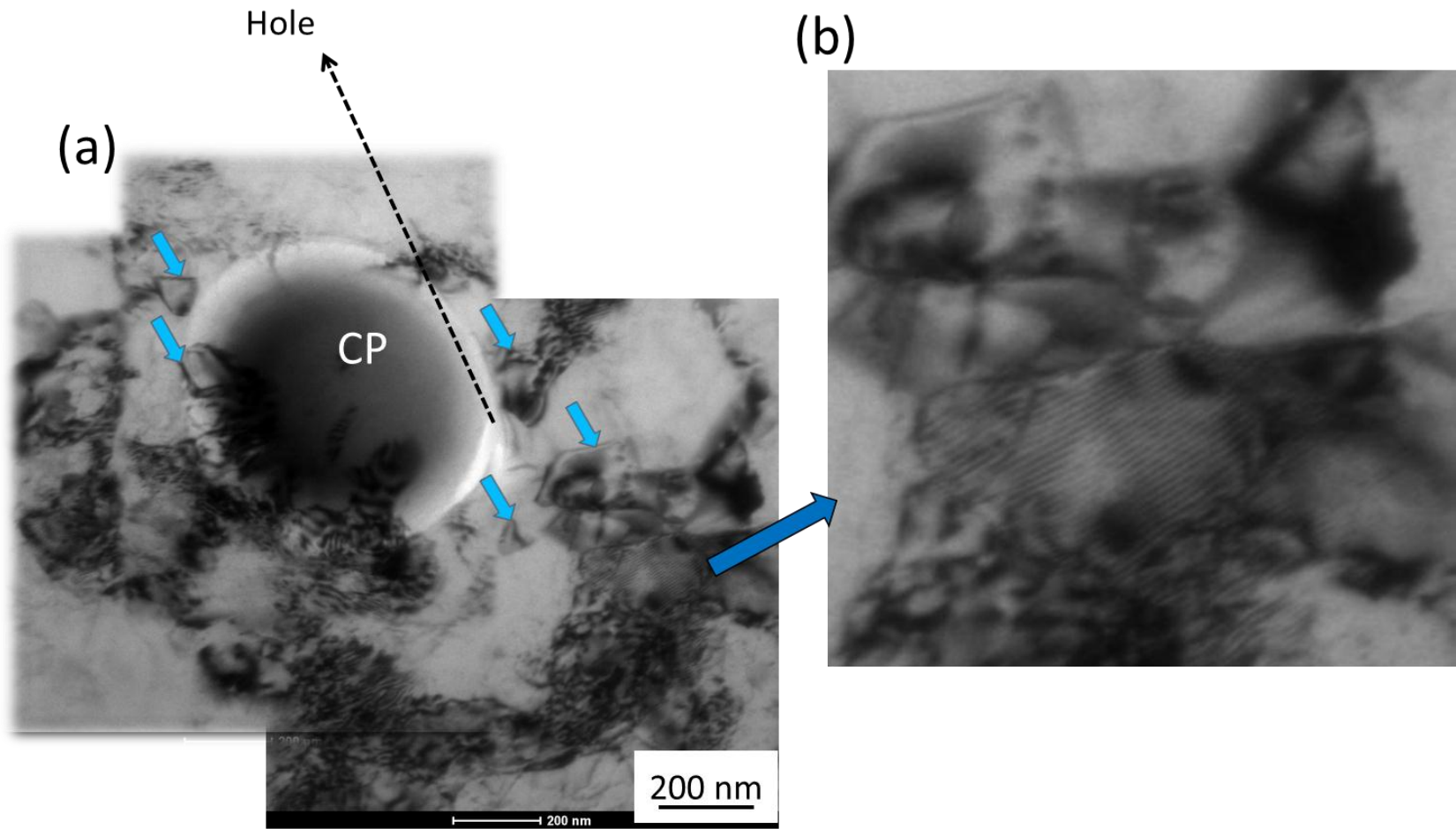


Figure 4. 12: TEM micrographs of CR Al 6061 alloy annealed at 150 °C for 1 hour; a) Evolution of very fine grains at the periphery of coarse particles (CP), b) Enlarged view of the area indicated with arrow in **Figure 4.12(a)**.

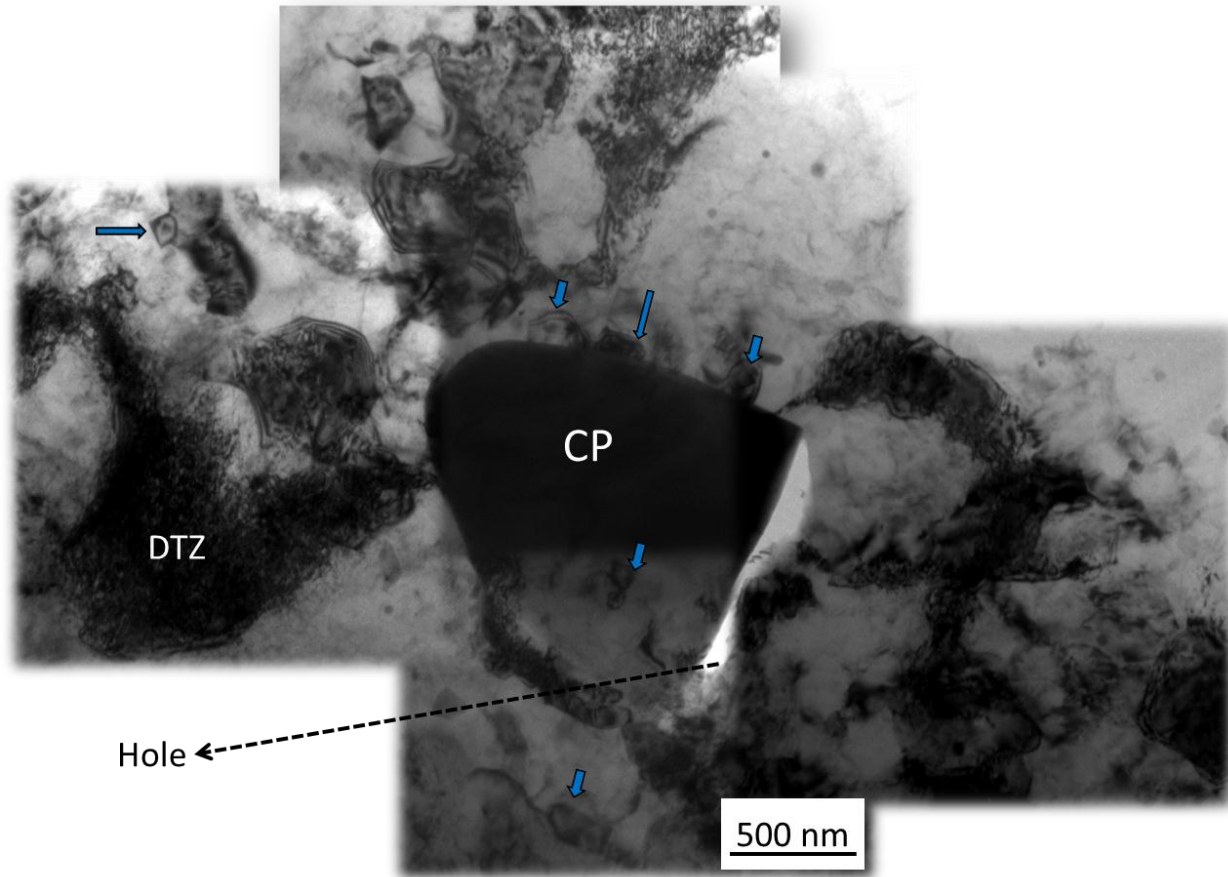


Figure 4. 13: TEM micrographs of CR Al 6061 alloy annealed at 200 °C for 1 hour; Evolution of very fine grains at the periphery of big second phase particle (particle stimulated nucleation).

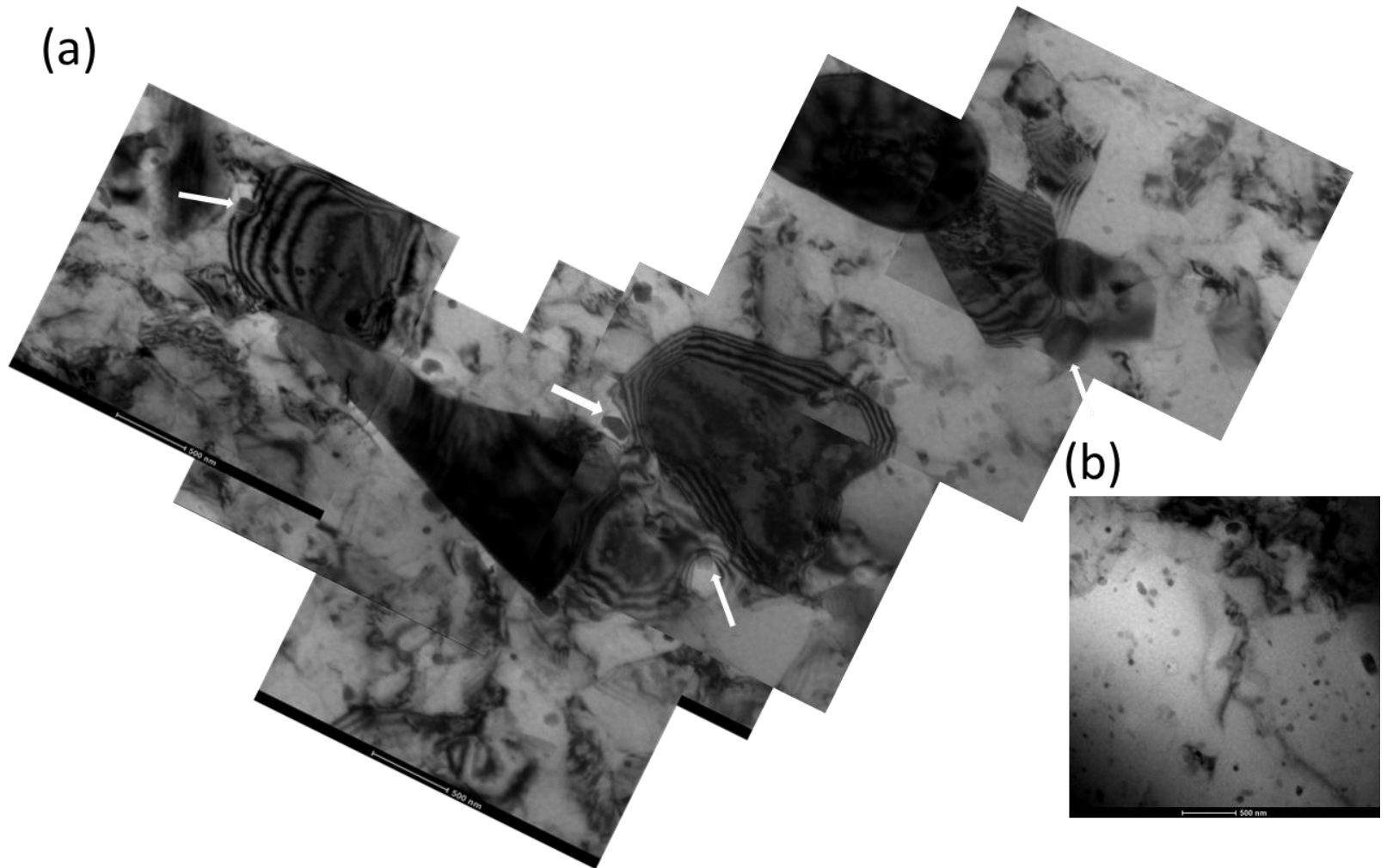


Figure 4. 14: TEM micrographs of CR Al 6061 alloy annealed at 250 °C for 1 hour; Pinning of second phase particles at the grain boundaries and grain faces.

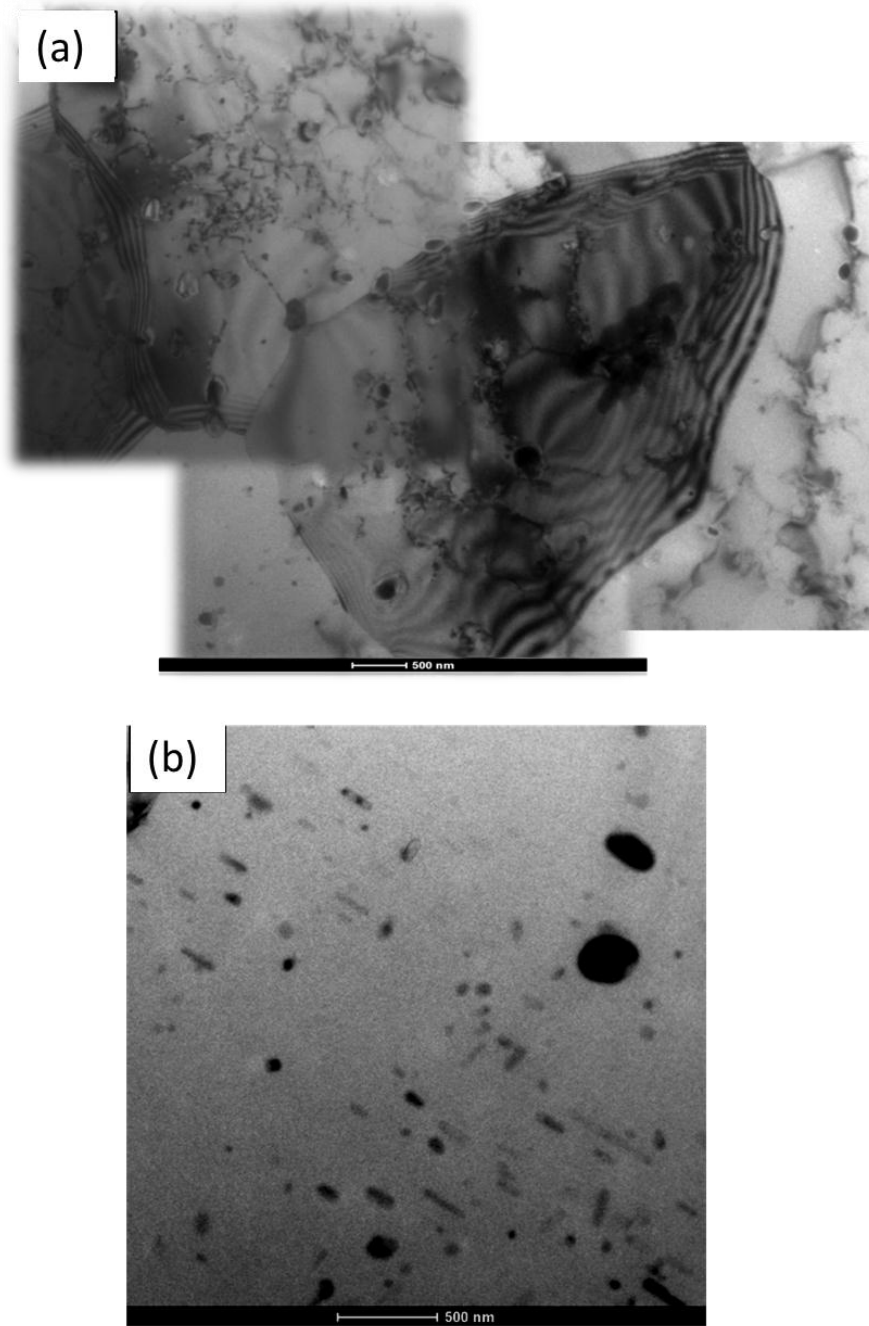


Figure 4. 15: TEM micrographs of CR 92% Al 6061 alloy annealed at 300 °C for 1 hour: a) Interaction of second phase particles at the grain boundaries and individual dislocations inside the grain, b) ‘ β ’ phase rod shaped stable precipitates oriented in particular direction.

4.3.3.2 EBSD studies

EBSD data for annealed material at 150 °C and 200 °C is shown in *Figure 4.16*. Annealing leads to formation of high fractions of high angle grain boundaries as evident from *Figures 4.16 to 4.18*. During the process of annealing, dislocations tends to form new grain boundaries and therefore its fraction increases. *Figure 4.16 (b)* indicates existence of high density of grain boundaries along with orientation gradients. With increasing annealing temperature to 200 °C, the microstructure possesses more fractions of HGBs (*Figure 4.16 (c)*). In *Figure 4.17 (d)* the black spots inside the oval represents unpartitioned area which corresponds to coarse second phase particles. Formation of UFGs with HAGBs can be observed in the *Figure 4.16 (d)*. However, there is no sign of recrystallization observed after annealing at 200 °C. EBSD micrographs of the CR material annealed at 250 °C are shown in *Figure 4.17*. A through observation of annealed samples indicates, there is a gradient of density of UFG from grain boundary region to the grain interior in parent grains. Grain orientation spread (GOS) maps indicates a sing of static recrystallization of UFG along the grain boundaries. However, the grain interiors are not affected much. The fraction of recrystallization is estimated as 5%. Annealing at 300 °C (*Figure 4.18*) resulted, microstructure with combination of coarse grains which are newly recrystallized and very fine grains formed through recovery. The recovered structure is not stable and it will undergo recrystallization upon increasing annealing time and temperature. However, material after annealing at 300 °C possesses microstructure with combination of very fine recovered grains with submicron size, newly recrystallized grains with an average size of 2-3 µm and coarsened recrystallized grains due to grain growth.

4.3.3.3 DSC studies

Figure 4.19 shows the DSC heat flow curves of CR Al 6061 alloy after annealing at temperatures from 150 °C to 250 °C with an interval of 25 °C. The heating rate applied is 15 °C/min. The DSC heat flow curve of 150 °C annealed material appears to be similar to the as CR 92% material (*Figure 4.6*), except flattening of low temperature peaks corresponding to clusters and G.P zone formation. These is no observable changes occurred in the high temperature peaks (> 150 °C). However with increasing annealing temperature to 175 °C, the intensity of β''/β' peak has reduced and low intensity endothermic is observed before the β''/β' peak formation.

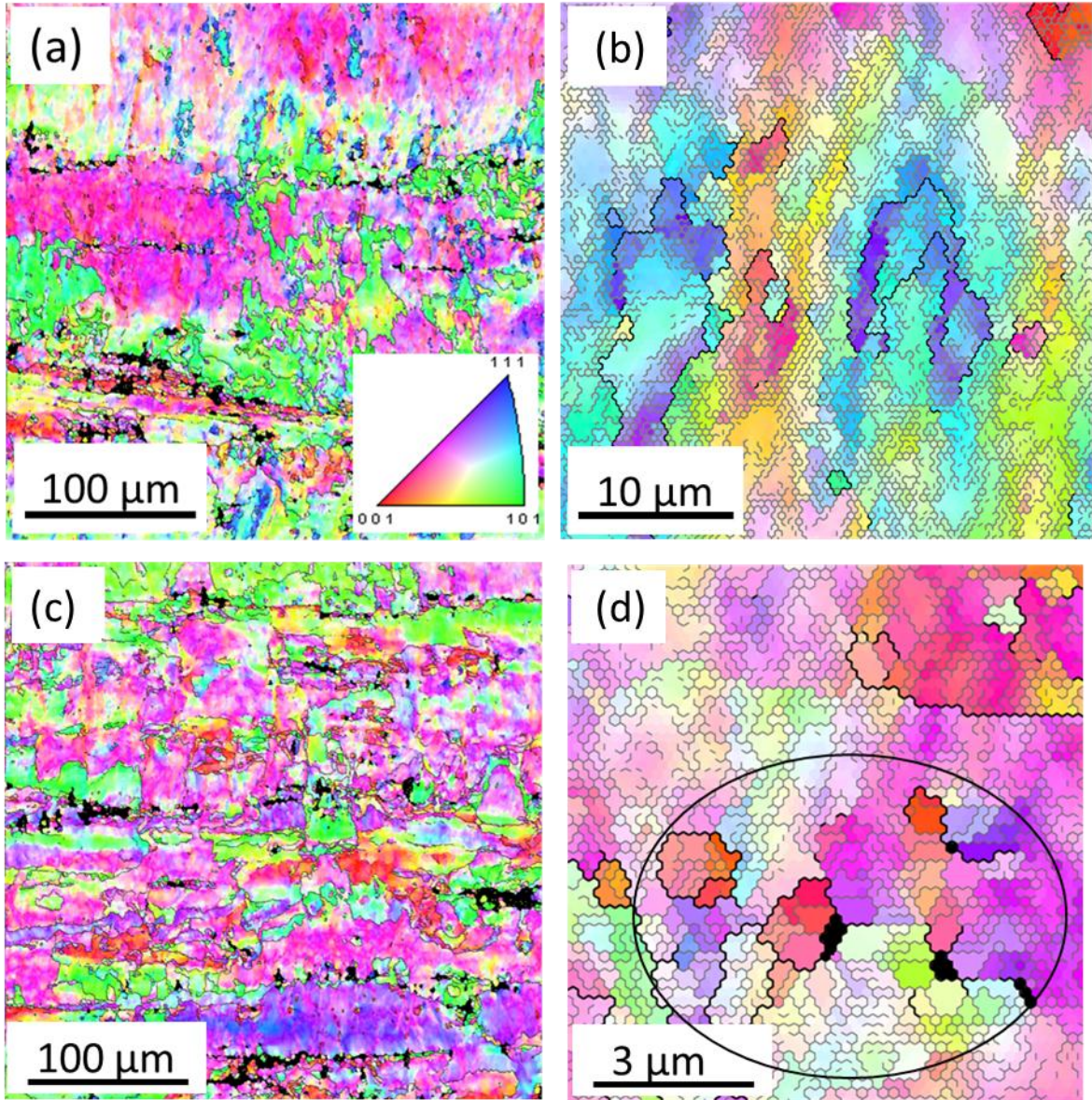


Figure 4. 16 : EBSD data of CR Al 6061 alloy; a) and b) are OIM micrographs of the alloy annealed at 150 °C, c) and d) are OIM micrographs of the alloy annealed at 200 °C. b) and d) are magnified view of cropped areas from (a) and (c) respectively.

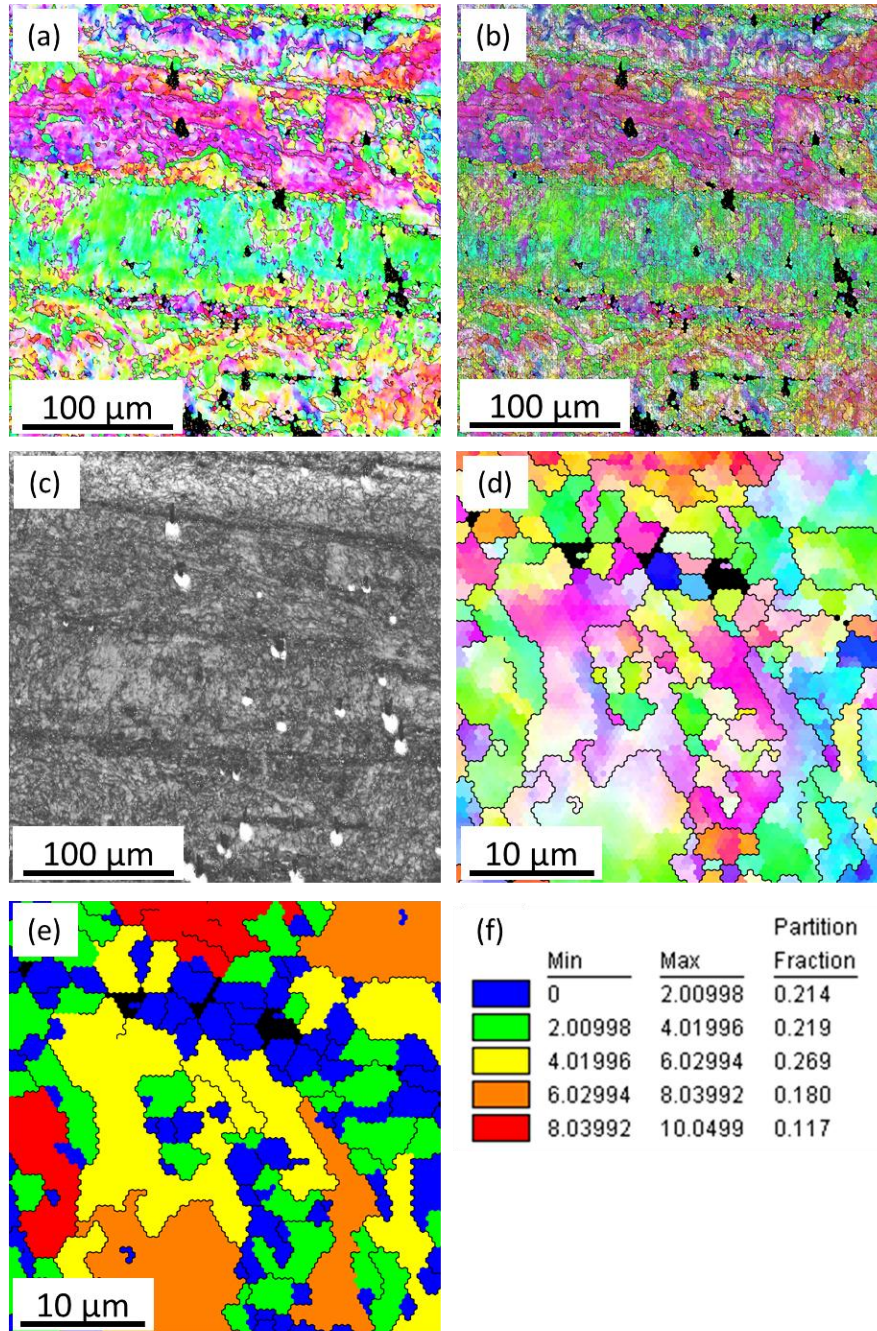


Figure 4.17: EBSD microstructures of CR Al 6061 alloy annealed at 250 °C for 1 hour; a) OIM shown with high angle grain boundaries, b) OIM shown with low angle grain boundaries, c) IQ map, d) Magnified view of area cropped from **Figure 4.17(a)**, e) Grain orientation spread (GOS) map of **Figure 4.17(d)**, f) GOS data.

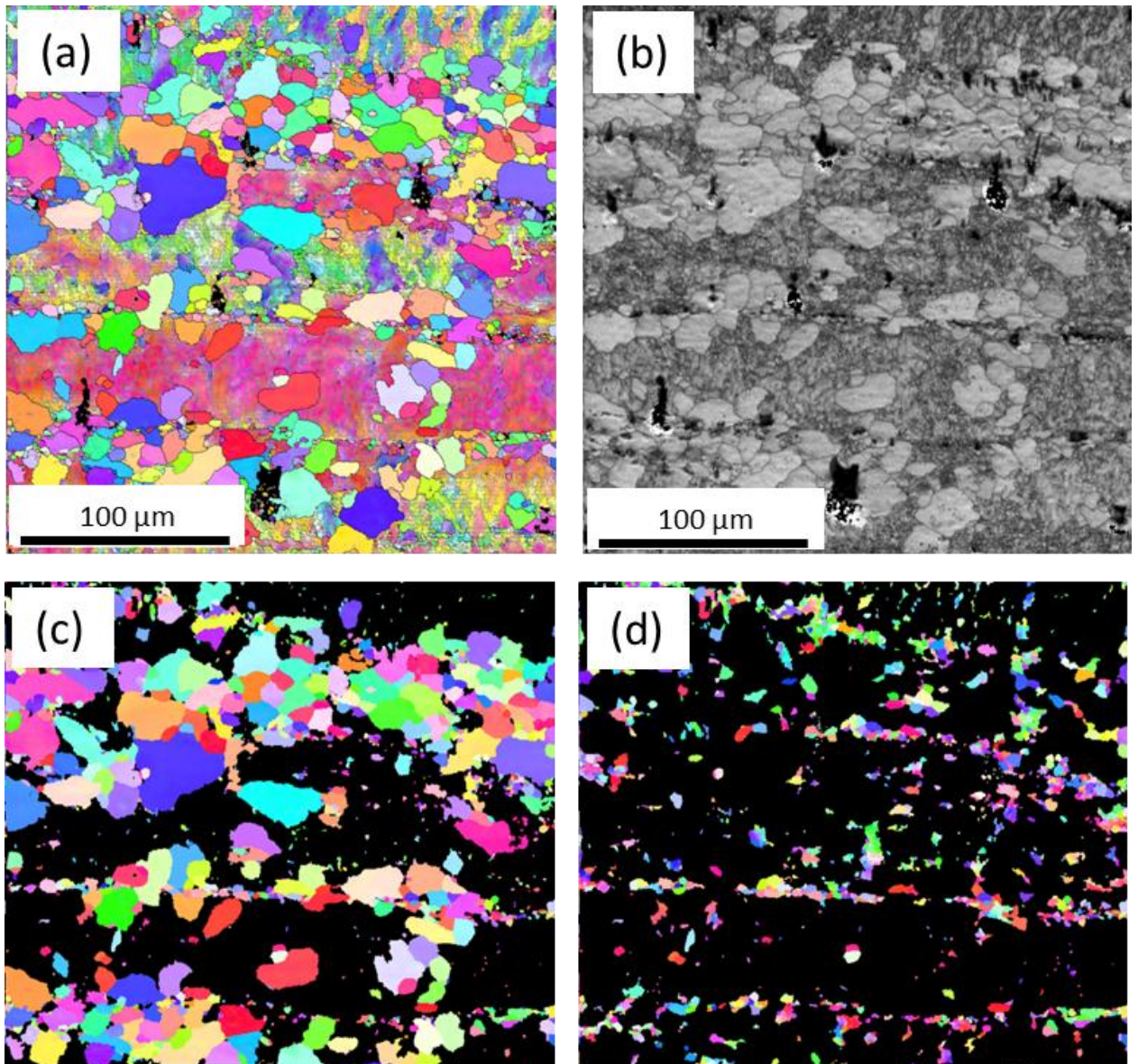


Figure 4.18: EBSD microstructures of CR Al 6061 alloy annealed at 300 °C for 1 hour; a) OIM showing distribution of low angle grain boundaries, b) IQ map, c) Recrystallized area portioned from **Figure 4.18(a)**, d) Portioned area with grain size less than 5 μm.

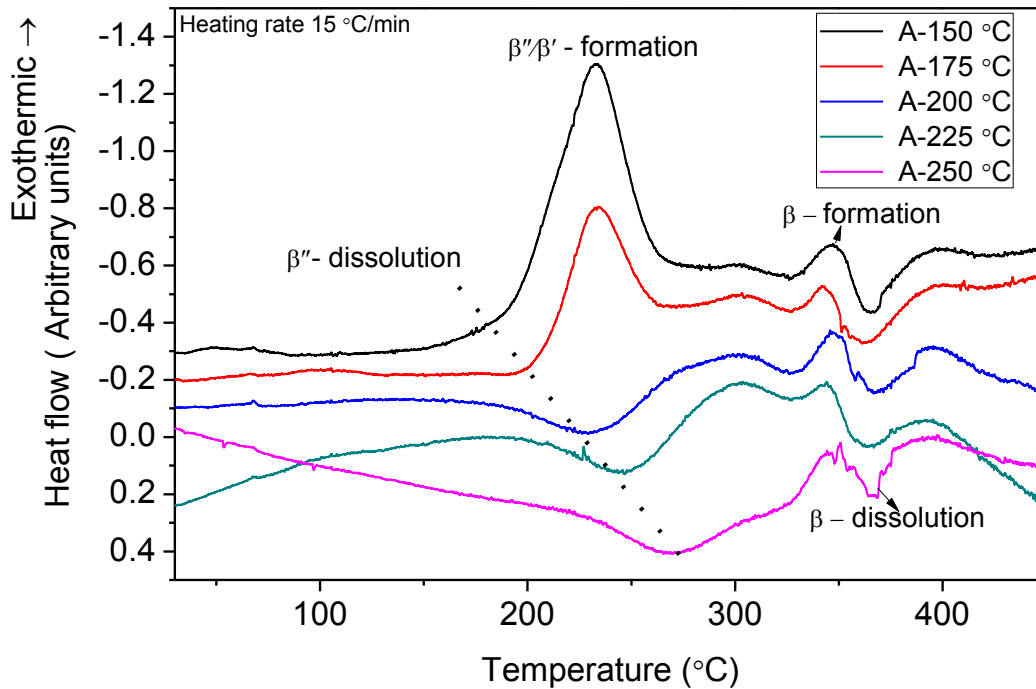


Figure 4.19: DSC heat flow curves of CR 92% Al 6061 alloy annealed at various temperatures.

With increasing temperature to 200 °C, the exothermic peak corresponding to β''/β' formation has disappeared, and the endothermic peak got deepen. It is attributed to complete formation of β''/β' phase after annealing at 200 °C. With further increasing temperature to 250 °C the endothermic peak has become deeper. However the position of the exothermic and endothermic peaks pertaining to equilibrium phase of Mg_2Si formation remains identical at all annealing temperatures.

4.3.3.4 XRD Results

Figure 4.20 depicts the XRD patterns of Al 6061 alloy after cryorolling, followed by annealing treatment at different temperatures. XRD was performed on Al 6061 alloy immediately after cryorolling. Cryorolled sample has shown a peak pertaining to undissolved AlFeSi phase and it does not show any peak corresponding to Mg_2Si phase. The peak corresponding to Mg_2Si phase appeared after annealing for 1 hour at 150 °C. The intensity of the peaks increased with increasing annealing temperature. The major second phases appeared in CR Al 6061 alloy after annealing treatment are Mg_2Si and AlFeSi.

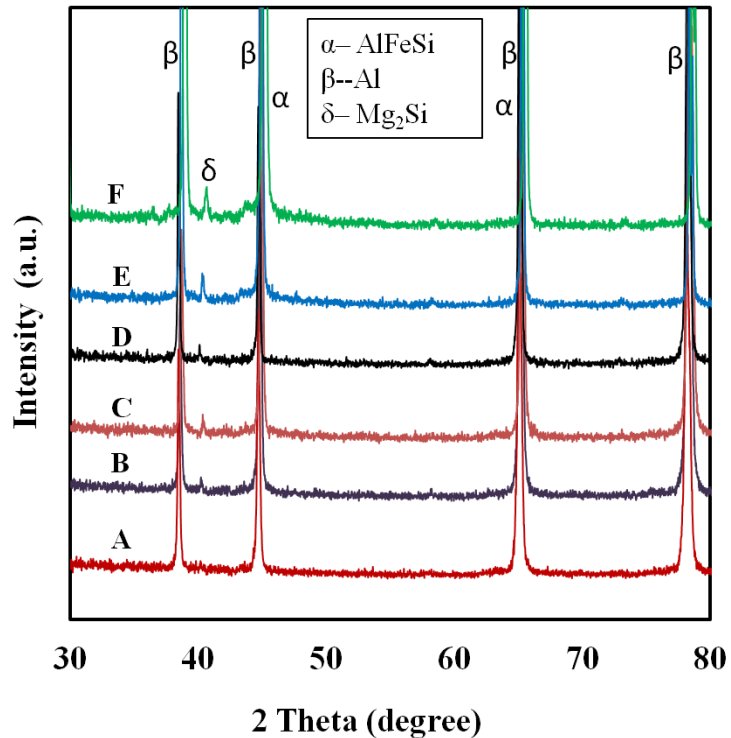


Figure 4.20: XRD patterns of CR Al 6061 alloy sample annealed at different temperatures for 1 hour: A) 0 °C, B) 150 °C, C) 200 °C, D) 250 °C, E) 300 °C, F) 350 °C.

4.3.4 Mechanical Properties

Thermal stability of Al 6061 alloy after cryorolling up to 92% reduction was analyzed by performing Vickers hardness test and tensile test at room temperature. *Figure 4.21(a)* illustrates the variation of Vickers hardness of cryorolled samples after annealing at temperature range from 150 to 350 °C for 1 hour along with the variation in the fraction of recrystallization. After annealing at 150 °C for 1 hour, the Vickers hardness value of Al 6061 alloy has increased from a value of about 101 HV to 114 HV, which can be attributed to precipitation hardening effect. The Vickers hardness value started dropping gradually from 114 HV to 108 HV after annealing at 200 °C. After annealing at 250 °C, the hardness drops suddenly from 108 HV to 70 HV and the drop proceeds with the same rate up to 300 °C. After annealing at 300 °C, the hardness nearly becomes constant at further temperatures. There is no remarkable change observed in the fraction of recrystallization till increasing annealing temperature up to 250 °C. After annealing at 300 °C, 50% recrystallization has occurred. However, the hardness value has dropped to the value equal or less than to the hardness of bulk material after solution treatment. This signifies the role of

precipitates on strengthening of the matrix. *Figure 4.21(b)* shows the variation in UTS, YS and % Elongation with increasing annealing temperature. The variation in UTS and YS has recovery effect. Further annealing after 150 °C, the ductility increased from 8% to 13% at 200 °C, 13% to 22% after annealing at 250 °C and from 22% to 30% after annealing at 300 °C. The variation in tensile properties has shown the same trend as observed in Vickers hardness variation. Simultaneous rise in strength (UTS-296 MPa to 340 MPa) and ductility (4.5% to 8%) is observed after annealing at 150 °C. The rise in strength and ductility is due to precipitation hardening effect and reduction of dislocation density, respectively.

4.4 Discussions

4.4.1 Effect of Annealing on Mechanical properties

The strengthening effect of Al 6061 alloy after cryorolling is due to combination of grain size strengthening, dislocation strengthening, and solid solution strengthening. Rolling at very low temperature induces accumulation of dislocations by suppression of dynamic recovery, which leads to high density of dislocations in the material [76]. After annealing at 150 °C for 1 hour, the increase in ultimate tensile strength (UTS 296 MPa to 340 MPa) and ductility (4.5% to 8%) is primarily due to formation of nanosized precipitates and recovery effect.

During annealing, dislocation density gets reduced due to recovery effect, which results in increase in ductility. The strengthening effect due to precipitation hardening and softening effect due to recovery are competing during annealing of cryorolled Al 6061 alloy. The rise in strength, observed in the sample after annealing at 150 °C reflects strengthening effect due to precipitation hardening, which dominates softening due to recovery. The slight drop in hardness from 114 HV to 108 HV after annealing at 200 °C indicated that softening effect due to annealing is dominating precipitation hardening effect. Annealing temperature beyond 200 °C, hardness and strength drop suddenly where the ductility increases significantly. The rise in ductility is mainly due to the formation of dislocation free equiaxed grains due to recrystallization effect. The softening effect due to recovery is much less than softening due to recrystallization [200]. Increasing annealing temperatures beyond 200 °C, precipitates lose its coherency with the matrix; hence its hardening effect is lost [110].

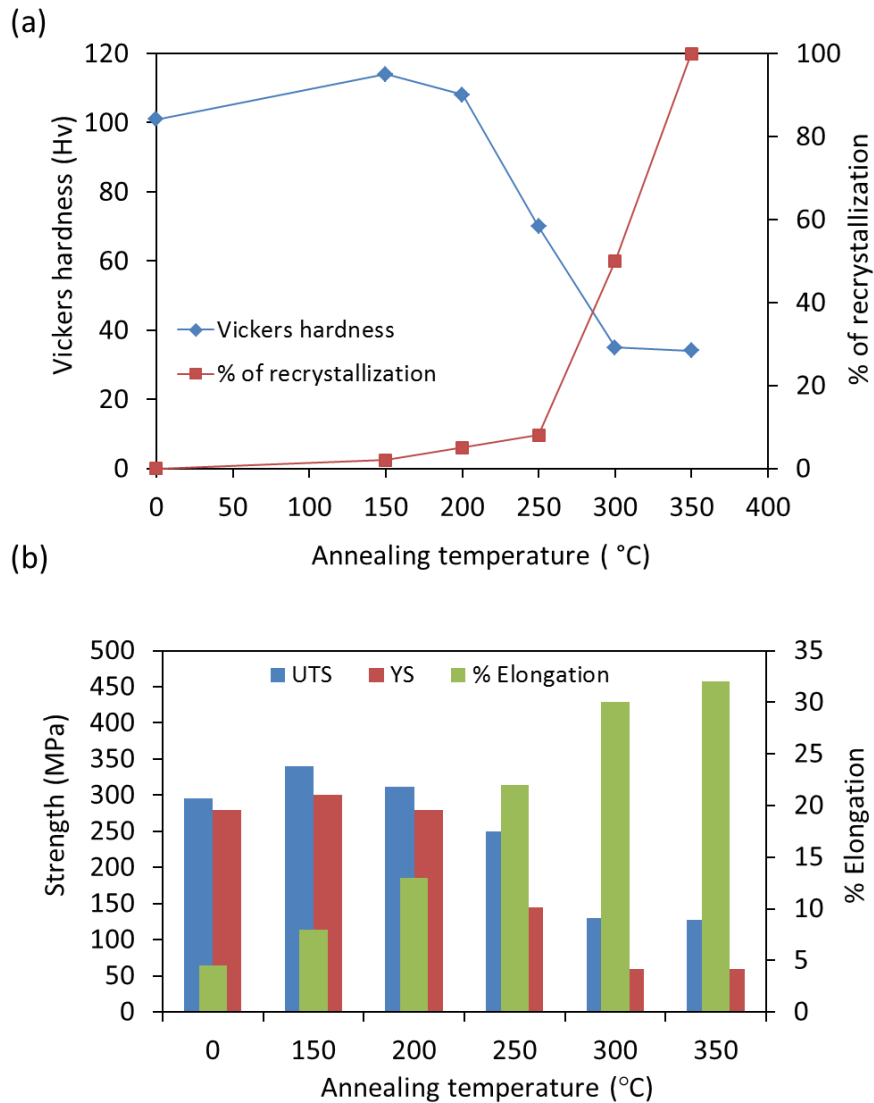


Figure 4.21: Variation in Mechanical properties of CR Al 6061 alloy with annealing temperature. a) Evolution of micro hardness and % of recrystallization with annealing temperature, b) Variation in tensile strength and ductility with annealing temperature.

As shown in *Figure 4.13*, alloy annealed after 250 °C for 1 hour have shown duplex microstructure consisting of equiaxed grains with 0.5 μ m to 1 μ m and slightly elongated grains. This observation is in agreement with literature on annealing behavior of Al 5083 processed by cryorolling and Al-Mg alloys processed by ECAE, reported by Y.B Lee et al, Morris et al, [200] [216], respectively. At annealing above 300 °C, hardness value became almost stable, and also

there is not much change observed in the strength and ductility values. 'β' phase precipitates in rod shape were observed in annealed sample at 300 °C. Presence of 'β' phase, which is incoherent with the matrix, does not show any strengthening effect.

4.4.2 Role of Second phase in evolution of microstructure during annealing

The major alloying elements in Al 6061 alloy are Mg and Si, and this will present in the form of dispersed particles which get dissolved in Al to form solid solution during solution treatment. During annealing treatment of cryorolled Al 6061 samples, precipitation takes place simultaneously with recovery and recrystallization. Precipitates will keep growing with increasing annealing temperature and play a significant role to stabilize the microstructure at high temperatures. This second phase effects on recrystallization occur as follows: i) Stored energy is increased by the particle which create extra particle - matrix inter phase or traps dislocations. ii) Large particles serve as nucleation sites for recrystallization. iii) Pinning of the grain boundaries by the particles [217]. TEM micrograph in *Figure 4.11(a)* reveals recovered microstructure after annealing at 150 °C along with very fine precipitates, which were marked in the micrograph. From the hardness evolution and XRD patterns of cryorolled samples annealed at different temperatures as shown in *Figure 4.20 & 4.21*, it can be concluded that these fine particles are corresponding to β" precipitates, which imparts strength to the materials with its coherency with the matrix. Presence of coarse second phase particles are acting as nucleation sites for evolution of dislocation free equiaxed grains as observed in the sample after annealing at 200 °C. Presence of duplex microstructure in the samples annealed at 200 °C (*Figure 4.13*) may be due to the heterogeneities in the sample. A discontinuous grain growth in samples after annealing at 250 °C results in a little variation in the grain size ranging from 0.5 μm to 1 μm. Continuous grain growth can be expected in the fine-grained microstructure with fraction of high angle grain boundaries more than 0.6 [49] [218]. Fraction of high angle grain boundaries in CR Al 6061 alloy is not sufficient enough for continuous grain coarsening to takes place [219]. Second phase particles are effectively controlling the grain growth by pinning effect at grain boundaries, leading to the stable microstructure with grain sizes $\leq 1 \mu\text{m}$ in the samples annealed at 250 °C. The volume fraction and the size of second phase particles play a major role in effective control of the grain growth. Grain growth of particle containing alloys depends on Zener drag pressure ($P_z = K (f \gamma/r)$), which acts against to the driving pressure for grain growth ($P_g = \alpha \gamma/D$). Where 'f' is the particle volume fraction, 'γ' is the grain boundary energy per unit area, 'r' is the particle

radius, 'D' is diameter of grains, α is geometric constant and 'K' is constant related to coherency [220] [221]. If $P_z = P_g$, it is known as equilibrium case. If $P_z > P_g$, then the Zener drag by second phase particle is expected to occur and if $P_z < P_g$, grain growth is expected to occur. Annealing after 300 °C, abnormal grain growth was observed which reflects that, at high temperatures, the available driving pressure for grain growth dominates Zener drag pressure exerted by the particle. It is clear that, CR Al 6061 alloy microstructure is thermally stable up to ≤ 250 °C.

4.5 Conclusions

In the present investigation, the effect of ageing and annealing on microstructure and mechanical properties of Al 6061 alloy processed through cryorolling was studied and the following conclusions are drawn.

1. Ageing at low temperature for long hours (125 °C) has resulted simultaneous increase in strength and ductility in CR 92% material. The similar behaviour has been observed in the CR 92% samples annealed at low temperature (150 °C for 1 hr). It can be attributed , strengthening effect due precipitaion hardnening overwhelms the softening effect due to recovery.
2. Annealing at 200 °C results in drop in strength (UTS- 340 MPa to 312 MPa) and increase in ductility (8% to 13 %) due to evolution of dislocation free grains by recovery. Drop in strength at annealing temperatures of 200 °C to 300 °C is drastic due to loss in precipittaion coherency with the matrix.
3. Presence of local heterogenities results in duplex microstructure consisting of equiaxed grains with grain size range from 150 nm-500 nm along with subgrain structure with full of dislocation content.Hence, a good combination of high strength (UTS-312 MPa) and elongation (13 %) is observed in samples annealed at 200 °C for 1 hour.
4. Annealing for 1 hour at different temperatures range from 150 - 300 °C reveals that submicron grains in CR 92% Al 6061 alloys are thermally stable up to a temperature 250 °C due to the effective retardation of grain growth through pinning of grain boundaries by Zener drag effect of fine second phase particles.

Chapter 5

Warm rolling

This chapter details about the effect of cryorolling followed by warm rolling on microstructure and mechanical properties of Al 6061 alloy. The first section of this chapter, describes about the effect of warm rolling on microstructural evolution and mechanical properties. In the second section, a comparative study is made between short annealing and warm rolling preceded by cryorolling on enhancement of strength and ductility of Al 6061 alloy. The observed mechanical properties are confirmed with microstructural features characterized by EBSD, TEM, DSC and XRD studies.

5.1) Effect of Cryorolling followed by Warm rolling on Microstructure and Mechanical Properties of Al 6061 alloy

5.1.1 Introduction

In precipitation hardenable Al 6061 alloy, cryorolling followed by low temperature ageing has resulted an appreciable increment in strength and ductility as reported in the chapter 4. This approach has been well established for many precipitation hardenable alloys [11] [13] [14] [201], as an effective method to achieve simultaneous increment in strength and ductility. However the raise in strength, in coarse grained Al 6061 alloy through precipitation hardening alone, is much higher than that achieved in UFG Al 6061 alloy. It is attributed to dominant softening effect by recovery during post cryorolling static ageing treatments. The reports on 5052 Al alloy indicates, the combination of cryorolling followed by warm rolling has resulted remarkable improvement in yield strength (YS) and ultimate tensile strength (UTS), and it was attributed to formation of fine precipitates during warm rolling after cryorolling [222]. This approach can be viable in precipitation hardenable alloys to enhance the precipitation hardening effect further [222] [223]. Cai et al., [148] have conducted dynamic ageing studies in Al-Mg-Si alloys through ECAP and reported that, dynamic ageing has led to significant reduction in ageing time from 1000 min to 10 min. And also notable increase in UTS is achieved through dynamic ageing. The superior mechanical properties observed in dynamic ageing are attributed to formation of fine precipitates through dislocation assisted precipitation mechanism. There is no reported literature on the mechanical and microstructural characteristics of precipitation hardenable alloy (Al 6061) subjected to cryorolling followed by warm rolling. Therefore, the present work has been focused to study the mechanical and microstructural characteristics of Al 6061 alloy processed through cryorolling followed by warm rolling and subsequent static ageing at low temperature.

5.1.2 Experimental

Al 6061 alloy samples were machined with 10×30×40 mm³ from “as-received” alloy plate and subjected to solution treatment at 530 °C for 3 hours followed by water quenching to room temperature. Cryorolling (CR) was performed to various percentages of reductions up to 70% and 90% reduction in liquid nitrogen temperature. In order to study the combined effect of CR and

warm rolling, CR Al 6061 plates with 70% reduction were further warm rolled to achieve total thickness reduction of 90%. For the further reference of the bulk solution treated, cryorolled, and cryorolled + warm rolled alloy are abbreviated as ST, CR, and WR, respectively. The procedure of cryorolling and warm rolling is explained in section 3.3. In order to study the effect of low temperature ageing, WR samples were aged at 100 °C, 125 °C, and 145 °C. Bulk ST and CR conditions were also subjected to ageing at 125 °C for a comparative study. The process flow diagram is shown in *Figure 5.1*.

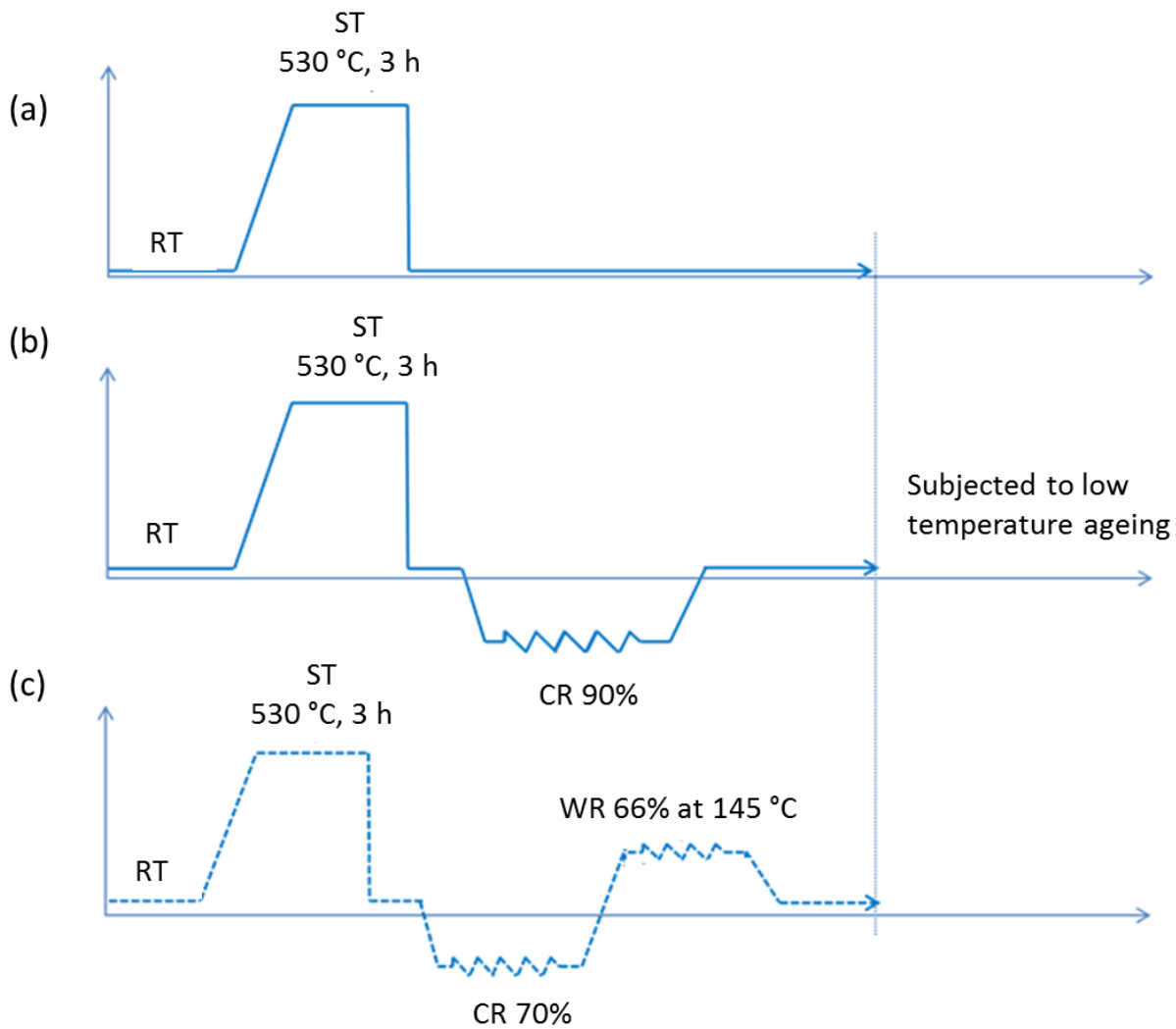


Figure 5.1 Process flow diagram.

Mechanical properties were evaluated by performing Vickers hardness test and tensile test at room temperature. For tensile testing, samples with dimensions according to ASTM E8 sub

size specimens with gauge length 25 mm were used. Tensile samples were prepared along the plane (RD-TD) parallel to the rolling direction. Minimum three samples were tested to obtain average value. Tinius Olsen machine was used with cross head speed as 1 mm/min. The microstructural evolution in CR, WR and their peak aged conditions was investigated through TEM and EBSD techniques. XRD and DSC techniques were employed to study the precipitation behavior.

5.1.3 Results

5.1.3.1 Effect of warm rolling and ageing on microstructure and mechanical properties

5.1.3.1.1 Hardness

Figure 5.2 shows the effect of CR and WR on the hardness of Al 6061 alloy at various strains. The hardness value of ST material has increased from 54 H_V to 93 H_V (nearly ~74%) after imparting true strain 1.2 (70% reduction) at cryorolling temperature. Further reduction of samples from 70% to 90% at the same temperature leads to increase in hardness about 5 H_V. On the other hand, the rise in hardness upon imparting reduction from 70% to 90% of the samples at warm temperature, 145 °C, was 27 H_V. The similar trend in hardness value of Al 5052 has been reported by Kang et al., [222] for the Al 5052 samples subjected to cryorolling followed by warm rolling. The increase in hardness of WR material is attributed to dynamic ageing effect during warm rolling.

To study the effect of low temperature static ageing, WR material was subjected to ageing at various temperatures, 100 °C, 125 °C, 145 °C for 1 to 80 hours. *Figure 5.3* shows the variation in hardness of WR material as a function of ageing time at various temperatures. It can be seen from the hardness plot that, the maximum hardening response (maximum hardness of 132 H_V, 10% increment) is achieved at 125 °C after an ageing time of 45 hours. Ageing beyond 45 hours at the same temperature results, a slight decrease in hardness, but the drop in hardness is not significant till 75 hours of ageing time. The creation of non-shearable precipitates during ageing has resulted increase in hardness after ageing at 125 °C for 45 hours. The hardening effect by precipitation is overwhelming the softening effect by recovery, depletion of solutes from the solid solution, and the structure coarsening.

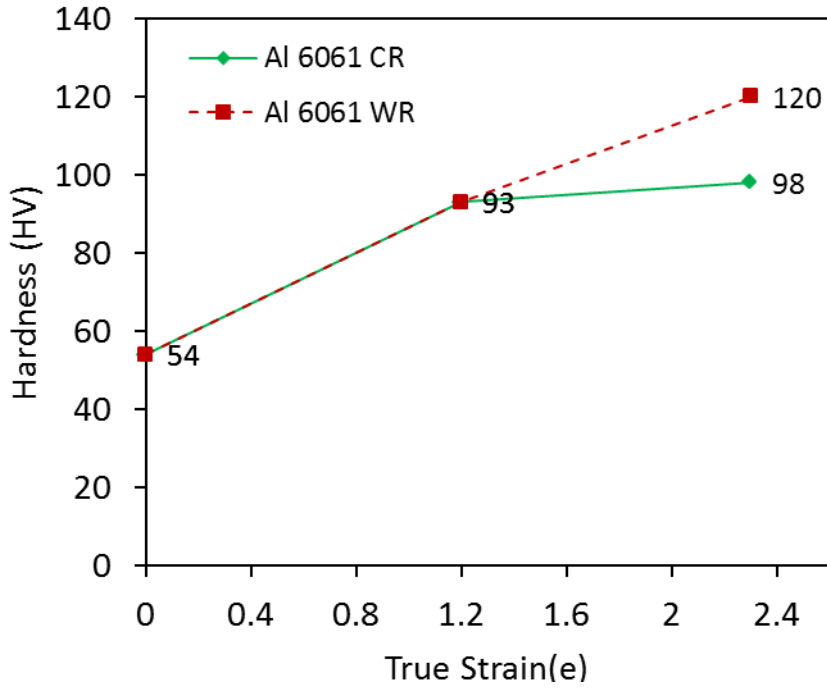


Figure 5.2: Effect of cryorolling and warm rolling on hardness behavior of Al 6061 alloy.

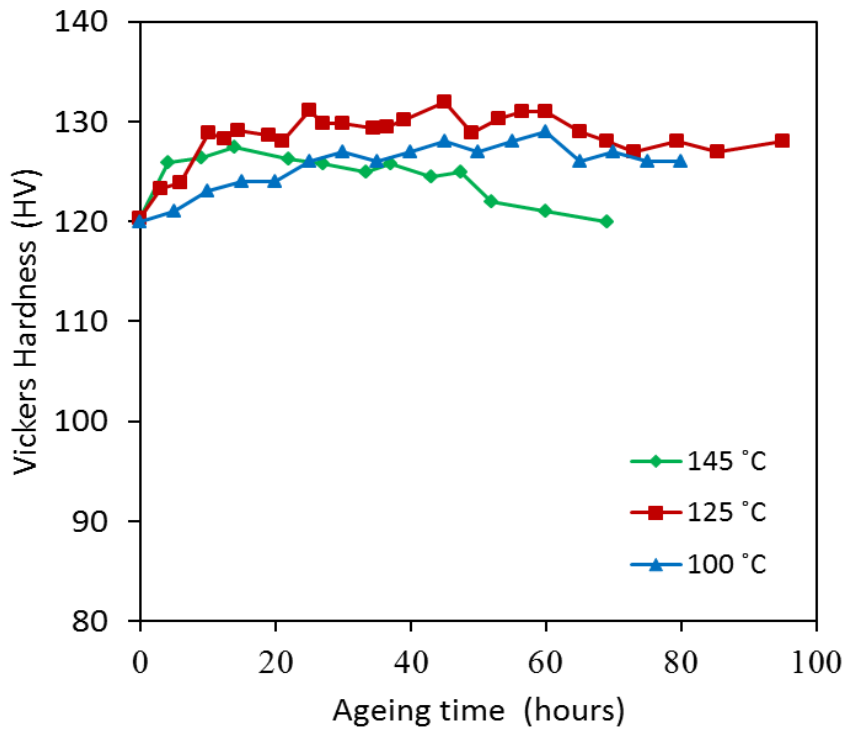


Figure 5.3: Vickers hardness of the WR sample after ageing at 100 °C, 125 °C and 145 °C as function of ageing time.

On the other hand, for the samples subjected to ageing at 145 °C, the increasing trend of hardness has been observed up to 18 hours, beyond which it drops. This drop in hardness after 45 hours and 18 hours at 125°C and 145 °C, respectively, can be related to dominance of the recovery, structure coarsening, and depletion of solutes in the solid solution over precipitation hardening effect. The maximum hardness achieved by ageing at 100 °C after 60 hours ageing time is less than that of it achieved by ageing at 125 °C. This suggests that 100 °C is not sufficient for the solute atoms to form coherent metastable phase precipitates (β'') to achieve maximum hardness.

Figure 5.4 shows the comparative study of hardness versus ageing time plots of Al 6061 alloy subjected to ST, CR and WR at an ageing temperature of 125 °C, which was found to be optimum for WR samples. In ST samples, the hardness increases from 54 HV to 98 HV for the ageing treatment of 72 hours. It is almost equal to the hardness of as-received Al 6061 alloy (T651) sample, where its hardness was 101 HV. This increase in hardness in ST sample can be purely attributed to the formation of metastable precipitates from solid solution. In case of CR sample after static ageing treatment at 125 °C for 53 hours ageing time, the maximum value of hardness achieved was 117 HV. This shows an increment of 19% with respect to the hardness of cryorolled sample. The percentage rise in hardness after peak ageing treatment of CR sample was approximately two times than that of WR sample where its percentage rise in hardness is 10% after peak ageing treatment at 125 °C for 45 hours.

5.1.3.1.2 XRD Analysis

The X-ray diffraction patterns of ST, CR, WR, WR + PA and CR + PA samples were shown in *Figure 5.5*. The starting material subjected to solutionizing and the quenching prior to cryorolling (ST) does not show any peak corresponding to Mg_2Si precipitate as shown in *Figure 5.5*. This indicates complete dissolution Mg_2Si in to the matrix during solution treatment [109]. The presence of Fe-rich phase (Al-Fe-Si) was observed in all conditions due to poor solubility of Fe in Al. ST material after rolling at liquid nitrogen temperature up to 90% reduction (CR) does not show any significant peak pertaining to the formation of Mg_2Si precipitate as seen in *Figure 5.5*. This shows effective suppression of dynamic ageing during rolling process at very low temperature [224]. Mg_2Si precipitate peak with increased intensity was observed in WR sample as seen in *Figure 5.5*, which exhibits higher hardness compared to CR sample.

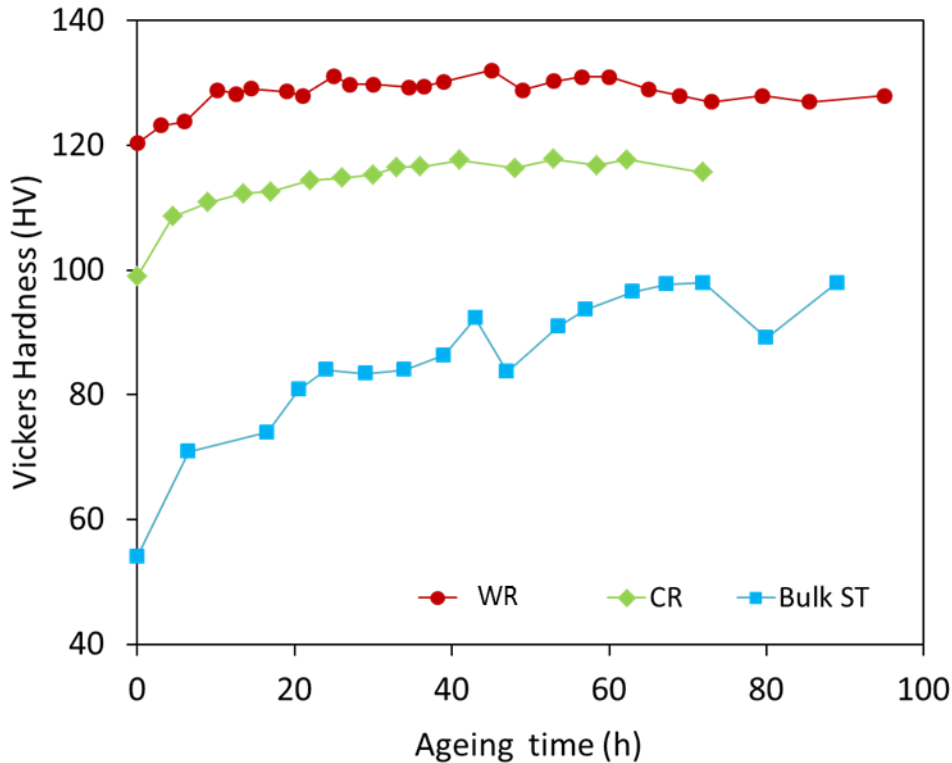


Figure 5.4: Vickers Hardness of ST, CR, WR of Al 6061 alloy aged at 125 °C as a function of ageing time.

This is due to dynamic ageing during WR. However, the intensity of peak becomes sharper for the CR and WR sample after subjected to peak ageing treatment at 125 °C for 53 hours and 45 hours respectively, which results in further increase in hardness of the samples. The observed hardness values are in tandem with XRD results.

5.1.3.1.3 DSC

DSC plots corresponding to CR, WR, CR+PA and WR+PA are shown in *Figure 5.6*. The detailed discussion about DSC results of ST and CR is made in the chapter 4. The DSC plot corresponding to WR sample is (*Figure 5.6*) appears to be same as that of CR sample with minor differences. The major exothermic peak (peak 3 at 233 °C) position is similar to the peak of CR sample but with less peak intensity. Also, the peaks at low temperature corresponding to the formation of Mg/Si co-clusters and G.P Zones became flat as compared to initial conditions.

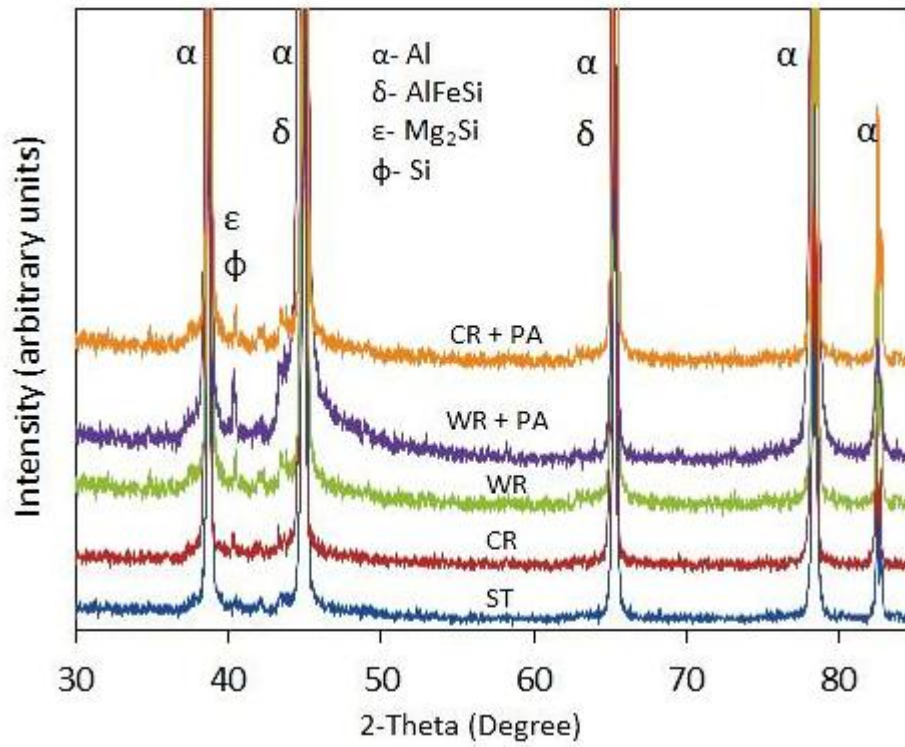


Figure 5.5: XRD patterns of ST, CR, WR, WR + PA and CR + PA Al 6061 alloy.

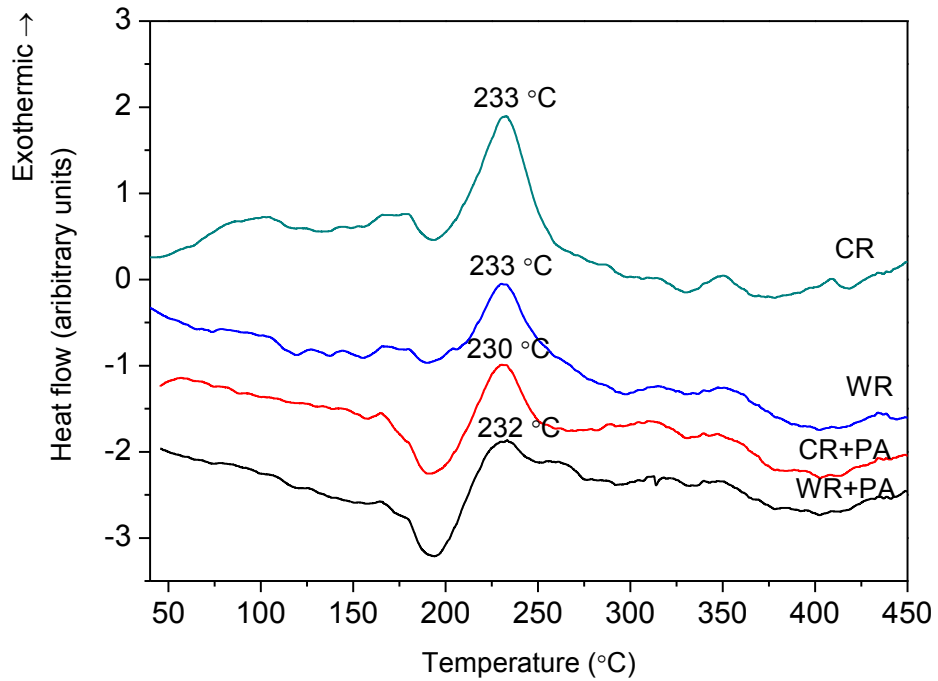


Figure 5.6: DSC thermograms of Al 6061 alloy; CR, WR, CR+PA, WR+PA.

However, the peak position of β precipitates was identical in both the conditions (CR, and WR). The reasons for flattening of low temperature peaks and decrease in intensity of peak 3 at 233 °C can be drawn from hardness plots of CR and WR sample shown in *Figure 5.2*.

The increase in hardness of WR sample as compared to CR sample symbolizes that precipitation of clusters/G.P zones occurred during warm rolling at 145 °C. The precipitation in WR sample occurs because of enough driving force available for it through deformation strain and deformation temperature during warm rolling. In *Figure 5.6*, DSC plots of CR + PA and WR + PA samples has shown with endothermic peak followed by exothermic peak between 160 °C and 275 °C are corresponding to dissolution of β'' and formation of β' precipitates respectively. The strengthening phase in this alloy was found to be the coherent metastable β'' precipitates [12] [136] [138] [212] [213] [214] . Maximum hardness value was achieved for CR (117 H_V) and WR samples (132 H_V), after artificial ageing treatment at 125 °C at 53 hours and 45 hours, respectively as shown in *Figure 5.4*. The disappearance of exothermic peaks at low temperature and presence of endothermic peak, are noticed from the DSC analysis.

5.1.3.1.4 Microstructure

a) Optical microstructure

Figure 5.7 shows the optical microstructure of starting material after solid solution treatment. Since the “as-received” material was in the form of rolled plate, the microstructure possesses elongated grain structure along the rolling direction. In this study, the microstructural investigation of rolled samples was performed on the RD-TD plane.

b) EBSD

The electron back scattered diffraction (EBSD) micrographs of the ST material on rolling plane is shown in *Figure 5.8*. In *Figure 5.8(b)*, image quality (IQ) map shows black color spots aligned along the rolling direction. These are corresponding to undissolved constituent particles. Blue lines indicate high angle grain boundaries. The microstructure of ST condition shows slightly elongated grains with an average width of 45 μm .

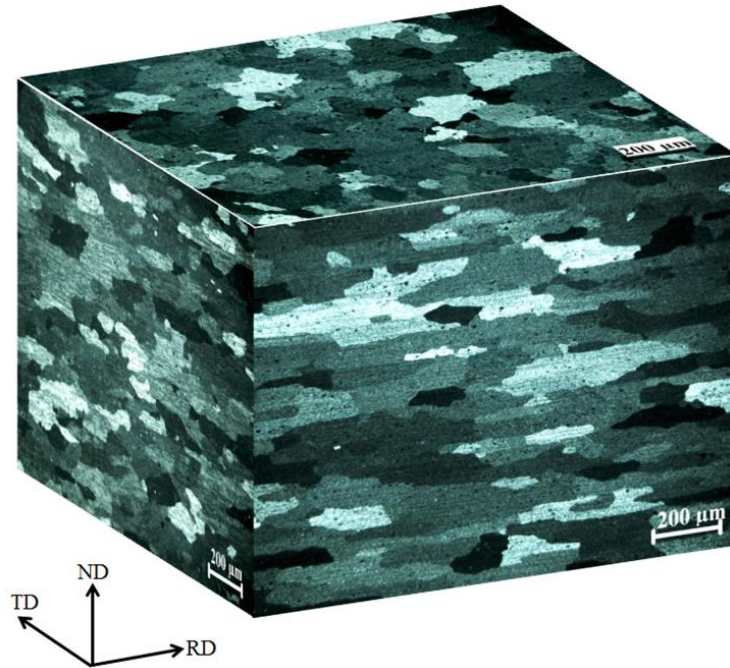


Figure 5. 7: Optical microstructure of coarse grained material after solid solution treatment (ST).

Figure 5.9 shows EBSD micrographs of CR and WR material, where Figure 5.9 (a) and (b) are corresponding to orientation image micrographs (OIM) of CR and WR material respectively. The corresponding IQ maps are shown in Figure 5.9 (c) and (d). Figure 5.9 (e) and 5.9 (f) are the magnified images of cropped area from Figure 5.9 (a) and (b). In OIM micrographs, the grey lines depict LAGBs ($1-15^\circ$) and black lines represent HAGBs ($>15^\circ$). From the EBSD micrographs, it is evident that, the microstructure of CR possesses subgrains with predominantly LAGBs. Whereas in WR material the fraction of LAGBs has decreased and the fraction of HAGBs has increased (Figure 5.10). During warm rolling dynamic recovery is promoted which results increased misorientations of low angle grain boundaries and better structural refinement.

c) TEM

The effect of CR and WR on microstructure of Al alloy was examined through TEM along the plane parallel to rolling direction and their TEM micrographs are shown in Figure 5.11. The microstructure of the CR sample (Figure 5.11 (a)) shows the presence of heavily deformed grains with high density of dislocations. Cell structures with unclear grain boundaries are seen from the micrograph (Figure 5.11 (a)). Whereas in case of WR samples, the fuzziness in the

grain boundaries has decreased due to recovery effect and the subgrain boundaries are becoming clear. Also, the presence of fine precipitates are observed in all WR samples as shown with arrow marks in *Figure 5.11 (b)*.

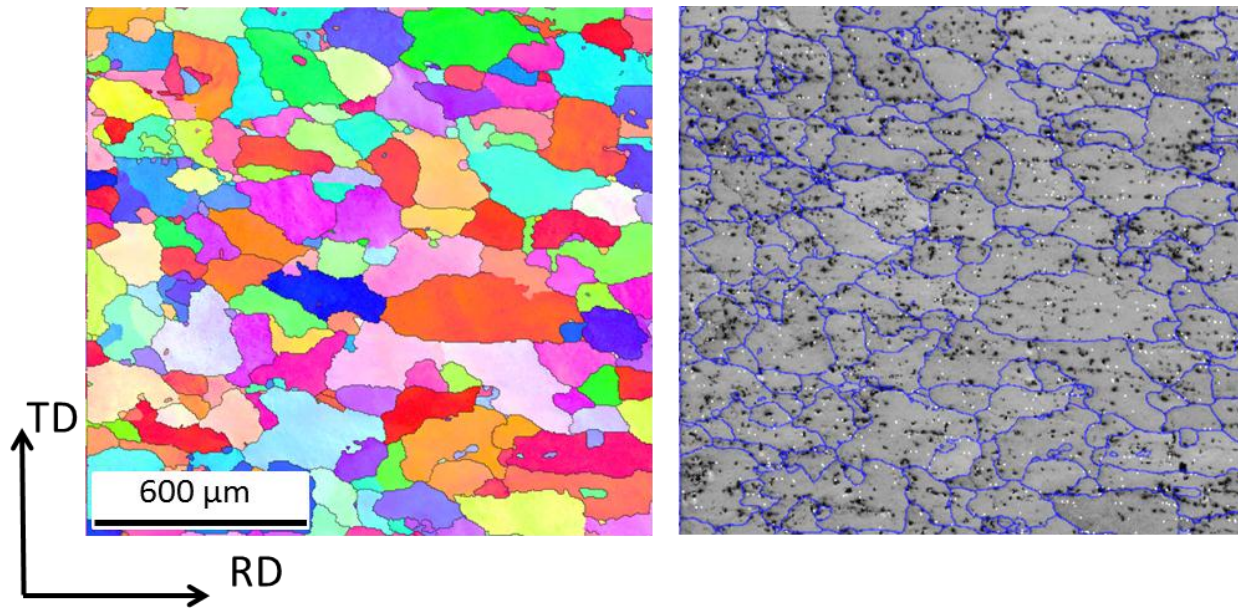


Figure 5.8: EBSD micrographs of ST material on rolling plane; a) Inverse pole figure map, b) Image quality map with grain boundaries.

The improvement in hardness with increasing warm rolling temperature is in accordance with the observed TEM results. TEM micrographs of peak aged conditions of CR and WR are shown in *Figure 5.12*. After peak ageing treatment, the samples show well defined ultrafine grains with clear boundaries with mean size of 300 nm. In addition to this, there are some very fine crystallites with 100–200 nm size with dislocation free interiors. These dislocation free grains contribute to increase the ductility of the material. During ageing process, dislocation density has reduced in CR+PA and WR+PA samples compared to CR and WR samples due to annihilation of dislocations by recovery process.

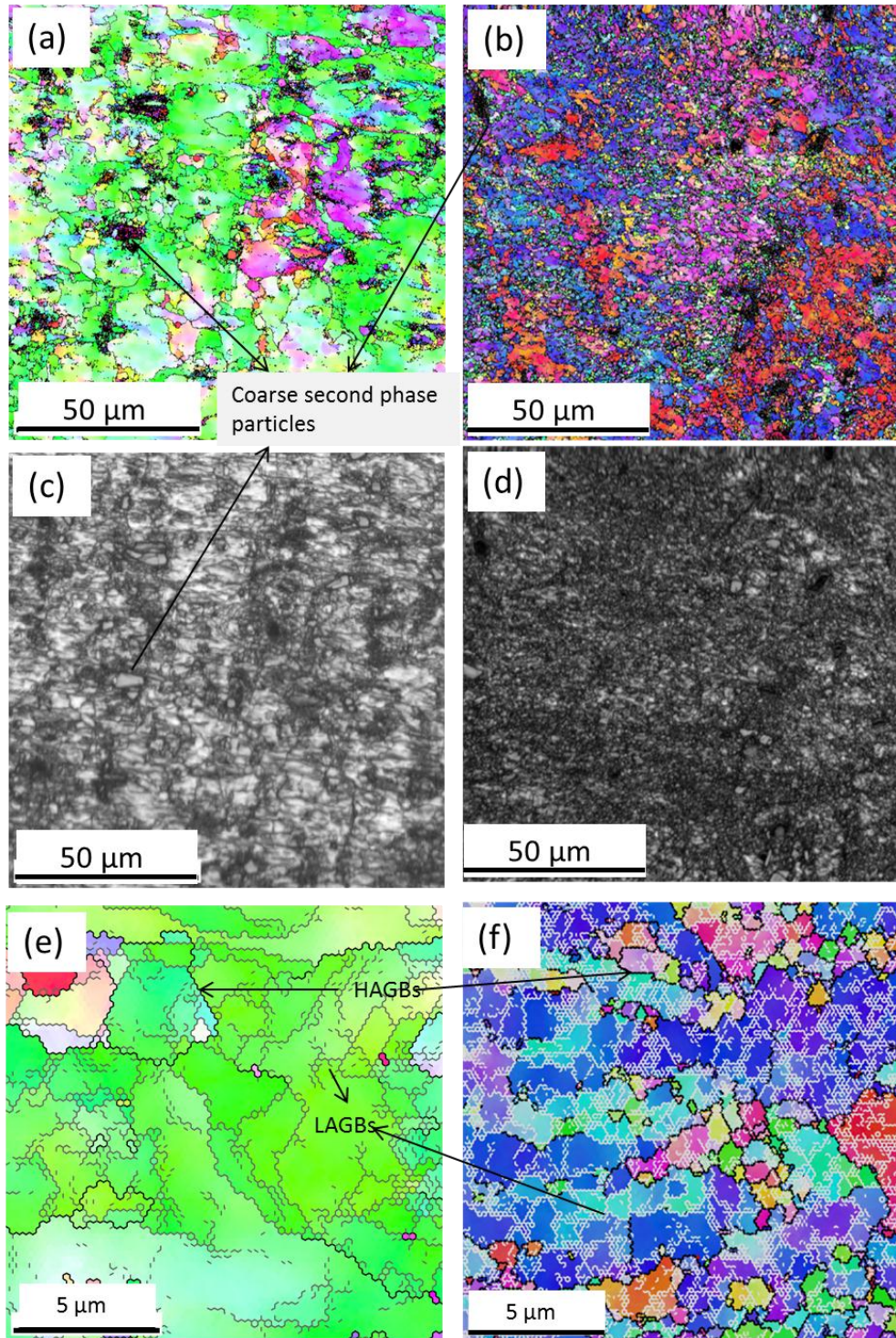


Figure 5.9: EBSD micrographs of Al 6061 alloy after CR and WR; a) & b) OIM maps with larger area, c) & d) are IQ maps of a) & b), e) & f) OIM maps representing small area with LAGBs and HAGBs of CR and WR materials.

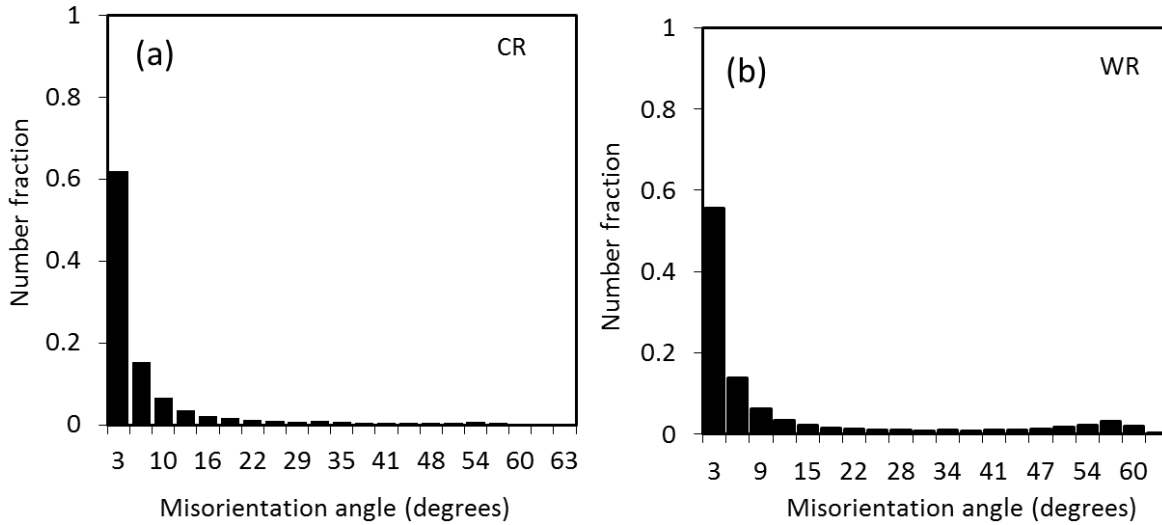


Figure 5.10: Misorientation angle distribution in Al 6061 alloy after ; a) CR , b) WR

5.1.3.1.5 Tensile properties

Based on the hardness plots of various heat treated conditions of Al 6061 alloy, tensile test was performed at room temperature. *Figure 5.13* shows Engineering stress–strain plots of ST, CR, WR, T6, CR + PA, and WR + PA samples. The interpreted values of YS, UTS and % elongation of stated conditions from *Figure 5.13* are shown in *Table 5.1*. CR + WR sample has shown a large enhancement in the UTS and YS of 376 and 364 MPa, respectively, as compared to ST, T6, CR and CR + PA samples; whereas, the UTS and YS of the CR sample are 296 and 280 MPa, respectively, with an elongation of 4.5%. The percentage increase in UTS and YS of CR sample when compared to its bulk ST condition is 61.7% and 330.7%, respectively. The elongation observed in WR sample is 5%, which is almost same to the CR sample. The enhancement in the strength of CR sample is mainly by the combined effect of high dislocation density, partial grain refinement, and solid solution strengthening. WR sample has shown much higher UTS (376 MPa) and YS (364 MPa) than that of CR samples (UTS-296 MPa, YS-280 MPa). This large enhancement in the strength of WR sample can be attributed to dynamic ageing during warm rolling at 145 °C for 20 min, partial grain refinement, and solid solution strengthening.

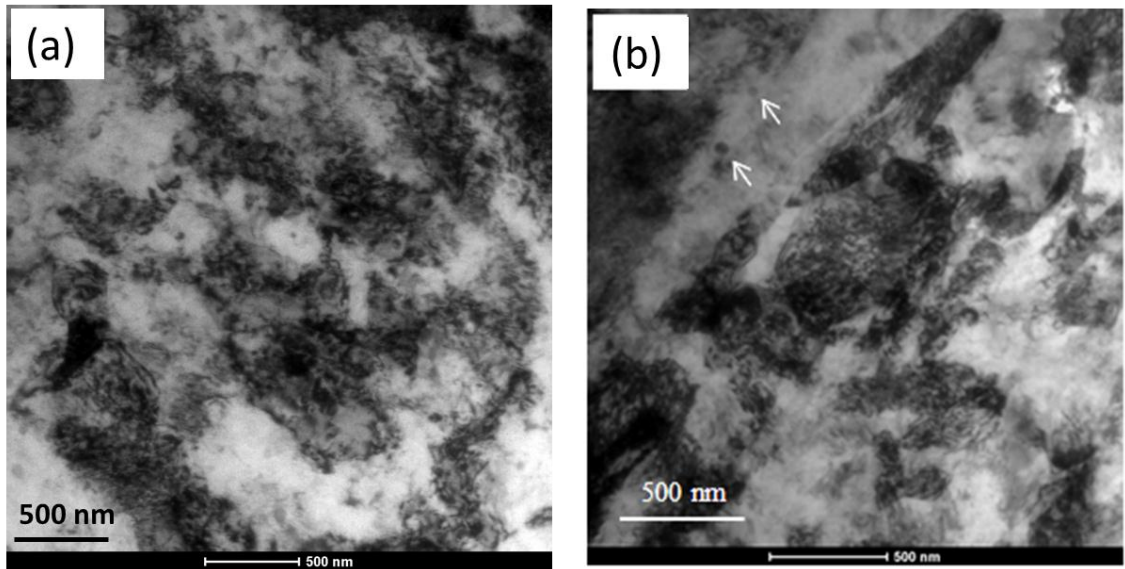


Figure 5.11: TEM micrographs of Al 6061 alloy; a) CR, b) WR.

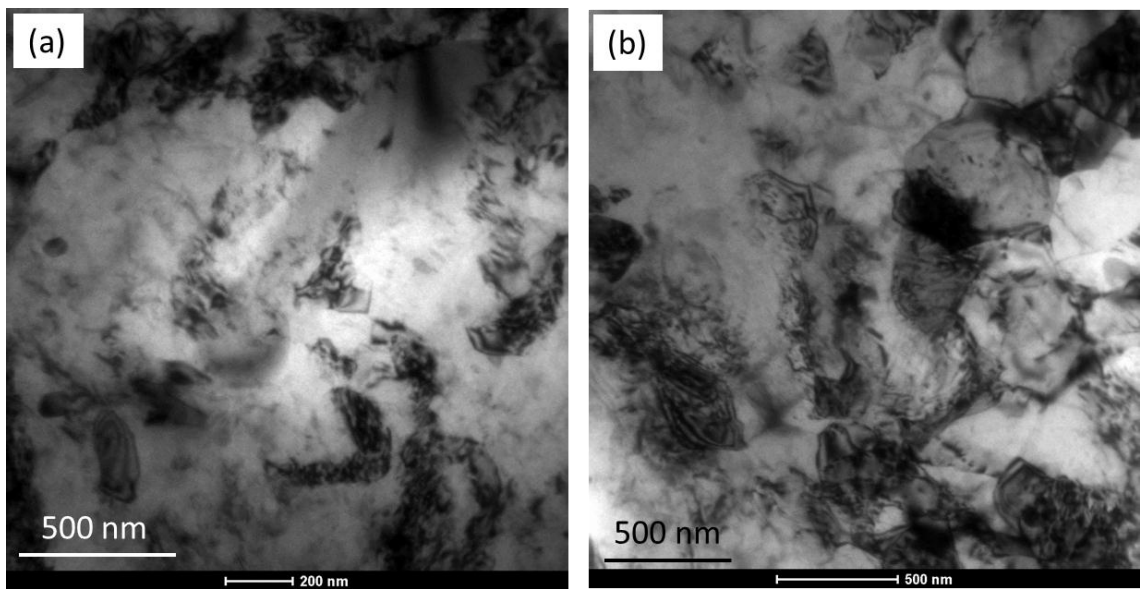


Figure 5.12: TEM micrographs of Al 6061 alloy (a) CR + PA, (b) WR + PA

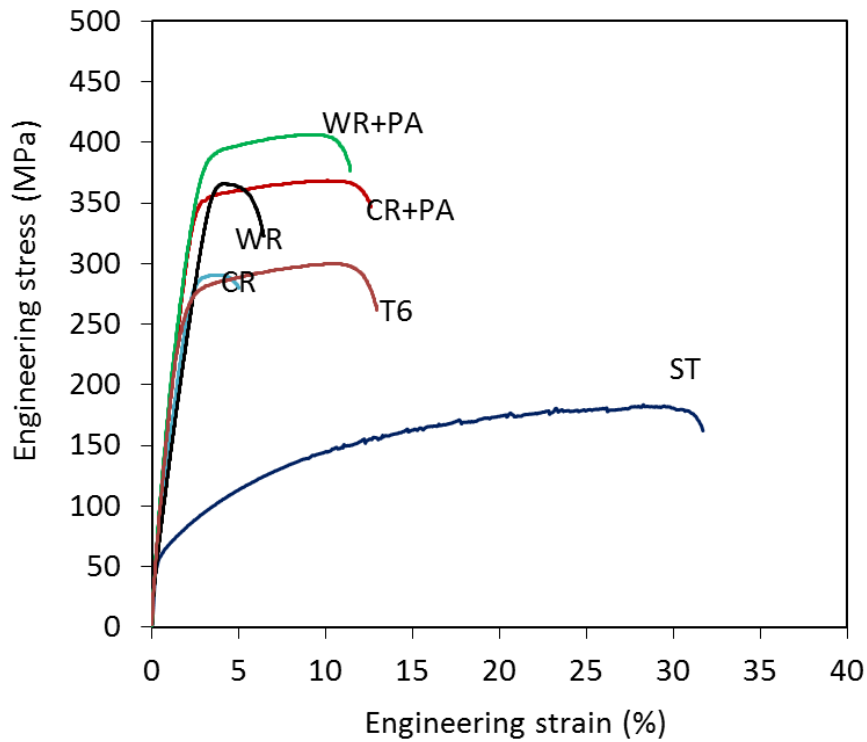


Figure 5.13: Stress–strain curves of various heat treated conditions of Al 6061 alloy (A) ST, (B) T6, (C) CR, (D) CR + PA, (E) CR + WR, (F) WR + PA.

Table 5.1: Variation in UTS, YS and elongation values of (a) ST, (b) T6, (c) CR, (d) CR + PA, (e) WR, (f) WR + PA.

Process condition	UTS (MPa)	YS(MPa)	% Elongation
ST	183	65	30
ST+PA	305	278	12
CR	296	280	4.5
CR+PA	365	305	11.3
WR	376	364	5
WR+PA	406	380	10

The high density of precipitates generated during warm rolling has acted as an obstacle to trap dislocations and leads to increased dislocation density. It has compensated for the decrease in strength caused by recovery effect during warm rolling, and increased the strength further by 27% as compared to CR sample. The UTS and YS after low temperature ageing, at 125 °C for 53 and 45 hours, of CR and WR, respectively, have increased with no cost of ductility. WR + PA sample shows a maximum strength of 406 MPa with 10% elongation at break. The ultimate tensile strength of T6 condition was 301 MPa with 12% elongation only. The ductility observed in CR + PA sample was 13% more than WR + PA sample. This may be due to decrease in dislocation density by recovery effect during ageing process is more in CR + PA sample than WR + PA sample.

5.1.3.2 Microstructure stability and thermal stability of WR alloy

In many applications materials with thermodynamically stable microstructures with high strength and ductility are preferred. Achieving thermally stable microstructures in UFG materials is an intriguing task. In the previous subsection (section 5.1.3.1) it was demonstrated that cryorolling followed by warm rolling (WR) is more effective approach than cryorolling alone to enhance the strength and ductility in Al 6061 alloy. However it is necessary to understand microstructural and thermal stability of WR Al 6061 alloy.

Figure 5.14 shows the variation in Vickers hardness of WR and CR material with increasing annealing temperature. By annealing at 150 °C for 1 hour, there is a considerable increase in hardness in both WR and CR material, which is in association with precipitation hardening effect. By increasing annealing temperature to 175 °C, WR material has retained its hardness, however in CR material, drop is observed. By increasing to 200 °C, hardness of both the materials has started devolving, which can be attributed to dominant recovery effect. The hardness of WR and CR materials after 200 °C annealing is equivalent to the hardness of bulk material at T6 condition. At lower temperatures of annealing, hardness of the WR material is considerably higher than the CR material. Annealing temperature beyond 200 °C, there is sharp fall in hardness in both WR and CR materials. *Figure 5.15* shows the DSC heat flow curves of WR material annealed at different temperatures ranging from 150 °C to 300 °C with an interval of 25 °C.

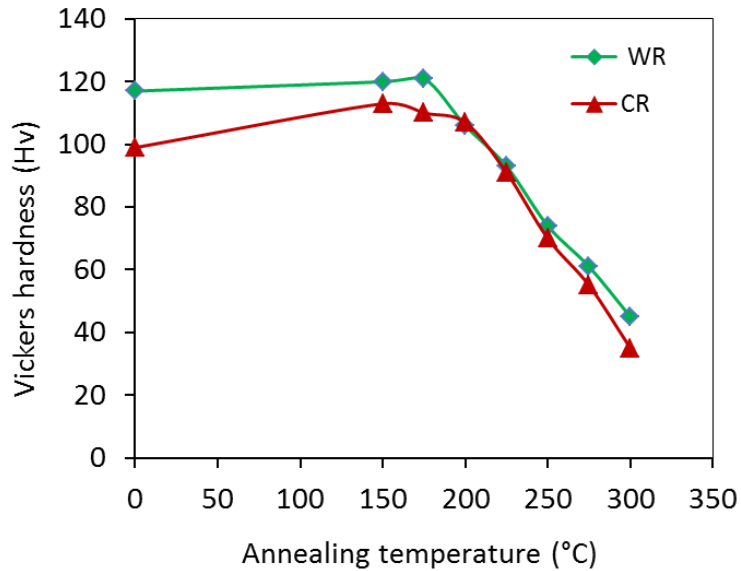


Figure 5.14: Variation in hardness of Al 6061 alloy with different thermo mechanical processing; CR and WR.

The thermal behavior of WR material is similar to the CR material as discussed in the chapter 4.3.3.4. By increasing annealing temperature, the intensity of endothermic peak corresponding to dissolution of strengthening phase (β''/β') has increased. The signal of dual peaks that appears in the major exothermic peak in the range of 180 to 275 °C of WR material annealed at 150 °C and 175 °C indicates the rise in hardness of WR material after annealing at 175 °C, is due to the formation of β'' precipitates. By annealing at 200 °C, the formation of β'' has been completed. And by annealing at 250 °C, β' formation has been completed.

The microstructural stability of WR Al 6061 alloy annealed at various temperatures was investigated through EBSD technique. *Figure 5.16* shows the OIM maps along with IQ maps of annealed samples at various temperatures from 150 °C to 250 °C. With increasing annealing temperature, UFG formation through structural rearrangement is observed. Annealing at 250 °C has resulted formation of fine grains through recovery and recrystallization. Recrystallization is observed mainly at high strained zones nearby coarse second phase particles. Presences of such particles are promoting the grain refinement. The size and distribution of the subgrains that forms after annealing is depends up on the stored energy of the starting material.

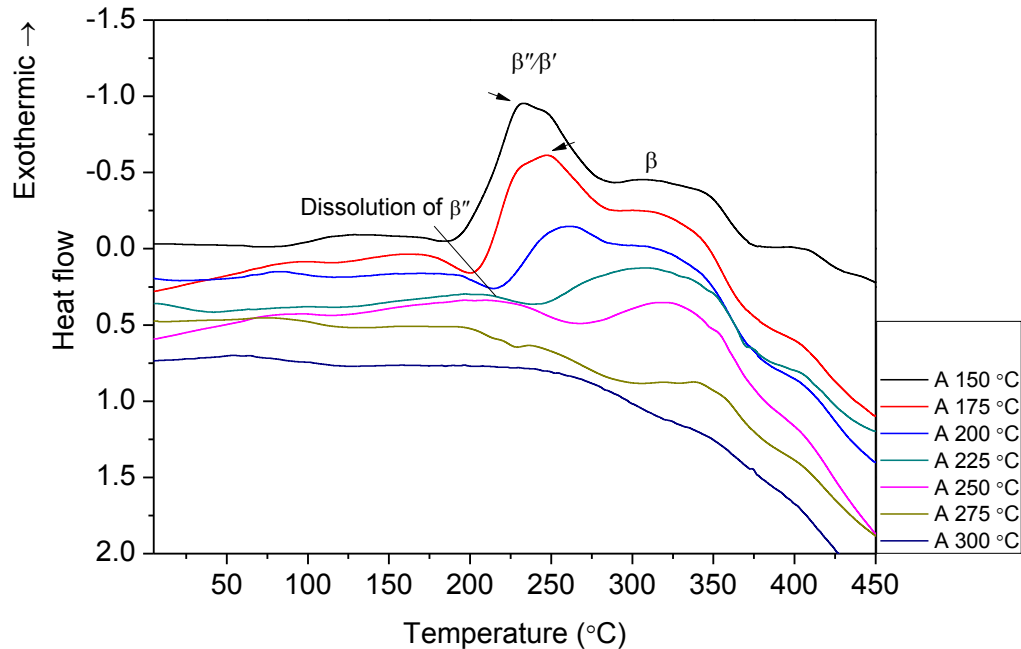


Figure 5.15: DSC heat flow curves of WR Al 6061 alloy after annealing for 1 hour at different temperatures.

For comparative study CR samples have been subjected to annealing at 250 and 300 °C for 1 hour, the corresponding microstructure is shown in *Figure 5.17 and 5.18*. The size and distribution of the subgrains are much finer and homogeneous in CR material as compared to WR material. It can be attributed to high stored energy in CR material due to increased density of lattice defects by suppression of dynamic recovery. On the other hand it leads to faster recrystallization and unstable microstructure. Annealing at 300 °C has resulted formation of coarse grains through recrystallization. The fraction of recrystallized area (20%) observed in WR material is lower than that (70%) observed in CR material.

5.1.4 Discussions

Effect of cryorolling on improvement of strength (YS, UTS) has been realized in several metals and alloys [14] [76] [111] [199]. During plastic deformation at liquid nitrogen temperature, suppression of dynamic recovery enhances the accumulation of dislocation density in the material, which led to significant improvement in the hardness and strength of the material [13]. The improvement in hardness and strength of the CR material is primarily due to solid solution strengthening, dislocation strengthening, and sub grain boundary strengthening. As a result of high densities of accumulated dislocations, the material is unable to accept adequate dislocations during tensile testing, which results in poor uniform elongation. Hence, ductility of the CR

material has dropped from 30% (ST material) to 4.5% (CR 90% material). Cryorolling followed by warm rolling imparts significant improvement in hardness and strength over CR material. It can be attributed to precipitation hardening effect due to dynamic ageing, in addition to dislocation strengthening, sub grain boundary strengthening and partially dislocation strengthening effect. Due to CR strain in the material, large numbers of nucleation sites are provided for precipitation during subsequent WR, which in turn leads to rise in hardness and strength in WR material. It is reported that during dynamic ageing, the nucleation of precipitates is dislocation assisted process [148] [225]. During WR, three possible phenomenon could occur simultaneously as follows; i) softening effect by dynamic recovery due to cross slip and climb of dislocations, ii) work hardening effect due to plastic deformation, iii) precipitation hardening effect due to precipitation of second phase from the matrix. From the DSC results, it can be concluded that the improvement in mechanical properties of warm rolled material is predominantly due to precipitation of nanoclusters/ G.P zones due to dynamic ageing effect during warm rolling and their active engagement in pinning and accumulation of dislocation during warm rolling. Upon ageing at low temperature has resulted in improvement in hardness properties of warm rolled material. The peak hardness achieved for the samples during ageing at 125 °C for 45 hours might be due to the creation of non-shear able precipitates, which dominates over recovery, depletion of solutes from the solid solution, and the structure coarsening.

The hardness behavior of precipitation hardenable alloys during ageing can be explained by the interaction of four competing factors such as i) reduction in dislocation density due to recovery, ii) formation of non-shearable precipitates, iii) depletion of solutes in the solid solution, and iv) sub-structure coarsening as reported in the literature [153]. It was anticipated that after warm rolling, heat treatment may reduce the strength, but strength and ductility both were improved due to precipitation of β''/β' phase from the matrix. The ductility has improved due to decrease in dislocation density by recovery process during peak ageing treatment; it causes dislocation free rooms inside the grains, which enables to accumulate more dislocations. The increase in ductility could also be due to generation of high density of nanosized precipitates, which provides effective sites for trapping and accumulation of dislocations [191]. The superior microstructural and thermal stability of WR material over CR material was attributed to reduced lattice defects by restoration processes during warm rolling.

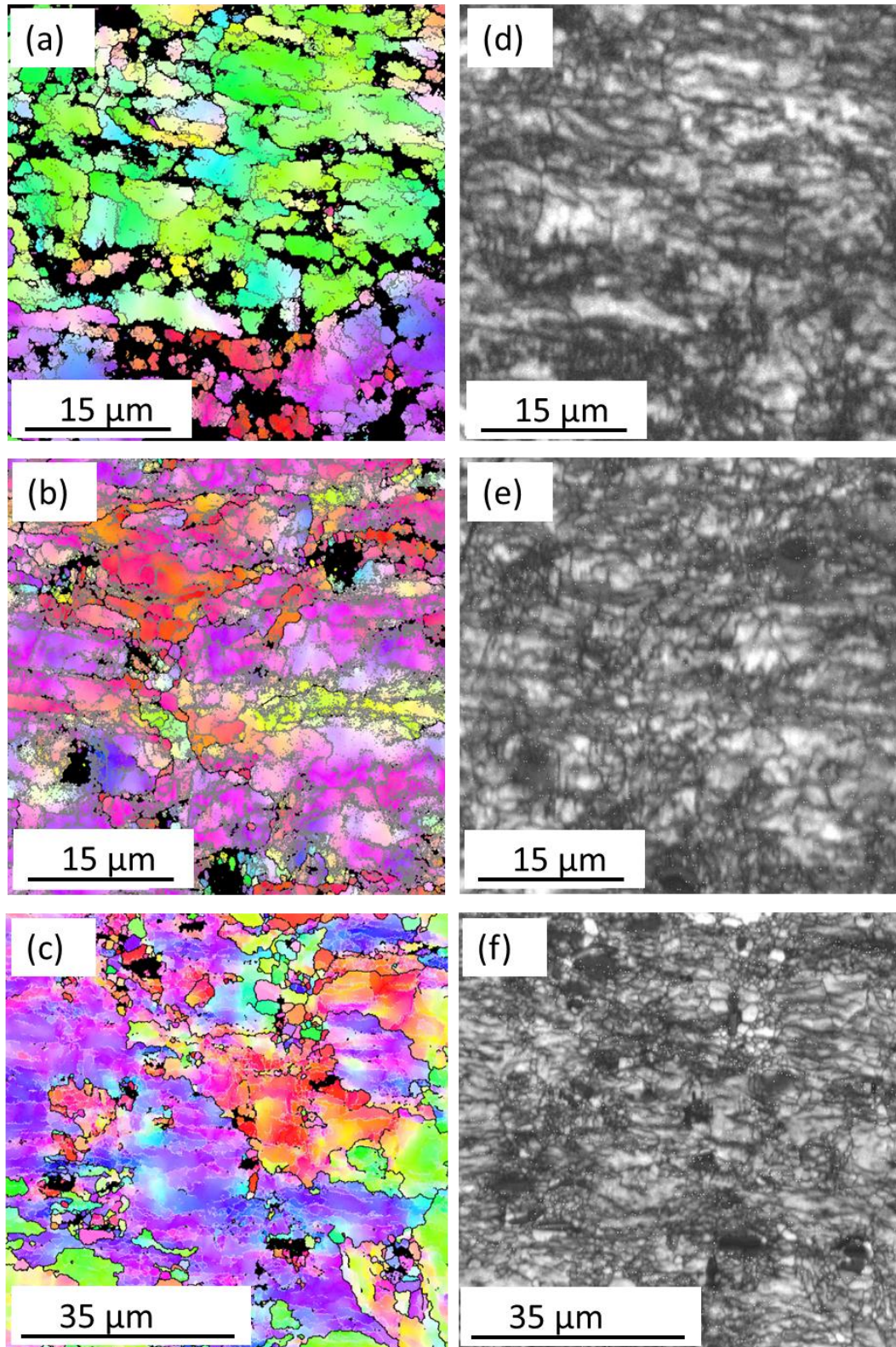


Figure 5.16: EBSD micrographs of WR Al 6061 alloy after annealing at different temperatures; 150 °C, 200 °C and 250 °C.

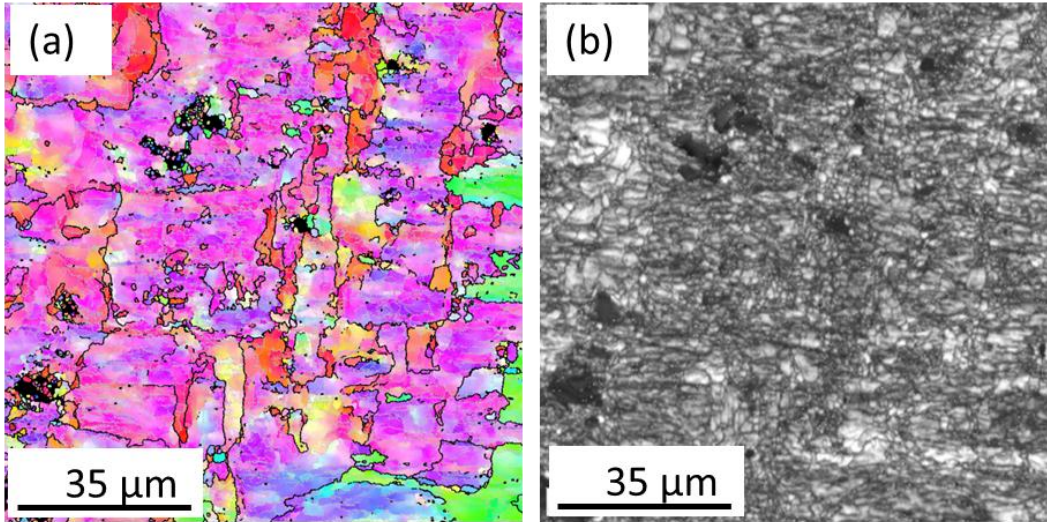


Figure 5.17: EBSD micrographs of CR Al 6061 alloy annealed at 250 °C for 1 hour.

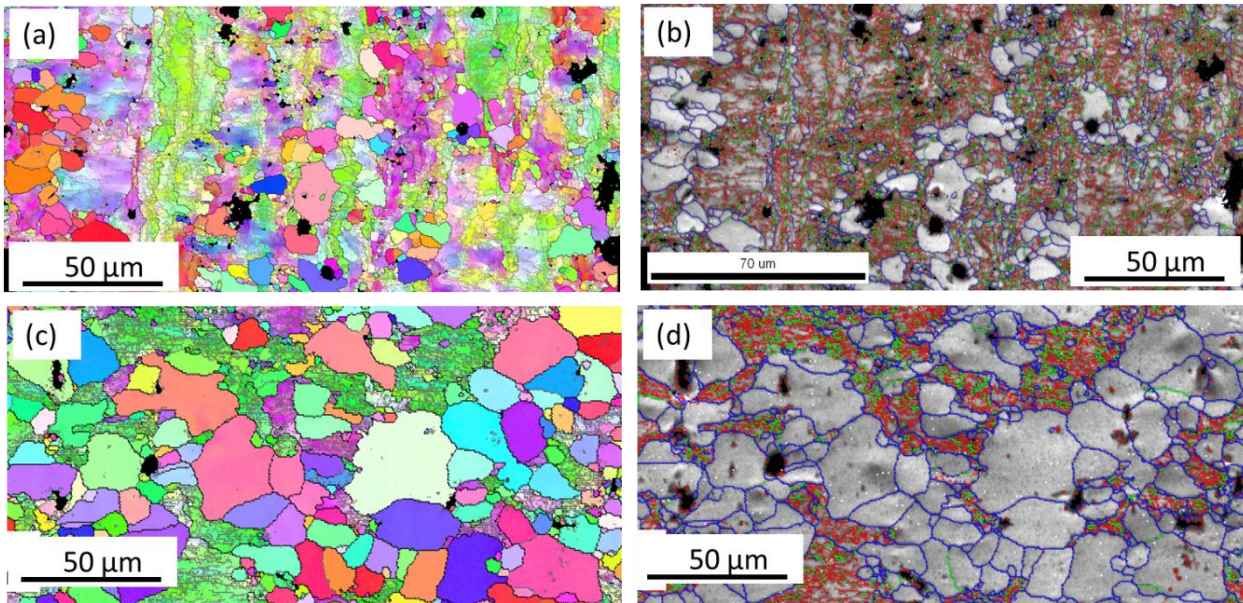


Figure 5.18: EBSD micrographs of Al 6061 alloy annealed at 300 °C for 1 hour; (a) and (b) Orientation image micrograph and Image quality map of WR Al 6061 alloy, (c) and (d) Orientation image micrograph and Image quality map of CR Al 6061 alloy.

5.1.5 Conclusions

The combined effect of cryorolling and warm rolling on mechanical properties and microstructural evolution of Al 6061 alloy has been investigated. The effect of low temperature ageing on strength and ductility of WR samples has been studied and compared with bulk solution treated aged, cryorolled aged samples. Also the microstructural and thermal stability of WR material was investigated.

- 1) A significant enhancement in strength (376 MPa) and partial improvement in ductility (5%) was observed in WR sample as compared to CR samples. After subsequent low temperature ageing treatments of WR samples, the optimum ageing condition to obtain maximum strength was found to be 125 °C for 45 h. It may be mentioned that the time to peak strength in WR sample (45 hours) has been reduced as compared to CR samples (53 hours) at same ageing temperature (125 °C).
- 2) The enhancement in strength of WR + PA sample, subjected to ageing, is found to be 7.9%. However, in CR + PA sample, increment in strength was 23.3% as compared to CR sample. The overall improvement in strength of WR + PA sample as compared to starting condition solution treated condition (ST) was 122%; whereas, in CR + PA sample, it was 99%.
- 3) From EBSD and TEM analysis, it is evident that both CR and WR samples exhibit high density of dislocations and substructures with ill-defined grain boundaries. The fraction of low angle grain boundaries has slightly reduced and high angle grain boundaries have slightly increased in WR sample. This may be due to dynamic recovery effect during warm rolling at 145 °C after cryorolling, which lead to partial improvement in ductility. The fraction of low angle grain boundaries were more in CR sample, may be due to effective suppression of dynamic recovery at liquid nitrogen temperature. In addition to high density of accumulated dislocations in WR samples, a high density of nanosized precipitates is evident from the TEM micrographs.
- 4) Significant enhancement in strength of WR sample is attributed to the cumulative effect of precipitation hardening and pre-accumulated high density of dislocations during cryorolling. In WR + PA sample, enhancement in strength is caused by the precipitation of remnant second phase particles in the solid solution after warm rolling followed by ageing process as evident from TEM analysis. DSC results of Al 6061 alloy of ST, CR,

WR, WR + PA, CR + PA conditions are in tandem with hardness behaviour and TEM results. The improved ductility of WR + PA (from 5% to 10%) is attributed to formation of ultrafine grains as well as reduction in dislocation density during ageing process.

- 5) WR material has shown better microstructural and thermal stability than CR material. However the structural refinement is better in CR material after annealing at 250 °C as compared to WR material.

5.2 Effect of post cryorolling treatments on microstructure and mechanical properties of Al 6061 alloy

5.2.1 Introduction

Post deformation annealing is one of the strategies to improve ductility by reducing the dislocation density through recovery and recrystallization. But the improvement in ductility through this approach is at the cost of strength. Wang et al., [76] have developed bimodal type microstructure through post deformation short annealing where the micrometer sized grains are embedded in a matrix of nanocrystalline grains. Based on this approach, many studies have been published recommending bimodal structure to improve tensile ductility of ultrafine grained/nanostructured material. Panigrahi et al., [109] [226] [227] have investigated the effect of rolling temperature, deformation strain and post cryorolling ageing on the mechanical and microstructural characteristics of 6XXX and 7XXX alloys. In addition to this, it was also reported that the combination of post cryorolling short annealing followed by low temperature ageing has resulted superior strength and ductility as compared to just cryorolling followed by low temperature ageing [182] [228]. It is evident from the recent studies that cryorolling followed by warm rolling is a lucrative approach to enhance strength and ductility significantly than the existing approaches in precipitation hardenable alloys [229] and [230]. The significant improvement in strength of Al 6061 alloy upon cryorolling followed by warm rolling is due to the dynamic ageing effect as observed in the previous section of this chapter. The strength and ductility of the alloy were further improved by static ageing at low temperatures [229]. In the present section, an attempt is made to investigate the effect of warm rolling followed by low temperature ageing on enhancement of mechanical properties of cryorolled Al 6061 alloy. It is compared with the Al alloys subjected to post deformation short annealing (200 °C for 10 min) followed by low temperature ageing. A thorough investigation of effect of warm rolling on strength and ductility of Al 6061 alloy was made by employing hardness and tensile testing. The obtained mechanical properties were substantiated through transmission electron microscopy (TEM) and differential scanning calorimetry (DSC) and X-Ray diffraction techniques.

5.2.2 Experimental details

Samples with initial dimensions of $10 \times 30 \times 40 \text{ mm}^3$ were cut from as received plate, and solution treated (ST) at 520°C for 3 hours in a muffle furnace and quenched immediately in water at room temperature. Cryorolling (CR) was performed up to 80% and 90% (i.e., from 10 mm to 2mm and 1mm thickness) thickness reductions. CR samples with 80% reduction were subjected to warm rolling at 200°C to achieve total reduction of 90% and referred as WR1. The detailed procedure of CR and WR is described in the chapter 3.3. Total soaking time given during warm rolling was 10 min. CR samples with 90% reduction were subjected to short annealing (SA) at 200°C by dipping the samples in oil bath furnace for 10 min. The WR1 and CR+SA samples were subsequently artificially aged at different temperatures 100°C , 125°C , 150°C . To investigate the effect of WR1, CR+SA and their respective ageing conditions on mechanical properties, Vickers hardness testing and tensile testing was performed at room temperature. To observe the precipitation evolutions, XRD and DSC testing are performed. Microstructural characterization was performed using FEI-Technai 20 G2S- Twin TEM operated at 200 kV. In the present study the final thickness of the samples was 1 mm. TEM samples were prepared on the plane parallel to the rolling direction.

5.2.3 Results

5.2.3.1 Hardness

Figure 5.19 shows the hardness variation in Al 6061 alloy after ST, CR, CR+SA and WR1. The hardness of solutionized sample has increased from 52 Hv to 96 Hv after cryorolling up to 90% (2.3 true strain) thickness reduction. Hardness of CR samples after short annealing for 10 min at 200°C has increased from 96 Hv to 105 Hv. The increment in hardness is due to static ageing of material during short time annealing at 200°C . Hardness of WR1 sample was observed as 114 Hv, which is the 8% higher as compared to CR+SA sample. Increment in hardness of WR1 sample reflects the effectiveness of warm rolling after cryorolling in improving the mechanical properties of the material. *Figure 5.20* shows the hardness data of CR+SA and WR1 Al 6061 alloy as a function of ageing time at various temperatures 100°C , 125°C , and 150°C . It was observed that at all three different ageing temperatures, CR+SA samples have shown peak hardness lower than the WR1 sample. Peak ageing conditions were found to be 125°C at 27 h

and 125 °C at 35 h for WR1 and CR+SA conditions respectively. The peak hardness value (126 Hv) for WR1 condition is significantly higher than the peak hardness value (117 Hv) of CR+SA sample. The time taken for achieving peak hardness in WR1 sample is significantly reduced.

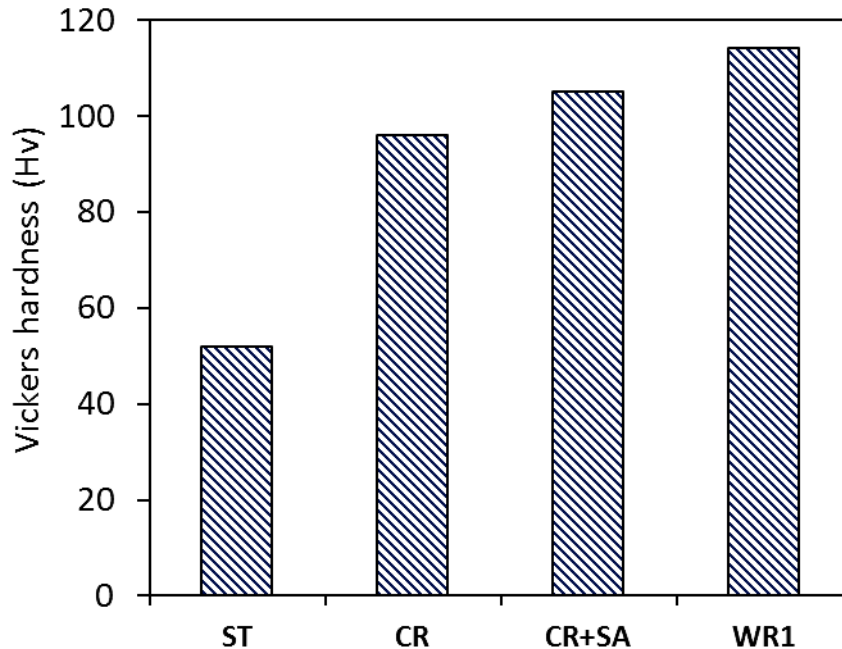


Figure 5.19: Hardness behaviour of Al 6061 alloy at various heat treated conditions; ST, CR, CR+SA, WR1.

5.2.3.2 DSC Study

To study the effect of warm rolling and short annealing of cryorolled samples on the precipitation evolution, DSC test was performed. *Figure 5.21* shows the typical DSC plots of Al 6061 alloy subjected to different processing conditions obtained with 20 °C/min heating rate. The *Figure 5.21(a)* shows DSC plot for Al 6061 alloy corresponds to the CR+SA. The behavior of the curve is similar to the CR 93% sample discussed in chapter 4. However the intensity of the initial peaks corresponding to clusters and G.P zones were reduced. *Figure 5.21 (b)* shows DSC thermogram corresponding to WR1 sample. In both the conditions, only single peak corresponding to strengthening phase similar to CR sample within the temperature range 200 °C - 275 °C was observed. The peak position is identical to the peak observed in CR sample but with reduced intensity. Whereas, in WR1 sample, peak intensity has decreased as compared to CR+SA and its position is shifted to low temperature side. The peaks related to formation of clusters and co-clusters of Mg and Si atoms are flattened.

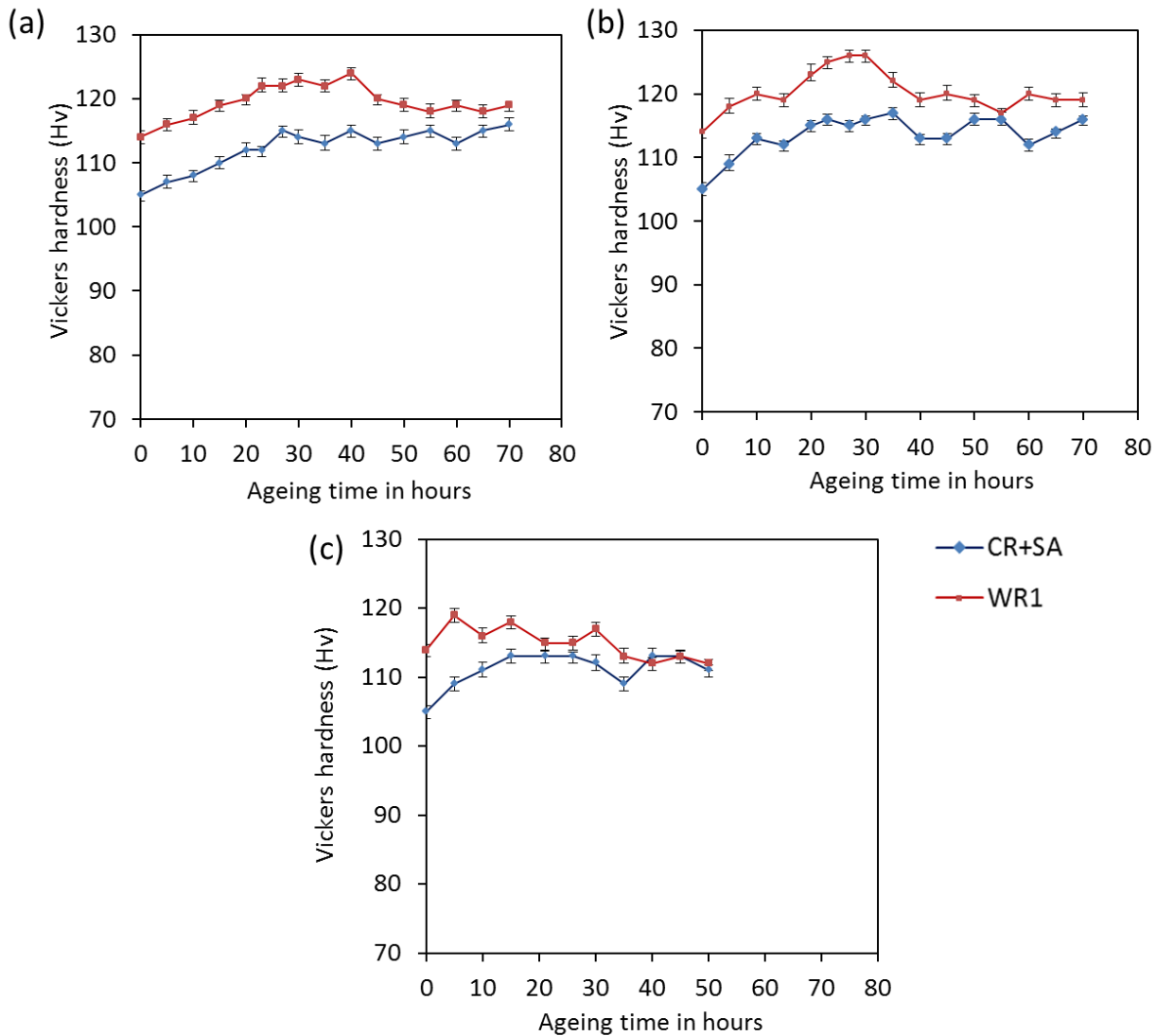


Figure 5.20: Variation in Vickers hardness of the CR + SA and WR1 sample after ageing at 100 °C (a), 125 °C (b), and 150 °C (c) as function of ageing time.

5.2.3.3 XRD analysis

X-ray diffraction analysis of CR+SA, WR1, SA+PA and WR1+PA of Al 6061 alloy is shown in *Figure 5.22*. Mg and Si are the major elements in Al 6061 alloy which imparts strength to Al matrix by forming Mg_2Si precipitates during ageing. The X-Ray diffraction analysis of ST and CR material was discussed in the previous section. In *Figure 5.22*, XRD profiles

corresponding to CR+SA and WR1 samples, have shown a small intensity peak corresponding to Mg_2Si precipitate. The intensity of the peak has further grown in SA+PA and WR1+PA samples.

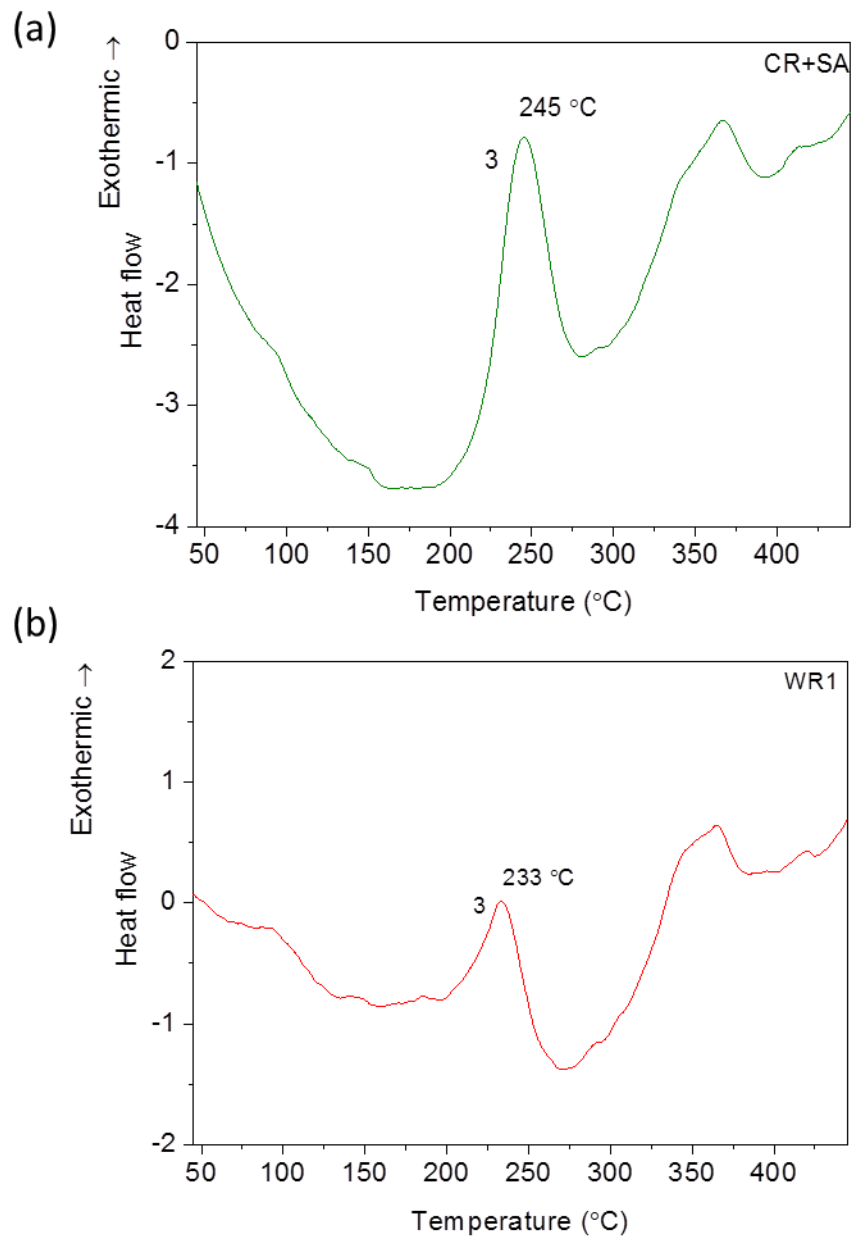


Figure 5.21: DSC thermograms of Al 6061 alloy; a) CR+SA, b) WR1

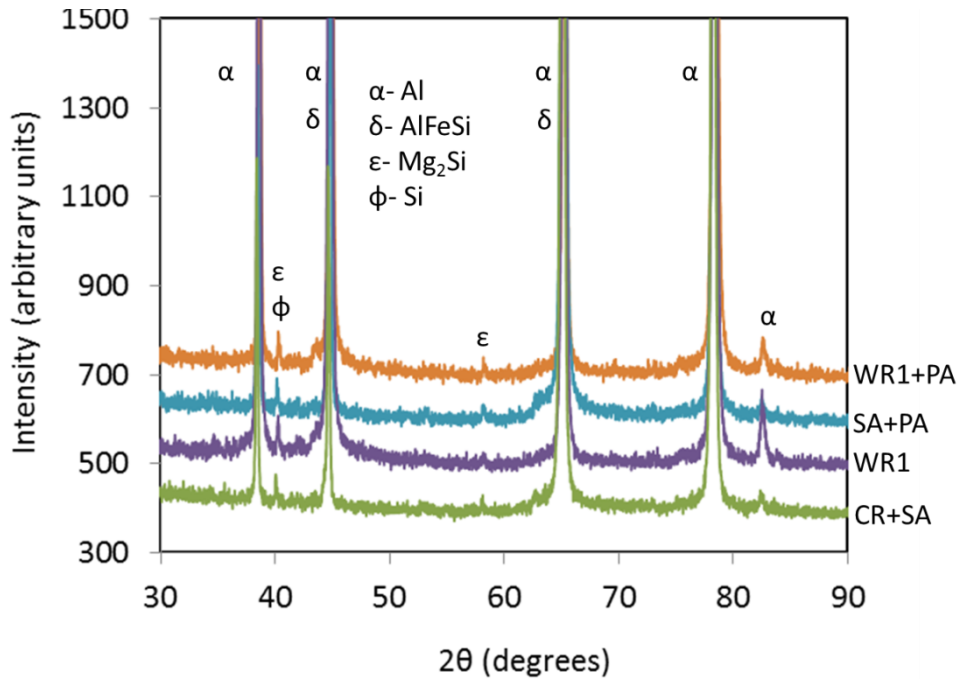


Figure 5.22: XRD patterns of Al 6061 alloy processed through various conditions: CR + SA, WR1, SA + PA, WR1 + PA.

5.2.3.4 Microstructure

Figure 5.23 shows the TEM micrograph of CR, CR+SA and WR1 sample. In CR sample, (*Figure 5.23(a)*) the formation dislocation cell structure with high density of dislocations with an average width of 200 to 300 nm was observed. The boundaries of this cell structure are of low angle grain boundaries ($\leq 15^\circ$). These cell walls are formed with complex dislocation tangles [156]. The microstructure of CR+SA sample, in *Figure 5.23 (b)*, has shown the formation of sub grain structure with an average size of 150-300 nm. The dislocation density has decreased when compared to CR sample due to static recovery or recrystallization effect during short annealing at 200 °C for 10 min. *Figure 5.23(c)* depicts the partially recovered structure with full of dislocation tangled zones. The TEM micrographs of SA+PA and WR1+PA samples are shown in *Figure 5.24*. The dislocation density has reduced in both CR+SA and WR1 samples after peak ageing treatment due to static recovery effect. During static recovery process, the ill-defined cell walls, that are formed during cryorolling has transformed into more regular dislocation network and form sharp low angle grain boundaries. The dislocation content inside the subgrains got reduced, but still some regions are found with high density of dislocations. *Figure 5.25* shows the TEM

image of precipitates observed in SA+PA sample. *Figure 5.25(a)* is a dark field TEM image showing distribution of precipitates (white spots in *Figure 5.25(a)*) under low magnification. *Figure 5.25(b)* shows the bright field TEM image of SA+PA sample at some other location. It is evident from the *Figure 5.25(a) and (b)* heterogeneous distribution of these precipitates. *Figure 5.25(c)* shows very fine spherical and needle shaped precipitates (marked with arrows in *Figure 5.25(c)*) at higher magnification. The average diameter of the spherical shaped precipitates of about 6 nm and the average length of the needle shaped precipitates is 11 nm. The spherical shapes are believed to be end sections of needle shaped precipitates. The corresponding SAED pattern is shown in *Figure 5.25(d)*. *Figure 5.26* shows the TEM images of precipitates and corresponding SAED pattern observed in WR+PA sample.

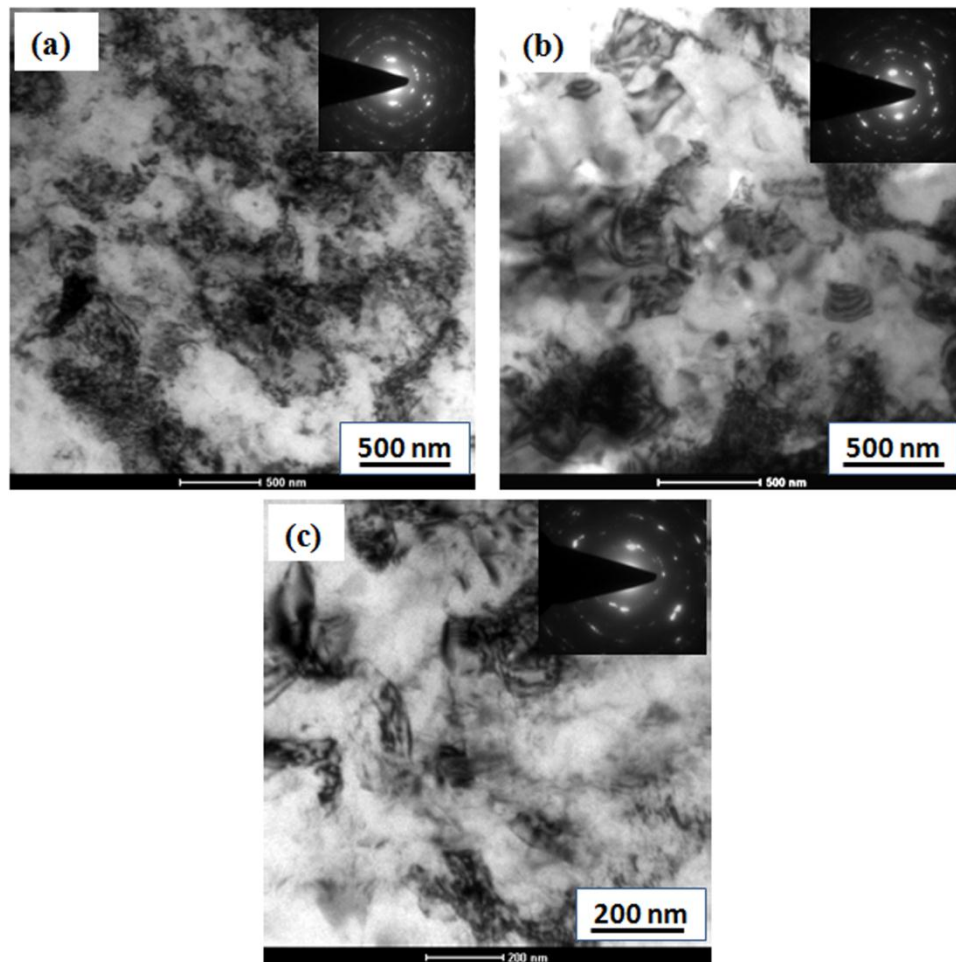


Figure 5.23: TEM micrographs of Al 6061 alloy processed through various conditions: (a) CR, (b) CR + SA, (c) WR1.

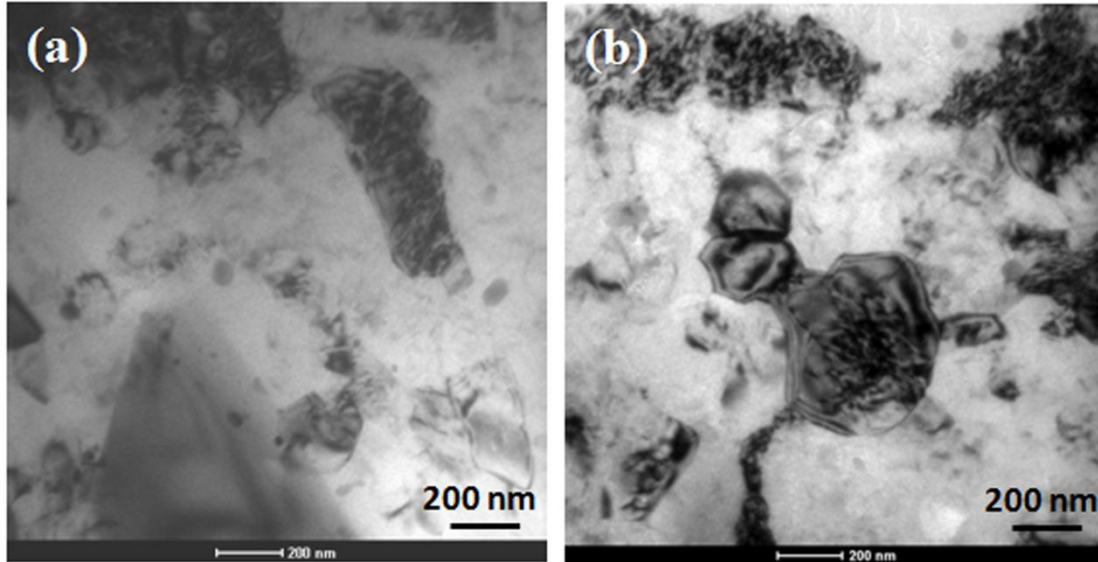


Figure 5.24: TEM micrographs of CR + SA and WR1 Al 6061 alloy after peak ageing treatment: (a) SA + PA, (b) WR1 + PA.

Figure 5.2.8(a) shows BF TEM images of very fine needle shaped precipitates at lower magnification. The average diameter and length of the needle shaped precipitates (marked with arrows in *Figure 5.2.8(b)*) are found to 2.5 nm and 8 nm respectively.

5.2.3.5 Tensile properties

The yield strength (YS) and ultimate tensile strength (UTS) of the starting material after cryorolling up to 90 % reduction has increased from 65 MPa to 280 MPa and 183 to 296 MPa respectively (*Figure 5.27*). The improvement achieved in YS and UTS is 330% and 61.7%, respectively. Thus, cryorolling showed greater influence on YS than UTS [199]. However, the tensile ductility has reduced from 30 % to 4.5 %. Short annealing treatment at 200 °C for 10 min after cryorolling leads to increase in YS (285 MPa) and UTS (310 MPa). The improvement in ductility observed in short annealed samples (7.5%) is higher than that of warm rolled samples (6%). The improvement in yield strength and UTS in WR1 samples as compared to CR samples are 14% and 10% respectively. XRD plots of WR1 sample in *Figure 5.22* shows the presence of Mg_2Si peak, which indicates the formation of precipitates during warm rolling at 200 °C. The significant improvement in YS and UTS of WR1 samples can be attributed to the fine precipitate particles evolved during warm rolling which will act as barriers for dislocation movement and increases the dislocation accumulation, thus reduces the dynamic recovery effect. CR+SA and

WR1 samples after subjecting to peak ageing treatment at 125 °C for 35 hours and 27 hours respectively, showed the simultaneous improvement in strength and ductility. Due to the effect of static recovery during short annealing treatment in SA+PA sample, the strength achieved is inferior to the WR1+PA samples.

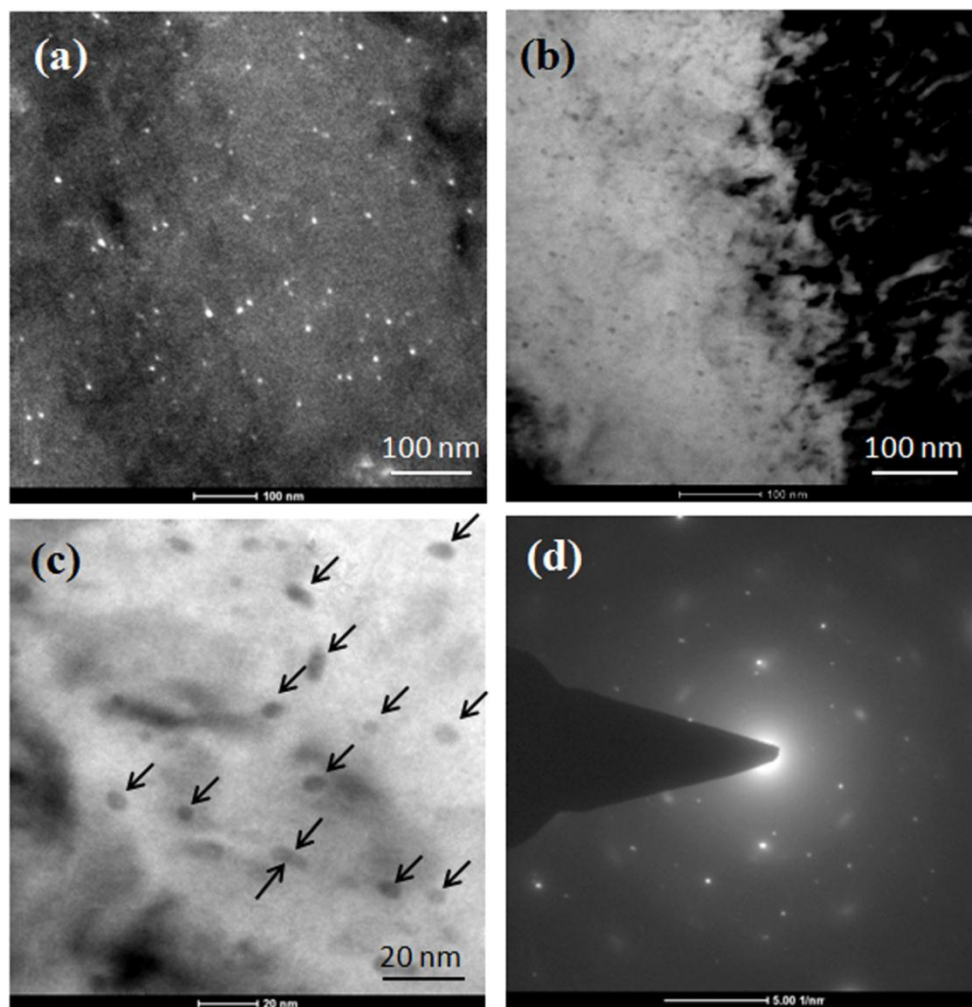


Figure 5.25: TEM image of precipitates in SA + PA sample: (a) dark field image of precipitates at lower magnification, (b) bright field image of precipitates at lower magnification, (c) bright field image of spherical and needle shaped precipitates at higher magnification, (d) SAED pattern of image shown in **Figure 5.25 (a)**.

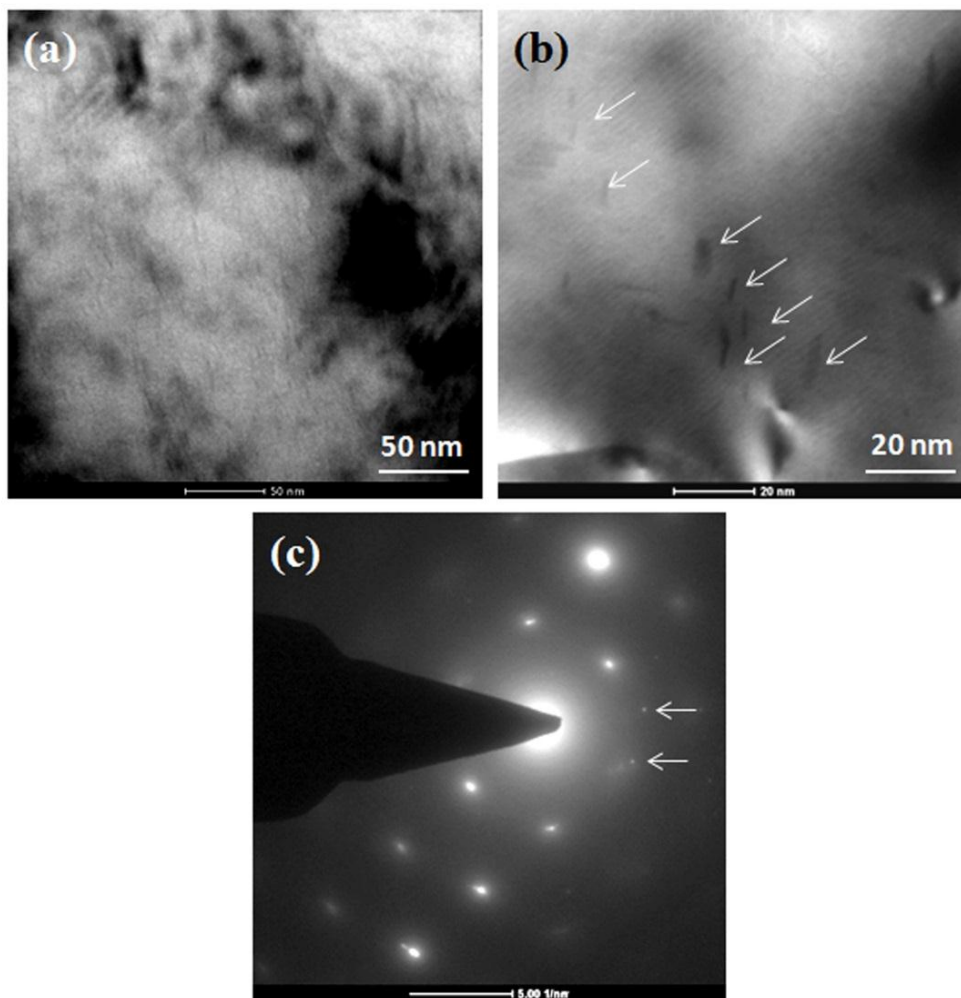


Figure 5.26: TEM image of precipitates in WR + PA sample: (a) bright field image of precipitates at lower magnification, (b) bright field image of needle shaped precipitates at higher magnification, (c) SAED pattern of image shown in **Figure 5.26 (a)**.

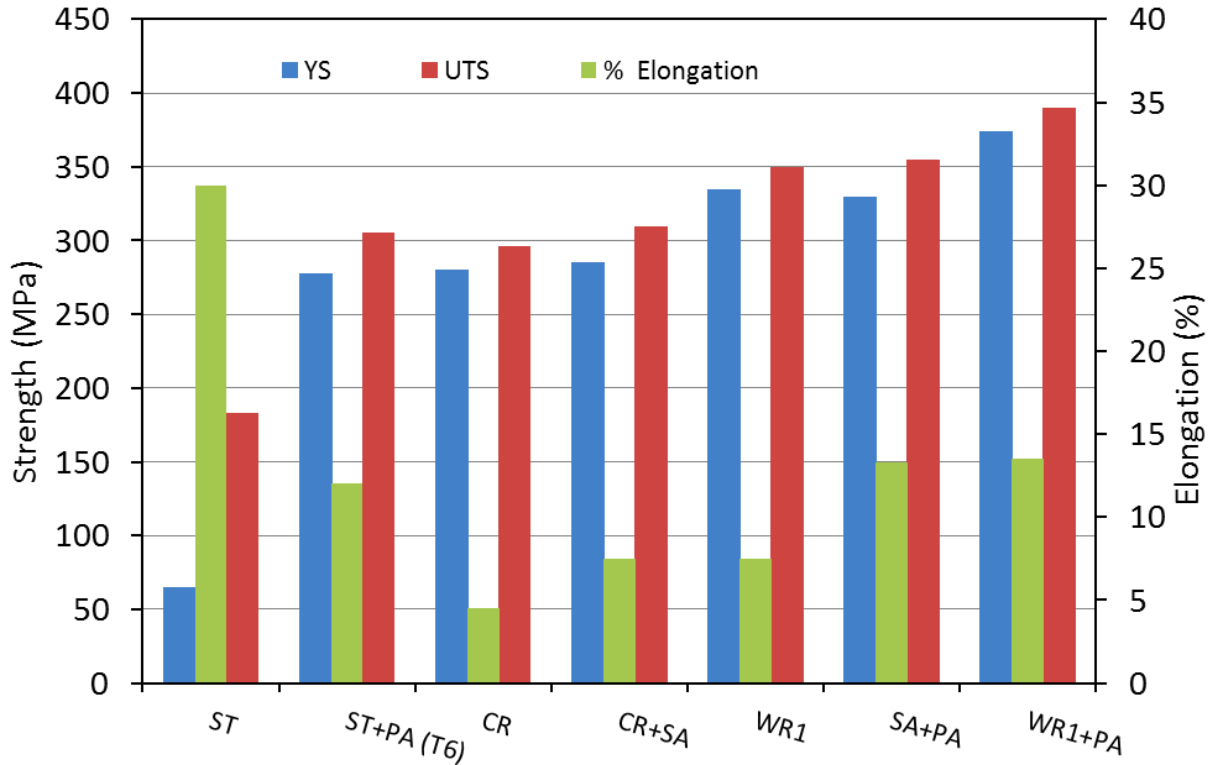


Figure 5.27: Variation in UTS, YS and elongation values of Al 6061 alloy processed through various conditions; ST, T6, CR, CR+SA, WR1, SA+PA, WR1+PA.

5.2.4 Discussion

It is clear from the obtained results that, the approach of warm rolling followed by static ageing in Al 6061 alloy has shown significant impact on enhancing mechanical properties. The hardness and YS received by CR samples is due to the presence of high dislocation density in the deformed material. The effect of CR on mechanical properties was discussed in the previous section. The mechanical properties of the CR material were improved further by short annealing treatment at 200 °C for 10 min. The ductility has improved from 4.5% to 7 %. In the literature, attempts were made to improve strength and ductility simultaneously by: i) controlling microstructure to develop bimodal and multi modal grain size distribution, ii) enhancing the work hardening rate by nano precipitation, and iii) by tailoring dislocation configurations [13] [76] [182] [191] [228] [231] [232]. It was observed from the TEM micrographs of CR+SA sample, *in Figure 5.23(b)*, that the formation of very fine equiaxed dislocation free sub grains in the range of 200 to 250 nm occurred. It can be reasoned that the improvement in ductility of CR+SA is due to

the formation of fine dislocation free grains during annealing at 200 °C for 10 min which can accommodate for more dislocations during deformation leads to increase in ductility. Increase in hardness and yield strength of CR+SA sample attributed to evolution of Mg₂Si precipitate from the Al matrix which is evident from XRD plots in *Figure 5.22*. The DSC thermogram of CR+SA in *Figure 5.21 (a)* shows the peak corresponding to the formation of intermediate precipitate forming and with flattening of peaks pertaining to formation of clusters and co-clusters of Mg and Si at low temperature side. These nanosized precipitates will act as a barrier for motion of dislocations, contributing to the increase in strength and hardness [233].

The hardness (114 Hv) and strength (YS-322 MPa, UTS-350 MPa) of WR1 sample are significantly higher than CR and CR+SA samples. The percentage increment in strength values of WR1 sample are YS - 15%, UTS - 18% as compared to CR sample and UTS - 13%, YS - 14% as compared to CR+SA samples. The XRD pattern of WR1 sample *Figure 5.22* shows, the presence of low intensity Mg₂Si precipitate peak. The DSC plot of WR1 sample in *Figure 5.21(b)* shows that the peaks corresponding to the formation of solute rich clusters and co-clusters are flattened. It is a clear indication that dynamic ageing was promoted during warm rolling [148]. The similar behavior was observed in the previous section where, the Al 6061 alloy warm rolled at 145 °C. The hardness achieved in WR sample was 122 Hv, which is more than the hardness achieved in the WR1 sample. The lower value of hardness observed in WR1 compared to WR is due to processing at high temperature (200 °C), which accelerates the dynamic recovery effect. Another reason could be the percentage of deformation. The purpose of choosing 200 °C as a warm rolling temperature in the present investigation was to develop microstructure during deformation so as to improve the ductility simultaneously with strength. The microstructural changes in WR1 sample under the TEM examination is shown in *Figure 5.23(c)*. TEM micrograph reveals very fine grains (100 nm) which are formed due to recovery or recrystallization. The superior tensile strength properties achieved in WR1 sample compared to CR+SA samples might be due to the size and distribution of the precipitates in WR1 samples, and also the nature of the grain boundaries. Kapoor et al., [234] observed the softening effect in multi-axial forged commercial pure Al alloy due to decrease in geometrically necessary dislocation density which are mainly associated with low angle grain boundaries and increase in high angle grain boundary fraction. During short annealing reduction in dislocation density through annihilation of dislocations and transformation of low angle grain boundaries to high

angle grain boundaries reduces the strengthening effect and increases ductility. The more hardness and strength with improved ductility in WR1 sample might be due to the presence of fine well developed cell structure which is essential for strengthening of ultrafine grained materials.

The CR+SA and WR1 samples were subjected to artificial ageing at different temperatures for understanding its influence on microstructure and mechanical properties. WR1 sample has shown more hardness after ageing at 125 °C for 27 hours. The ageing kinetics has been accelerated in WR1 sample as compared to CR+SA samples which is evident from the DSC thermo gram of WR1 sample. Gang et al., [229] have reported that the reason for superior properties of WR1 sample of Al 6061 alloy compared CR sample is due to the presence of high density of very fine β'' and β' precipitates. But, the ductility achieved in their studies was very low (~ 5%). Warm rolling at 200 °C in the present study has promoted grain refinement by recovery or recrystallization which attributes to increase in ductility (13%) and formation very fine precipitates (*Figure 5.26*). TEM micrographs of WR1 sample after peak ageing treatment shown in *Figure 5.26* which shows high density of very fine precipitates (average dia.- 2.5 nm, length -8 nm) distributed in the sample, which attributes to increase in strength (YS-374, UTS-390). The precipitates observed (*Figure 5.25*) in peak aged CR+SA (125 °C, 35 hours) are coarser (average dia.- 6 nm, length -11nm) in size compared to peak aged WR1 sample. The major strengthening phase in Al-Mg-Si alloys are believed to be β'' which is in needle shape. The size and distribution of precipitates can play a significant role in enhancing strength and ductility of a material. Cai et al., [148] have made systematic comparison of static and dynamic ageing of Al-Mg-Si alloy, and reported that the UTS of dynamically aged alloys is higher than that of alloy subjected to static ageing due to improved precipitation kinetics. The role of size of precipitates along with grain size and dislocation density in improving strength of the material can be understood from the following equation proposed by Peterson et al., [235]

$$\sigma_y = \sigma_0 + k_1\mu b/r + k_2d^{-\alpha} + k_3\mu b\sqrt{\rho} \text{ ----- (5.1)}$$

where σ_y and σ_0 are the total yield strength and yield strength of the matrix, b is the burgers vector, μ is the shear modulus, r is the mean radius of the precipitate, d is the mean grain/subgrain diameter, α is the stress/microstructure-dependent parameter, ρ is the density of

dislocations and k_i ($i = 1, 2, 3$) are the constants. The yield strength is inversely proportional to the mean radius of the precipitates. The size and distribution of the precipitates can be varied by varying deformation temperature and deformation rate as reported by Cai et al., and Kang et al., [148] [236]. It is clear from the above discussion that cryorolling in combination with warm rolling at 200 °C followed by low temperature ageing imparts higher strength and good ductility to precipitation hardenable Al alloys due to the favorable size and distribution of precipitates.

5.2.5 Conclusions

We have investigated the effect of cryorolling followed by warm rolling at 200 °C on improving strength and ductility of Al 6061 by comparing with cryorolling followed by short annealing at 200 °C for 10 min through detailed studies of microstructure and mechanical properties using TEM, XRD, DSC, Vickers hardness test and Tensile test and the following conclusions are made:

- 1) Material processed through WR1 resulted, increase in strength (UTS-350 MPa, YS-333 MPa) compared to CR + SA (UTS-310 MPa, YS-238 MPa).
- 2) The improvement in strength and ductility of WR1 sample is attributed to dynamic ageing and the formation of fine dislocation free sub cell structure during warm rolling.
- 3) In WR+PA sample fine needle shaped β'' precipitates with an average diameter and length of 2.5 nm and 8 nm were observed. Whereas in SA+PA sample coarse spherical and needle shaped precipitates with an average diameter and length of 6 nm and 11 nm were observed
- 4) The strength and ductility of WR1 samples has further increased up to 390 MPa, 13 % respectively after low temperature ageing at 125 °C for 27 hours. This improvement in strength and ductility is attributed to static recovery effect and formation of very fine needle shaped precipitates during artificial ageing.

Chapter 6

Precipitation behavior

This chapter describes the precipitation behavior of Al 6061 alloy processed through various thermomechanical routes. It contains two sections. In the first section, precipitation sequence and microstructural evolution in Al 6061 alloy processed through cryorolling (CR) and cryorolling followed by warm rolling (WR) was studied using low temperature DSC, TEM and hardness measurements. Activation energies of various phases of precipitates in CR and WR materials are calculated and compared with bulk ST material. In the second section, low temperature DSC studies were conducted for Al 6061 alloy processed up to various strain levels at liquid nitrogen temperature. Effect of deformation strain on the activation energies of various precipitates phases is discussed. Furthermore, natural ageing studies were conducted on CR and ST alloy by employing DSC and hardness measurements.

6.1 Precipitation behavior of Cryorolled and Warm rolled Al 6061 alloy

6.1.1 Introduction

The post-cryorolling heat treatments through low temperature ageing, annealing, warm rolling of the Al 6061 alloy led to simultaneous enhancement in strength and ductility through nano precipitation as reported in the chapters 4 and 5. The sequence, size, type and distribution of precipitates play a crucial role in determining the final properties of the material. Precipitation kinetics and its evolution of bulk Al alloys have been studied by several investigators using DSC and TEM [138] and [210]. The introduction of dislocations influences the precipitation kinetics and its sequence by providing heterogeneous nucleation sites and thereby accelerated precipitation kinetics is observed by [237] [238][239]. The effects of cold rolling on the precipitation processes in Al–Mg–Si alloys have been studied extensively [12] [212] [237] [240] [241] [242] [243]. Lee et al., have reported the enhanced precipitation reaction and altered precipitation sequence by cold rolling in Al alloy [240]. Christman et al., Panigrahi et. al, and Matsuda et al., have reported that cold rolling accelerates the ageing process with increasing dislocation density [241] [242] [244]. Hirata and Matsuo have reported that plastic deformation reduces the activation energy for the intermediate β' phase formation and the needles nucleate preferentially on dislocations [241]. The kinetics of hardening has been enhanced by two ways: (i) adding alloying element, Cu to Al–Mg–Si resulted in enhanced hardening kinetics [245] and [246], (ii) Presence of structural defects such as dislocations and low angle grain boundaries in cryorolled Al alloys has promoted faster precipitation kinetics through enhancement of the nucleation events [12]. The stimulation of the precipitation process could be attributed to introduction of high dislocation densities in the Al alloy due to cryorolling immediately after solution treatment. Hence, it is essential to render an insight into the precipitation hardening behavior of cryorolled material for optimizing the properties and realize the simultaneous improvement of strength and ductility in Al–Mg–Si alloys. The microstructural evolution and mechanical properties of Al 6061 alloy processed through CR and CR followed by WR conditions were discussed in chapter 4 and 5. The WR material has shown 27% improvement in UTS (390 MPa) as compared to CR material. Further, low temperature ageing of WR material resulted in 7% improvement in UTS. The literature on precipitation kinetics of cryorolled and

warm rolled alloys and their influence on mechanical properties are very limited. Therefore, the present work has been envisaged to investigate the precipitation kinetics in deformed Al alloy through DSC and TEM, which would enable to elucidate their role in deformation behavior of ultrafine grained materials.

6.1.2 Experimental

Samples with $10 \times 30 \times 40 \text{ mm}^3$ were machined from the as-received material and subjected to solution treatment (ST) at $530 \text{ }^\circ\text{C}$ for 3 hours followed by cold water quenching to room temperature. The ST alloy was subjected to CR and cryorolling followed by warm rolling (WR) processes as shown in *Figure 6.1*

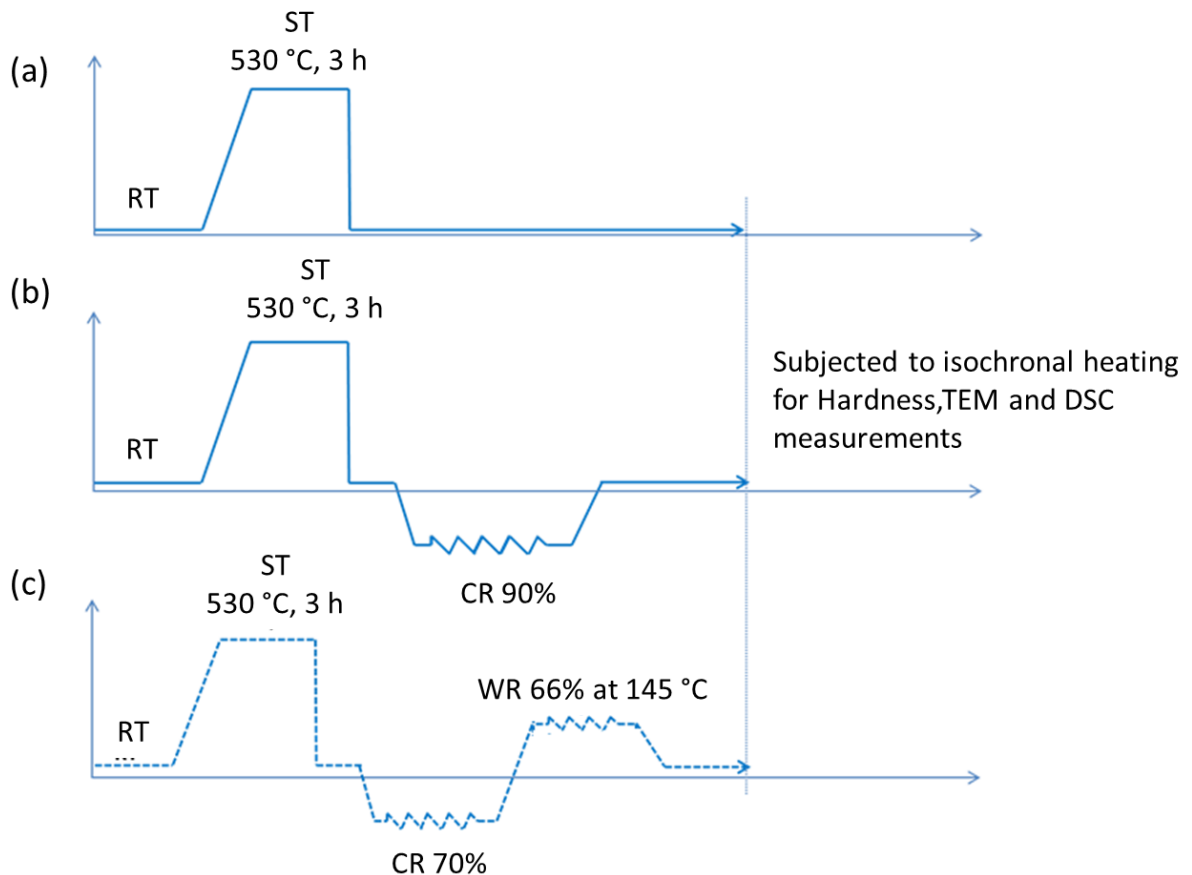


Figure 6.1: Process flow charts of ST, CR and WR.

In the first step, the ST material was deformed up to 70% and 90% thickness reductions through cryorolling (CR). Detailed procedure for cryorolling was discussed in chapter 3.3. In the second step 70% CR samples were subjected to warm rolling at 145 °C up to 66% deformation. The “WR” in the present study refers to the CR (70% reduction) alloy subjected to warm rolling (66% at 145 °C). To study the effect of CR and WR on the precipitation behavior and its kinetics, DSC measurements were carried out by using a low temperature differential scanning calorimeter, Perkin Elmer DSC 8000 under a nitrogen atmosphere at the rate of 20 ml min⁻¹ to reduce the oxidation. All the samples were tested from -5 °C to 450 °C and tests were run at least two times to ensure reproducibility. DSC was precooled up to -10 °C before loading the samples and allowed for 3 min to get equilibrated before starting the test. ST, CR and WR materials are used as specimens and pure Al annealed at 450 °C for 3 h followed by furnace cooling was used as a reference material for all the specimens. The weights (30 mg) of both specimens and reference material were maintained constant for DSC testing. All conditions were tested with heating rates of 10, 15, 20 and 25 °C/min. For ST condition, samples with 5 mm diameter and 0.6 mm thick were punched and subjected to ST at 530 °C for 3 hours followed by water quenching to room temperature were used. Whereas in CR and WR conditions, 5 mm discs were punched from processed sheets and then used for DSC testing. Baseline correction was performed to isolate the heat effects of transformation reactions corresponding to specimen from the data of reference sample. To understand the precipitation behavior of CR and WR material more thoroughly hardness measurements were taken on the samples heated isochronally with 20 °C/min heating rate up to various peak temperatures that are obtained through DSC testing. In order to substantiate the DSC and Vickers hardness results, the microstructural investigation was performed along normal plane. Transmission electron microscopy (TEM) investigation was carried out in a FEI Technai 20 electron microscope operated at 200 kV.

6.1.3 Results and discussions

6.1.3.1 DSC studies

Figure 6.2 (a) shows DSC thermograms of Al 6061 alloy of ST, CR and WR conditions obtained with the heating rate of 20 °C/min over the temperature range of 0 to 450 °C. The close up of peaks formed at low temperatures (from 0 to 150 °C) is shown in *Figure 6.2 (b)*. The standard precipitation sequence in the material after solution treatment as reported in the

literature is as follows [247] [248] [249]: super saturated solid solution (SSSS) \rightarrow clusters \rightarrow G.P. zones \rightarrow $\beta'' \rightarrow \beta''$ and $\beta' \rightarrow \beta$ (Mg₂Si) phase.

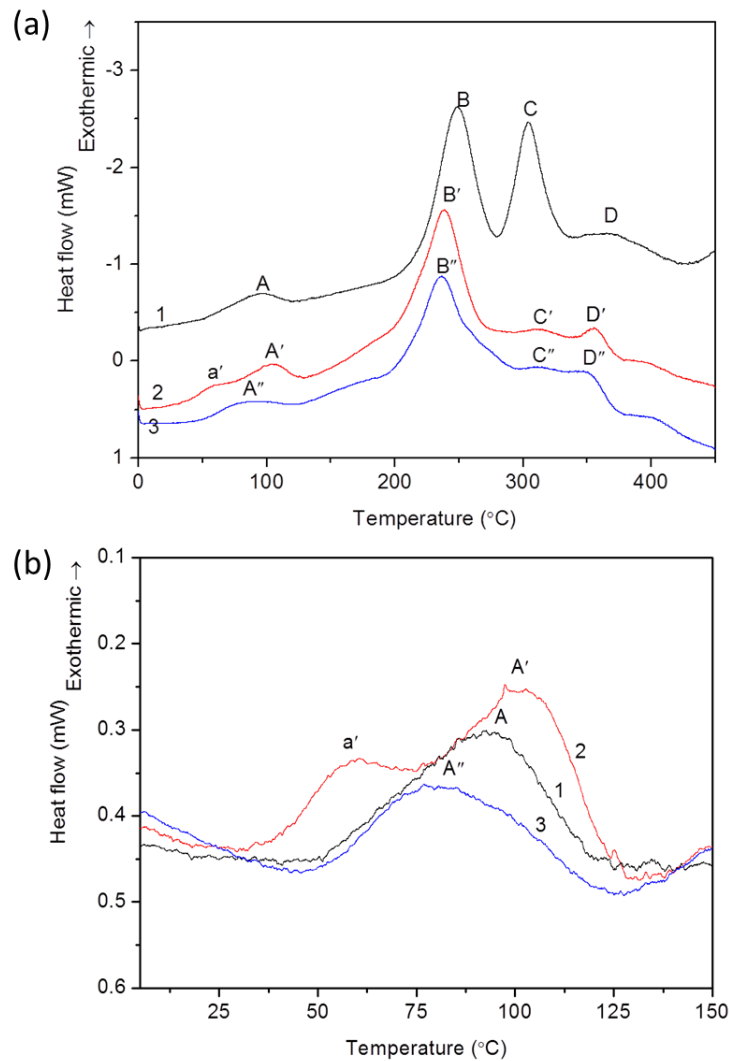


Figure 6.2 Typical DSC thermograms of Al 6061 alloy at various heat treated conditions: (a) ST (1), CR (2) and WR (3) and (b) close up view of image (a) showing only low temperature peaks.

In the DSC thermogram of ST material (*Figure 6.2 (a)*) the numbers of exothermic peaks within the range of 20–450 °C are tandem with the published results [138] and [210]. A single broad exothermic peak (peak A) at low temperatures (from 40 to 130 °C) is attributed to the formation of nanoclusters. Edwards et al., [138] have characterized isothermally aged sample using atom probe field-ion microscopy (APFIM) and reported that the clustering process involves the

following sequence as “*formation of Si, Mg atom clusters*→ *dissolution of Mg clusters*→ *formation of Mg/Si co clusters*”. In the recent reports, through low temperature differential scanning calorimetry of samples, quenched in iced water has shown two exothermic peaks at low temperatures (from 20 to 130 °C) and these two peaks are attributed to the formation of different types of nanoclusters i.e., cluster (1) and cluster (2), [142] and [237]. At low temperatures (from 20 to 150 °C), there are three clustering reactions, which occur in two stages as reported in the literature [250]. However, the peaks corresponding to individual clustering reactions were not clearly resolvable. The first two reactions get completed after 1 h at room temperature. The third reaction continues up to 2 weeks at room temperature. These clusters play a significant role in further strengthening of the material through artificial ageing. The two large exothermic peaks (peaks B and C) observed between 200 and 340 °C correspond to the primary and secondary strengthening phases, β'' and β' . The hump observed between 340 and 420 °C could be due to the formation of stable phase β . The position of the peaks is scan rate dependent. It is seen from the plot of ST material (*in Figure 6.2 (a)*) that no peak corresponding to the formation and dissolution of G.P. zones is observed. Matsuda et al., have observed fine G.P. zones with monolayer or multi-layer structures in the Al–Mg–Si alloy aged at 70–150 °C for 60 kilo seconds [244]. With further peak ageing treatment, the G.P. zones with multilayered structures transformed in to random type precipitates. It was reported in the earlier work that the peak observed at 264 °C in the present study, is actually overlapping of two peaks corresponding to G.P.-I zones with unknown structure of dot like precipitates and G.P.-II zones (β'' precipitates) with monoclinic structure of needle shaped precipitates in the sample tested after immediate water quenching [138] and [210]. The formation of unresolved doublet consisting of two superimposed peaks is not common in all scan rates. *Figure 6.3 (a)* shows the sign of superimposition of peaks only in the DSC thermogram with 10 °C/min scan rate, it was disappeared with increase in scanning rates. It is evident from DSC plot of ST material (*Figure 6.3(a)*) that the lack of endothermic signal between the peaks corresponds to clusters, β'' and β' phases. It ensures that there is no dissolution activity involved during transition from clusters to β'' and β' phases. It is just a transformation reaction [243].

DSC thermogram of CR sample obtained with 20 °C/min heating rate is shown in *Figure 6.2 (a)*. Unlike ST sample, CR material has shown two clear exothermic peaks (peaks a' and A') at low temperatures (from 25 to 130 °C).

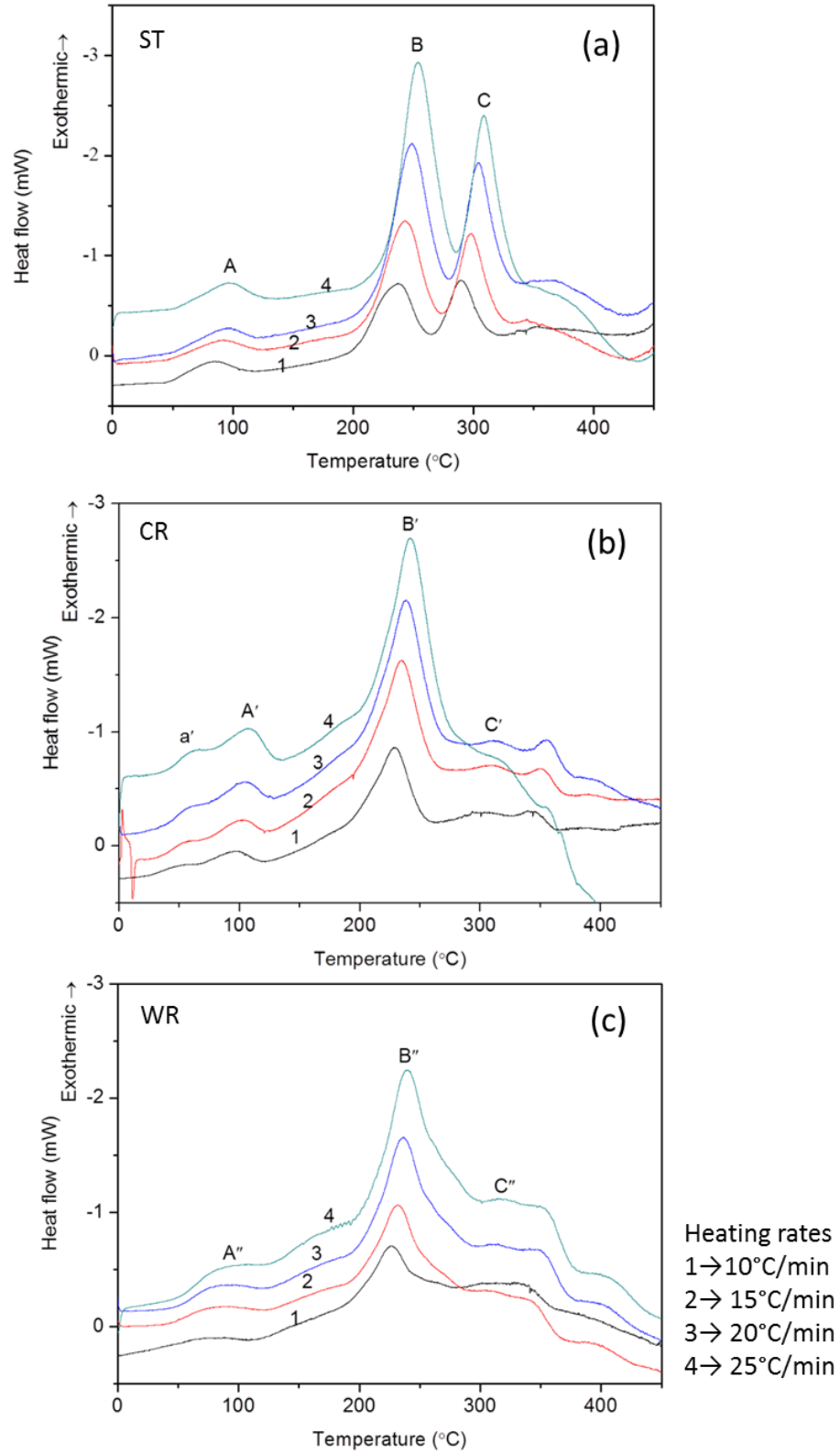


Figure 6.3: DSC thermograms of Al 6061 alloy at various heat treated conditions with various heating rates: (a) ST, (b) CR, and (c) WR.

The close up view of the peaks is shown in *Figure 6.2(b)*. Compared to the single exothermic peak at 92 °C in plot corresponding to the ST material, the peak a' has moved to low temperature (57 °C) side and the peak A' has moved towards high temperature side (104 °C). These two peaks are similar to the reported results by Serizawa et al., in undeformed as quenched material [142]. They can be attributed to the formation of nanoclusters, cluster (1) and cluster (2). Formation of cluster (1) is probably due to Si atoms and cluster (2) is due to Mg atoms [250]. But Serizawa et al., have observed both Mg and Si atoms with varying ratios in the formation of cluster (1) [142]. The mechanisms of clustering at low temperatures is yet to be established but the formation of distinct peaks at low temperatures in CR material as compared to the ST material could be due to the interaction of solute atoms with vacancies and dislocations. During CR, introduction of dislocations could cause annihilation of quenched vacancies by acting as a vacancy sinks [212]. This could cause to delayed formation of cluster (2), and therefore shifting of the reaction peak towards high temperature. On the other hand, a shifting of cluster (1) peak towards low temperature side could be due to the dislocation assisted formation. There is no significant peak corresponding to the formation and dissolution of G.P. zones. Another major difference observed with the DSC plots of ST material to CR material is the exothermic peak (peak B') in the temperature range 190 °C to 275 °C, which indicates that, CR has significantly affected the precipitation sequence during ageing. Peak C' has been completely suppressed in CR material. After CR, the position of the peak has shifted to low temperature side (238 °C) compared to ST material (249 °C), which indicates acceleration of ageing kinetics in CR material. The nature of the peak B' is similar to the reported literature [212] [237] [239] [243] and [251].

DSC thermogram of WR material obtained with heating rate of 20 °C/min is shown in *Figure 6.2 (a)*. The peaks at low temperature in *Figure 6.2(b)* show the nature of the plot of WR material is similar to the ST material but with reduced intensity and shifting of peak towards low temperature. This peak is considered to be due to the formation cluster (2). The increase in hardness of WR (117 Hv) material compared to CR (98 Hv) material could be due to the formation of clusters (1) [230]. The major difference between DSC plot of ST and WR material is presence of single exothermic peak (B'') like CR material in the range of 180 °C to 300 °C, believed to be related to strengthening phase and shifting of peak to low temperature side (236 °C). The intensity of the peak has been reduced after WR but full width at half maximum has increased as compared to ST and CR material. Increase in full width at half maximum indicates

the reaction associated with peak B'' is being influenced by the successive reaction. The reason for decrease in intensity of peaks B' and B'' in CR and WR material compared to ST material could be due to the trapping of Mg and Si atoms by tangled dislocations generated by CR and WR and hence, reduction in volume fraction of precipitation [240]. *Figure 6.3* shows the DSC thermograms of ST, CR and WR materials obtained at different heating rates of 10, 15, 20, 25 °C/min. With increase in heating rate, all peaks are shifted to high temperature side, indicates the rate of formation is controlled by the reaction kinetics [252]. In the present investigation, Kissinger analysis is used to calculate the activation energy for evolution of clusters and strengthening phase in ST, CR and WR material. Activation energy is calculated by using Kissinger's equation [253] as given below:

$$\ln\left(\frac{B}{T^2}\right) = -\frac{E}{RT} + \text{constant} \text{-----(6.1)}$$

where B is the heating rate; E is the activation energy for the evolution of precipitates, R is a universal gas constant; T is the specific temperature such as T_p . Kissinger plots (*Figure 6.4*) were obtained using T_p of ST, CR and WR materials with various heating rates. In ST material, peaks corresponding to cluster formation, β'' and β' phases (peak A, peak B and peak C) were analyzed to calculate activation energy. Whereas, in CR and WR material, cluster peaks and major exothermic peak corresponding to strengthening phase formation were taken for calculating activation energies. The obtained activation energies from CR and WR material were compared with its bulk ST material. Kissinger plots corresponding to ST, CR and WR materials are shown in *Figure 6.4*. From the slope of the straight lines, the obtained activation energies along with peak temperatures at different heating rates were shown in *Table 6.1*. Since in ST material, observed single peak corresponds to cluster formation, it is denoted as peak of C 1/2. The value of activation energy obtained for C 1/2 formation in ST material is 88 kJ mol⁻¹. Whereas, in CR material, the energies associated with formation of C1 and C2 are 56 and 87 kJ mol⁻¹, respectively. This shows that formation of C1 is faster than C2. The value associated with C2 formation in CR material is very close to the C1/2 value. The obtained values in the present study are higher than that of reported values for Al–Mg–Si alloy [249]. This could be due to the composition difference in the material. It was reported by Gupta et al., that the ratio of Mg and Si could influence the activation energies for the cluster formation [249].

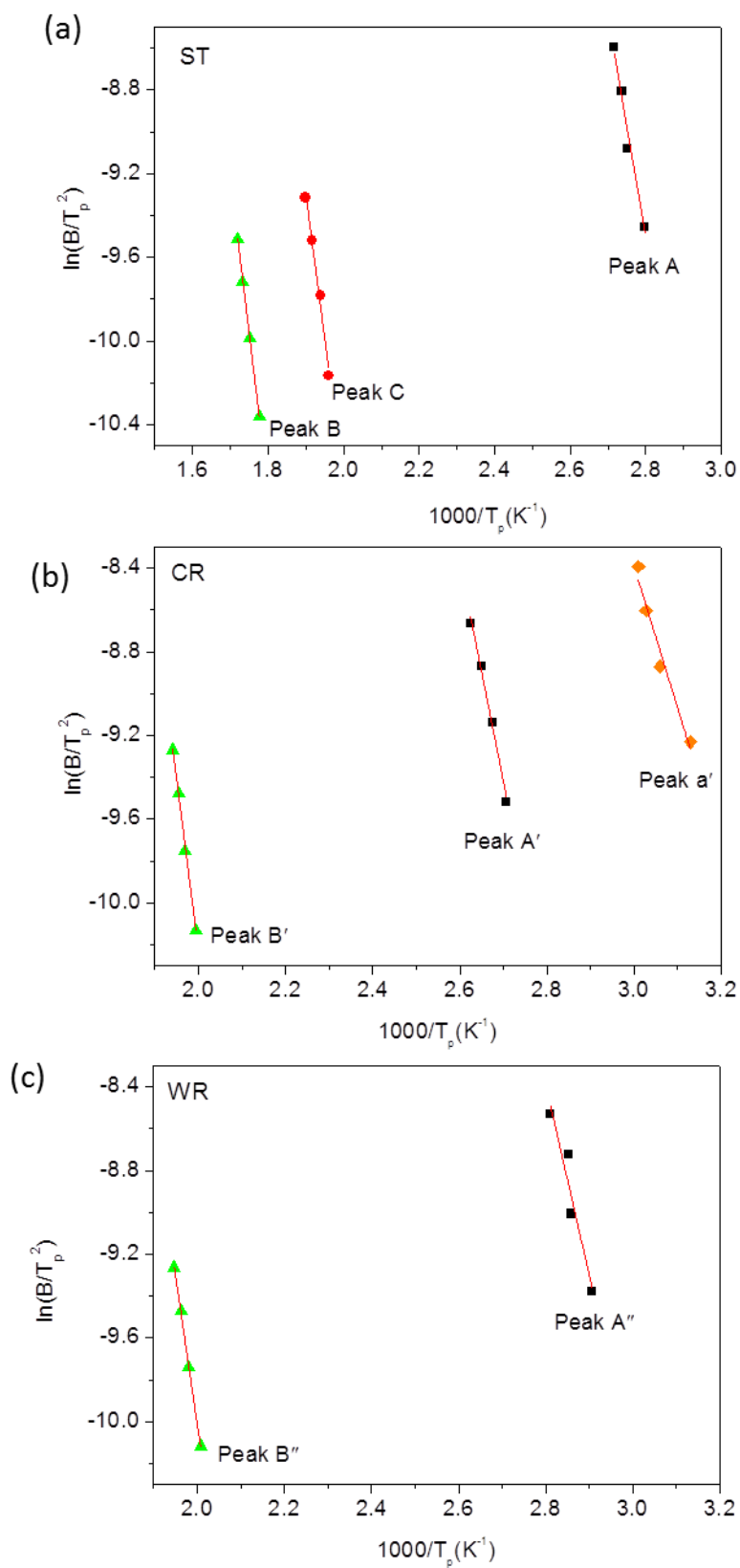


Figure 6. 4: Kissinger plots for the various exothermic peaks in ST, CR and WR material.

Table 6.1: Peak temperatures and activation energies of various processed conditions.

Heating rate (°C/min)	ST			CR			WR	
	Peak A (C 1/2)	Peak B (β'')	Peak C (β')	Peak a' (C1)	Peak A' (C2)	Peak B' (β''/β')	Peak A'' (C2)	Peak B'' (β''/β')
10	84	237	290	47	96	229	71	226
15	90	243	298	54	101	234	77	232
20	92	249	304	57	104	238	78	236
25	95	254	308	59	108	242	83	240
Activation energy (kJ mol ⁻¹)	88	114	124	56	87	136	75	132

The value lies in the range from 45 to 90 kJ/mol for the alloys with different Mg to Si ratios. In WR material, the activation energy for C2 formation is found to be 75 kJ mol⁻¹, which is lower than that of ST and CR material. In ST material, after sudden quenching from 530 °C to room temperature, excess vacancies are quenched in. In the presence of excess vacancies, diffusion of solute proceeds at a rate equal to that for migration of vacancies [252]. Thus, the activation energy required for cluster formation is close to the activation energy required for the vacancy migration [251]. It was reported that the migration energy of vacancies in Al–Cu and Al–Cu–Mg alloys are in the range of 41–66.9 kJ/mol [252]. In the present investigation, the obtained value (88 kJ mol⁻¹) is higher than the reported value. During CR, introduction of high density of dislocations influences the concentration of quenched in vacancies. Thus, the precipitation kinetics of the alloy gets altered. The dislocations can influence the precipitation kinetics of clusters by two ways as follows: (1) dislocations causes annihilation of vacancies thereby slow down the precipitate formation. (2) Dislocations can accelerate the precipitation kinetics through increasing diffusion rates of solute atoms by acting as short circuit paths. In CR material, C1 formation was accelerated and C2 was retarded. In ST material, the activation energy obtained for the β'' formation (from peak B) is 114 kJ mol⁻¹. Chen et al., have reported that the activation energy for β'' formation in Al 6061 alloy as 135 kJ mol⁻¹, which is higher than the value observed in the present investigation [252]. Gaber et al., have reported that the average activation energy associated with the precipitation of β'' in the excess Si and excess Cu alloys are 78.2 kJ mol⁻¹ and 69.2 kJ mol⁻¹, respectively [253]. This shows that there is no consistency in the reported literature. These values are significantly lower than the bulk diffusion energies for the main alloying elements (Si: 124, Mg: 131, Al: 142 kJ mol⁻¹) [229] and [254]. In ST material,

peak C is believed to be due to β' formation. The obtained activation is 124 kJ mol^{-1} . It is in well agreement with those obtained by Chen et al., in the Al 6061 and this value is same as the bulk diffusion energy of Si (Si: 124 kJ mol^{-1}) [252]. It can be inferred that the formation of β' is Si-diffusion control reaction.

In CR material, the obtained activation energy corresponding to peak B' is 136 kJ mol^{-1} . Interestingly, this value is higher than the energy associated with peak B in ST material. It is well reported in the literature that plastic deformation after solution treatment causes to reduction in activation energy due to existence of dislocations [12], [241], [251] and [255]. Dislocations can increase the low temperature diffusivity by providing high diffusivity paths [240]. But, this has been observed commonly in low and mild deformed materials. Also, inducing severe deformation in the material leads to increase in tangled dislocation density and thick dislocation cell walls. These will not assist for the diffusivity of the precipitation forming species during subsequent ageing [240]. This would increase the energy barrier for precipitate formation. In deformed materials due to the complex phenomena by precipitation/dissolution reactions and the recovery and recrystallization, the rate of precipitation reaction gets altered significantly [239]. The higher activation energy value of peak B' in CR material compared to that of peaks B and C in ST material indicates that deformation induced dislocations and sub-grain boundaries have retarded the formation of β'' and its transformation to β' . In WR material, the obtained activation energy for the peak B'' is 132 kJ mol^{-1} , which is nearer to the value for peak B' in CR material. The absence of dissolution peak before exothermic peak B'' indicates the formation strengthening phase directly from precursor clusters/G.P. zones.

6.1.3.2 Hardness evolution

Figure 6.5 shows the variation in hardness with respect to temperature (isochronal heating) along with DSC thermograms of ST, CR and WR material. The samples were heated with same heating rate ($20 \text{ }^\circ\text{C/min}$) as applied to the DSC testing. The hardness of the ST material immediately after quenching was 44 Hv. The behavior of the hardness is influenced by the various precipitation reactions (*Figure 6.5(a)*) that occur in the sample during ageing. At lower temperatures ($<150 \text{ }^\circ\text{C}$) as it was discussed earlier, the low intensity peaks are attributed to formation of clusters. With increasing temperature, the hardness has increased to 70 Hv at $121 \text{ }^\circ\text{C}$. Formation of clusters has shown significant effect on increasing the hardness of the matrix. The maximum hardness (98 Hv) was obtained at $275 \text{ }^\circ\text{C}$ where the β'' formation completes.

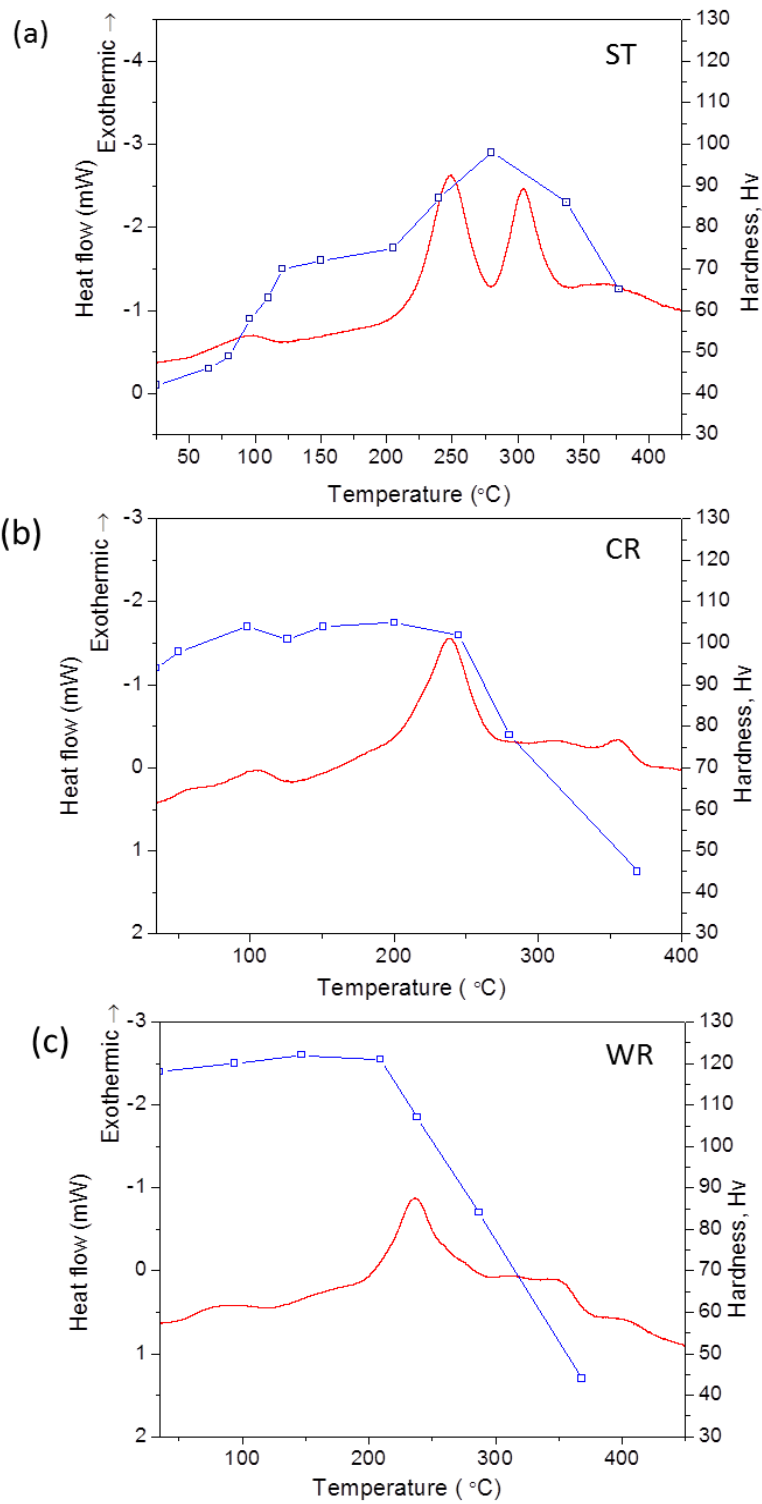


Figure 6.5 DSC thermograms obtained with 20 °C/min heating rate along with the hardness plots of Al 6061 alloy: (a) ST, (b) CR, and (c) WR.

There is no hardness drop observed between cluster formation and β'' precipitation. It indicates no dissolution of clusters before β'' precipitation. At the end of the exothermic peak corresponding to β' precipitation, the observed hardness was 86 Hv. This drop in hardness can be attributed to transformation of β'' to β' phase. With further increase in the temperature to 377 °C, where the β phase (Mg_2Si) completes, the hardness has dropped to 71 Hv. The hardness profile with increasing temperature is matching with the exothermic reactions occurring in DSC thermogram.

Figure 6.5(b) depicts the hardness plot of CR material along with DSC thermo-gram obtained with heating rate of 20 °C/min. The initial hardness of CR material is 94 Hv. The higher hardness of CR material compared to ST material can be attributed to existence of high dislocation density and grain refinement. Since the deformation was given at very low temperature (near liquid nitrogen temperature), it was expected that all the solute atoms would remain in the matrix. So, the obtained hardness is purely due to grain boundary strengthening, dislocation strengthening, and solid solution strengthening. With increasing temperature isochronally, hardness has increased up to maximum 105 Hv at 200 °C. This indicates the rise in hardness is a result of hardening by solute clusters overwhelming the softening effect by recovery. Further increasing temperature, the hardness has dropped down. At 275 °C where the exothermic reaction ends, the observed Vickers hardness is 78 Hv. This is lower than the hardness obtained in ST material after the exothermic peak related to β' formation. In CR samples, the hardness evolution is influenced by recovery and recrystallization during ageing.

Figure 6.5 (c) shows the hardness plots of WR material with respect to isochronal heating temperature along with the DSC thermogram. The total soaking time during warm rolling at 145 °C was 20 min. The initial hardness of WR material at room temperature was 118 Hv. The trend in variation of hardness with increasing ageing temperature in WR material is similar to CR material. Despite the suppression of peak at low temperature corresponding to solute cluster (1), the slight increment in hardness has been observed. The increment in hardness with respect to ageing time in the lower temperature region could be due to hardening effect by the formation of remnant solute atoms as clusters or G.P. zones. At the end of the major exothermic peak (peak B"), the obtained hardness is 84 Hv, which is nearly same to the hardness obtained after formation of β' phase in ST material. To understand more clearly about the precipitation behavior and the type of precipitates forming at the major exothermic peaks observed in CR and WR

material, TEM investigation was performed at the peak temperatures and end of the peak temperatures.

6.1.3.3 TEM studies

Figure 6.6 (a) & (b) shows the bright field TEM micrograph of ST sample heated up to end of the exothermic peaks (peaks B and C). In *Figure 6.6(a)*, fine needle shaped β'' precipitates are seen through strain field contrast and the distribution is homogeneous throughout the matrix. *Figure 6.6(b)* shows the coarse rod like precipitates corresponding to β' distributed homogeneously throughout the matrix. The obtained TEM results for ST sample are in agreement with the published literature [138]. TEM microstructure of the CR sample heated to 238 °C with heating rate of 20 °C/min revealed two types of precipitates (*Figures 6.7 and 6.8*). *Figure 6.7(a)* shows very fine dot and needle shaped precipitates taken in dark field imaging mode. These fine dots are ends of the needles seen along the length direction. The average diameter of the needle shaped precipitates is 7 nm. *Figure 6.7(b)* shows various lengths of needle shaped precipitates ranging from 10 to 80 nm at higher magnification as observed at different location from the same sample. *Figure 6.8* shows rod shaped coarse precipitates where the end sections are circular in CR sample heated to 238 °C. The average diameter of these rods is found to be 35 nm. The absence of second major exothermic peak corresponding to β' formation in the temperature range of 250–350 °C in CR sample indicates its suppression. However, the TEM micrographs of the sample heated up to 238 °C shows existence of two kinds of precipitates. It can be inferred that these two different precipitates are β'' and β' upon comparing them with the reported literature for these precipitates [138] [210]. *Figure 6.9* shows the dark field TEM micrographs of CR sample heated to 275 °C at end of the exothermic reaction (peak B') with 20 °C/min. *Figure 6.9(a)* shows the coexistence of β'' and β' precipitates. The needle and rod like precipitates with different sizes can be observed. There are two possible phenomena, which are expected to occur in CR sample. (i) Simultaneous formation of both phases β'' and β' from the precursor. (ii) Coexistence of different sizes (diameters) of needle and rod shaped precipitates, which indicates transformation of β'' and β' over increasing temperature.

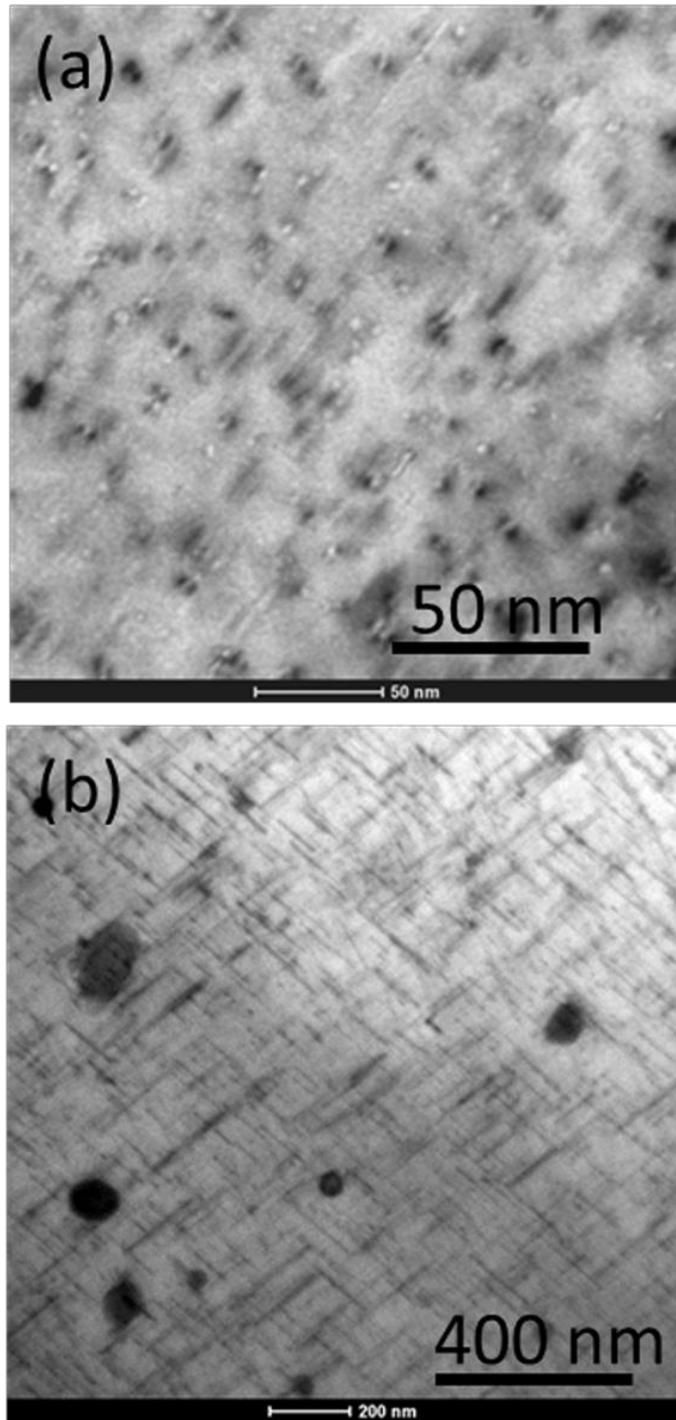


Figure 6.6: Bright field TEM micrograph of ST material isochronally heated up to end of the major exothermic peaks: (a) peak B and (b) peak C.

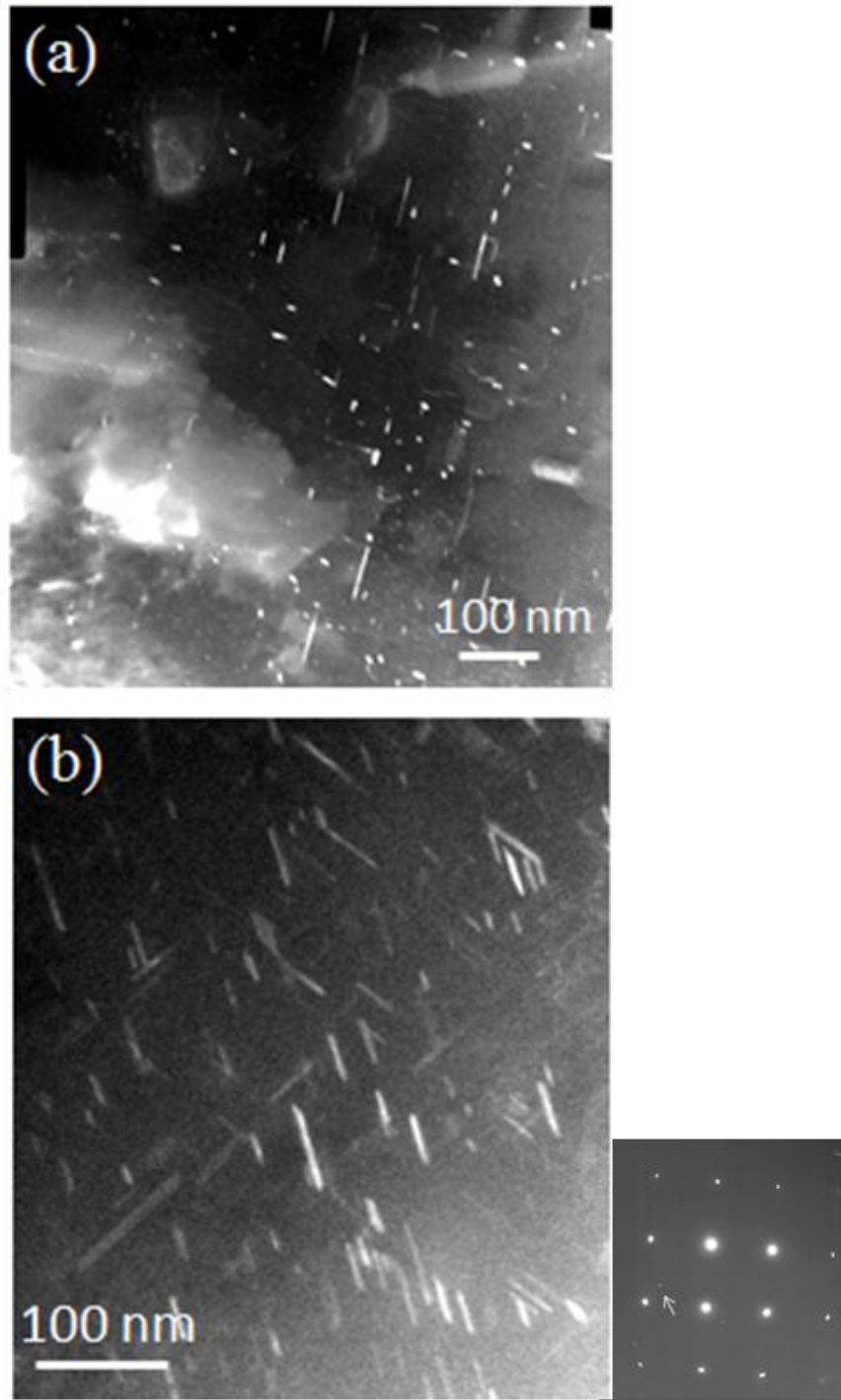


Figure 6.7: Dark field TEM micrographs and $(B\frac{1}{4}[001]Al)$ SAED for CR material heated to 238 °C (half reaction temperature) with 20 °C/min heating rate: (a) needle shaped β'' precipitates at lower magnification, (b) β'' precipitates at higher magnification observed at different location and $(B\frac{1}{4}[001]Al)$ SAED micrograph.

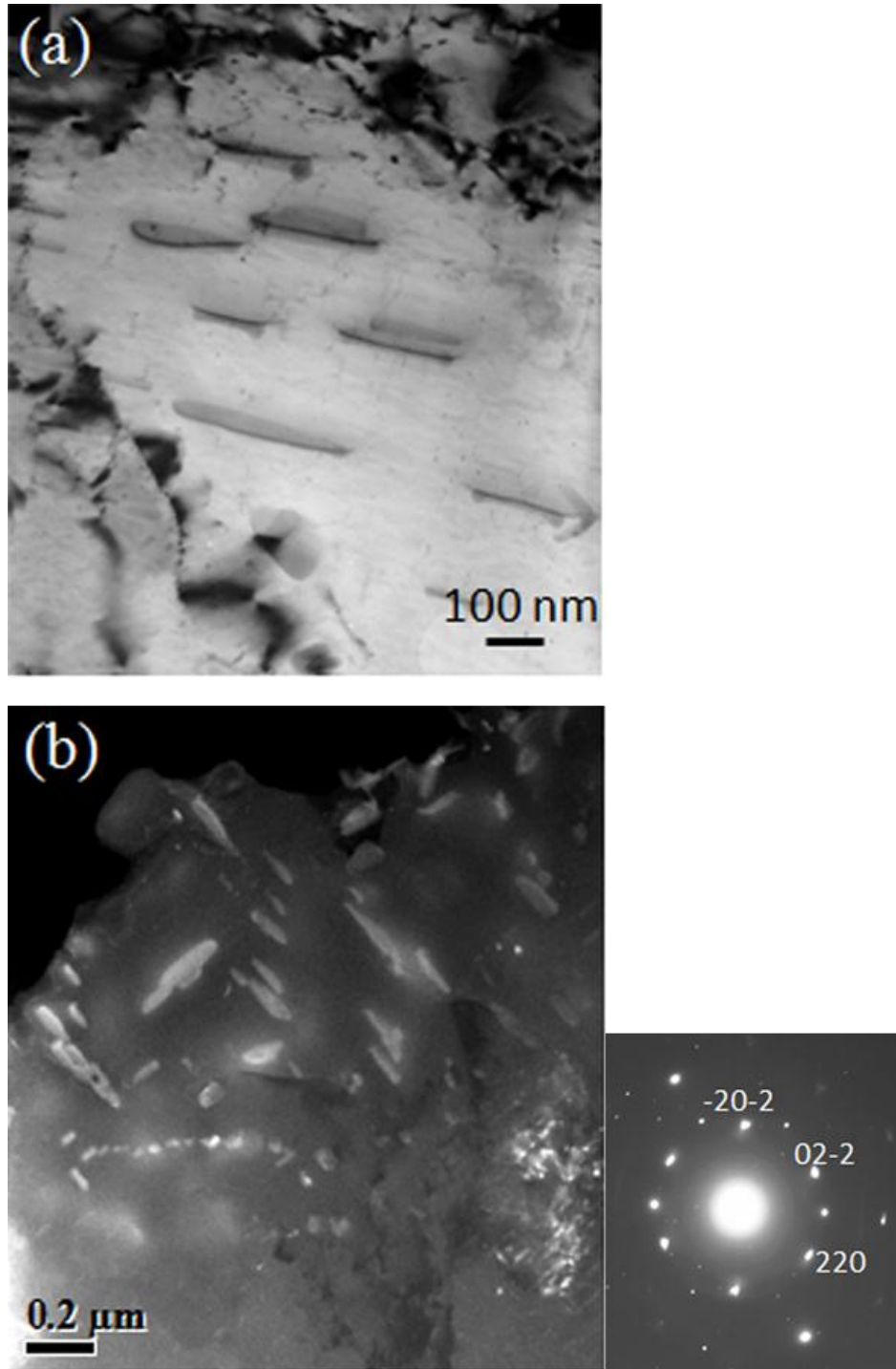


Figure 6.8: TEM micrograph of CR material heated to 238 °C (half reaction temperature) with 20 °C/min heating rate: (a) Bright field TEM micrograph rod shaped β' precipitates, (b) Dark field TEM micrograph of rod shaped β' precipitates observed at different location and $(B^{1/4}[111]Al)$ SAED micrograph.

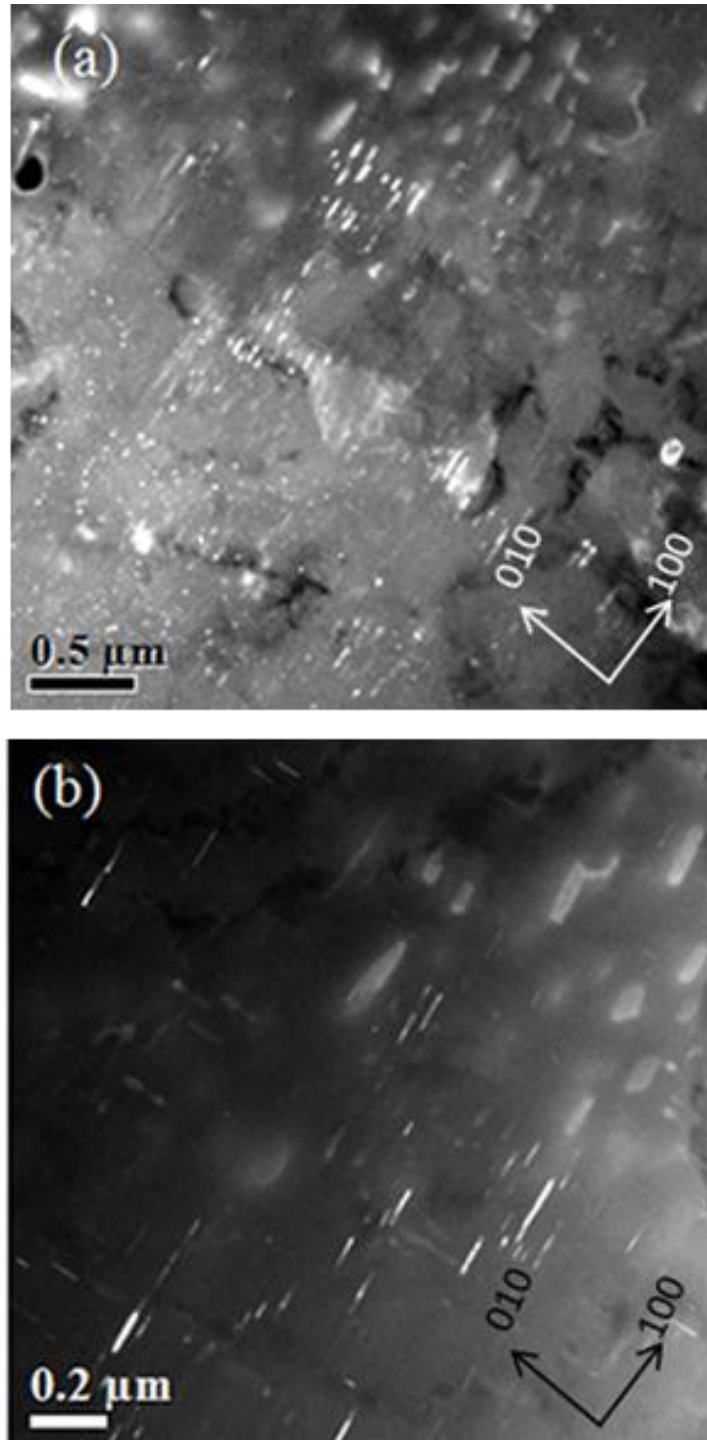


Figure 6.9: Dark field TEM images of CR material heated to 275 °C (end reaction temperature) with 20 °C/min heating rate. Co-existence of very fine and coarse precipitates corresponding to β'' and β' precipitates at (a) lower magnification and (b) higher magnification

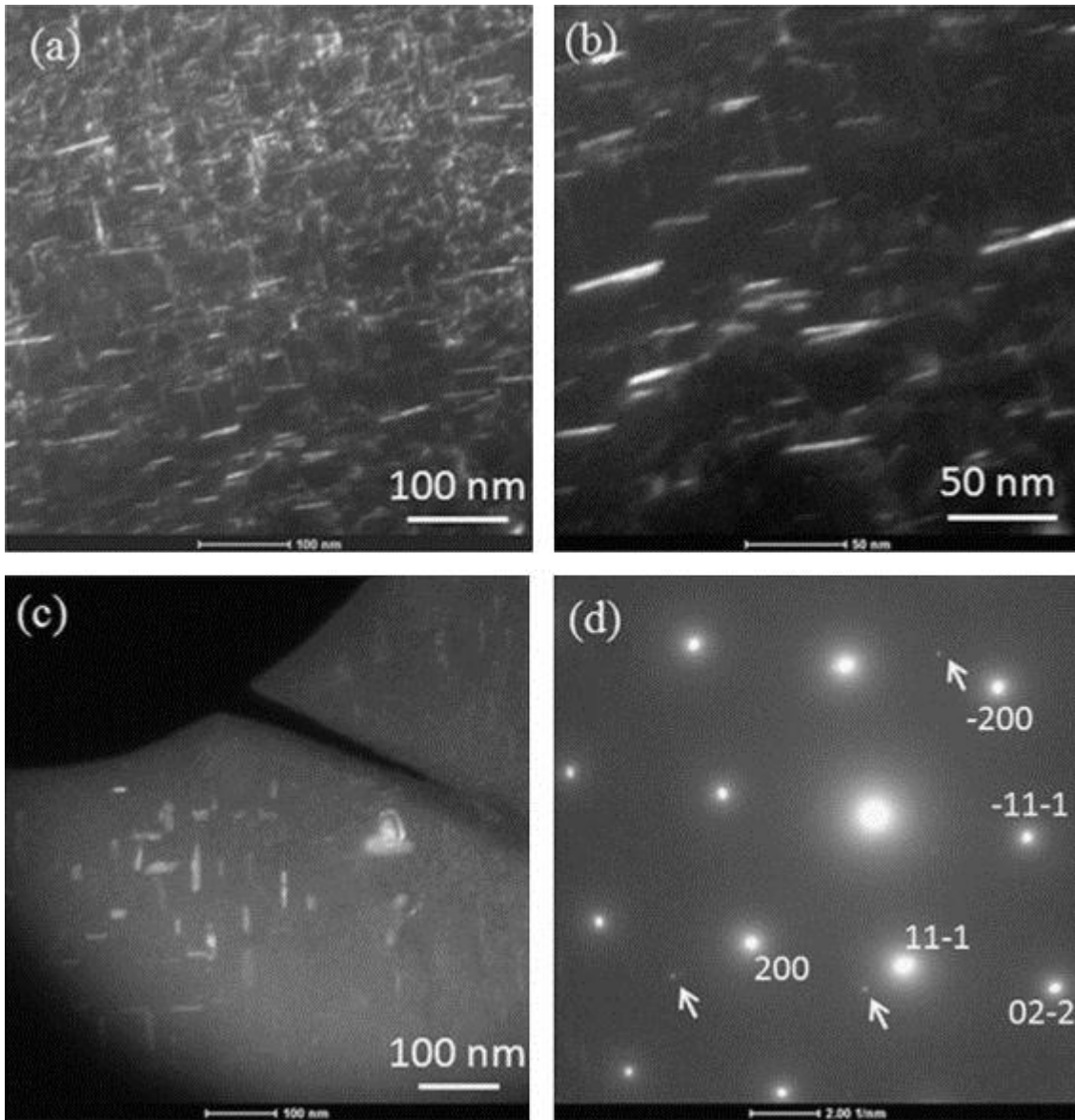


Figure 6.10: Dark field TEM micrographs of WR material heated to 236 °C (half reaction temperature) with 20 °C/min heating rate: (a) needle shaped β'' precipitates at lower magnification, (b) magnified view of figure (a), (c) existence rod shaped β' precipitates in the same sample and (d) (B=[011]Al) SAED micrograph for Figure 6.10 (a).

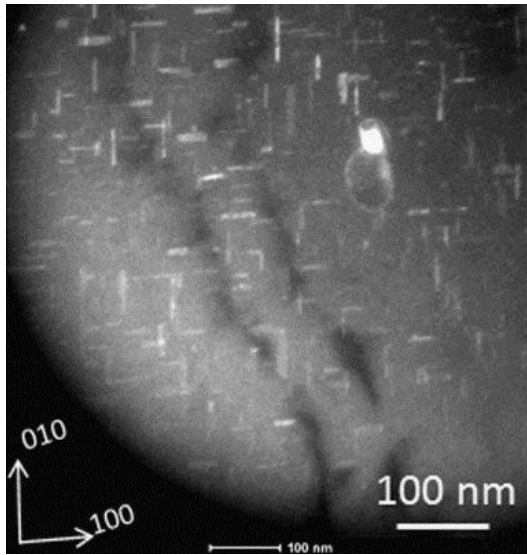


Figure 6.11: Dark field TEM micrographs of WR material heated to 295 °C (end reaction temperature) with 20 °C/min heating rate, showing fine β' -rod shaped precipitates.

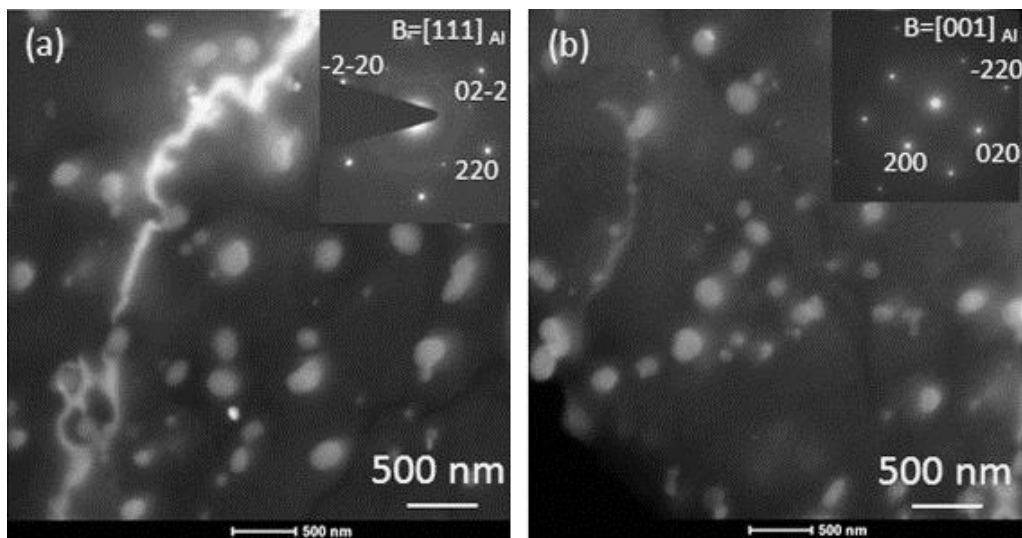


Figure 6. 12: Dark filed TEM micrograph along with SAED patterns of CR and WR material heated to 365 °C with 20 °C/min heating rate: (a) CR and (b) WR.

TEM micrographs of WR material aged up to temperatures of the exothermic peak (peak B'') 237 °C in WR DSC thermo-gram is shown in *Figure 6.10*. The primary difference observed in TEM micrographs of WR material at peak temperature with respect to CR material heated up to at peak temperature is the size and distribution of the precipitates. Very fine scale precipitates in the range of 1-2.5 nm diameter with number density is observed in WR material. Along with β'' , β' precipitates were also observed with an average diameter of 10 nm, which are much finer than the β' precipitates observed in CR material. After completion of the reaction (at 295 °C), most of the β'' precipitates were transformed to β' (*Figure 6.11*). The microstructural evidence (*Figure 6.10(a)–(c)*) of coexistence of β'' and β' strengthens the fact of higher activation energy associated with the peaks B' and B'' in CR and WR material, respectively. *Figure 6.12* shows platelets of equilibrium β phase (Mg_2Si precipitate) observed in the CR and WR samples heated to 365 °C. The strengthening contribution from this precipitate is very little.

6.1.4 Conclusions

The effect of deformation through CR and WR on the precipitate evolution and its kinetics in Al 6061 alloys has been investigated through DSC, hardness measurements and TEM. The conclusions are made as follows:

- 1) The significant changes have occurred in DSC thermo-grams of CR and WR samples. The formation of two distinct exothermic peaks at low temperatures corresponding to formation of nanoclusters was observed in CR alloy. The major exothermic reaction peaks have shifted to lower temperature side in CR (heating rate 20 °C/min, peak B'-238 °C) and WR material (heating rate 20 °C/min, peak B''-236 °C) compared to ST material (heating rate 20 °C/min, peak B-249 °C).
- 2) Cryorolling has resulted, accelerated formation of cluster (1) and retardation of cluster (2) formation as observed from DSC results in the present work.
- 3) The activation energies associated with major exothermic peaks in CR (peak B'-136 kJ mol⁻¹) and WR (peak B''-132 kJ mol⁻¹) were considerably higher than the energy associated with the peak B in ST material (114 kJ mol⁻¹).
- 4) Micro-structural investigation through TEM reveals the coexistence of β'' and β' at the half reaction temperature (peaks B' and B'') in CR and WR materials.

- 5) The unusual behavior of increase in activation energy of material after CR and WR could be due to the existence of large volume fraction of subgrain boundaries along with high dislocation tangled zones, which could have caused retardation of precipitate formation.
- 6) In CR material, the precipitate features are coarser than WR material.

6.2 Effect of deformation strain on precipitation behavior of Al 6061 alloy

6.2.1 Introduction

As evident from the previous section of this chapter, the precipitation phenomenon in UFG Al-Mg-Si alloys is not same as compared to coarse grained counterpart. CR strain has brought significant changes in early stage and medium stage precipitation of the Al 6061 alloy. It is well reported that the strengthening contribution from major strengthening phase depends on its precursors (clusters), which forms during early stages even at room temperature [142]. It is very essential to understand the early stage precipitation behavior in cryorolled Al-Mg-Si alloys to exploit its maximum contribution of strengthening during service conditions. However, the precipitation process in Al-Mg-Si alloys is very complex. Dutta and Allen [210] have employed Differential scanning calorimetry (DSC), Transmission electron microscopy (TEM) techniques to study the precipitation sequence in undeformed Al-Mg-Si alloy [210]. Investigation of early stage precipitation at low temperatures is difficult through TEM due to limitation in resolution and experimental constraints arising from structural changes taking place at very fast rate even at room temperatures within a few minutes [250]. Later Edwards et al., [138], have used atom probe field ion microscopy (APFIM) along with DSC and TEM to resolve the early stage precipitation and their proposed sequence is “*SSSS*→ *independent clusters of Mg and Si atoms*→*co-clusters that contain Mg and Si atoms* → *small precipitates of unknown structure*→*β*” *needle-shaped precipitates* → *B' lath-shaped precipitates and β' rod-shaped precipitates* → *β (Mg₂Si)*”. However, the problem associated with APT is sample preparation, as it consumes several hours and within that time structural changes could occur. Most of the APT studies were performed on structurally stabilized samples. The techniques such as low temperature differential scanning calorimetry and resistivity measurements could be used to study the early stage precipitation in Al alloys immediately after quenching process [256]. Positron absorption life time technique is used recently to study the early stage precipitation.

There are no reported studies on evolution of clusters in the Al 6061 alloys during cryogenic deformation. Therefore an attempt is made in this section, to understand the cluster evolution and its influence on the major strengthening phase with increasing strain at cryogenic deformation. Also, the effect of strain on activation energies of major strengthening phase has been calculated through Kissinger analysis. Also, the natural ageing behavior of deformed and

undeformed material has been characterized by using low temperature differential scanning calorimeter (DSC).

.6.2.2 Experimental details

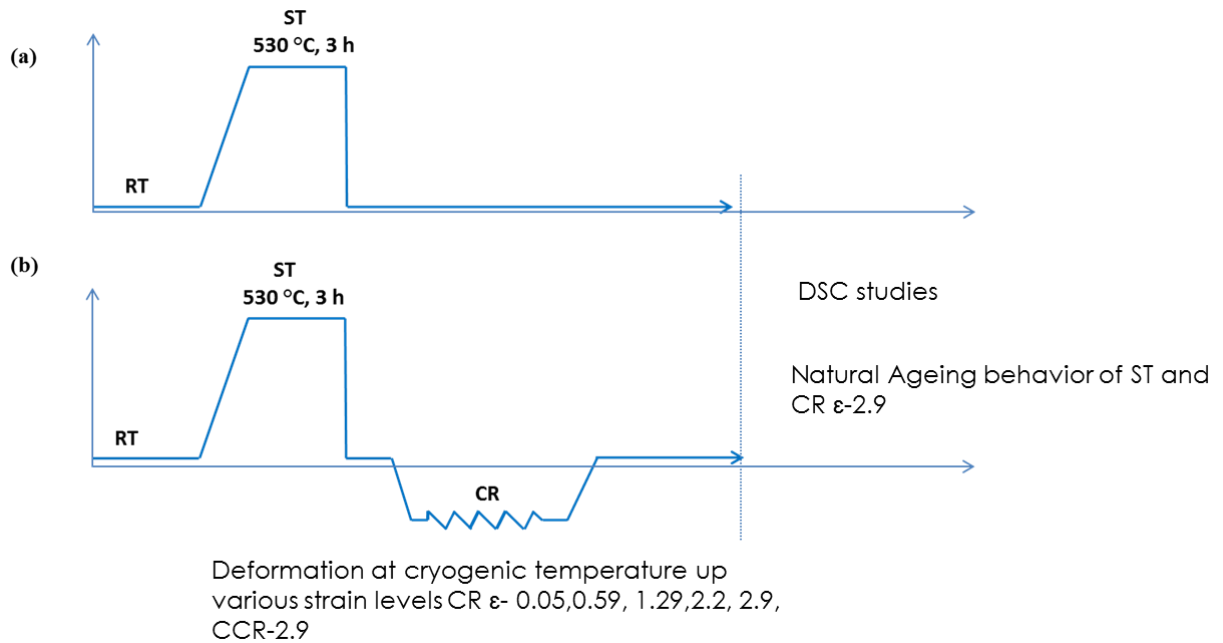


Figure 6.13: Process flow chart of various conditions in the present work.

Al 6061 alloy with different thickness reductions were machined to achieve different strain levels. They were solid solution treated at 530 °C for 3 hours in a muffle furnace, subsequently iced water quenched. After quenching, samples were immediately cryorolled up to required thickness reductions. In all conditions, the final thickness of the sheet is 0.7 mm, which is punched to produce samples for DSC measurements. The cryorolled samples were kept at liquid nitrogen temperature, until DSC measurements were done. The samples with ST condition and cryorolled to maximum strain respectively were kept at room temperature for different ageing times to study the natural ageing effect. Adequate care is taken to obtain samples with desired testing conditions. Perkin Elmer's low temperature differential scanning calorimetry was used for DSC measurements. The starting temperature of the test scan is -10 °C. Before testing, the samples were loaded into the DSC and allowed for 2 to 3 minutes to achieve thermal

equilibrium. Heating rate with 15 °C/min was used for all the experiments. Pure Al with same weight as samples weight was used as reference during measurements. The base line correction was performed by subtracting the heat flow curve of sample with that of reference. *Figure 6.13* shows the process flow diagram of various conditions used in the present investigation. In the present study, the samples are punched before solid solution treatment to avoid the influence of deformation on the sample. In case of deformed samples, after deformation up to required strain, it was punched and immediately tested.

6.2.3 Results

Figure 6.14 shows the typical DSC curve of supersaturated solid solutionized (SSSS) Al 6061 alloy obtained with a heating rate 15 °C/min. The SSSS is obtained by ST at 530 °C for 3 hours followed by iced water quenching. There are four individual exothermic reaction peaks, those are believed to be corresponding to nanoclusters (C1/C2), β'' , β' , β (Mg_2Si), which are in similar to the alloy quenched to water at room temperature as reported in the previous section. At high temperatures (> 150 °C), the precipitation evolution and sequence of the SSSS material is well studied by many researchers [138] [210]. At low temperature, the evolution of precipitates is yet to be established.

6.2.3.1 Effect of strain

6.2.3.1.1 Cluster peaks evolution

Figure 6.15, 6.16 and 6.17 shows the effect of strain on the evolution of DSC peaks corresponding to precipitation process obtained with heating rate of 15 °C/min. *Figure 6.15* shows peaks obtained at low temperature (< 150 °C) corresponding to the clusters. To induce lowest strain, the samples are punched from the sheet after ST and it has been considered as 5% deformation [212]. Maximum up to true strain of 2.9 is given by unidirectional rolling and cross rolling. At low temperatures (*Figure 6.15*), it is interesting to note that in the lowest strained (0.05) sample, the cluster peak has disappeared. The similar behavior has been reported in Al-Mg-Si alloys by Yucler Birol [212] [257]. By punching the sample after solution treatment and before DSC analysis in Al 6061 alloy, the cluster peak has been suppressed. On the contrary, intensity of the cluster peak has been reduced [212] in Al 6082 alloys.

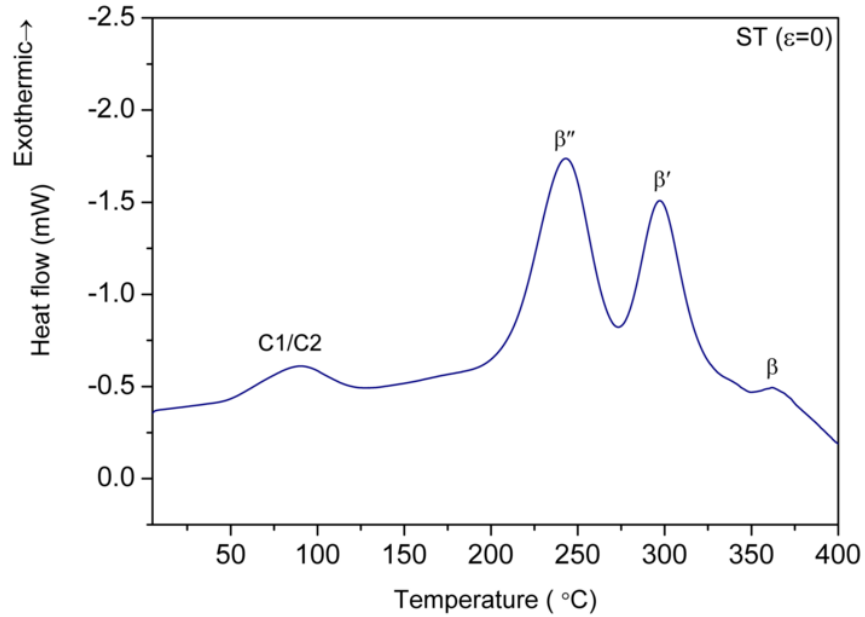


Figure: 6.14: DSC heat flow curve of the Al 6061 alloy after ST for 3 hour followed by iced water quenching.

With increasing strain to 0.59, two distinguished cluster peaks were observed, besides that, the first and second cluster peaks have moved slightly to lower and high temperature side, respectively, with respect to the cluster peak temperature of undeformed sample (ST, $\epsilon=0$). With increasing strain from 0.59 to 2.9 through unidirectional rolling process, there is no substantial change in the number and position of the cluster peaks. Even in cross rolled sample with strain 2.9, the DSC behavior is similar to the unidirectional rolled sample with same strain.

Effect of chemical composition of cluster peaks

Figure 6.16 shows the effect of chemical composition on clustering behavior observed through DSC measurements. Materials with varying Mg and Si content (Al 6061, 6063, and 6351 alloys) samples were subjected to same percentage of reduction under cryogenic temperature. The nature of the DSC curves remains same. The intensity of the cluster 2 peak is reducing with decreasing Mg content. This indicates that intensity of the cluster formation is strongly dependent on % of Mg and Si.

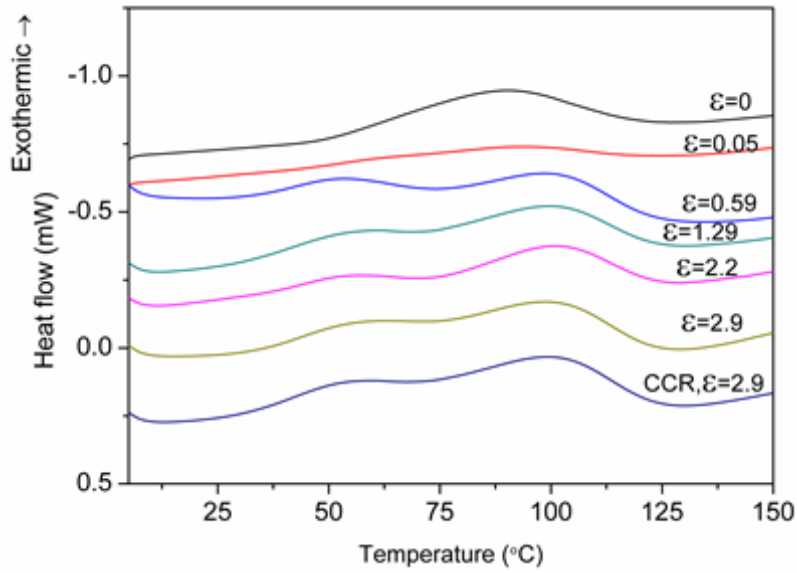


Figure 6.15: DSC heat flow curves in the range 10°C – 150 °C of CR material with different strain.

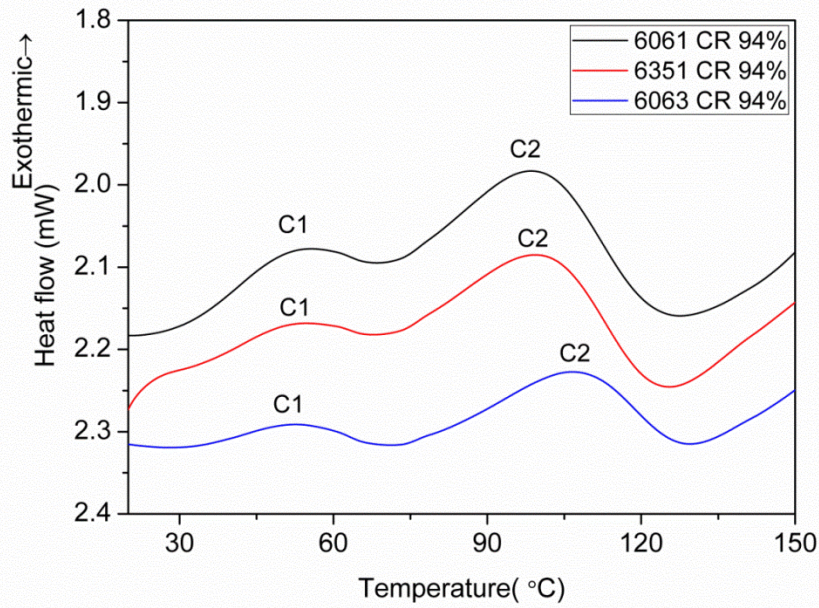


Figure 6.16: Effect of chemical composition on cluster peak formation in Al alloy deformed at cryogenic temperature up to true strain of 2.9.

6.2.3.1.2 β''/β' phase formation

At high temperature ($> 150\text{ }^{\circ}\text{C}$), peaks corresponding to β'' and β' phase (*Figure 6.17*) were altered with deformation. At lowest strained sample, the intensity of the β' phase peak has been reduced, but the position of the peaks is same as undeformed sample. Whereas in the sample with strain ε - 0.59, the β' phase peak has completely disappeared. The initiation temperature of precipitation reaction and peak temperatures of the β'' have shifted to lower temperature side. The heat associated with reaction peak has been reduced which indicates the reduction of precipitates formed [240]. With increasing strain from 0.59 to 2.9 through unidirectional rolling, the behavior is same but the sample cross rolled up to 2.9 strain, the position of the β'' peak has moved towards high temperature. Suppression of β' phase with deformation has been observed by several authors [12] [212] [240] [257] [258] [259].

To understand the effect of deformation on thermal behavior of precipitation hardenable Al 6061 alloy, material with T6 and overaged conditions are cryorolled and compared with cryorolled pure aluminum (*Figure 6.18 and 6.19*). In ST material (*Figure 6.18(a)*), suppression of second major exothermic peak and the shifting of first major exothermic peak towards low temperature side are observed. In T6 condition sample (*Figure 6.18(b)*), endothermic peak at $250\text{ }^{\circ}\text{C}$ corresponding to dissolution of β'' phase and exothermic peak at $300\text{ }^{\circ}\text{C}$ corresponding to formation of β' phase are observed. After CR, β'' dissolution peak has disappeared and β' formation peak has shifted to low temperature side. The intensity of the exothermic peak has been reduced by peak broadening. In T6+CR material at temperature around $300\text{ }^{\circ}\text{C}$, a small hump is observed followed by low intensity sharp peak at $350\text{ }^{\circ}\text{C}$. These two peaks are commonly observed in deformed materials and it is believed that they are corresponding to recovery and recrystallization process. In T6+CR samples, disappearance of endothermic peak (dissolution of β'' phase) indicates the possibility of direct transformation of β'' to β' by deformation induced dislocations. *Figure 6.19 (a)* shows DSC heat flow curves of overaged (OA) condition of Al 6061 alloy and its deformed condition at cryogenic temperature. This condition has been chosen because the peaks corresponding to recovery and recrystallization process in deformed material are not influenced by precipitation and its dissolution processes.

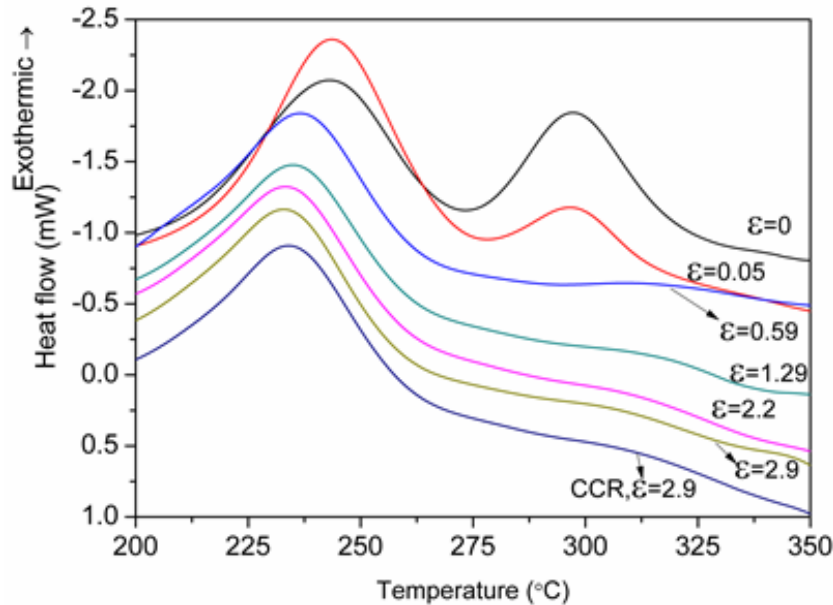


Figure 6.17: DSC heat flow curves in the range 200 °C – 350 °C of CR material with different strain.

OA material shows almost flat curves with no observable peaks. Its deformed condition has shown two clear exothermic peaks. This confirms that the two peaks are due to recovery and recrystallization. The recovery process takes place in wide range of temperatures (from 205 °C to 345 °C) but the recrystallization process occurs in narrow range of temperatures. *Figure 6.19(b)* shows DSC heat flow curve of pure Al cryorolled up to 90% reduction. Peak corresponding to recovery is not significant but the recrystallization peak is clearly seen.

6.2.3.2 Natural ageing behavior of ST and CR material

Figure 6.20 and 6.21 shows the natural ageing behaviour of ST material. For the natural ageing (NA) up to 20 minutes, with increasing natural ageing time, the position of the cluster peak is shifting towards high temperature side along with increasing heat associated with the exothermic reaction (*Figure 6.20*). For ensuring reproducibility, the measurements have been repeated thrice, which requires further validation by electron microscopic investigation. With increasing NA time, intensity of β' has been decreased. *Figure 6.21* shows the DSC flow curves corresponding to NA from 30 min to 5 days. After 5 days of NA, the cluster peak (*Figure 6.21(a)*) has been almost flattened. The respective dissolution peak (endothermic) prior to the β'' phase peak is increasing. After 5 days, the endothermic peak has become deep and widened. The

intensity of β' peak has been reduced but β'' phase peak is not affected much. In CR material (Figure 6.22), the natural ageing behavior is obvious, because of distinct cluster peak formation. At the beginning, cluster 1 has started forming and continued up to 20 minutes (Figure 6.22(a)).

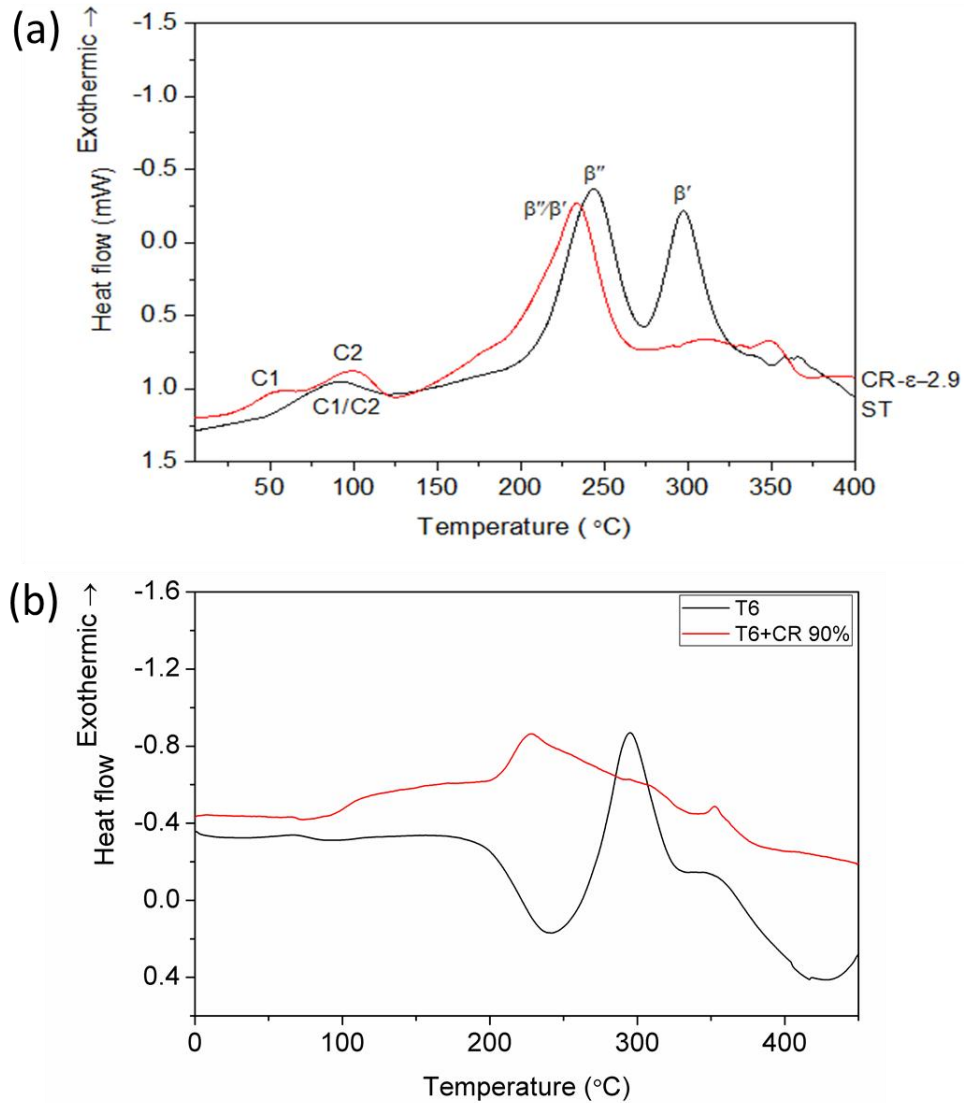


Figure 6.18: Effect of cryorolling on thermal behavior of Al 6061 alloy; a) ST, b) T6.

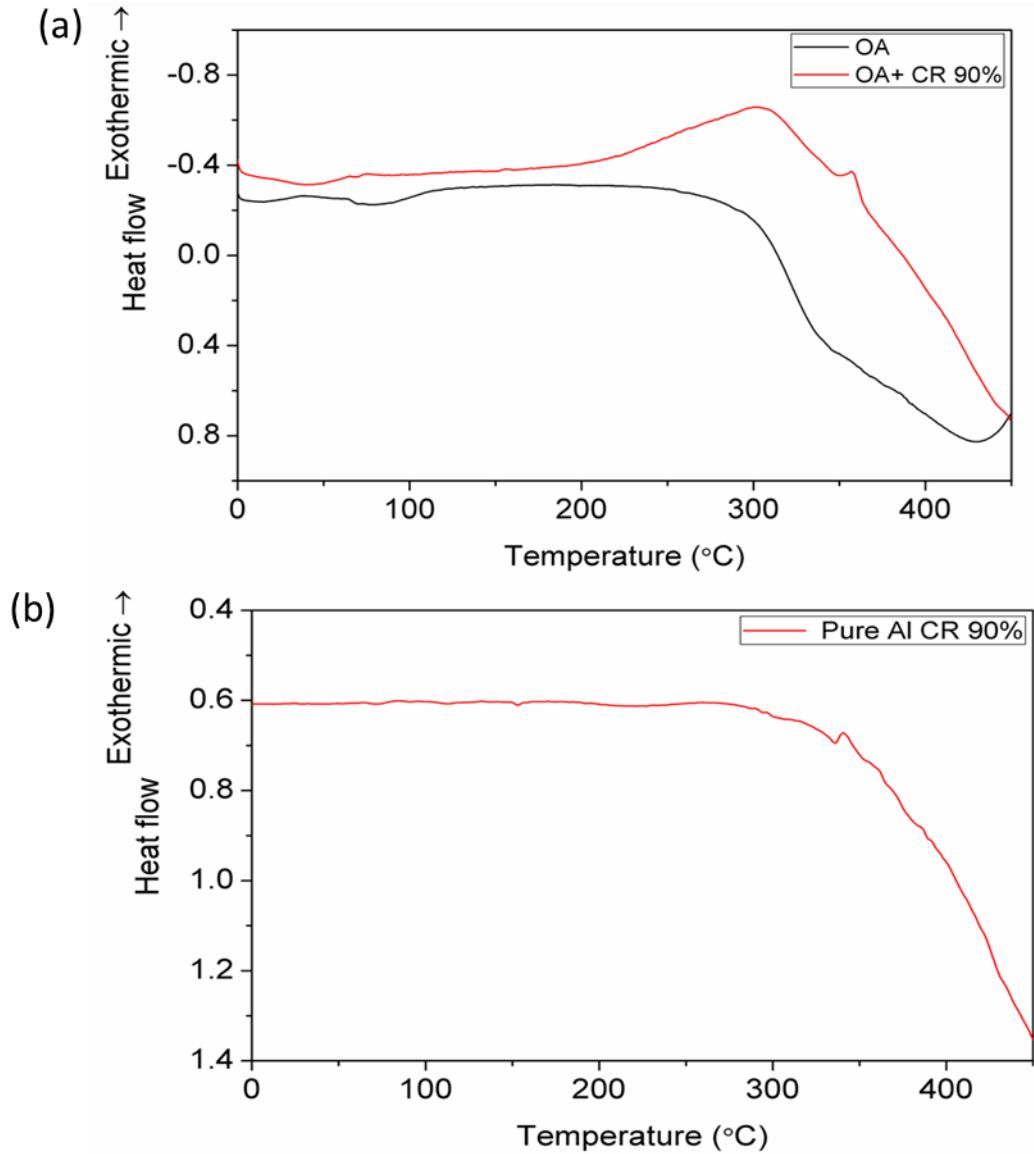


Figure 6.19: Effect of cryorolling on thermal behavior of Al 6061 alloy; a) OA, b) Pure Aluminum.

The behavior of the cluster 2 peak indicates that, up to 20 min, (i.e., until the formation of cluster 1) it has not been affected. The intensity of the cluster peak 2 has been reduced after 20 minutes and continued up to 24 hours (*Figure 6.22(b)*). Sample with NA of 5 days shows complete formation of clusters in CR material. The corresponding cluster dissolution peak (endothermic reaction) prior to the β''/β' peak is very shallow and narrow as compared to the dissolution peak observed in ST material. With increasing cluster 2 formations, the change in endothermic peak is not much. It indicates clearly that the dissolution peak is attributed to

clusters 1 in CR material. *Figure 6.23* shows NA behavior of ST and CR material for longer duration (19 days). The position of the major strengthening phase peaks remains same, but the endothermic peak in ST material is several times large than that observed in CR material. The behavior of cluster peaks and β' peaks indicates that the former has more influence on β' than β'' .

Figure 6.24 shows precipitation behavior of CR material while keeping at $-20\text{ }^{\circ}\text{C}$ for longer hours. For the samples produced by cryorolling, after solid solution treatment and cryorolling process, samples are stored below the quenching temperature to suppress the precipitation process, and they are preserved until required ageing treatment is given. There is no significant change in the cluster peak formation for the sample kept up to 10 hours, whereas in the sample stored up to 19 days, cluster peak 1 has completely formed and the respective dissolution peak (narrow) is observed.

6.2.3.3 Effect of strain on activation energy

Reaction peak temperatures of the ST and CR up to different strains obtained at different scan rates such as 10, 15, 20, 25 $^{\circ}\text{C}/\text{min}$ were used to calculate the activation energy for β''/β' formation. Kissinger analysis is employed to estimate the activation energies. The activation energy corresponding to β'' formation in ST material is 78 kJ/mol. Upon cryorolling up to 5%, it has dropped to 57 kJ/mol. With increasing percentage of deformation from 5% to 65% the value has raised to 134 kJ/mol which has not changed much with further increase in % of deformation.

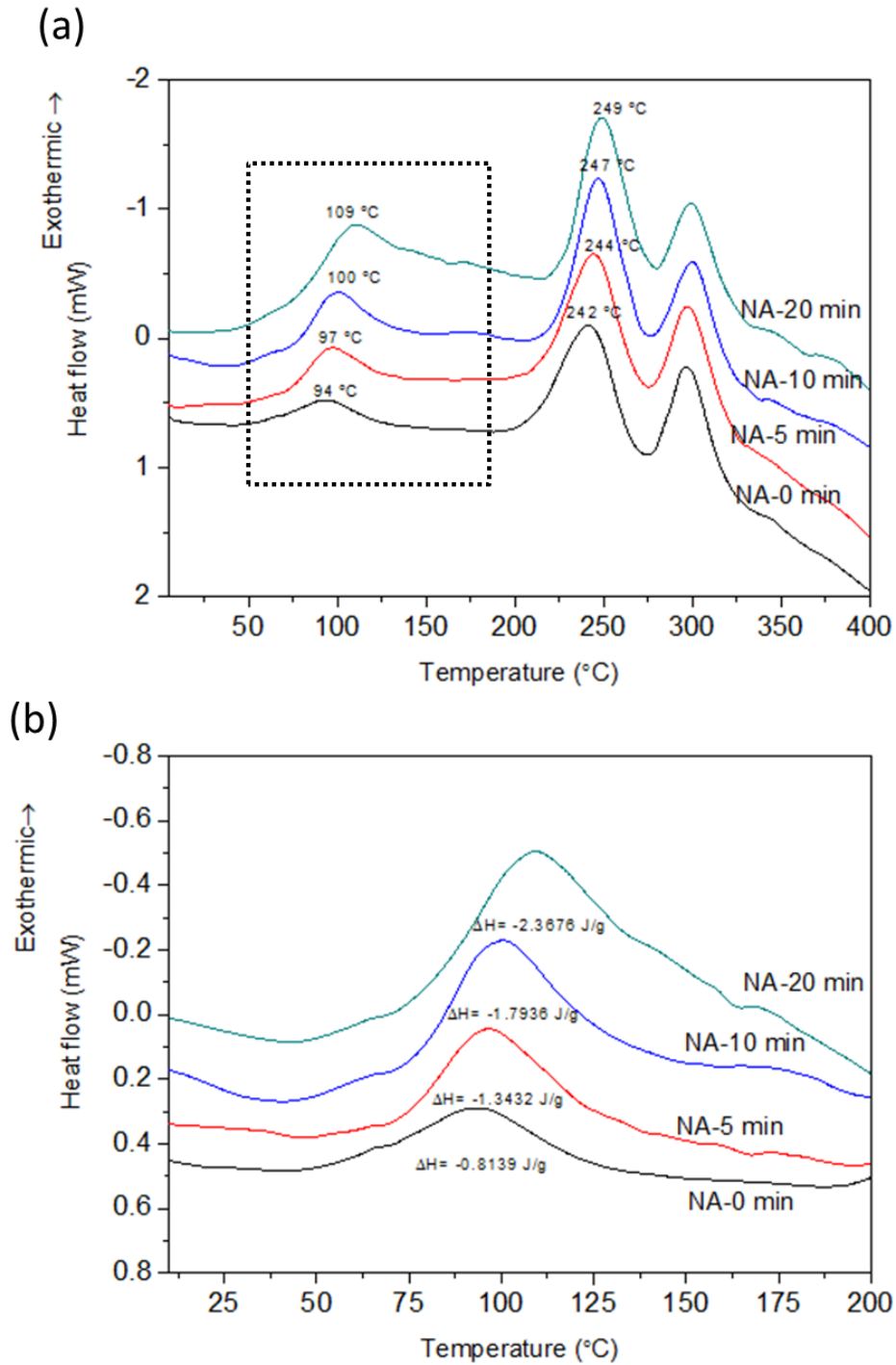


Figure 6.20: Natural ageing (NA) behavior of ST material; a) NA time up to 20 min, b) magnified view of cluster peaks in Figure (a).

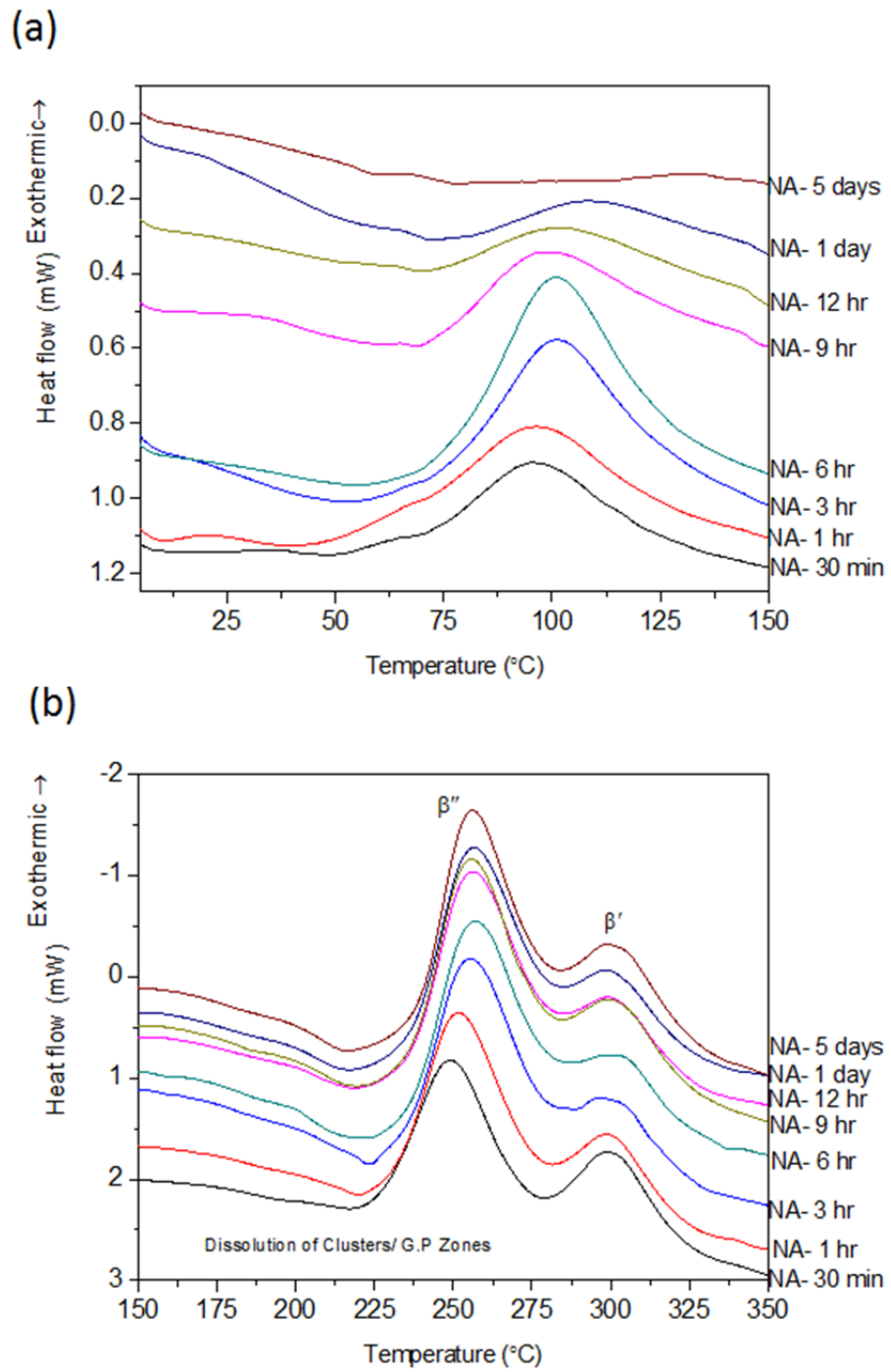


Figure 6.21: Natural ageing (NA) behavior of ST material for longer hours

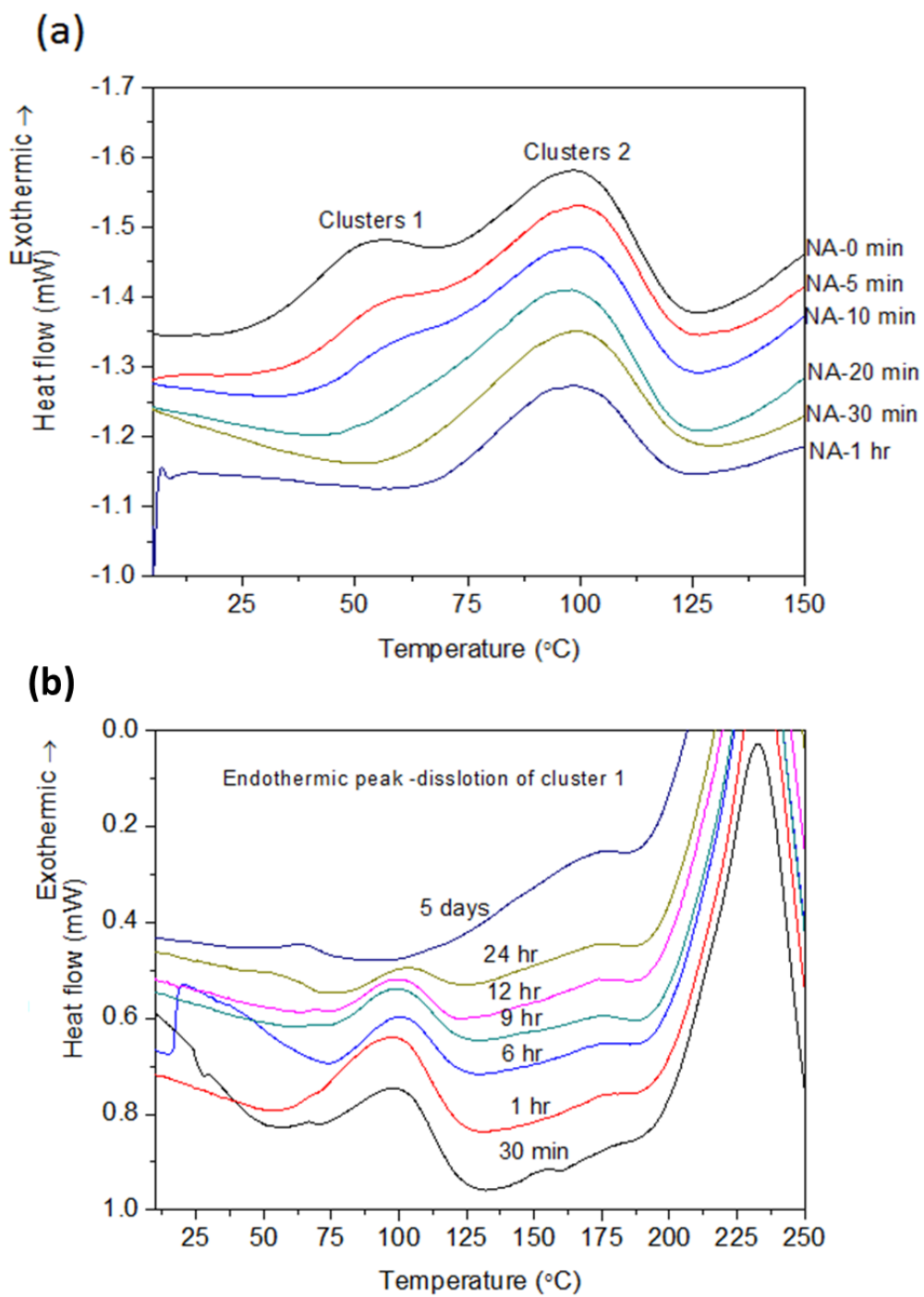


Figure 6. 22: Natural ageing (NA) behavior of CR material; a) NA time up to 1 hour, b) Natural ageing (NA) behavior of CR material for longer hours

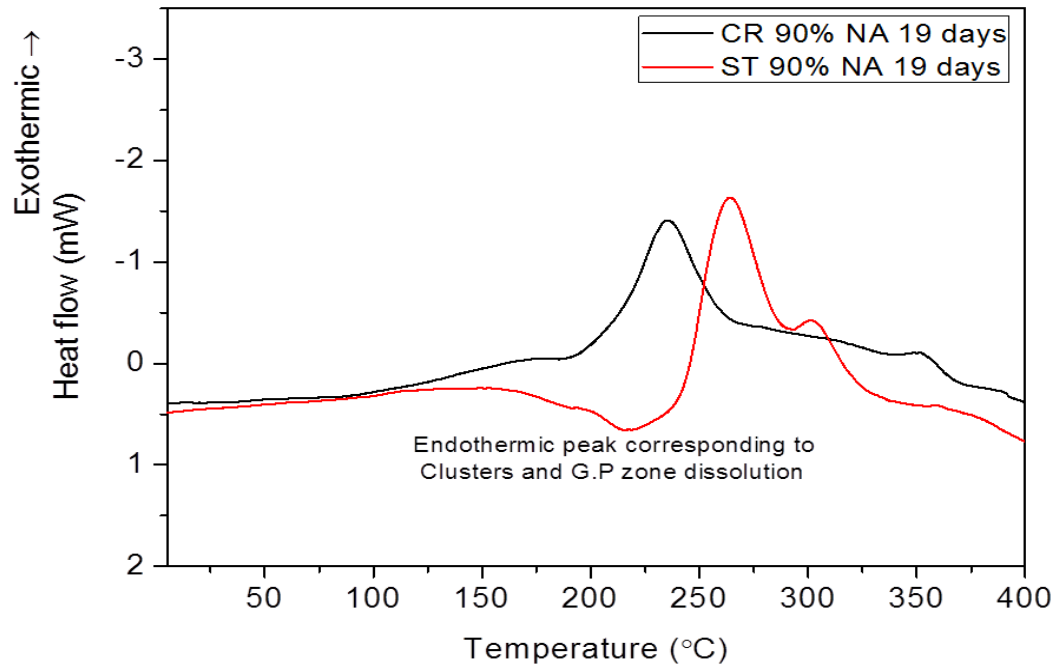


Figure 6.23: NA behavior of ST and CR material for 19 days.

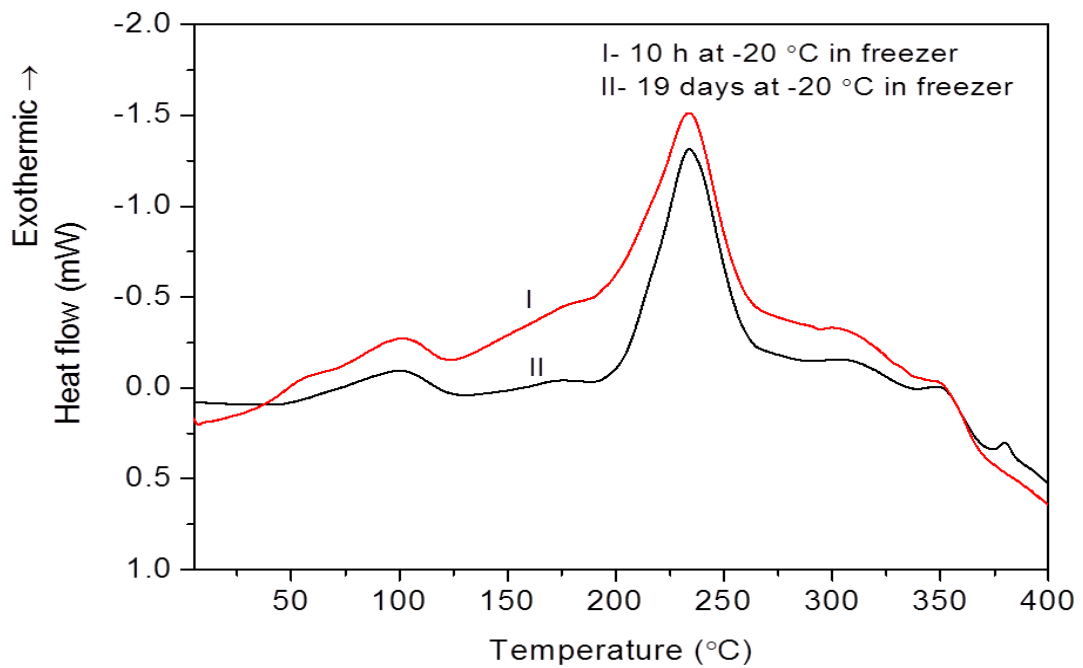


Figure 6.24: Ageing behavior of CR material at -20 °C

6.2.4 Discussions

6.2.4.1 Cluster formation and Natural ageing behavior

In industrial practice after solid solution treatment, Al-Mg-Si alloys are artificially aged at around 160-180 °C to strengthen the matrix. Due to unavoidable delay before subjecting to artificial ageing, solid solution treated material undergo natural ageing. It was observed that natural ageing has negative effect on further strengthening of the matrix by artificial ageing [260]. This problem has been addressed by several researchers [261] [262] [263]. Esmaeili et al., have observed that natural ageing prior to artificial ageing has decreased the rate of precipitation and it results in slow hardening rate in the naturally aged alloys [263] [262]. The reason for negative strengthening response of naturally aged alloy is due to the formation of clusters of Mg and Si that forms at room temperature. It reduces the amount of solute that is available for formation of β'' phase during artificial ageing. It is essential to understand the type and natures of clusters that form at room temperature and its role on β'' phase formation. Serizawa et al., [142] have reported two peaks at low temperature corresponding to nano clusters, i.e., Cluster (1) and Cluster (2) in Al-Mg-Si alloy with 0.95 mass pct of Mg and 0.81 mass pct of Si [142] . This has been confirmed through 3D Atom probe tomography. It is also reported that cluster (1) has led to decreased number density of the β'' phase, whereas Cluster (2) enhanced the formation of β'' phase. Later Chang et al., [250] have studied the natural ageing behavior of 0.59 wt. pct Mg and 0.82 wt pct Si containing Al alloys by employing low temperature differential scanning calorimetry. They have reported three cluster reactions at low temperature viz., Cluster 0, Cluster 1 and Cluster 2. However, there is no further evidence for the existence of Cluster 0. It is possible that Cluster 0 peak observed earlier [250] could be due to noise in the data.

In the present investigation, Al 6061 alloy with 1.01 wt pct Mg and 0.67 Pct Si has shown single peak at low temperatures. The chemical composition of the alloy used earlier [142] is nearly same to the alloy used in the present condition. It is possible that peaks corresponding to cluster (1) and cluster (2) in the ST sample have overlapped. The presence of two individual peaks in deformed samples strengthens the assumption as to overlapping of peaks in ST sample. According to the precipitation sequence proposed by Edwards at al., [138] at low temperatures, after the formation of individual clusters of Si and Mg in the Al – 0.8 wt pct Mg- 0.79 wt pct Si alloy, Mg clusters got dissolved, which was followed by formation of co clusters of Mg and Si.

However, there is no proof through DSC data for the dissolution of Mg clusters. It is assumed that, simultaneous formation of Cluster 1 and Cluster 2 occurs in ST material.

As shown in *Figure 6.20*, with increasing natural ageing time up to 20 min, the peak area is increased and the peak temperatures are shifted to high temperature side. After 20 minutes of NA, the peak area is decreased and the change in peak temperature is not significant with respect to NA time. Decreasing peak area with NA time is expected. This has also been reported by Chang et al., [250]. Cluster 2 peak formation has completed within 5 days of NA. However, in the alloy with 0.59 wt. pct. Mg and 0.82 wt. pct. Si, cluster (2) peak has been extended up to two weeks [250]. This indicates the percentage of Mg and Si influences the rate of precipitation. If the area of the peaks is correlated with the volume fraction of precipitates by increasing NA time, after 20 min, the area of cluster formation peak has decreased and the respective dissolution peak area has increased. The interesting observation is that NA has more effect on the β' phase formation than β'' phase. With increasing NA time, the area of the peak corresponding to β' phase has reduced without affecting β'' . It is a positive phenomenon, since the major contribution to strengthening comes from β'' phase, which is metastable and coherent with the Al matrix.

NA behavior in CR material shows cluster (1) & (2) peaks have disappeared after 20 minutes and after 5 days, respectively. Cryorolled material has shown similar behavior to ST material. By cryorolling up to true strains of 2.9, the rate of precipitation during NA has not been affected much. Cryorolling has reduced the intensity of dissolution peak corresponding to clusters. After immediate quenching to room temperature, material possesses excess vacancies, which results in fast ageing process [264] leading to rapid formation of clusters. The broad endothermic peak indicates that the clusters formed at room temperature in ST material are not stable. Whereas, in cryorolled material, the low intensity endothermic peak is due to cluster (1). Stable endothermic peak reveals the formation of cluster (2) at room temperature, which is stable and further grown in to β'' phase. The intensity of β''/β' phase peak has not been affected with NA like β'' phase peak in ST material. The effect of NA on the hardness behavior of ST and CR materials is shown in *Figure 16*. The slopes of hardness curve of both materials are nearly same. The time taken to complete cluster formation and hardness behavior in CR and ST material illustrates the effect of NA on cluster formation in CR and ST material is nearly same.

6.2.4.2 Activation energy

Reports on comparative studies of ageing behavior in Al 6061 alloy and its metal matrix composites (MMC) have shown accelerated ageing behavior in MMC [240] [255] [265] [266]. It was suggested that, due to thermal mismatch between the reinforcements and the aluminum matrix, dislocation density of the material has increased. Therefore, the diffusivity of the precipitation-forming species has increased due to pipe diffusion. It is also reported that the high dislocation densities provides heterogeneous nucleation sites for the precipitate. The similar behavior has been observed by Christman et al., in cold rolled Aluminum alloy [267]. Lee et al., have observed the effect of degree of rolling on the precipitation behavior of Al 6061 alloy. They have reported that cold rolling has influenced the sequence of precipitation and it has reduced the amount of precipitation [240]. It is evident, based on the several studies that that deformation has caused shifting of reaction initiation and peak temperatures towards lower temperatures as compared to unreformed samples [12] [212] [257] [258] [268]. The shifting of peaks to low temperatures side could enhance the precipitation reaction rates but the activation energies of deformed samples have shown that it does not affect much on the rate of reaction [240] [269].

Lee et al., [240], have reported that with cold rolling facilitates faster precipitation transformation as compared to undeformed material. However, with increasing degree of cold rolling, the precipitation rate has not been changed. With increasing deformation, tangled dislocation density and thickness of dislocation cell walls, would not assist for diffusivity of the precipitation forming species as reported in their work [240]. Quainoo et al., have reported that with increasing level of cold work of AA 6111, decrease in the activation energy of β'' formation has reduced due to high energy states induced in the material as a result of cold working [270]. However, the maximum percentage of deformation examined was 5% in their work. This is in agreement with the activation energy values obtained after 5% deformation in the present work as compared to its bulk. On the other hand, with increasing cryorolling to true strain of 0.59, higher activation energy values are obtained. With further increasing cryorolling to higher strains (2.9), the value has not changed much. Rolling at cryogenic temperatures enhances the dislocation accumulation by suppressing dynamic recovery. TEM microstructures of cryorolled Al 6061 alloy shows the presence of high dislocation tangled zones and subgrain boundaries with increased thickness. Obtained activation energy values and microstructural observations strengthen the opinion that with increasing degree of deformation, the diffusivity of solute species would get decelerated and therefore reaction rates become sluggish. It also strengthens

the statement that solute atoms are trapped by tangled dislocations. Cold rolling to a 5% deformation before pre-aging is an effective process to improve the BH response of Al–0.95 mass% Mg–0.81mass% Si alloys. Thus, CR-PA-NA process is in effective process scheme to increase strength of the alloy on a limited BH treatment period.

6.2.4.3 Effect of quenching temperature

Quenched- in vacancies are created by rapid quenching from solution treatment temperature of the alloy. Their amount depends on the rate and temperature of quenching. Quenched- in vacancies play a major role in the formation kinetics of precipitation of hardening phases in Al-Mg-Si alloys by promoting the diffusion of solute elements [271] [272] In the present investigation, material quenched at room temperature has shown slightly higher activation energy values than that of samples quenched at iced water. The obtained activation energy for β'' phase in room temperature quenched Al 6061 alloy is 114 kJ/mol. It is higher than the value (78 kJ/mol) obtained for the alloy quenched in iced water. The difference in activation energy values of the strengthening phase after cryorolling in both different quenched alloys is reduced.

6.2.5 Conclusions

The following conclusions are made based on the precipitation kinetics studies of Al 6061 alloys subjected to cryorolling.

- 1) Deformation resulted in clear separation of cluster peaks at low temperatures in CR samples.
- 2) Deformation up to 5% suppresses the formation of nanoclusters along with reducing the intensity of β' phase.
- 3) The higher activation energy values of β''/β' phases in CR material with deformation beyond 5% indicates, less availability of thermal vacancies available to promote diffusion in severely deformed materials.

- 4) Natural ageing behavior of ST and deformed material has shown that the complete cluster formation is taking place within two days of ageing.
- 5) The activation energy associated with various phases in ST and deformed materials with various strains are calculated. With increasing strain up to 5%, the activation energy is dropping (from 78 to 57 kJ/mol) beyond that, it is increasing and remains stable. This indicates that beyond 5% deformation, with increasing strain, there is no significant change in the precipitation behaviour.

This chapter describes the following experimental investigations performed on Al 6061 alloy such as

- i) Effect of cryoforging followed by low temperature ageing on microstructure and mechanical properties of Al 6061 alloy.
- ii) Evolution of microstructural homogeneity in cryoforged Al 6061 alloy.

The mechanical properties of ultrafine grained Al 6061 alloy are explained using the microstructural features and the phases are characterized by using Optical microscopy, FE-SEM/EBSD, TEM, and DSC techniques.

7.1 Effect of Cryoforging Followed by Low temperature Ageing on Microstructure and Mechanical Properties of Al 6061 alloy

7.1.1 Introduction

Cryorolling has been successfully used to develop UFG structure in metals and alloys with wide range of stacking fault energy. However it possesses some disadvantages also. The materials with high stacking fault energies such as Al and its alloys exhibit ultrafine grains with predominantly low angle grain boundaries, due to lower induced strains (~ 2.6) after cryorolling [110]. Since the material shape gets changed during rolling unlike other SPD techniques, it is difficult to induce high strain to the deformed material. Other SPD techniques such as ECAP, ARB, and HPT have been successfully operated at room temperature and above room temperatures to achieve UFG structures in Al metal and alloys. The mechanism of grain refinement has been well understood. However, the literature on micro structural evolution and mechanical behavior of aluminium alloys subjected to very large deformation strain at cryogenic temperature is scarcely available. Especially in precipitation hardenable alloys, the fact that several structural defects are generated during the course of grain refinement, will have an influence on the precipitation sequence, morphology, size, and distribution, its coherency with the matrix and precipitation kinetics as reported in the literature. It ultimately affects the strengthening contribution arising from precipitation hardening of the alloy. In conventional coarse grained materials after solid solution treatment followed by water quenching, the age hardening response is very significant which imparts remarkable improvement in strength. On the other hand, in UFG materials, the similar improvement in strength is scarcely reported [146] [273]. In order to obtain maximum strengthening from precipitation, it is necessary to have a precise control over the precipitation kinetics. Most of the SPD techniques are used to produce UFG structure at room temperature or above room temperature [274] [275]. This results in uncontrolled precipitation growth. Deforming at very lower temperature than its quenching temperature of the alloy like cryorolling could control the precipitation process by suppressing the diffusion, but the resultant microstructure contains larger fraction of low angle grain boundaries filled with high dislocation densities [115] [230]. This is attributed to limitation in imparting high enough strain during deformation to obtain high angle grain boundaries.

Adopting MDF at cryogenic temperature facilitates to achieve higher strain levels, which leads to formation of ultrafine grained structure with high angle grain boundaries with reduced dislocation interiors in supersaturated solid solution material [276]. It is expected that such a type of microstructure could contribute to significant improvement in strengthening of the matrix through precipitation hardening. Hence, the aim of present work is to investigate the effect of MDF at LNT on microstructural evolution and mechanical properties of Al–Mg–Si alloys. The influence of cumulative strain on hardness and tensile properties of the Al alloys at intermediate steps was examined through Vickers hardness testing and tensile testing. A systematic study on micro- structural evolution with increasing strain at mesoscale and microscale by using optical microscopy and TEM was made in the present work. The role of deformation strains and temperature for the grain refinement in the Al alloys was substantiated through detailed TEM analysis of the forged samples. Effect of low temperature ageing on work hardening behavior of the UFG alloy is investigated. Strengthening contributions from various factors in UFG alloy are estimated with the existing models and compared with its coarse grained counterpart.

7.1.2 Experimental procedures

Rectangular samples with $27 \times 30.5 \times 33 \text{ mm}^3$ were machined from the as received plate and solution treated at $520 \text{ }^\circ\text{C}$ for 3 hours and water quenched at room temperature. The samples were subjected to MDF at 77 K using friction screw forging machine. The first forging axis was parallel to the rolling direction of the starting sample. The direction of the sample is changed for every pass at an angle of 90° . The sample dimension ratio 1:1.13:1.22 was maintained constant throughout the processing. MDF at cryogenic temperature was performed by filling the die with liquid nitrogen and its level was maintained up to sample height during forging. After every pass, the sample is allowed to attain thermal equilibrium with liquid nitrogen by giving 5-10 min soaking time. Strain per pass is fixed as $\Delta\epsilon_i = 0.2$ (where ‘i’ number of passes) and maintained constant throughout all passes. The cumulative strain after one cycle of MDF was $\sum\Delta\epsilon_n=1 = 0.6$ (where ‘n’ is number of cycles). In the present study, MDF was carried out to cumulative strains of 1.8, 3.6, 5.4 i.e., 3, 6, 9 cycles, respectively. After 4 cycles, the samples are reshaped by maintaining sample dimension ratio constant. Samples were successfully forged up to 9 cycles. After MDF, samples were prepared by sectioning along the plane perpendicular to the last forging axis i.e., the highest dimension side.

Microstructure evolution and mechanical properties were studied after MDF at different cumulative strains ($\sum\Delta\varepsilon_{n=3} = 1.8$, $\sum\Delta\varepsilon_{n=6} = 3.6$, $\sum\Delta\varepsilon_{n=9} = 5.4$). Tensile tests were performed at room temperature on H25K-S Tinius Oslen tensile testing machine by preparing small size samples with 8 mm gauge length. The schematic diagram of tensile sampling and hardness measurements is shown in *Figure 7.1*. The total length of the sample is 27 mm and width and thickness of gauge length section are 3 mm and 1.5 mm, respectively. At least four samples were tested to check the reproducibility. Starting coarse grained microstructure was investigated through optical microscopy under polarized light. Microstructure of deformed and aged samples after 9 cycles was investigated through EBSD. Scanning electron microscopy (SEM) was used to examine the fractured surface of tensile samples.

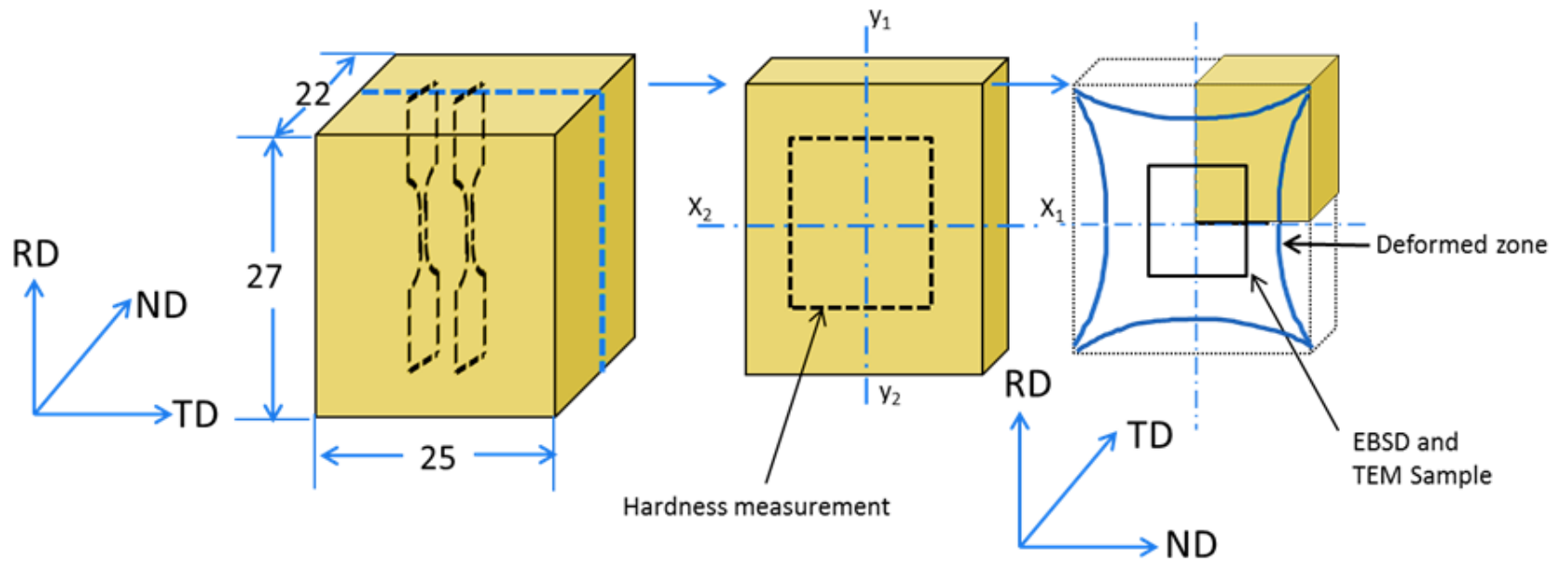


Figure 7.1: Schematic representation for sampling of tensile testing, hardness measurements and microstructural characterization.

7.1.3 Results

7.1.3.1 Microstructure (before ageing)

Optical Microstructure

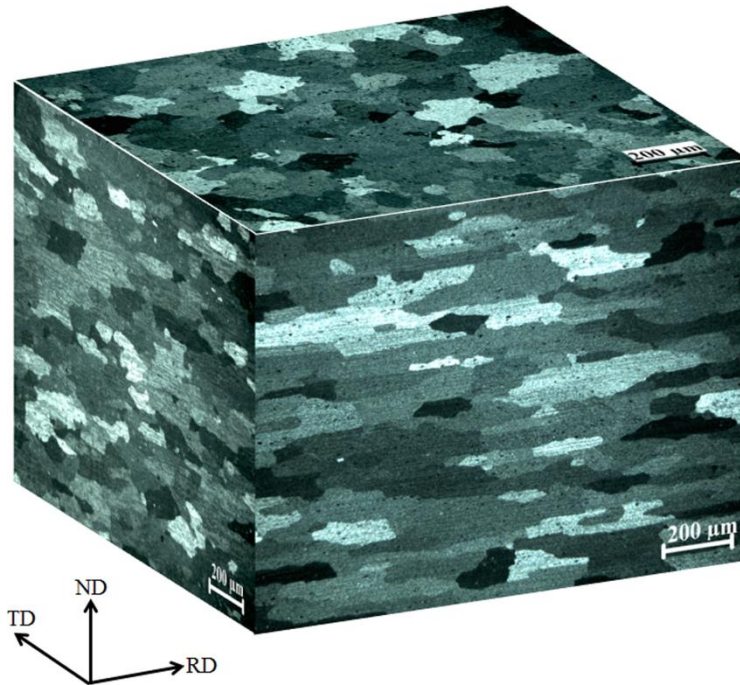


Figure 7.2: Optical micrograph of as-received material after solution treatment. Images were taken under polarized light.

Optical micrographs of Al 6061 alloy after solution treatment is shown in *Figure 7.2*. The initial microstructure shows elongated grains with an average length of 300 μm . *Figure 7.3* shows a series of distinctive optical microstructures evolved after subjecting to MDF at 77 K. *Figure 7.3(a)* shows 3 cycle's ($\sum\Delta\varepsilon_{n=3} = 1.8$) MDFed sample, where the distinction between grain interiors and grain boundaries was vague. It has shown deformed microstructure consisting of deformation bands in various directions which are clearly visible under polarized light. With increasing number of MDF cycles up to 6 ($\sum\Delta\varepsilon_{n=6} = 3.6$), the density of deformation bands has further increased and S-band formation was observed (marked with arrows in *Figure 7.3(b)*) [50]. These observations are in agreement with the Kobayashi et al., [50] reported on MDF of pure copper at 195K. It is evident from *Figure 7.3(c)* that after 9 cycles MDF, the microstructure got fully perturbed and filled with deformation bands. It can be noticed that with increasing MDF

strain, the density of deformation bands has increased with the reduction of the band gap. In *Figure 7.3(c)* and *(d)* areas marked with oval shows development of cross deformation bands, observed in 9 cycles MDFed sample. These similar features are called as microshear bands by Kobayashi et al., Rosen et al., and Hurely et al., [50] [277] [278].

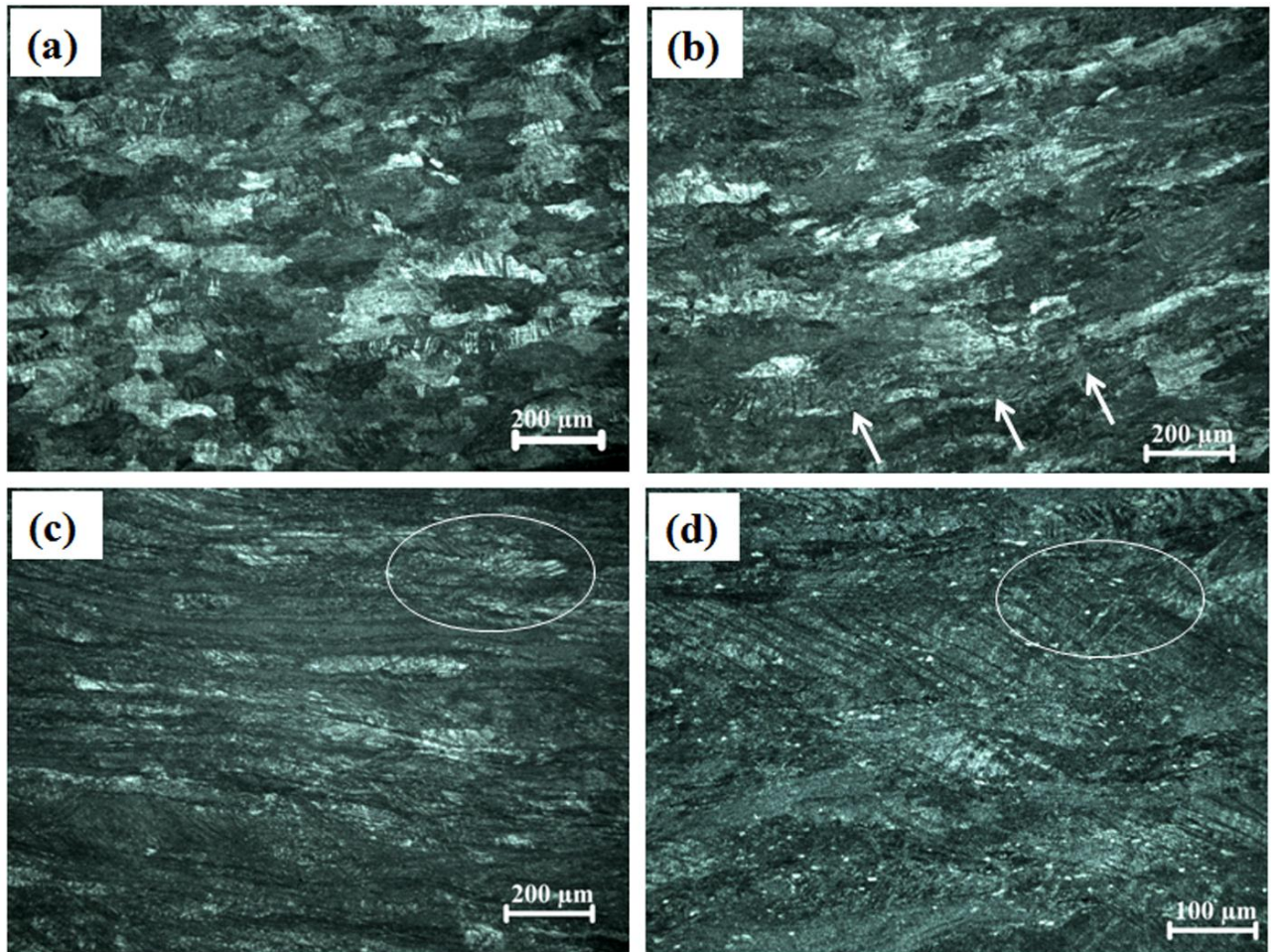


Figure 7.3: Optical micrograph of Al 6061 alloy along the RD-TD plane after MDFA at 77 K: a) after 3 cycles ($\sum \Delta\epsilon=1.8$), b) after 6 cycles ($\sum \Delta\epsilon=3.6$), c) after 9 cycles ($\sum \Delta\epsilon=5.4$), d) after 9 cycles showing deformation bands.

TEM

Figure 7.4(a) shows the TEM micrograph corresponding to MDF up to 3 cycles. Formation of sub grains with an average size of 500 nm along with presence of high density of dislocations was observed. The SAED micrograph shown (as inset) in *Figure 7.4(a)* reveals the presence of low angle grain boundaries. Sub-grains are formed nearly equiaxed structure with dense dislocation walls. Formation of equiaxed subgrain structure is not uncommon in MDF. *Figure 7.5* shows the TEM micrograph corresponding to MDF up to 3 cycles at different area. It is seen that a regular lamellar structure (indicated with dotted lines in *Figure 7.5*) consisting of sub grains aligned along with the direction of deformation band with an average spacing of 350 nm. The width of the lamellar structure is around 1.5 μ m. The boundaries of these elongated dislocation cells/subgrain are called as geometrically necessary boundaries (GNB) and the alignment of these boundaries are in parallel to the planes of maximum shear in aluminium alloys as reported in the literature [278] [279]. Dislocations generated during nonuniform plastic deformation are known as geometrically necessary dislocations (GND) [280]. The density of GND within the grains or sub grains plays significant role in strengthening of the material [234]. Liu et al., [85] have observed similar lamellar structure consisting of elongated dislocation cells aligned along with the shear bands observed in AA 3104 alloy subjected to MDF. Hurely and Humphreys [278] have reported presence of fine scale dislocation cells along the direction of deformation bands in 20% and 50% cold rolled (equivalent true strain 0.22 and 0.7) single phase aluminum alloy. The character of the sub grain boundary determines the way of hardening the material [234]. In the present study sample MDFed up to 3 cycles ($\sum\Delta\varepsilon_{n=3} = 1.8$) has shown predominantly low angle grain boundaries. Low angle grain boundaries are essentially array of dislocation which imparts dislocation strengthening to the material [234]. *Figure 7.4(b)* shows TEM microstructure corresponding to MDF up to 6 cycles, where the sub grains with an average size of 350 nm were observed. The dislocation density has increased with increasing strain and suppression of dynamic recovery leads to formation of fine sub grain structure. At the different zone of the same TEM sample of 6 cycles MDF has shown lamellar structure like 3 cycles MDF sample. The presence of subgrains with lamellar boundaries (average width of 250 nm) and high density of dislocations was observed (*Figure 7.6*).

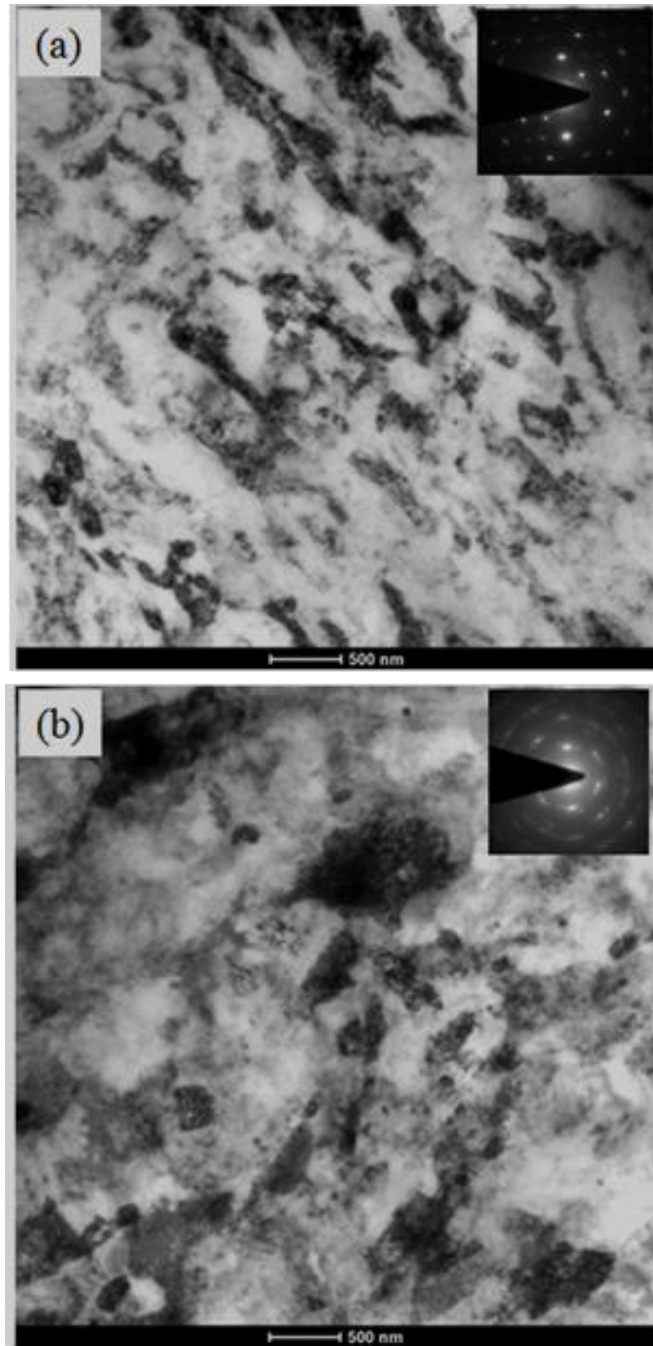


Figure 7.4: TEM Microstructures of MDF at 77 K, along with corresponding SAED pattern in inset: a) after 3 cycles ($\sum \Delta\varepsilon=1.8$), b) after 6 cycles ($\sum \Delta\varepsilon=3.6$).

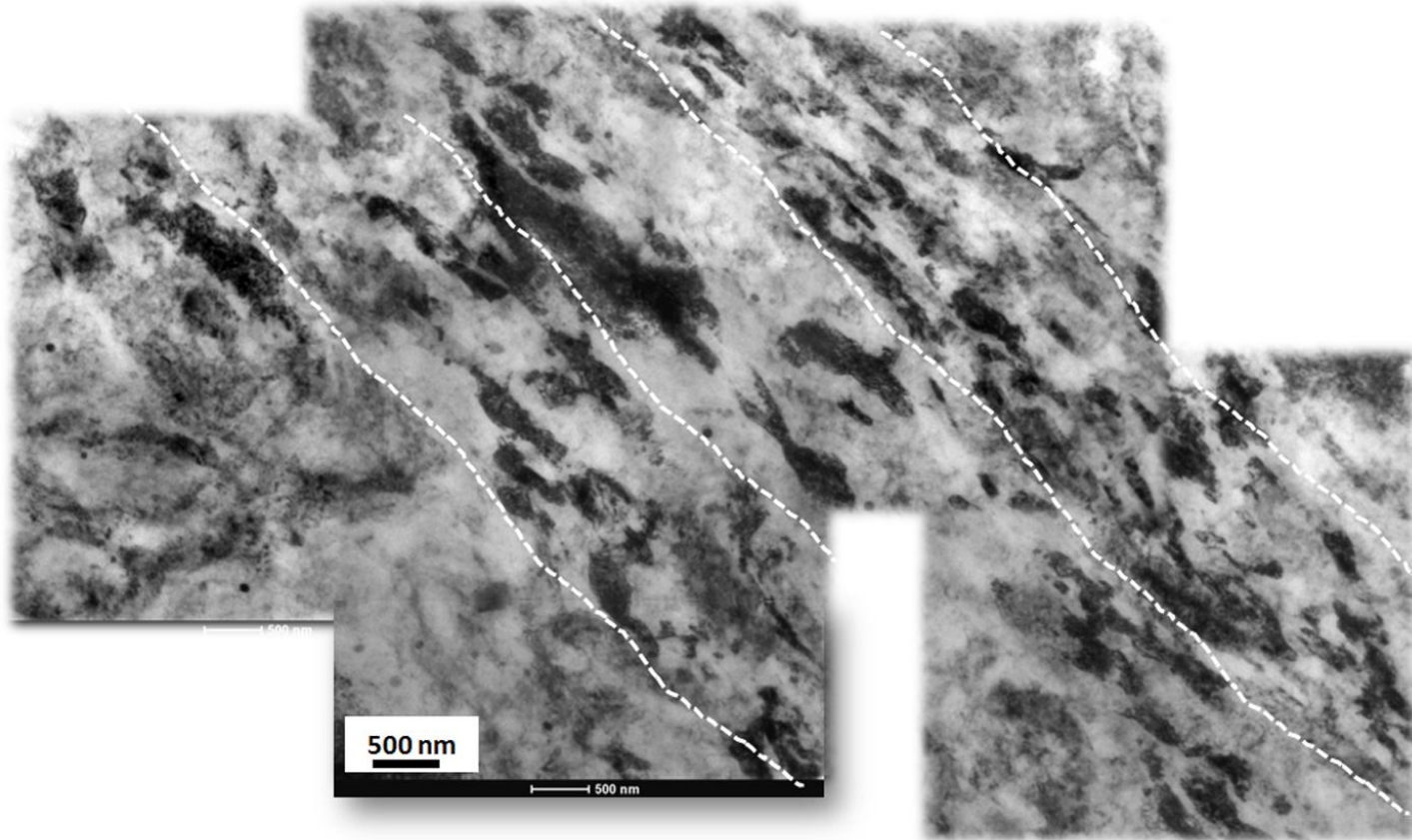


Figure 7.5: TEM Microstructures of MDF at 77 K, after 3 cycles ($\sum \Delta\varepsilon=1.8$). Area between dotted lines shows deformation bands with lamellar structure.

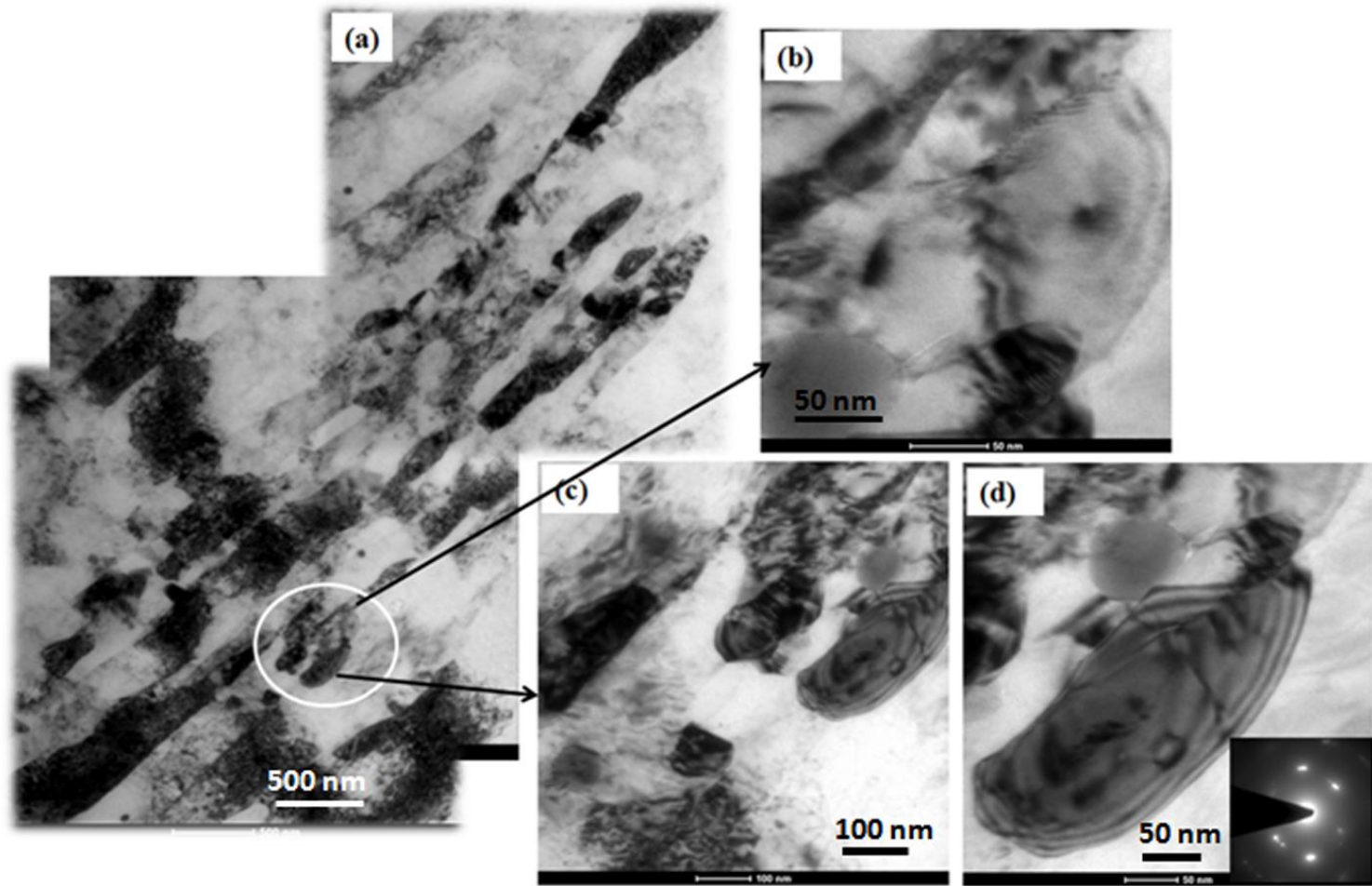


Figure 7.6: TEM Microstructures of MDF at 77 K, after 6 cycles ($\sum \Delta\varepsilon=3.6$). a) Microstructure at the deformation band .b), c), d) magnified view of encircled area shown in **Figure 7.6a**.

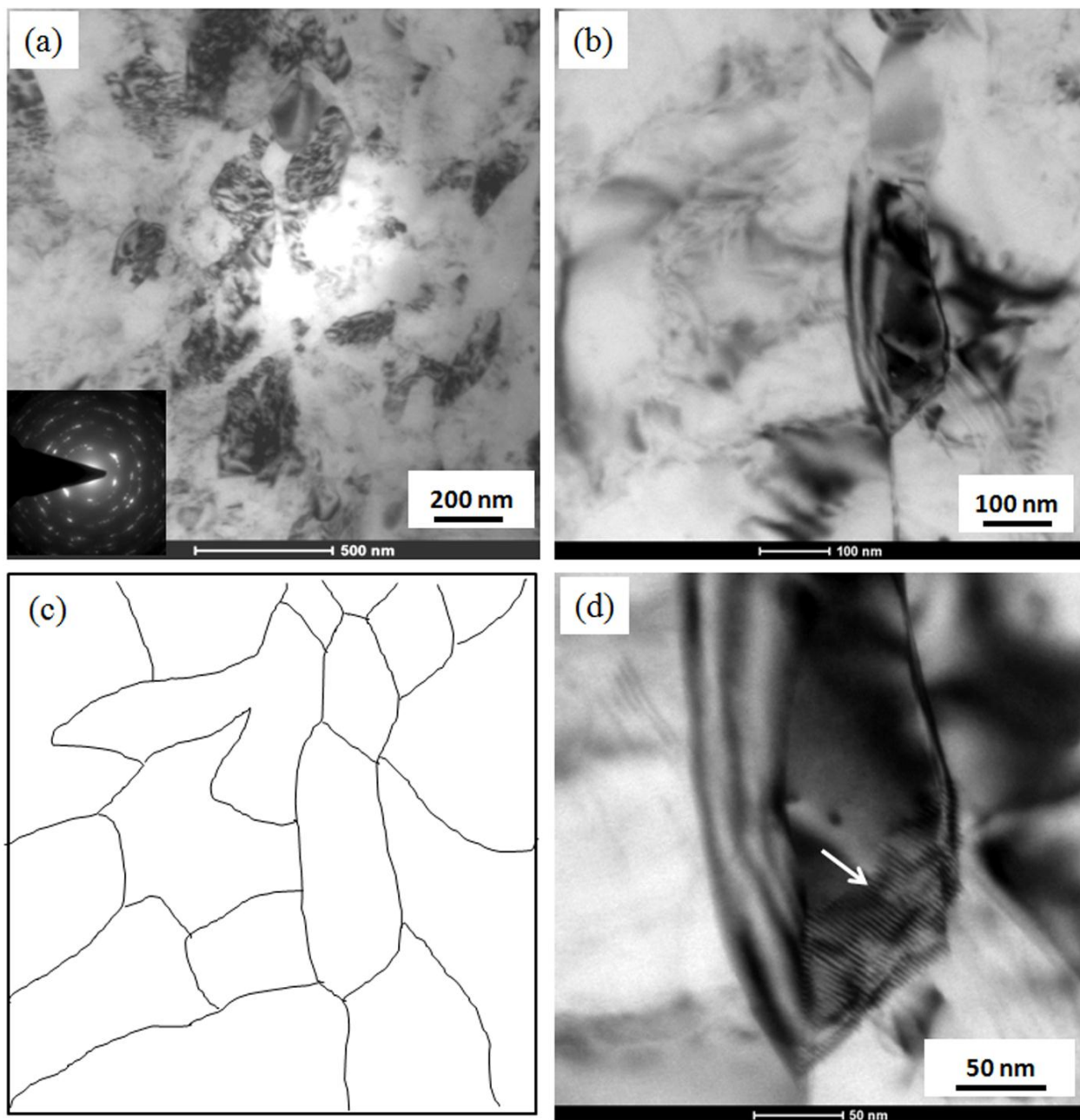


Figure 7.7: TEM Microstructures of MDF at 77 K, after 9 cycles ($\sum \Delta\varepsilon=5.4$). a) Bright field with SAED pattern , b), Bright field image showing recovered sub grain structure, c) Hand drawn sketch of sub grain boundaries of **Figure 7.7(b)** ,d) Magnified view of subgrain seen in **Figure 7.7(b)** , arrow mark indicates array of dislocations at the boundary.

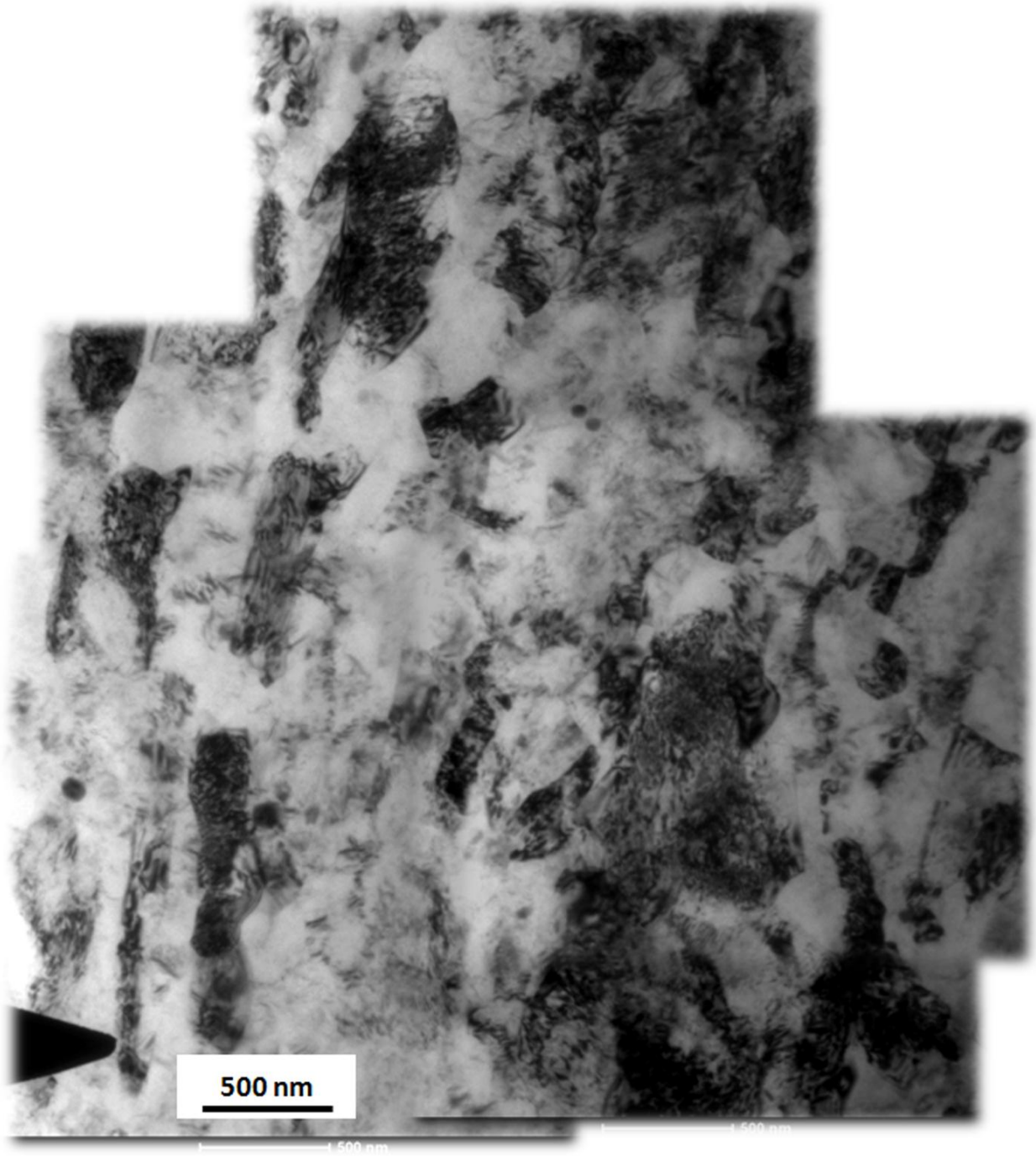


Figure 7.8: TEM Microstructures of MDF at 77 K, after 9 cycles ($\sum \Delta\epsilon=5.4$).

Figure 7.6(b), (c), (d) shows the magnified view of area encircled in *Figure 7.6(a)*, where the formation of very fine sub grains with an approximate size of 70-100 nm can be observed in *Figure 7.6(b),(c)* shows typical recovered sub grain structure with an average size of 100 nm with decreased dislocation density inside the grains. *Figure 7.6(d)* shows the magnified view of fully recovered grain with its corresponding SAED pattern.

The microstructures corresponding to 9 cycles MDF are shown in *Figure 7.7&7.8*. In *Figure 7.7(a)*, the microstructure shows nearly equiaxed fine-grained structure with an average size of 250 nm. The corresponding SAED pattern of *Figure. 7.8(a)* (in inset) taken with 1.5 μm aperture shows that microstructure contains high angle grain boundaries. *Figure 7.8(b) &(c)* (free hand sketch of sub grain boundaries, in *Figure 7.7(b)* are shown in *Figure 7.7(c)* shows very fine sub grain structure with an average size of 150 nm. *Figure 7.7(d)* shows recovered sub grain with Moire fringes. With increasing strain from 1.8 to 5.4, the lamellar grain structure with low angle grain boundaries slowly transforming to equiaxed grain structure with high angle grain boundaries as evident from the *Figure 7.8*. With increasing strain, the misorientation between dislocation boundaries has increased and transformed into high angle grain boundaries. These high angle grain boundaries provide grain boundary strengthening (Hall-petch relation) to the material. Even at high cumulative strains ($\sum\Delta\varepsilon_{n=9} = 5.4$), presence of dislocation inside the sub grains along with high density of dislocation zones are seen. This may be due to processing at cryogenic temperature leads to suppression of dynamic recovery. After 9 cycles MDF formation of equiaxed grain structure with high angle grain boundaries and the presence of high dislocation densities leads to grain boundary strengthening and dislocation strengthening to the material.

7.1.3.2 Mechanical properties (before ageing)

Variation in hardness with increasing cumulative strain at LNT is shown in *Figure 7.9(a)*. The hardness of starting material (solutionized and water quenched) was 54 Hv. After subjecting to MDF at LNT up to $\sum\Delta\varepsilon_{n=3}=1.8$, hardness has increased from 54Hv to 91 Hv. It is evident from *Figure 7.9(a)* that with increasing cumulative strain, the hardness is increasing for the samples processed under LNT condition. The rise in hardness at lower strains is more due to rapid work hardening than that of it at higher strains. In the present study, samples were MDFed up to 9 cycles without any cracks in the sample during forging. The raise in hardness of Al 6061 alloy with same initial grain size after rolling at liquid nitrogen temperature (CR) was 97 Hv

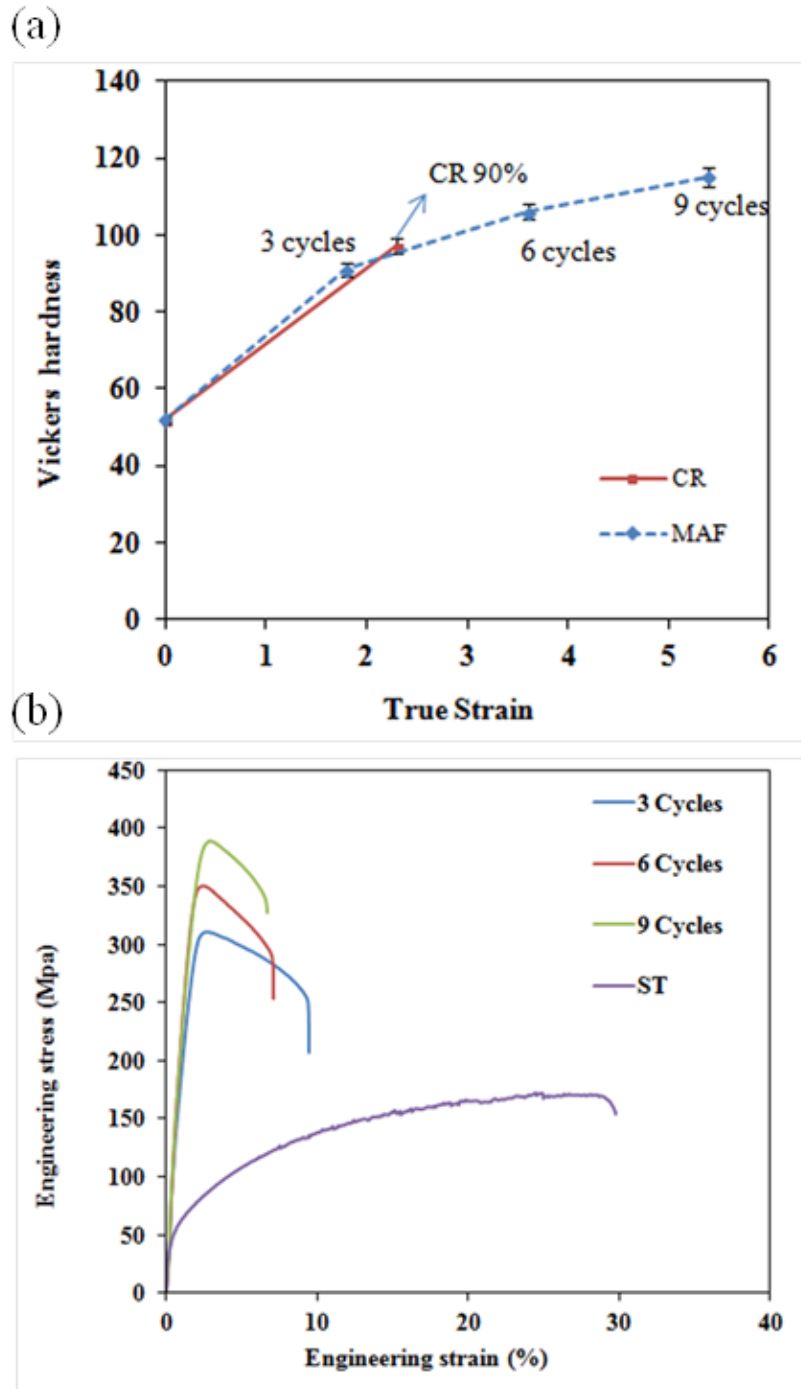


Figure 7.9: Mechanical properties of MD Fed Al 6061 alloy; a) Variation in Vickers hardness with increasing MDF strain at 77K, b) Engineering stress Vs Engineering strain plots of Al 6061 alloy, Starting solution treated condition, MD Fed conditions at 77 K up to different cumulative strains $\sum \Delta\epsilon=1.8$ (3 cycles), $\sum \Delta\epsilon=3.6$ (6 cycles), $\sum \Delta\epsilon= 5.4$ (9 cycles).

(true strain =2.3), which shows that MDF at CR shows the similar trend [230]. With increasing cumulative strain up to 3.6 at LNT, hardness has increased from 91 Hv to 106 Hv, which shows that the acceleration in hardness, with doubling the strain has come down. The slope of the hardness curve has decreased further shows the tendency of achieving saturation. After MDF up to $\sum\Delta\varepsilon_{n=9}=5.4$ at LNT hardness has increased up to 115 Hv. In pure Al, softening behavior was observed after deforming up to cumulative strain of 4.6 through multi axial forging, in channel die, at room temperature [234]. It is due to decrease in dislocation density and transformation of low angle grain boundaries in to high angle grain boundaries [234]. In the present study, even at cumulative strain 5.4 has not shown drop in hardness. The formation of nanosized grains formed through recovery, observed at lamellar structure, corresponds to deformation band zones at $\sum\Delta\varepsilon_{n=6}=3.6$. Transformation of low angle grain boundaries in to high angle grain boundaries was observed by analyzing SAED micrograph of MDF 9 cycles ($\sum\Delta\varepsilon_{n=9}=5.4$). The sub grain size has reduced with increasing strain. Also, the high density of dislocations is still present even after 9 cycles of MDF. This may be due to the effect of deformation temperature, which suppresses the dynamic recovery and increases the dislocation density. In high stacking fault energy materials like aluminum, dynamic recovery/restoration are more active at room temperature, which causes reduction in strengthening effect by decreasing dislocation density. There is strong evidence in the literature that processing at very low temperatures (cryogenic) inhibits dynamic recovery which further leads to accumulation of dislocations to higher steady state level compared to room temperature processing [76] [227] [281]. In contrary to this, Chatterjee et al., [282] have observed decrease in dislocation density in ECAPed Al-Mg alloy processed at cryogenic temperature (cryo ECAP) than at room temperature. It is reported that the deviations are due to different strain path and associated microstructure in cryo ECAP process [283]. The results obtained in the present study are in agreement with reported literature [283] on AA 5052 alloy processed through MAF in confined channel die forging under LNT. The deformed material at LNT has shown better strength due to high dislocation densities compared to RT deformed material.

Tensile tests of starting material and samples after MDF at LNT are performed at room temperature. The recorded test results are shown in *Figure 7.9 (b)*. The solutionized and water quenched sample has shown lowest yield strength (YS-50 MPa) and ultimate tensile strength (UTS-180 MPa) with 30% percentage of elongation. It is observed that with increasing strain, the YS and UTS have increased from YS-50 MPa and UTS-180 MPa (solution treated and water

quenched sample) to YS-380 MPa, UTS-388 MPa. The increase in strength with increasing strain is in correspondence with the hardness increment. This increment in strength is purely due to the sub grain boundary strengthening, dislocation strengthening, and solid solution strengthening. The starting material is solution treated and water quenched, where the second phase is completely dissolved in the matrix. By performing MDF at liquid nitrogen temperature, the diffusivity of second phase from the matrix is reduced [85]. Among the above mentioned contributors in strengthening of ultrafine grained material, dislocation strengthening plays significant role [234]. The drop in the percentage of elongation to failure of 3 cycles MDFed sample is 22% (30% to 8%). With increasing strain by increasing number of MDF cycles from 3 to 6, percentage of elongation to failure has dropped from 8% to 5%. Whereas, the further increasing strain by increasing number of MDF cycles from 6 to 9, the drop in percentage of elongation to failure is only 0.5%. The percentage elongation to failure is decreasing from 30% to 8% after 3 cycles MDF is common observation in severely deformed sample. On the other hand, the material after 9 MDF cycles, evolution of very fine sub grain structure and transformation of low angle grain boundaries to high angle grain boundaries are observed. The presence of high dislocation density is due to continuous generation of dislocations during forging at high strain rate, which imparts high strength and steady state ductility.

7.1.3.3 Fractographs

The fractured surfaces after tensile testing are shown in *Figure 7.10*. To understand the tensile behavior of Al 6061 alloy subjected to MDF at cryogenic temperature, the fractured surface was observed through SEM. *Figure 7.10(a)* shows the fractured surface of initial condition after solid solution treatment without MDF. The fractograph shows typical ductile failure with large sized dimples. With increasing MDF cycles, the average dimple size has decreased as shown in *Figure 7.10 (b), (c) and (d)*. After 9 cycles of MDF, the dimple size has reduced to very fine (~ 300 nm) as shown in *Figure 7.10(d)* inset. The average grain size observed after 9 cycles of MDF is 250 nm (estimated from TEM micrograph (*Figure 7.8*)), where the observed dimple size is nearly matching with the grain size. The size of the dimple formation during fracture depends on the initiation site and number of voids nucleated at the grain boundaries [284]. The observations made in UFG material (after 9 cycles MDF) are in consistence with reported literature by Ko et al., and Padap et al., [284] [285] in UFG pure titanium and AISI 1016 steel.

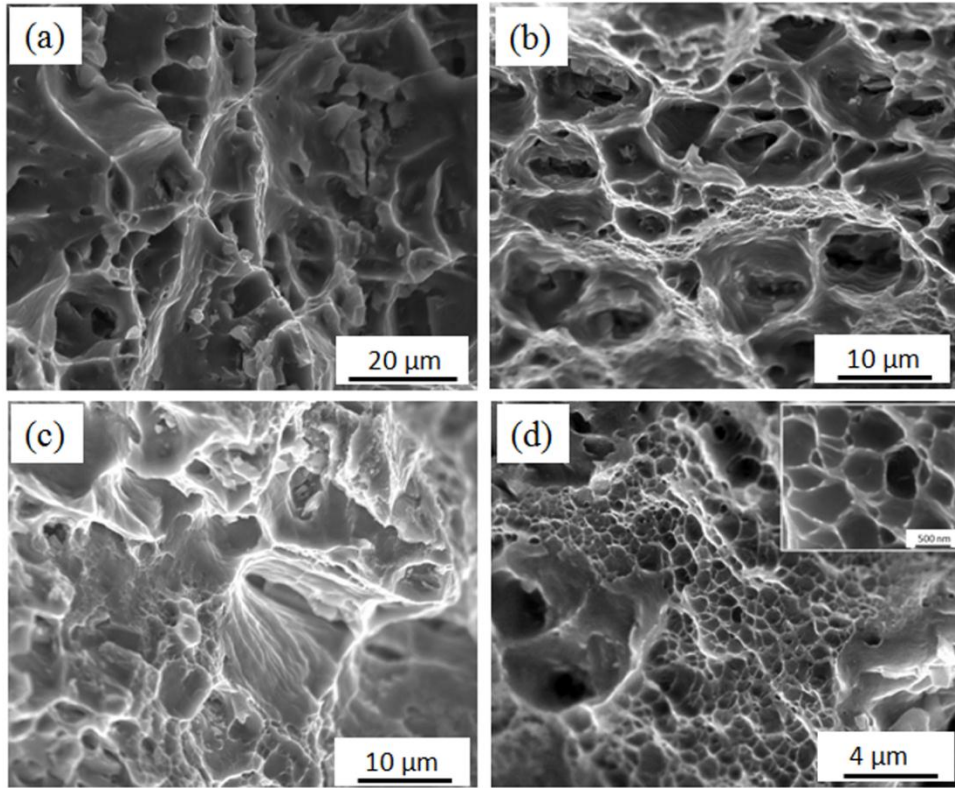


Figure 7.10: SEM fractographs of tensile samples; a) Solution treated condition ($\sum \Delta\varepsilon=0$), (b) after 3 cycles ($\sum \Delta\varepsilon=1.8$), c) after 6 cycles ($\sum \Delta\varepsilon=3.6$), d) after 9 cycles ($\sum \Delta\varepsilon=5.4$).

7.1.3.4 Mechanical Behavior (After Ageing)

a) Vickers hardness

Figure 7.11 shows the variation in hardness after ageing treatment at 125 °C in coarse grained bulk Al 6061 alloy, after solid solution treatment (ST) and MDFed alloy after different MDF cycles. Figure 7.11(a) shows that the maximum hardness is achieved in MDFed alloy after ageing up to 45 hours. Whereas in ST material the maximum hardness is achieved after ageing up to 80 hours. The improvement of hardness in forged samples, 9 cycles MDF sample has shown more than the rest of the samples (Figure 7.11(b)). The rise in hardness in bulk material is nearly 2.7 times more than the difference between 9 cycles MDF and its aged condition sample. The maximum hardness achieved in coarse grained sample is 98 Hv. Whereas, in forged samples, for 3, 6, and 9 MDF cycles, the maximum hardness is 104 Hv, 119 Hv, and 132 Hv, respectively.

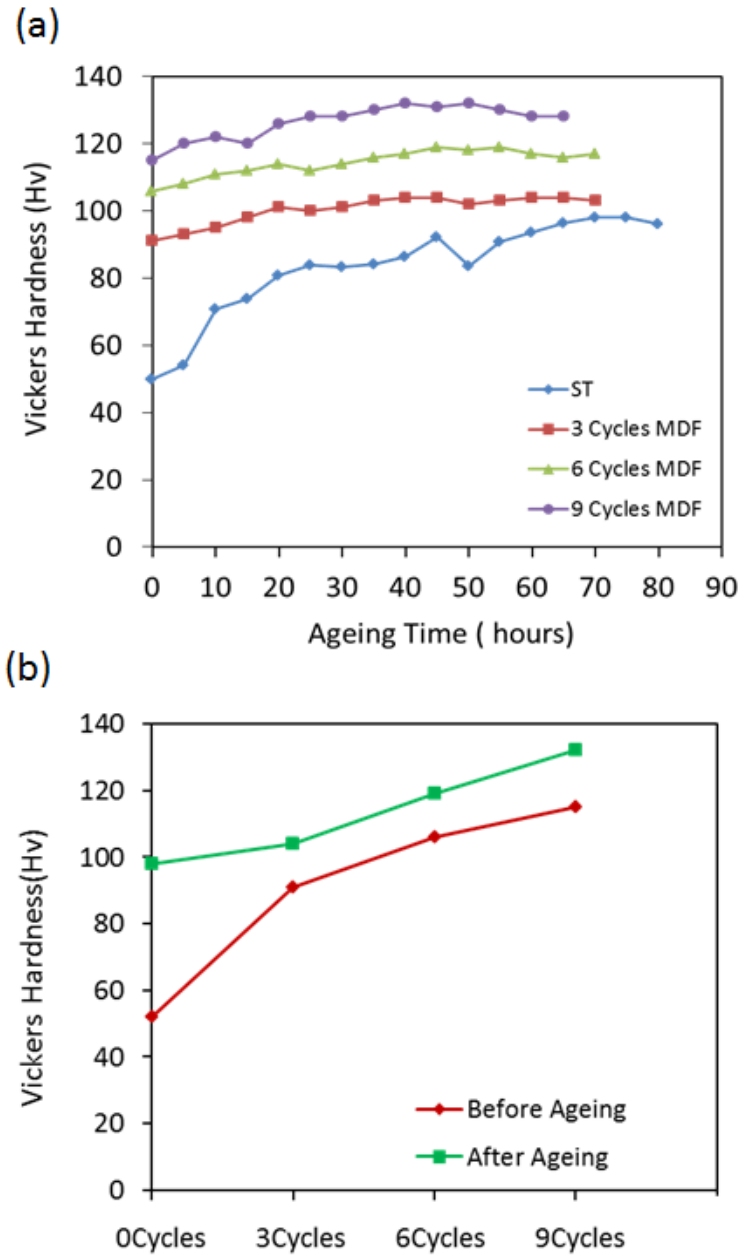


Figure 7.11: Vickers hardness behavior of bulk coarse grained solution treated material (ST) and MDFed material, ageing at 125 °C; a) Variation in hardness versus ageing time plot, b) Variation in hardness of ST and MDFed material before and after ageing treatment.

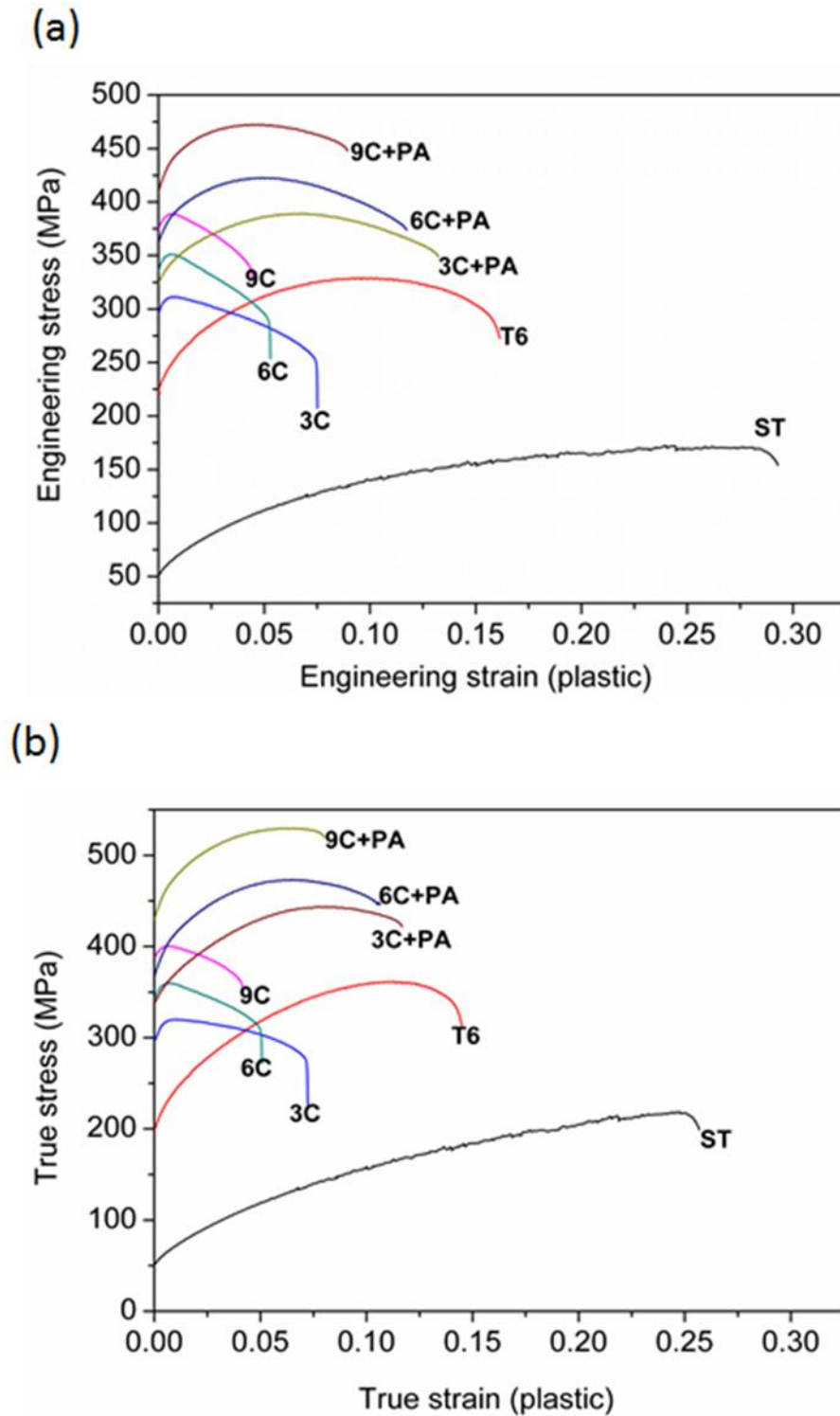


Figure 7.12: Tensile testing plots of Al 6061 coarse grained alloy and MDF alloy with and without ageing; a) Engineering stress versus Engineering strain, b) True stress versus True strain

b) Tensile testing

Figure 7.12 shows the tensile properties of Al 6061 alloy MDFed up to 3, 6 and 9 cycles with and without ageing treatment. The behavior of Al 6061 after cryo forging up to 3, 6, 9 cycles are discussed in section 7.1.2.2. After MDF, samples have shown poor work hardening rate. The uniform elongation in MDF samples, with increasing MDF strain, has decreased due to poor dislocation accumulation capability and necking formation at early stage. After peak ageing treatment, the uniform elongation has increased due to increased work hardenability of the alloy. The YS and UTS of all different MDFed samples have increased along with ductility. The sample subjected to 9 cycles of MDF has shown highest strength (472 MPa) with plastic strain – 0.089 after peak ageing treatment. The plastic strain has significantly increased with ageing treatment. The summary of hardness and tensile properties as a function of MDF strain and MDF followed by ageing is listed in *Table 7.1*

Table 7.1 Mechanical properties of Al 6061 alloy after MDF followed by peak ageing treatment.

Sample Condition	Hardness (Hv)	YS(MPa)	UTS(MPa)	Strain (plastic)
ST	52	50	172	0.29
T6	98	220	330	0.16
3C	91	295	310	0.075
6C	106	334	350	0.052
9C	115	374	388	0.044
3C+PA	104	324	389	0.132
6C+PA	119	361	422	0.117
9C+PA	132	409	472	0.089

7.1.3.5 Microstructure (after ageing)

EBSD

The EBSD micrographs of Al 6061 alloy after MDF up to 5.6 true strain at cryogenic temperature and its peak aged condition are shown in *Figure 7.13*. EBSD data is used to evaluate the strengthening contribution from dislocations (geometrically necessary dislocations, GND) and grain boundaries (including dislocation cell structures). *Figure 7.14* shows the grain average

misorientation (GAM) profiles of as forged and its peak aged samples and they are used to determine the dislocation density. The GAM values for as forged and its peak aged condition are 1.2° and 0.7° degrees, respectively. The GAM value has reduced upon ageing treatment, which is obvious due to annihilation of dislocations while rearranging themselves to form subgrain structure. It is a simplest method to determine dislocation density but it gives only the local information about the microstructure. In the EBSD micrographs, black lines indicate high angle grain boundaries (HAGB, $>15^\circ$) and grey lines indicate low angle grain boundaries (LAGB, $2^\circ < 15^\circ$). After forging, fractions of low angle grain boundaries are more in the sample. Grains with high angle grain boundaries are filled with several subgrain structures, and orientation gradients can be observed within the subgrain structures. Upon ageing, high angle grain boundaries have evolved with clear interiors and coarsening of subgrain structure has occurred. The grain boundary spacing has increased after ageing treatment from 240 nm to 310 nm. In *Figure 7.13.b*, marked area shows, where the elongated grains are aligned (approximately 45° to the axis of the sample) in the micro shear band.

TEM

Figure 7.15 shows the TEM microstructure of 3 cycles forged sample after ageing treatment. The TEM micrographs of aged samples show a clear contrast of elongated ultrafine grains with neighbour area with an average length and width of 600nm and 400 nm respectively. UFGs with reduced dislocations can also be observed. *Figure 7.16(a)* shows TEM micrograph of 6 cycles forged and aged sample. Mixed type of microstructure with dislocation free UFGs with an average size of 200 nm and dislocation tangled zones can be observed. *Figure 7.16 (b) and (c)* shows TEM microstructure of 9 cycles forged and aged material in bright field and dark field modes. Very fine grains in the order of 200 nm with reduced dislocations at the interiors can be seen. In the area of $2 \times 2 \mu\text{m}$, several UFGs are observed. Very fine grains even in the order of 100 to 150 nm also can be seen in the micrograph. These dislocation free grains play critical role in enhancing the work hardenability of the material. *Figure 7.17* shows the various kinds of precipitates observed in 3 cycles forged and aged material. In *Figure 7.17(a)*, it is evident that precipitates in circular shape in the range of 80 to 100 nm are observed. Dark field micrograph in *Figure 7.17(b)* shows circular and elongated type precipitates distributed in dense.

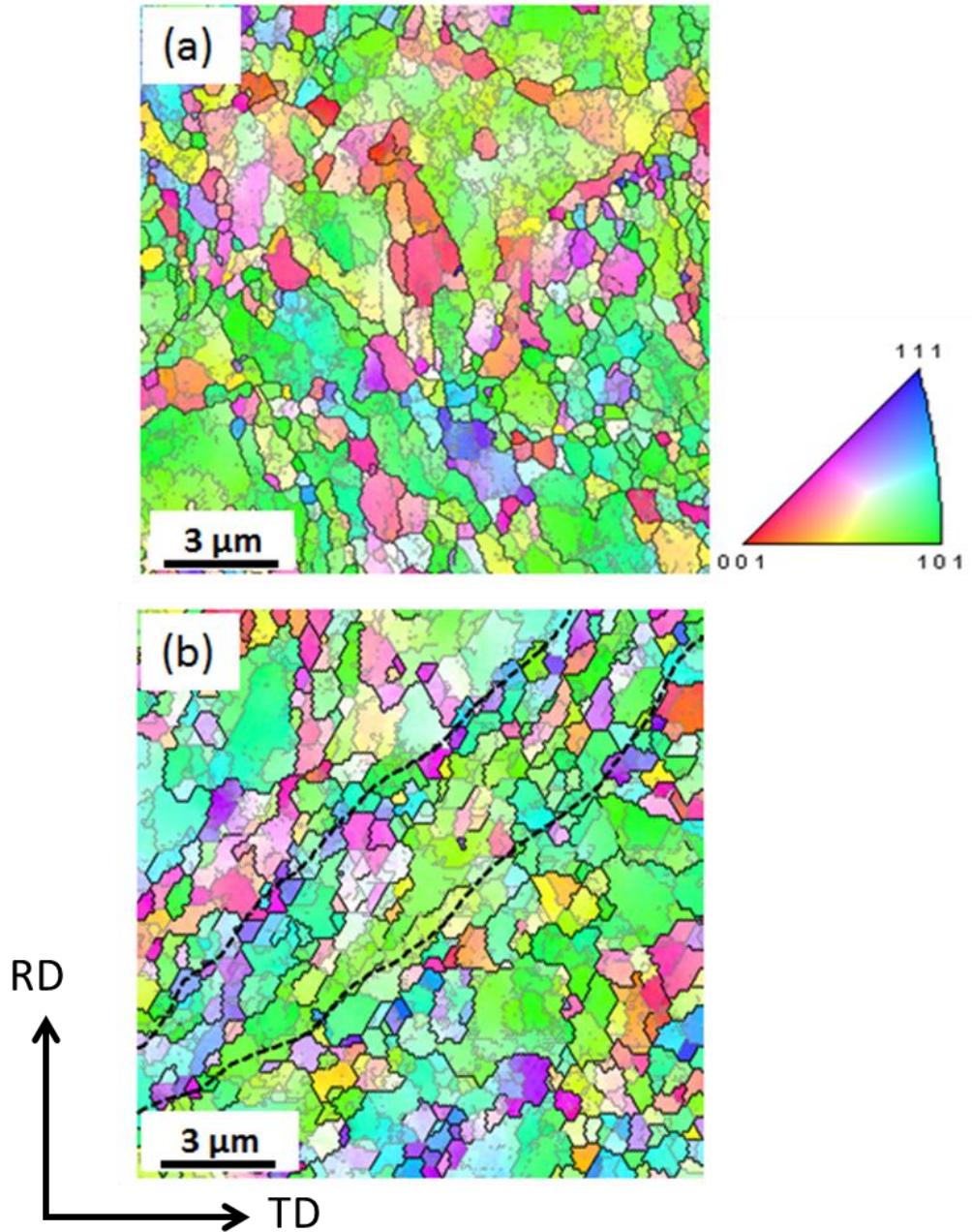


Figure 7.13: Inverse pole figure maps of Al 6061 alloy after MDF up to 9 cycles; a) without ageing, b) with ageing

In contrast to *Figure 7.17 (a) and (b)*, *Figure 7.17 (c)* shows very fine needle shaped precipitates in the range of 8 to 10 nm width. Our previous investigations indicate the possibility of presence of post β'' type precipitates in deformed Al 6061 alloy. The coarse precipitates could be β' precipitates, which are semi coherent with the matrix. The similarity observed in precipitate morphology of 3 cycles and 6 cycles forged materials has shown the coexistence of circular and

needle shaped precipitates. The needle type precipitates observed in 6 cycles are very fine (2-4 nm diameters) as shown in *Figure 7.18*. *Figure 7.19* corresponds to precipitate morphologies observed in 9 cycles forged and aged material.

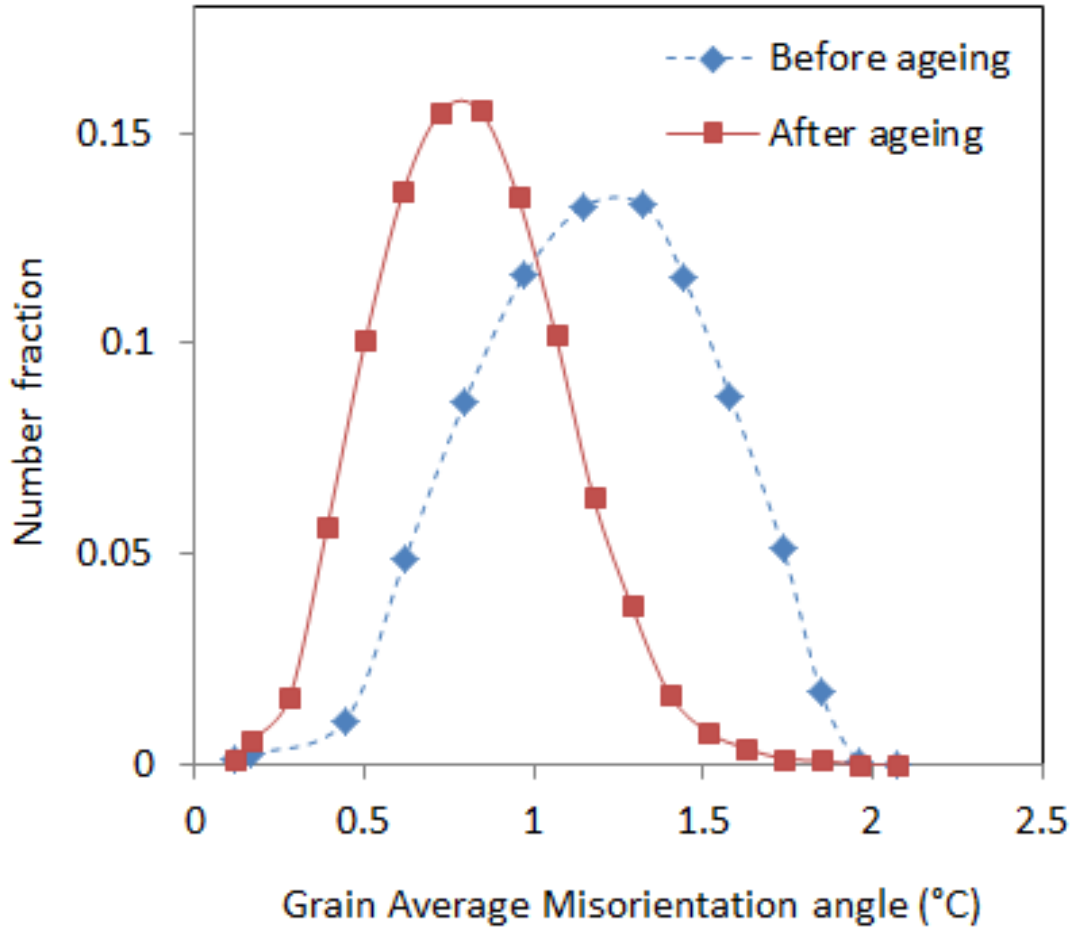


Figure 7.14: Grain average Misorientation (GAM) profiles of 9 cycles MDF material before and after ageing treatment.

The number density of circular type precipitates is very less as compared to lower strained material. It is also composed of different size of needle shaped precipitates. The aspect ratio of the needle shaped precipitates is very high. *Figure 7.19(c)* shows fine needle precipitates with in the subgrain structure. The approximate size of the precipitates is observed to be 1.1 nm.

7.1.3.6 Fractographs (after ageing)

Figure 7.20 shows the SEM micrographs of fractured surfaces of cryoforged Al 6061 alloy at different strains after ageing treatment. *Figure 7.20(d)* shows the back scattered electron micrographs of fractured surface where the coarse second phase particles are located at the center of the dimple. It indicates a nucleation of void starting at the second phase particles and grows to form dimple. Energy dispersive spectroscopy (EDS) analysis has shown that the coarse second phase particles are composed of Fe, Si and Mg. In all three forged and aged conditions, the fractured surface features show predominantly a ductile type of fracture. The presence of these impurities will lead to early stage of void nucleation and reduction in uniform elongation.

7.1.4 Discussions

After multi directional forging up to 9 cycles (5.4 true strains), the ultrafine grained structure with average size of 200 nm and high fraction of high angle grain boundaries has been produced in the bulk alloy. Tensile test results indicate significant improvement in strength (UTS- 388MPa) as compared coarse grained T6 condition (UTS- 330 MPa) with reasonable ductility. The ductility of the material is restored with increased work hardenability, upon ageing treatment, as shown in tensile test data (*Figure 7.12*). TEM microstructures after ageing clearly demonstrate the formation of dislocation free fine crystals with nano sized precipitates in the matrix. After ageing, the grains with high angle grain boundaries have formed without increasing its size. The reduction in dislocations inside the grain boundaries has taken place, leading to dislocation cell coarsening. Low strained material has shown higher elongations but with reduced strength. The grain size observed in low strained material is slightly coarser than maximum strained material. The work hardenability of lower strained material is comparable with coarse grained material.

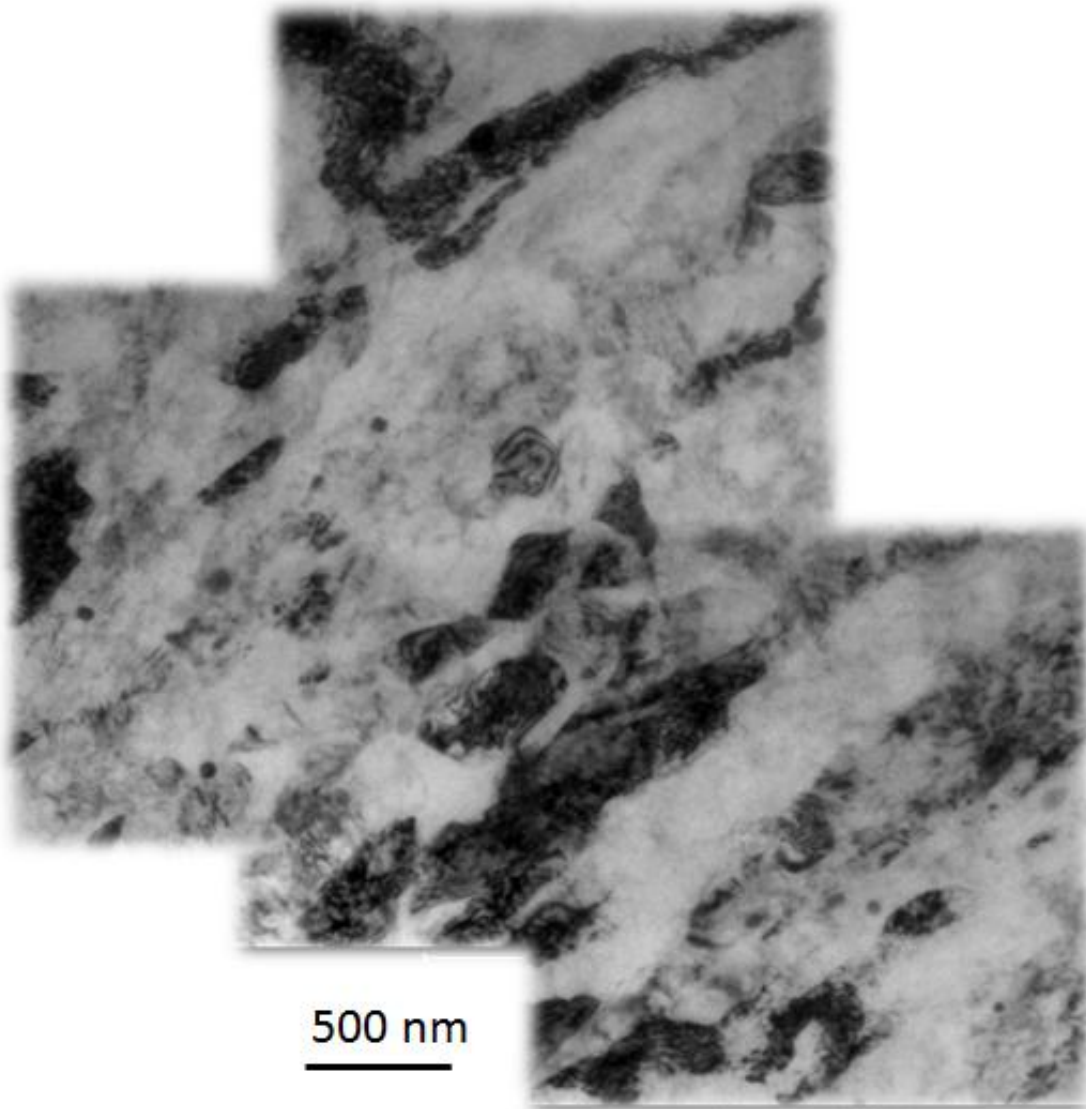


Figure 7.15: TEM microstructure of Al 6061 alloy after MDF up to 3 cycles followed by peak ageing treatment.

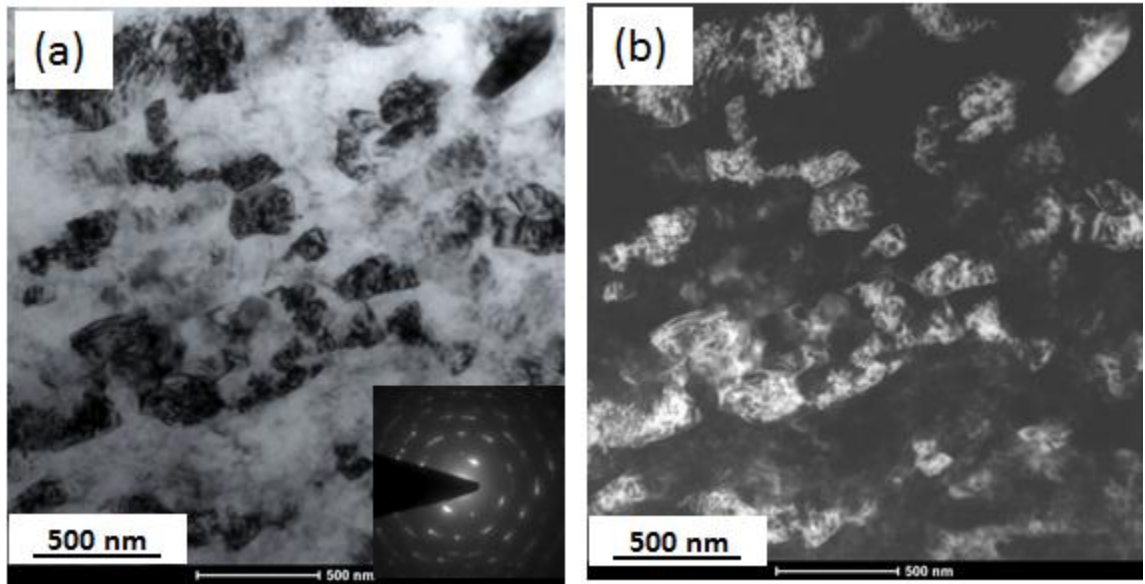
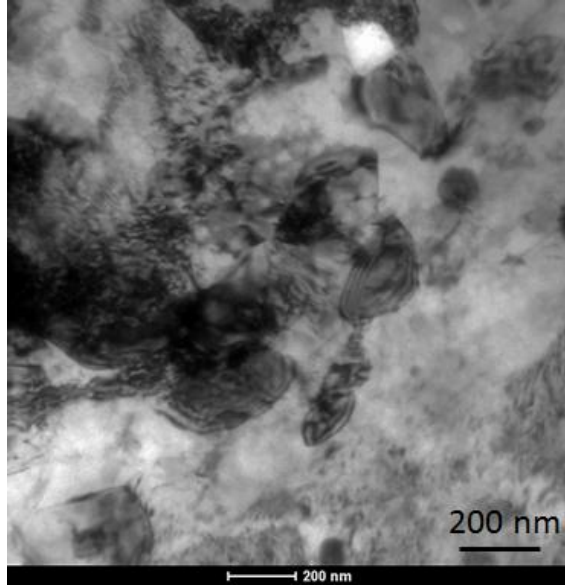


Figure 7.16: TEM microstructures of Al 6061 alloy after MDF with peak ageing treatment; a) 6 cycles, b) 9 cycles (Bright field micrograph), c) 9 cycles (Dark field micrograph)

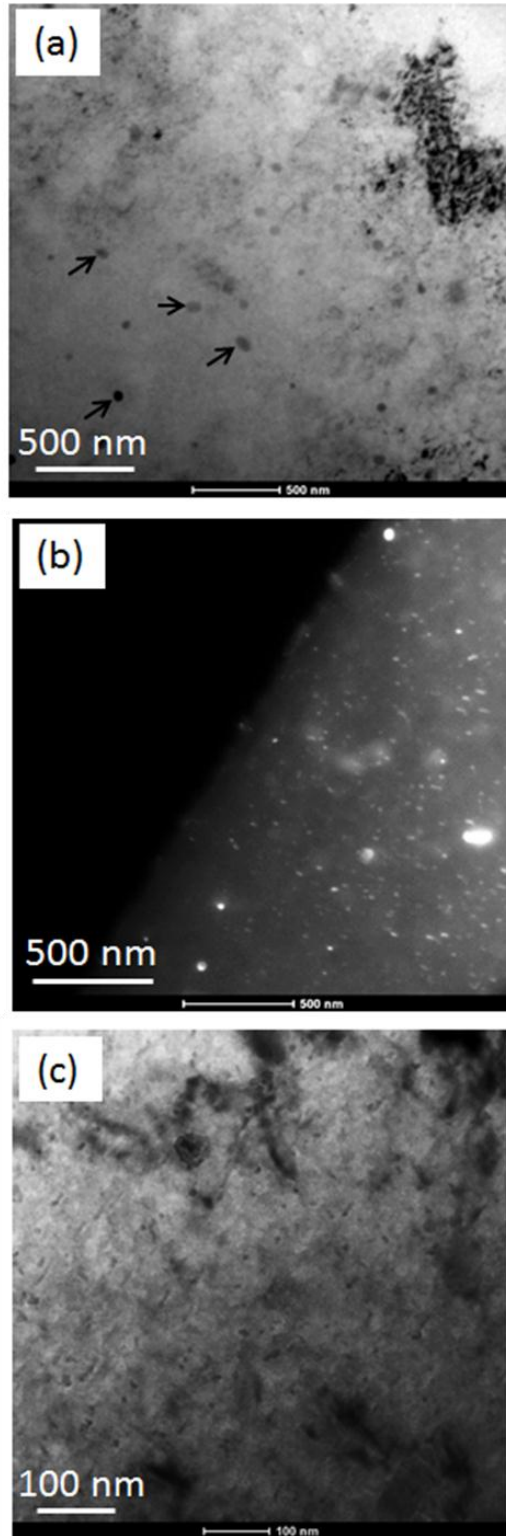


Figure 7.17: Various kind of precipitates that are observed in MDF 3 cycles after peak ageing treatment; a) Bright filed image of spherical shaped precipitates, b) Dark field image of precipitates, c) Bright filed image of needle shaped precipitates.

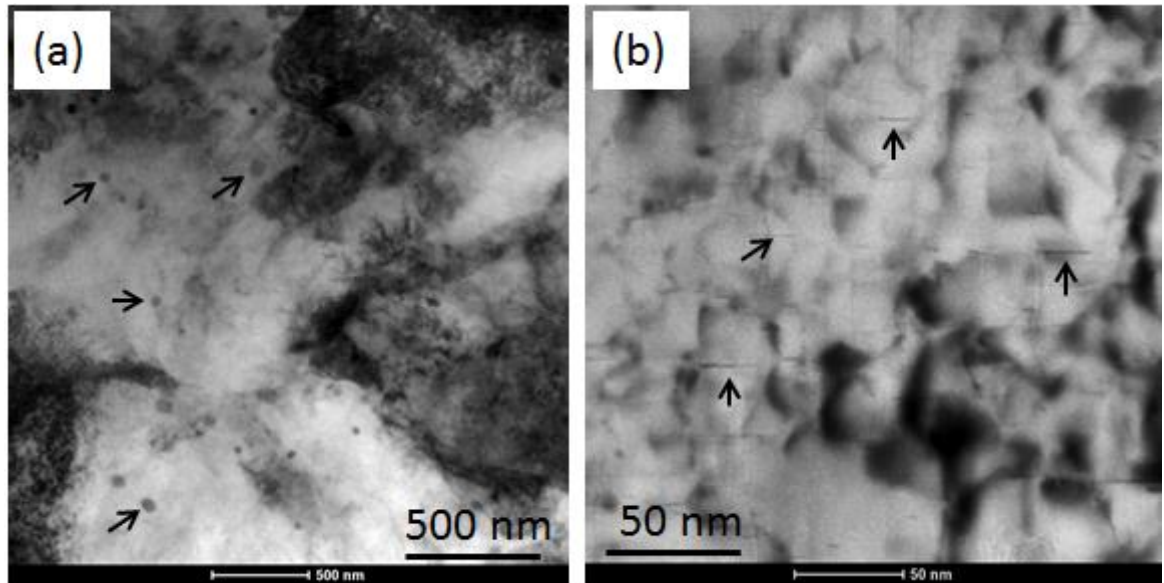


Figure 7.18 : Various type of precipitates in MDF 6 cycles after peak ageing treatment; a) Bright field image of spherical shaped precipitates, b) Bright filed image of fine needle shaped

UFG material often shows poor work hardenability due to onset necking behavior. There are several studies pertaining to the effect of several factors such as grain size, grain boundary character, second phase particles, and temperature on the work hardenability of the material [286] [287]. Among these factors, the results are quite consistent with respect to the effect of temperature on work hardening of the material. The onset of necking is observed in all 3, 6 and 9 cycles of MDF material due to poor work hardening rate. Work hardening is attributed to generation and accumulation of dislocations, which leads to pileups at the grain boundaries during deformation. TEM microstructures of as forged material up to 3 cycles show elongated subgrain structure filled with full of dislocations. Cryoforging has led to suppression of dynamic recovery, which precludes the annihilation of dislocation. The high density of dislocations inside the subgrains decreases the mean free path of mobile dislocations. With increasing deformation strain due to MDF, the strength of the material has increased because of Hall-Petch effect. TEM microstructure of 6 cycles of MDF shows evidence for fine dislocation free crystals in the order of 100 nm, which can accommodate only very few dislocations [288]. Thus, it leads to reduction

in work hardenability and increase in strength. The variation in the ratios of UTS to YS of all three different MDF samples is not much as it varies from 1.03 to 1.05. It was reported earlier that the character of the grain boundary influences the dislocation generation and its annihilation; ultimately it influences the work hardening rate. The influence of grain boundaries character is lower than the amount of dislocation content as evident from the present work.

7.1.4.1 Yield Strength

a) Before ageing

The YS of the 9 cycles MDFed material is estimated through various strengthening components as given below

$$\sigma_Y = \sigma_{SS} + \sigma_{Dis} + \sigma_{Gbs} \dots\dots\dots(7.1)$$

σ_{SS} is solid solution strengthening, the major alloying elements which contribute for significant solid solution strengthening in Al 6061 alloy are, Mg (1.01 at. Wt. %), Si (0.67 at.wt. %) along with small traces of Cu (0.2). Since Cu is in small amount, its strengthening contribution is neglected here. Mg and Si act as substitutional solutes in the Al matrix, which renders hardening effect through elastic distortions in the parent lattice. The elastic distortions are due to the difference in size and modulus of solute atoms with Al matrix. It leads to interactions with screw dislocations during deformation [289]. The effect of Mg content on work hardening rate is more as compared to its influence on YS [290]. In the present investigation, after solid solution treatment and water quenching, assuming Mg and Si are completely dissolved in to the Al matrix, the total contribution from Mg and Si is expressed by the relation given below:

$$\sigma_{SS} = \Delta\sigma_{Mg} + \Delta\sigma_{Si} \dots\dots\dots(7.2)$$

$$\Delta\sigma_{Mg} = AC^\beta \dots\dots\dots (7.3)$$

$$\Delta\sigma_{Si} = BC^\gamma \dots\dots\dots (7.4)$$

Where A, B, β , γ are constants and the values are shown in *Table 7.2* [291] [290] [292]. C is the concentration in wt% of Mg and Si, and the values are 1.01 and 0.67. By substituting the values in equations (7.2), (7.3), (7.4) the value of σ_{SS} is 19 MPa.

Grain boundary strengthening

The contribution from grain boundary strengthening to the yield strength of the as forged material is estimated by using grain boundary information obtained through EBSD data. It is well established that the microstructural evolution in SPD material takes place through formation of dislocation cell structures and its continuous transformation to UFG with HAGB. The as deformed state of material possesses several low angle grain boundaries along with high angle grain boundaries. It is evident from EBSD micrograph of as forged material that the presence of LAGB and HAGB might have different resistance against slip [165]. Hansen equation given below is used to estimate the strengthening contribution from both LAGB and HAGB.

$$\sigma_{Gbs} = \sigma_0 + [M\alpha G \sqrt{(3b\theta_{LAGB} (1-f)) + k \sqrt{f}}] D_B^{-1/2} \dots\dots\dots(7.5)$$

The values and definitions of σ_0 , M , α , G , b , k , f , D_B and θ_{LAGB} are listed in *Table 7.2*. The grain boundary strengthening is found to be 277 MPa for the forged material.

Dislocation strengthening

TEM micrograph of 9 cycles of as forged material has shown that the ultrafine grains are filled with high densities of dislocations. The interaction among them led to hindering its motion, causing dislocation hardening. This is estimated through Bailey–Hirsch relationship given below

$$\sigma_{Dis} = M\alpha G b \rho^{1/2} \dots\dots\dots(7.6)$$

Where ρ is dislocation density, is calculated by using GAM value obtained from EBSD data. It is calculated as $3.0511E+14 \text{ m}^{-2}$ in the as forged material after 9 cycles. By using ρ value in the equation (6), the contribution to the strengthening by dislocations is calculated as 88 MPa.

Dispersion strengthening

Back scattered diffraction image taken on coarse grained Al 6061 material shows existence of undissolved constituent particles with chemical compositions of Fe, Si, O, Mn, and Mg. It is possible that, at the time of forging at liquid nitrogen temperature, these particles could get fragmented, become finer and led to dispersion strengthening to the matrix.

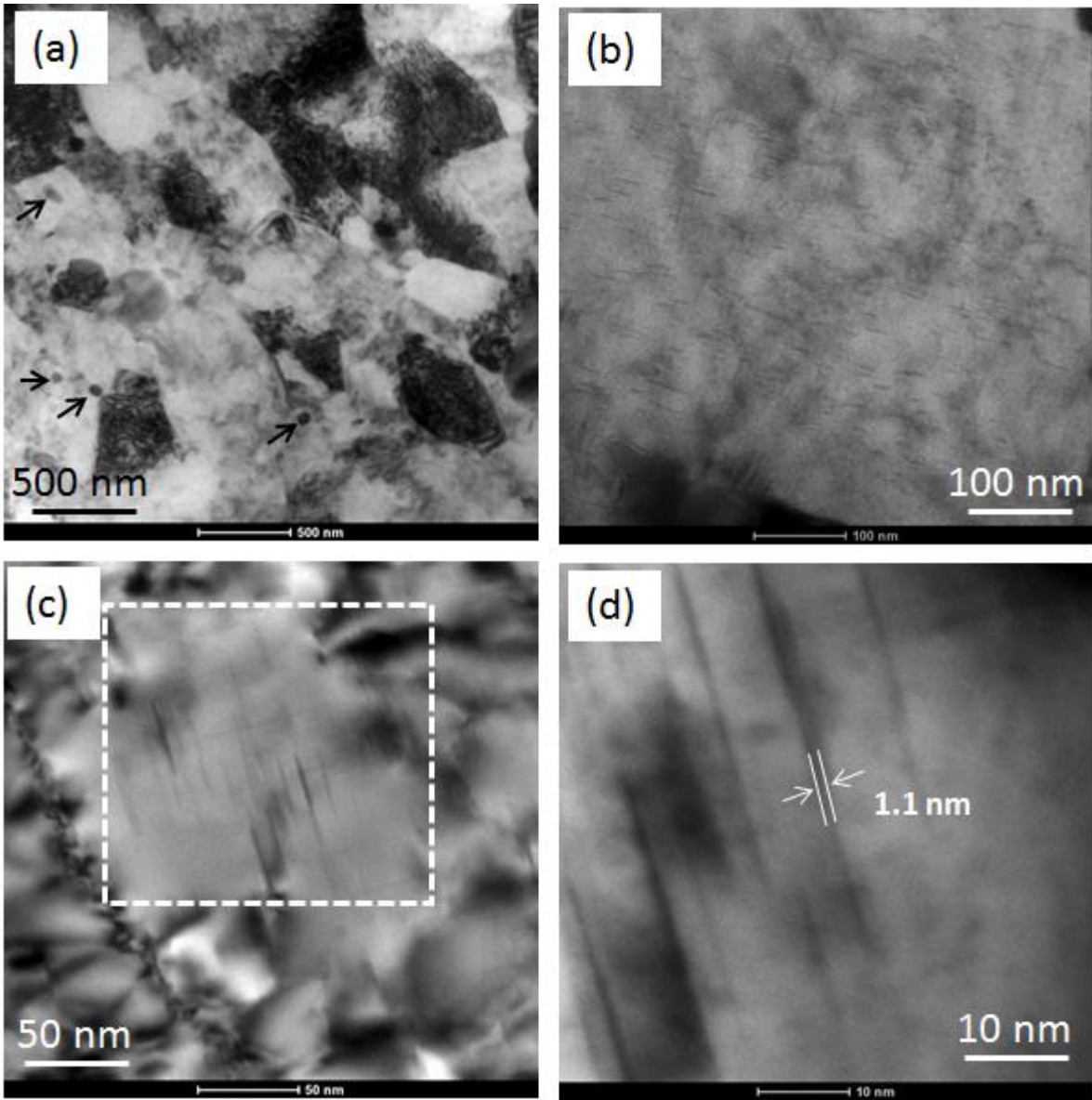


Figure 7.19: Various type of precipitates in MDF 9 cycles after peak ageing treatment; a) Bright filed image of spherical shaped precipitates, b) Bright filed image of needle shaped precipitates, c) Bright filed image of needle shaped precipitates with higher magnification, d) Bright filed image of area marked with square box in **Figure 7.19(c)**

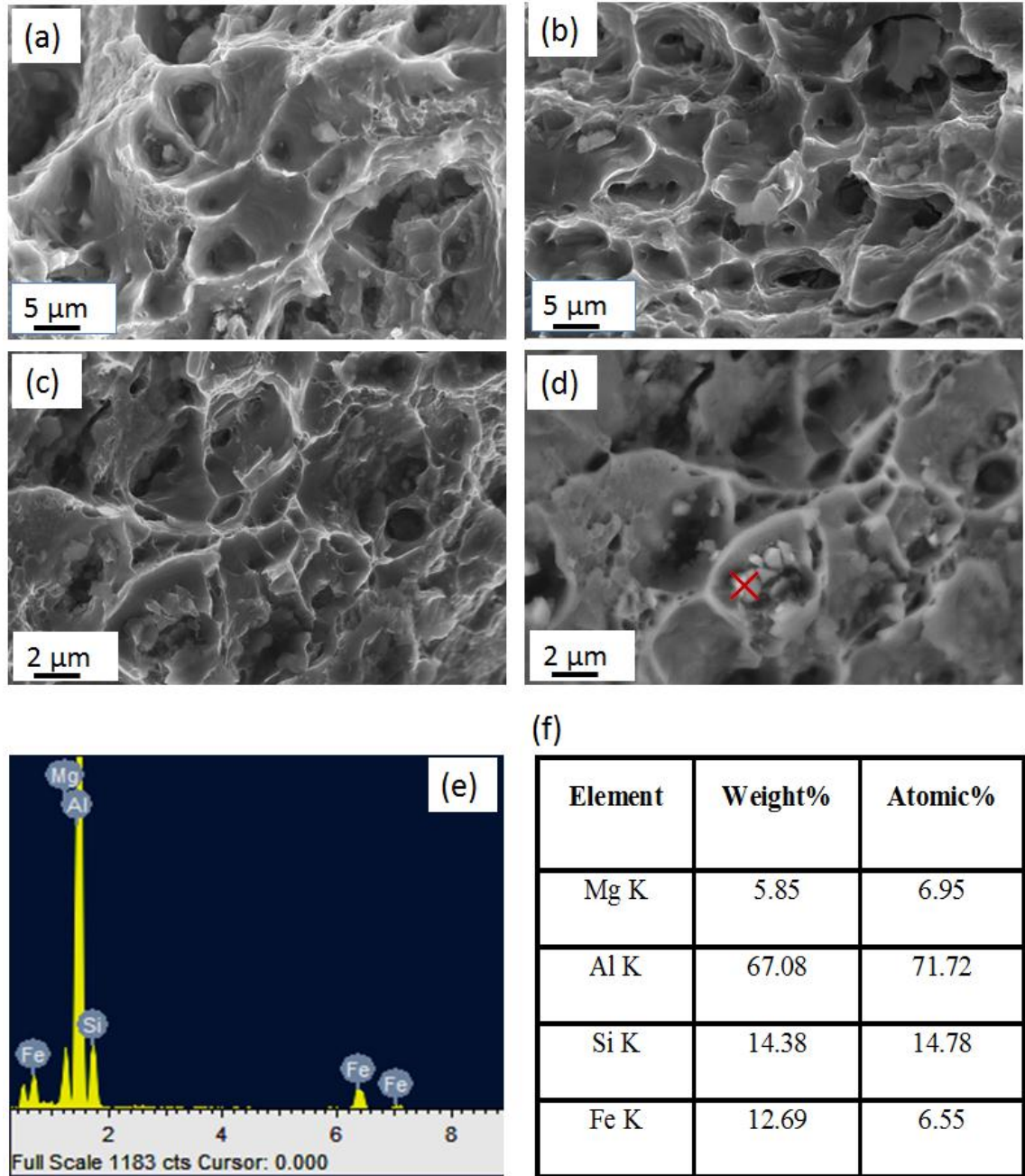


Figure 7.20: Fractured surface of Al 6061 alloy after MDF up to 3, 6 and 9 cycles followed by peak ageing; a) SEM image of 3 cycles b) SEM image of 6 cycles c) SEM of 9 cycles d) Back scattered electron image (BSE) of image shown in **Figure 7.20(c)**, e) EDS spectrum obtained from the point indicated in the **Figure 7.20(d)**, f) Elemental composition of EDS spectrum shown in **Figure 7.20 (e)**.

During deformation the particles act as an obstacles for dislocation motion, leads to accumulation of high dislocations densities surrounding to these particles and results evolution of very fine grains. *Figure 7.21* shows the fragmentation constituent particle and surrounded with very fine grains, few grains are attached to the surface of the broken particles. The dimensions of these particles are observed to be less than 2 μm . The disadvantage is due to the fact that it reduces the uniform elongation by acting as void nucleation sites during tensile testing.

b) After ageing

The significant improvement in mechanical properties is due to substantial changes in microstructural features in as forged material after peak ageing. The various strengthening mechanisms that contribute for increase in YS of peak aged material are dislocation strengthening, precipitation hardening, dispersion strengthening, and grain boundary strengthening through LAGBs and HAGBs. The total strength can be formulated as

$$\sigma_Y = \sigma_{SS} + \sigma_{Dis} + \sigma_{Gbs} + \sigma_{Ps} \dots \dots \dots (7.7)$$

The structural changes that occurred during ageing led to reducing the grain boundary strengthening by increasing the grain boundary spacing (from 0.24 μm to 0.31 μm) and reducing the GAM value (from 1.2° to 0.7°). The calculated value of strength is 239 MPa. The dislocation strengthening has dropped from 88 MPa to 59 MPa due reduction in dislocation density through recovery process. The major difference in strengthening of the matrix between as forged and peak aged condition is - solid solution strengthening. In peak aged material, it is expected that the fraction of solute content that remains in the matrix is negligible and it has completely precipitated out from the matrix during ageing. The process of precipitation hardening in Al alloys was first discovered by Wilm [293]. Strengthening of the matrix takes due to the interaction of dislocations with lattice strain created by misfitting of coherent precipitates. Orowan has proposed an equation to estimate the strengthening by non-shearable particles as given below [294] [295]. It is used for calculating dispersion strengthening due to hard particles.

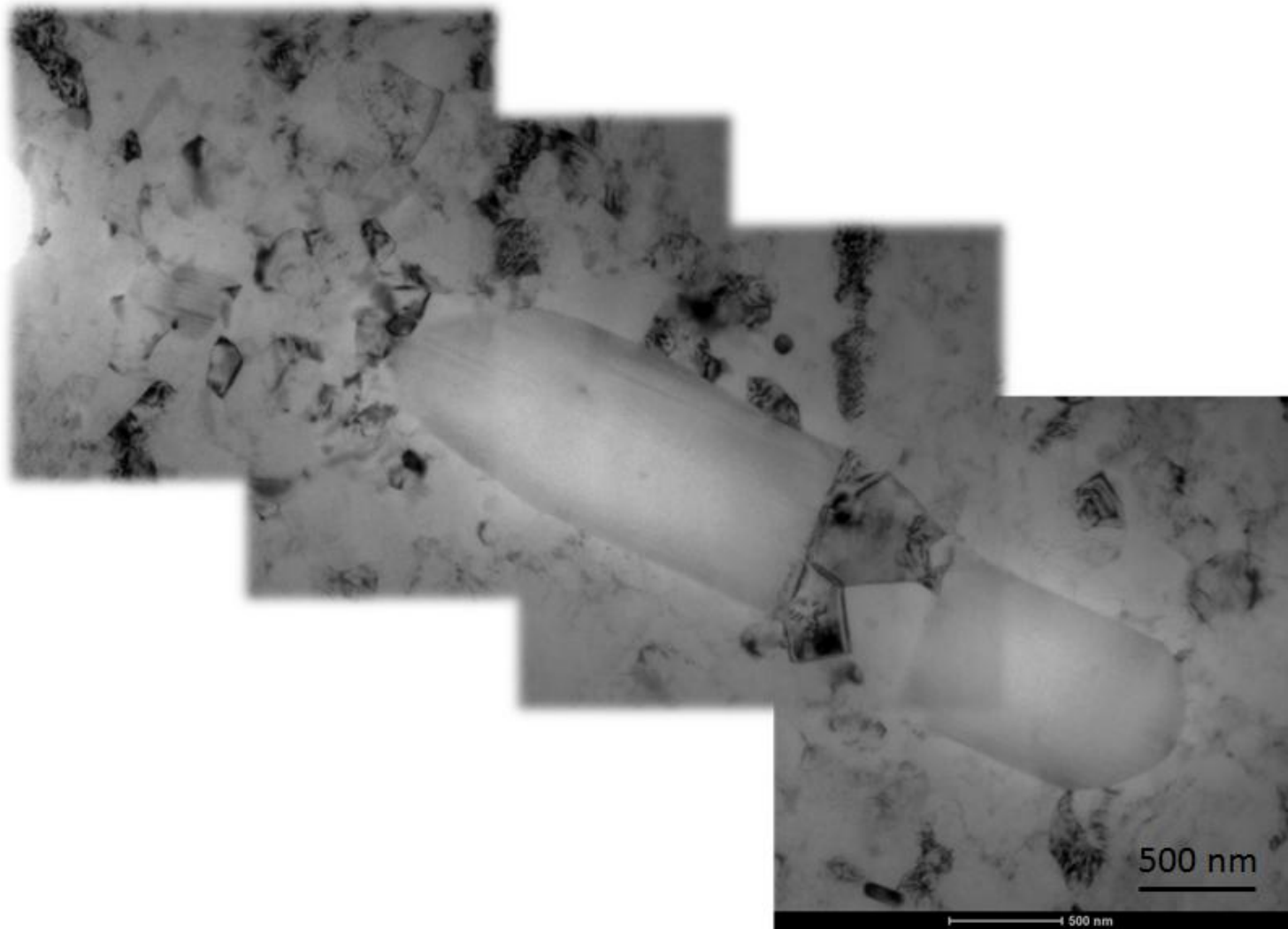


Figure 7.21: TEM micrograph of 9 cycles MDF material after peak ageing treatment, shows fragmentation of coarse second phase particles.

$$\Delta\sigma_0 = \frac{M(0.4Gb) \ln\left(\frac{2\bar{r}}{b}\right)}{\pi\sqrt{1-\nu} \lambda_p} \dots\dots\dots (7.8)$$

Where M, G, b, ν are determined in *Table 7.3*. The Orowan strengthening is mainly based on \bar{r} (the mean radius of a circular cross-section in a random plane for a spherical precipitate) and λ_p (the inter-precipitate distance).

In coarse grained Al 6061 alloy, the commonly accepted precipitation sequence is [210]

“*Super Saturated Solid Solution (SSSS) → Cluster formation/ G.P zones (coherent) → β'' (coherent) → β' (semi coherent) → β (stable Mg_2Si)*”.

At T6 condition in coarse grained material, the matrix renders strength mainly from β'' *meta stable phase*, which is coherent with the matrix. On the other hand in cryogenic deformed Al 6061 alloy, the observed sequence is (chapter 6)

Super Saturated Solid Solution (SSSS) → Cluster formation/ G.P zones (coherent) → β'' (coherent)/ β' (semi coherent) → β (stable Mg_2Si)” which is not same as bulk material.

As observed in the TEM micrographs, deformed material might possess both β'' and β' precipitates [269]. In both the cases (in bulk and deformed), it is expected that the strengthening of the matrix is from coherent/semi coherent precipitates of metastable Mg_2Si phase. In this case, the strengthening of the matrix is by dislocation shearing mechanism rather than Orowan dislocation bypass mechanism [295]. Moreover, Orowan dislocation bypass mechanism is often used for spherical, hard and non-coherent particles without lattice continuity between precipitates and matrix [296]. In Al 6061, the various phases exist as; β'' phase as needle shaped precipitates, β' as rod shaped precipitates and β as platelet shape. β is stable phase and it is completely incoherent with the matrix, and the strength rendering to the matrix is not significant. There is no parameter in Orowan’s equation accounting for intrinsic properties (i.e., chemical composition; crystal structure) and orientation of the precipitates with respect to matrix. In addition to this, the precipitate morphologies observed in aged samples indicate the size and distribution and type of precipitates may vary locally, due to inhomogeneous structural features in the material.

Table 7.2 Values of parameters used in the equitation's (7.2), (7.3), (7.4), (7.5), (7.6) and (7.8)

Notation	Meaning	Values	Unit
A	Constant	13.3	Dimensionless
B	Constant	8.8	Dimensionless
C	Solute content	-	Wt.%
β	Constant	1.13	Dimensionless
γ	Constant	1	Dimensionless
σ_0	Peierls-Nabarro stress	20	MPa
M	Taylor's factor	2.25	Dimensionless
α	Material dependent constant	0.3	Dimensionless
G	Shear modulus	26.2	(GPa)
b	Burgers vector	0.286	nm
k	constant	0.04	Dimensionless
f	Fraction of HAGB	0.28(before ageing)	Dimensionless
		0.44 (after ageing)	Dimensionless
D_B	Grain boundary spacing	0.24 (before ageing)	μm
		0.31 (after ageing)	μm
θ_{LAGB}	Average value of LAGB misorientations.	4.81	Degrees
		5.7	Degrees
ν	Poisson ratio	-	Dimensionless

Obliviously, difference in diffusion rates is possible with respect to grain interior, grain boundary, high dislocation tangled zones, partially and fully recovered grains. It may be mentioned that TEM observation is restricted to very narrow region. Owing to the above mentioned variances that influence the estimation of precipitation strengthening contribution in Al 6061 cryoforged and peak aged alloy, the strengthening contribution from precipitates is estimated by subtracting the other strength components from various mechanisms from yield strength of the peak aged MDFed material. The obtained value is considered to be due to precipitation contribution to the strengthening and it has been compared with the value obtained for T6 coarse grained alloy. The estimated yield strength in the as forged material is nearly

matching with the experimental value. In T6 bulk material, the improvement in yield strength due to precipitation hardening is 170 MPa. The drop in strength due to increase in grain boundary spacing and reduction in dislocation density in MDF 9 cycles peak aged material is 88 MPa. The experimental yield strength of the MDF 9 cycles peak aged material is 409 MPa. This shows that the raise in yield strength due to precipitation hardening in UFG material is 110 MPa, which is nearly nearly 35% lower than that of it in the coarse grained material. It can be attributed to presence of post β'' phase, which reduces the fraction of β'' phase. In addition to this, the coherency of β'' phase in UFG material is questionable. In deformed material, the presence of dislocations may affect the misfit strain that develops due to precipitates coherency with the matrix.

7.1.4.2 Work hardening rate and Ductility

In Al metal and alloys, the various factors that influence ductility of the UFG materials are grain size, grain boundary character, amount of dislocation density, size and nature of the second phase particles, and testing temperature by neglecting texture effect. In the present investigation, after MDF up to 9 cycles, the material possesses around 5% plastic deformation with very little uniform elongation. At lower strains, the % of plastic strain is quite reasonable, but it is with lack of uniform elongation. The uniform elongation of the UFG material depends on the fraction of HAGBs and dislocation density as reported in the literature [297] [298], [299] [300]. In the present study, in the as forged material, with increasing MDF strain, the fraction of high angle grain boundaries has increased but the grain size has reduced. Among the different forged conditions, the maximum strained samples possess relatively more fraction of high angle grain boundaries but failed at early stage without any sign of increment in uniform elongation. This indicates the role of dislocation density in enhancing % of plastic strain. Upon ageing treatment, the grain boundary spacing is increased and dislocation density is reduced as compared to the as forged material. This led to increase in mean free path for dislocation movement and enough space to accommodate dislocations, which resulted higher uniform plastic strain in the material.

7.1.5 Conclusions

1. An Al 6061 alloy, in super saturated solid solution state, has been subjected to multidirectional forging at cryogenic temperature up to maximum true strain 5.6. The starting material with grain size of 300 μm length and 80 μm widths has been refined to an average grain size of 250 nm.
2. The observation of tensile test results after cryoforging indicates that the material exhibits negative work hardening rate due to inability to accommodate dislocations during deformation. Low temperature ageing led to tremendous improvement in yield strength (YS-50 MPa), ultimate tensile strength (UTS-100 MPa) and work hardenability of the material at room temperature.
3. The high strength in 5.6 true strained peak aged material is attributed to partial solid solution strengthening, precipitation hardening, Orowan strengthening, grain size strengthening, and dislocation strengthening.
4. The increase in tensile elongation and work hardenability is attributed to formation of dislocation free fine crystals and effective pinning and accumulation of dislocations through fine nanosized precipitates.
5. The calculated precipitation strengthening from UFG material (90 MPa) is inferior to the value that obtained from undeformed coarse grained material (150 MPa). The reasons could be; i) the presence of dislocation has reduced the coherency of the precipitates with the Al matrix, ii) deformation led to transformation of β'' (fine needle shaped phase) to β' (rod shaped phase).

7.2 Evolution of microstructural homogeneity in cyoforged Al 6061 alloy

7.2.1 Introduction

The summary of the first section of this chapter suggests that UFG structures with reduced dislocations at the interiors would be beneficial to obtain better precipitation hardening response. Achieving dynamically recrystallized grains with dislocation free interiors in super saturated solid solution state is a challenge task due to technical difficulties in SPD processes. Kapoor et al., have conducted MAF through confined channel die forging at room temperature on commercial pure Al [234]. It was reported that, beyond equivalent strain 4.6, softening is observed. At equivalent strain ~ 6.8 , increased fraction of high angle grain boundaries are observed, on the contrary, geometrical dislocation density is reduced. It was reported that fraction of high angle grain boundaries and geometrical dislocation density are related inversely to the grain average misorientation (GAM). GAM is the measure for area fraction of dynamically recrystallized grains. It has been reported that, commercial pure Al has shown sign of formation of dislocation free grains through dynamic recrystallization after 4.6 strain at room temperature. Whereas in the present investigation even after true strain 5.4 softening has not been observed. However, TEM investigation shows deformed sample with true strain of 5.4 exhibits evolution of UFG/NS grains with reduced dislocations. With the aim of developing dislocation free grains, the deformation strain has been extended to maximum 6. It was difficult to extend the strain beyond 6 due to distraction of the sample dimensions by barreling.

Despite of the several advantages of MDF, the disadvantage is due to its strain localization. The inhomogeneity in deformation exists inherently in MDF process due to the existence of the dead zone between the punch and the surface of the sample. It was reported that with increasing strain, the degree of inhomogeneity has been decreased in closed die MDFed Al 6061 alloy at room temperature. Liu et al., [85] have observed large scale of shear bands due to strain localization in AA 3104 alloy processed by multiple constrained compressions. Shi et al., [301] have conducted simulation studies on effect of friction on compression load, effective strain, damage value and maximum principle stress during multi axial compressions. It was reported that increase in friction coefficient leads to increase in strain inhomogeneity. Proper measures have to be taken to reduce the friction coefficient for enhancing the homogeneity in the

microstructure. In the present work cryoforging has been performed while the sample was dipped in the liquid nitrogen. Hence it is difficult to apply lubrication. Also, the grain refinement in high stacking fault energy materials at room temperature takes place through slip. However the deformation at very low temperatures (-196 °C) has suppressed of dynamic recovery due to the restricted slip mechanism at very low temperature and the microstructural refinement may occur through the formation of large scale micro shear bands as observed in the previous section of this chapter. Therefore, in the present section, the objectives are twofold. i) To produce UFG structure with reduced dislocation densities in supersaturated solid solution state, and ii) To investigate the evolution of microstructure at various geometrical locations of the sample. The mechanisms of formation of ultrafine grains in the Al 6061 alloy during MDF were substantiated through detailed analysis of deformation and micro shear bands formed upon severe deformation of the sample through EBSD, and hardness measurements.

7.2.2 Experimental details

Samples with $27 \times 30.5 \times 33 \text{ mm}^3$ were machined and subjected to solution treatment at 520 °C for 3 hours followed by water quenching at room temperature. After quenching, samples were subjected to MDF at liquid nitrogen temperature. The detailed procedure for MDF at cryogenic temperature has been discussed in the previous section.

Samples were forged up to different cumulative strains ($\sum \Delta \epsilon_n = 1.8$ (3 cycles), $\sum \Delta \epsilon_n = 3.6$ (6 cycles), $\sum \Delta \epsilon_n = 6$ (10 cycles). In each forging pass, strain 0.2 ($\Delta \epsilon = \ln (h_0/h = 0.2)$) was applied and total strain after each cycle is 0.6. The mechanical properties of the deformed alloy were investigated through hardness by measuring it at room temperature. For this, samples after successive forging cycles (of 3, 6, and 10) were sectioned along the central plane, which is perpendicular to the last forging pass. Samples were polished through mechanical grinding to obtain mirror like polished surface. Measurements were recorded on the surface following rectilinear grid pattern with 8×10 vertical and horizontal traverses. Since the samples are solid solution treated prior to cryoforging, proper care was taken to prevent heat generation during sample preparation for hardness measurements.

The evolved microstructure at different cumulative strains before and after MDF was investigated through electron back scattered diffraction (EBSD) technique. For samples forged up to 3 cycles and 6 cycles, the EBSD scan was taken at center of the sample, whereas for 10

cycles forged sample, microstructural study was performed at various locations starting from center to edge on central plane. Standard polishing techniques were used to prepare the samples for characterization of microstructures using EBSD. The grain size and grain boundary misorientation were analyzed using Tex SEM Laboratories (TSL) orientation imaging microscopy software. The step size used for EBSD scanning of MDF samples with cumulative strain $\sum\Delta\epsilon_n = 1.8$ and $\sum\Delta\epsilon_n = 3.6$ was 100 nm, whereas for samples with cumulative strain $\sum\Delta\epsilon_n = 6$, it was 70 nm. *Figure 7.22* shows the sampling locations for hardness and EBSD measurements from the as forged blocks.

The DSC experiments were performed by using Perkin Elmer Pyris Dymond instrument under pure nitrogen atmosphere. The starting temperature is above the room temperature (30 °C). Samples with 0.7 mm thick are sliced from the core of the forged blocks. The samples weighing 30 mg were prepared by punching and grinding of sliced sheet. Proper care was taken during sample preparation to prevent heat generation in the sample. Pure aluminum with same weight was used as a reference sample.

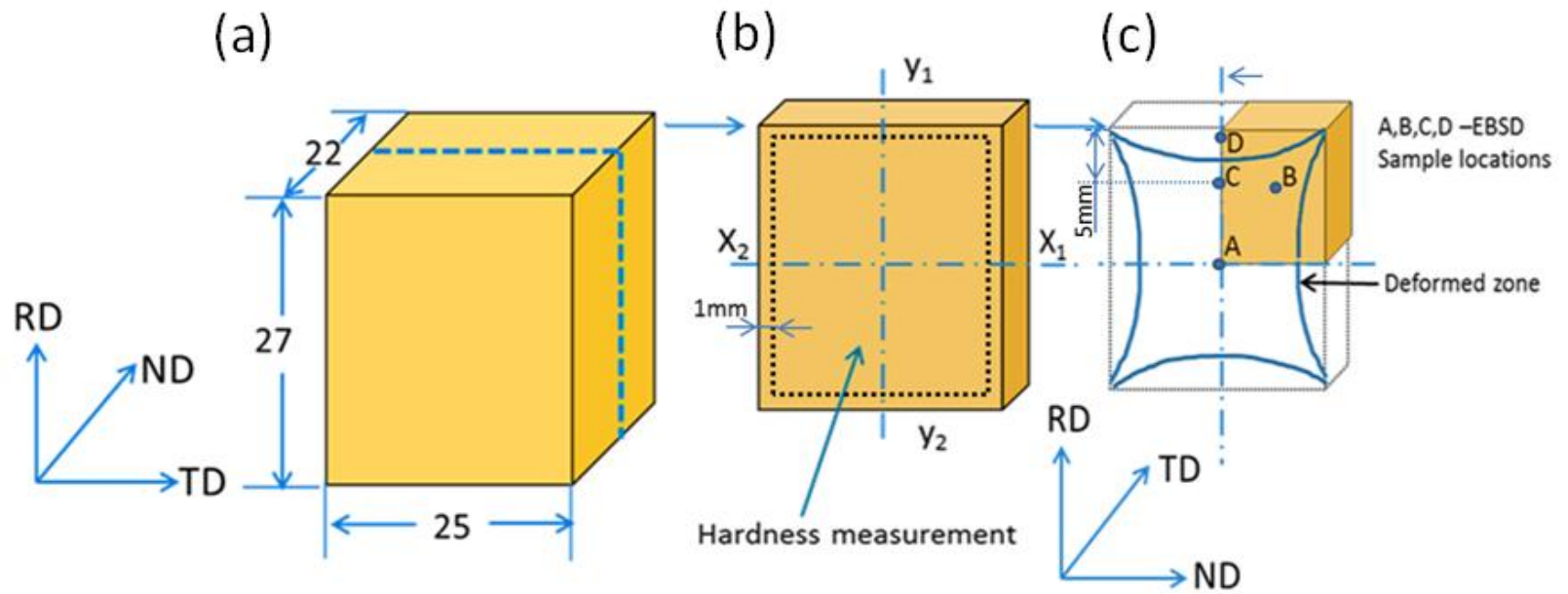


Figure 7.22: Schematic representation of sampling for mechanical and microstructural studies in MDF sample. (a) Sectioning of MDF sample, (b) Location of hardness measurements, (c) A – D represents location of EBSD scans.

7.2.3 Results

7.2.3.1 Variation in Hardness

Figure 7.23 shows the variation in hardness along the central plane in 3, 6 and 10 cycle's cryoforged Al 6061 alloy. The plots are generated by using individual hardness values at various locations from the center to surfaces. Total of 180 measurements were taken in each sample. At the edges, 1mm gap was given from the measurement zone. It is evident from the hardness contour plots that the average hardness value is increasing with increase in deformation strain. After 3 cycles, the maximum hardness observed at the center is 95 Hv, which is 75% larger than the unforged solid solution treated material. There is a drop in hardness while moving from center (95Hv) to the edge (83Hv), which is a typical behavior of multi directional forged sample. The similar trend is observed in all the strained samples. After 6 cycles, the maximum hardness observed at center is 107 Hv, whereas the minimum hardness observed at the edge is 97 Hv. After 10 cycles, the distribution of hardness on the surface indicates saturation point and interestingly the value at the center (117Hv) is reduced as compared to the value away from the center (120 Hv). Despite the slight difference in hardness values relatively from center to the area near to the surface, the overall increase in hardness is significantly higher as compared to the hardness of starting material. The hardness value recorded near to the surface in 10 cycles samples is 110 Hv and the dead zone is decreased with increasing strain. The obtained hardness distribution is used to elucidate the microstructure evolution at various geometrical locations of the sample through detailed EBSD analysis.

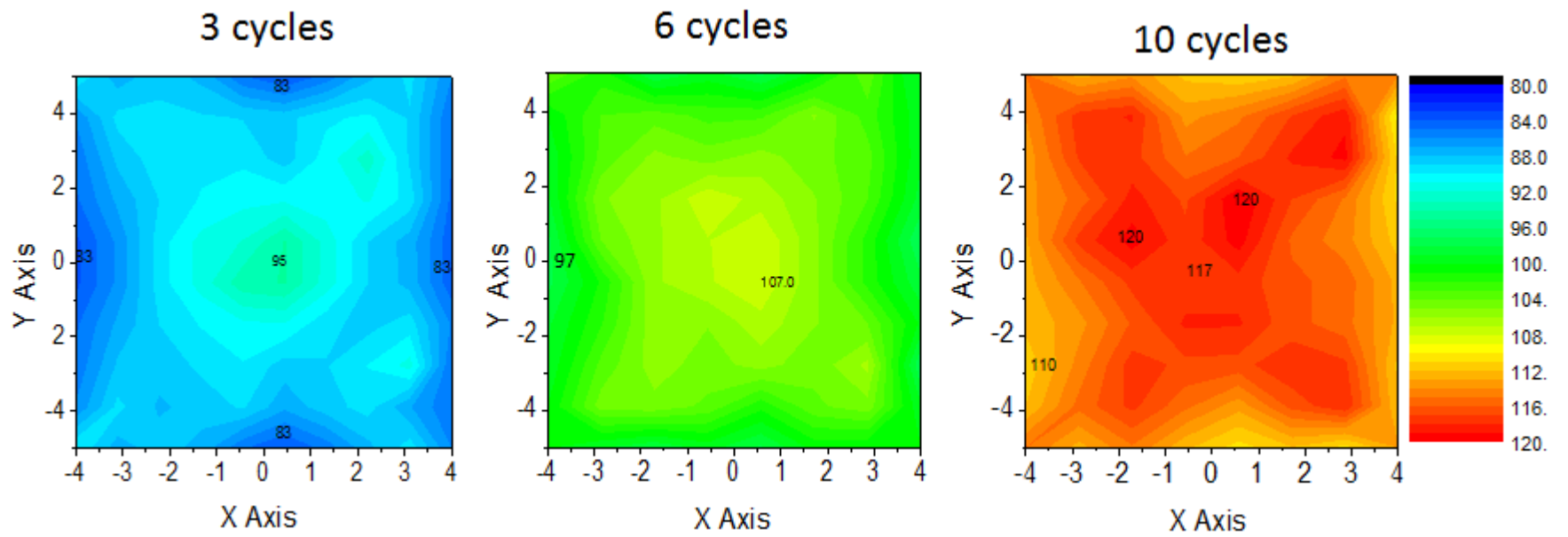


Figure 7.23: Vickers hardness distribution plots on central plane of MDF material with various MDF cycles; 3 cycles, 6 cycles, 10 cycles.

7.2.3.2 Evolution of Microstructure

After 3 Cycles

Figure 7.24 shows the EBSD micrographs of 3 cycles cryoforged (true strain ($\sum\Delta\epsilon_n = 1.8$)) Al 6061 alloy. The EBSD scan is performed at the center of the forged sample. *Figure 7.24(a)* shows orientation image micrograph, where the location “P” indicates the unindexed points due to the presence of coarse intermetallic particles. The data is not partitioned due to the removal of data points at high angle grain boundaries. In *Figure 7.24(b)* (Image quality map (IQ map)), white line indicates original grain boundaries, which corresponds to high angle misorientation. It is remarkable to see that after 3 cycles of MDF, the deformed microstructure contains very fine shear bands in various directions, which are typical features in MDFed material. The size of the shear bands at lower strains ($\sum\Delta\epsilon_n = 1.8$) observed in the present study are very fine as compared to the initial (coarse) grain size of the material. Hence hereafter they will be called as microshear bands (MSBs) [302]. The MSBs are restricted to within the coarse grains. According to Segal [303], typical features of shear bands (SBs) are as follows; i) They are planar very thin materials layers inside of which strains are significantly larger than outside, ii) An average distance between bands approximates to a cell size, iii) Crystallographic multi-slip activity in SBs results in gradually increased angles of misorientation along their boundaries, iv) SBs have non-crystallographic orientations that always follow to continual principal shears and it penetrate few grains without a noticeable deviation. Upon origination, SBs substitute a preexisting structure and define the final structure of heavily deformed metals.

Figure 7.24(c) represents the enlarged area inside the box shown in *Figure 7.24 (a)*. Layered structure with elongated grains aligned around 45 degrees to the sample axis can be observed. Black lines depicted with arrow marks shows strain induced grain boundaries, which are characterized by high angle boundaries (HAGBs) (misorientation $> 15^\circ$) and its fraction is estimated as 20%. The average spacing between HAGBs are found to be 1 μm . Blue lines indicated with arrow mark represents low angle grain boundaries (LAGBs) (misorientation $< 15^\circ$) in the range of $5^\circ - 15^\circ$ and its fraction is 23%. In addition to above two categories, LAGBs within the range of $2^\circ - 5^\circ$ are shown in grey color.

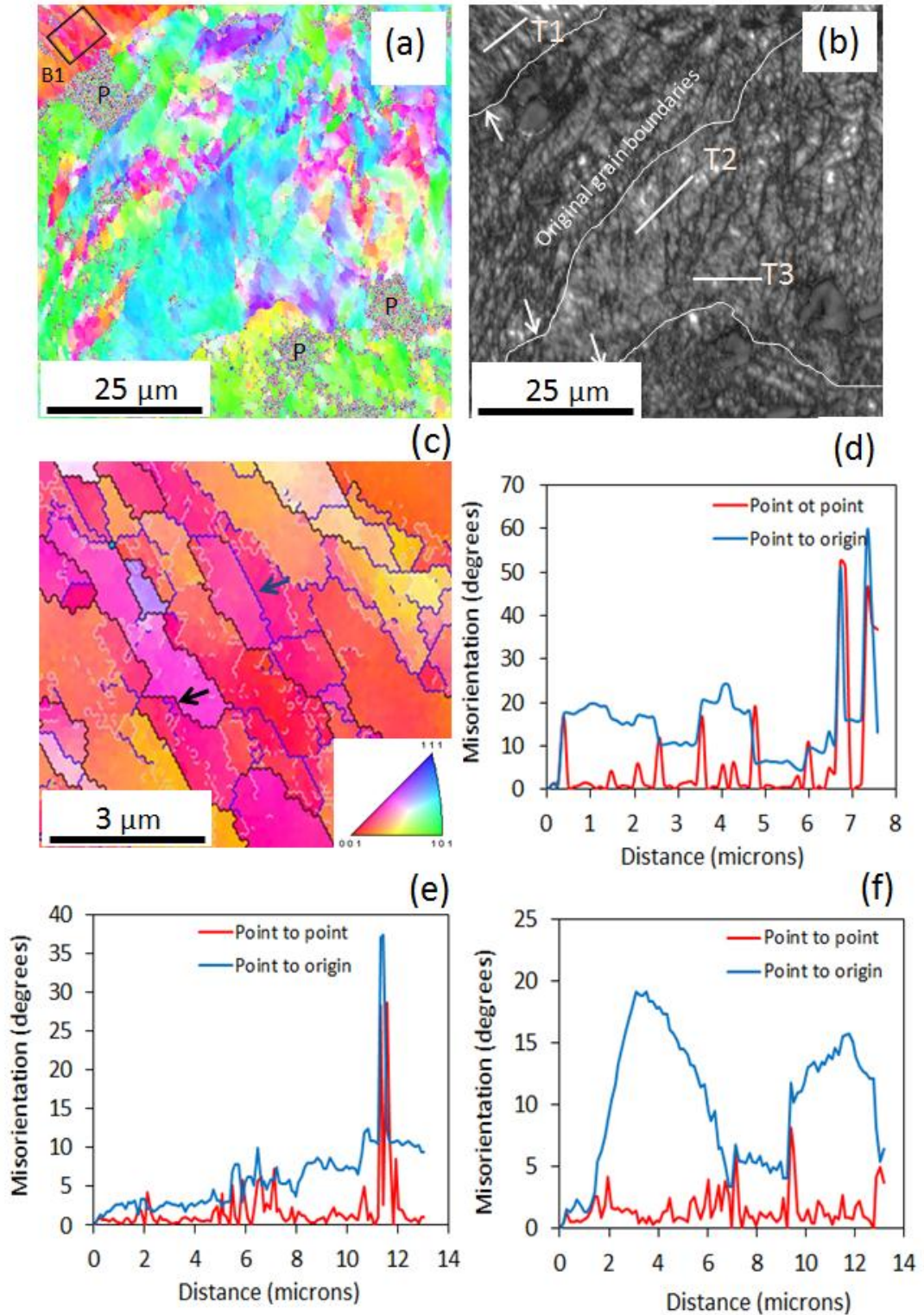


Figure 7.24: EBSD micrograph of 3 cycles MDF; a) Orientation image micrograph, b) Image quality map, c) Area marked with square box in the image (a), d) - f) Misorientation profiles along the line T1,T2 and T3.

Orientation gradients inside the individual subgrains indicate existence of dislocation densities. *Figure 7.24(d), (e), and (f)* shows the misorientation developed along the lines T1, T2 and T3. In misorientation profiles (*Figure 7.24 (d), (e), (f)*), the red line indicates the misorientation between point to point ($\Delta\theta$), whereas the blue line indicates the point to origin ($\Sigma\Delta\theta$). Each point corresponds to the step size of 0.1 μm used during the scan. Misorientation changes along T1 shows existence of several subgrains with an average width of 500 nm. The repetitive shear action between thin layers increases misorientation between them. Point to point misorientation along T2 and T3 indicates existence of subgrain structure with low angle grain boundaries. The band type structure is mainly observed in $\{001\}$ grains. During MDF, formation of MSBs plays a vital role in the formation of new UFGs. With increasing strain, new fine crystals are formed homogeneously throughout the material. Such a microstructural evolution can be observed from 10 cycles of MDFed sample.

After 6 Cycles

Figure 7.25 shows the EBSD results obtained from a sample MDFed up to cumulative strain of 3.6 at cryogenic temperature. From the orientation micrograph (*Figure 7.25(a)*), it is evident that two types of bands structures at different crystallographic orientations are seen. It is observed from *Figure 7.25 (b)*, that with increasing strain, the frequency of formation of MSBs has increased in different directions due to MDF. And also, the growth of MSBs to macro shear bands by spreading in to the neighboring grains with differing in crystallographic orientation with respect to parent grain can be observed. For a better visibility, these features are drafted through free hand sketch as shown in *Figure 7.25 (c)*. *Figure 7.25 (d)* shows the misorientation distribution along the line T1 in *Figure 7.25(a)*. Primarily two types of grain boundaries can be observed along the line T1. Type one is high angle grain boundaries, whose misorientation is more than 35° . The type two is the boundaries whose misorientation is in the range of 5 to 13° . Line T1 is taken in the region which has orientation close to $\langle 001 \rangle$. In contrast to line T1, T2 has been taken in region whose orientation is in $\langle 111 \rangle$. The type of microstructure is almost equiaxed in nature, which is developed through intersection of MSBs of different directions. Line T3 shows the region whose orientation is along $\langle 111 \rangle$. The misorientation distribution in *Figure 7.25* indicates that with increasing strain, the boundaries are transforming to high angle grain boundaries.

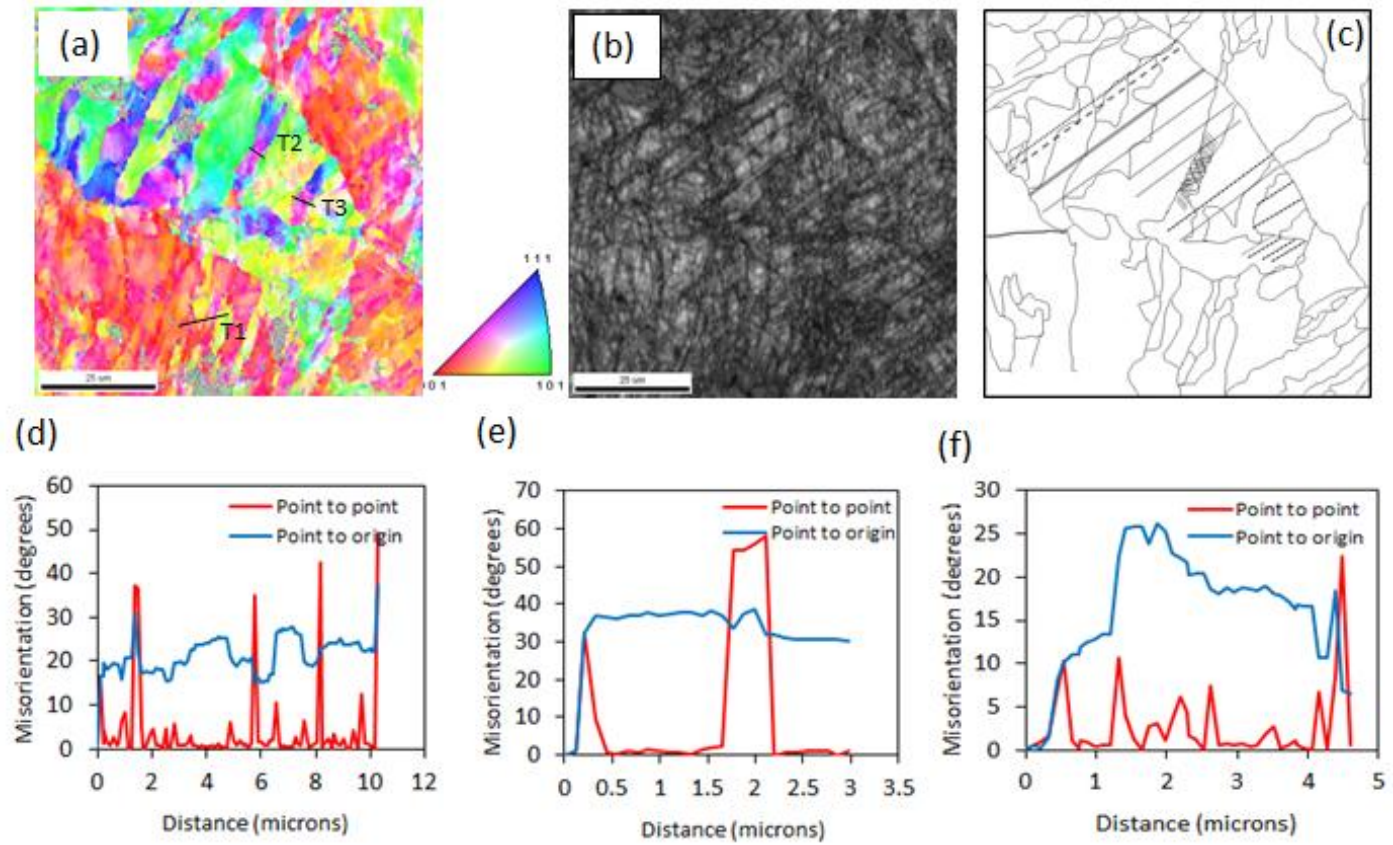


Figure 7.25: EBSD micrograph of 6 cycles MDF; a) Orientation image micrograph, b) Image quality map, c) Free hand sketch of MSB developed in 6 cycles MDF; d)-f) Misorientation profiles along the line T1, T2 and T3.

By changing the loading axis during MDF, it led to intersecting of MSBs which caused the formation of subgrain in the interior zone of intersecting MSBs.

After 10 cycles

Microstructure evolution and its homogeneity from the center to edge at various locations along the central plane were investigated in 10 cycles of MDFed sample. The locations of the EBSD scans were denoted as A, B, C and D as shown in *Figure 7.22(c)*. After 10 cycles of MDF, deformed structure with network of MSBs were observed from corner to corner by forming “X” shaped deformed zone. The position of ‘A’ indicates the location near to the center, where the intersection of shear bands from corner to corner takes place, ‘B’ is around 5mm distance from both, side and top edges, and ‘C’ indicates between center to edge (5 mm distance from top edge), whereas ‘D’ indicates at the near to the edge, which is in the dead zone.

Figure 7.26 shows the image quality map obtained through EBSD from the location A. The area of the scan is $40 \times 60 \mu\text{m}^2$ and it shows very fine subgrain structure with equiaxed morphology. *Figure 7.27* and *Figure 7.28* shows the area with $25 \times 25 \mu\text{m}^2$ dimensions, which were cropped from *Figure 7.26* and analyzed to estimate the fraction of HAGBs, LAGBs and dynamically recrystallized grains. For a clear distinguishing, image quality maps were overlaid with HAGBs (shown in green color in *Figure 7.27(b)*) and LAGBs (shown in red color *Figure 7.26(c)*). The area fraction of dynamically recrystallized grains is estimated as 0.31 (*Figure 7.28(a)*). The average grain size of the dynamically recrystallized portion is found to be $0.61 \mu\text{m}$ (*Figure 7.28(b)*). To estimate the dynamically recrystallized grains from EBSD micrographs, grain orientation spread (GOS) is used. For typical recrystallized grains, the value of GOS should be less than 1° . In *Figure 7.29* (at location B), image quality map with $30 \times 60 \mu\text{m}^2$ area has shown several hundreds of subgrain with nearly uniform size. The subgrain morphology is elongated in nature. *Figure 7.30* shows the cropped area ($25 \times 25 \mu\text{m}^2$) from *Figure 7.29*. The area fraction of dynamically recrystallized grains is estimated as 0.15 (*Figure 7.31(a)*). The average grain size of the recrystallized portion is found to be $0.41 \mu\text{m}$ (*Figure 7.31(b)*).

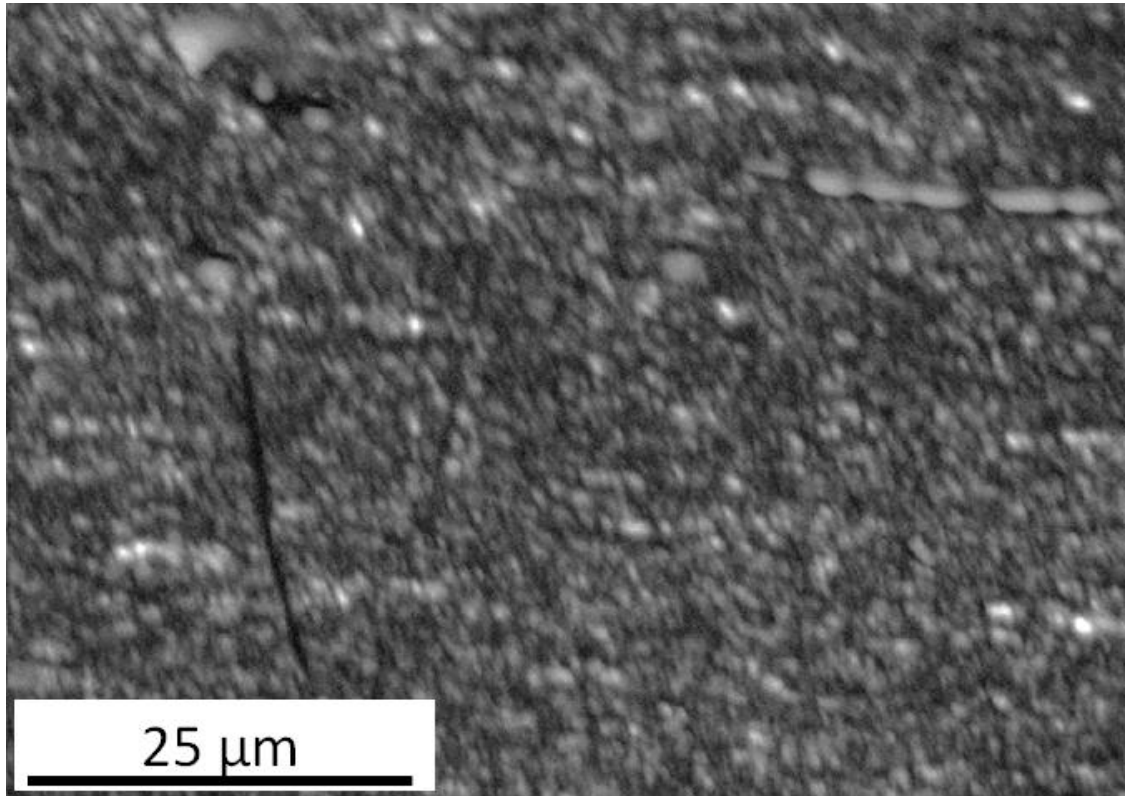


Figure 7.26: EBSD map (Image quality (IQ) map) of 10 cycles MDF Al 6061 alloy at location A shown in Figure 7.22(C).

EBSD scan taken from the location “C” as mentioned in the *Figure 7.22 (c)* is shown in *Figure 7.32*. Image quality map (*Figure 7.32 (b)*) shows the grain refinement through MSBs. As can be seen from the inverse pole figure and image quality map, the concentration of MSBs inside the grains has increased with increasing strain. The rectangular boxes marked in the inverse pole figure map (*Figure 7.32(a)*), show the grain refinement observed at various orientations. The morphology and size of the fine subgrain depend on initial orientation of the parent grain and loading axis. The grain size map and its distribution are shown in *Figures 7.32 (c) and (d)*.

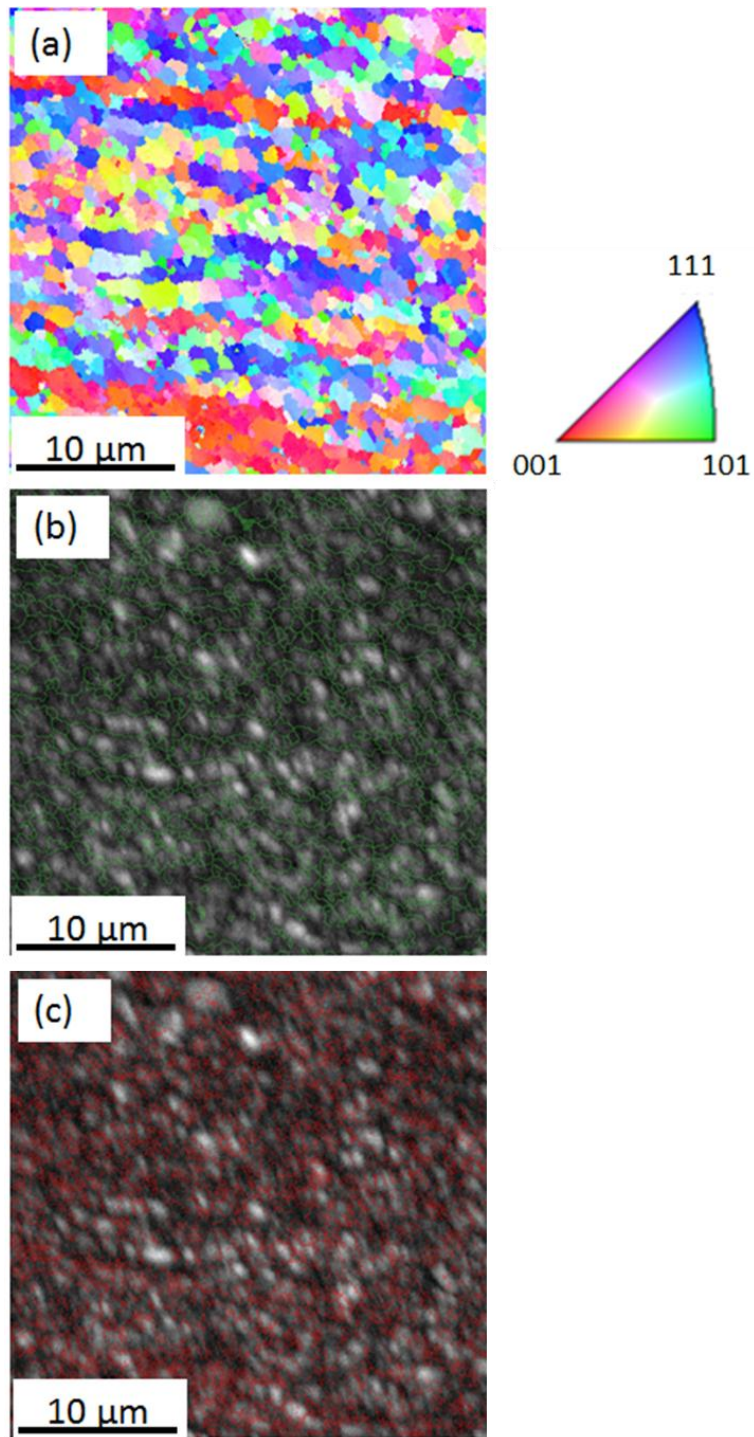


Figure 7.27: EBSD maps of cropped area from image shown in **Figure 7.27**; a) Inverse pole figure map, b) IQ map overlaid with high angle grain boundaries (green color); c) IQ map overlaid with low angle grain boundaries (red color).

Strain induced fine grains are primarily located along the grain boundaries of parent grains. It is evident from *Figure 7.32(c)*, at location C (in *Figure 7.22(c)*) that the microstructure primarily contains subgrain structure with low angle grain boundaries. *Figure 7.33(a)* shows the area cropped at the orientation parallel to $\langle 001 \rangle$ and it shows predominantly elongated grains. The average width of the elongated sub grains is found to be 850 nm. The misorientation angle of point to point varies from 3 to 15°.

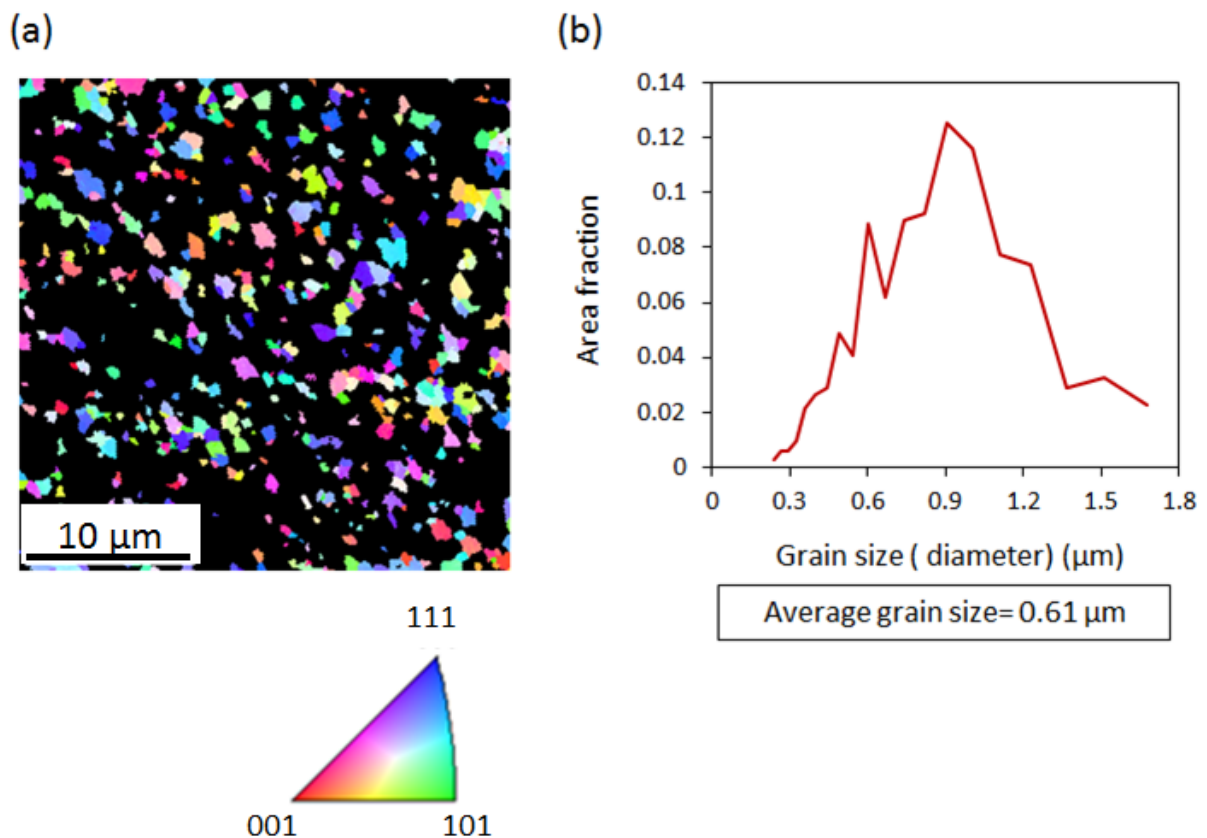


Figure 7.28: EBSD data of 10 cycles MDF Al 6061 alloy at location A as shown in **Figure 7.22 (c)**; a) Dynamically recrystallized grains partitioned using criteria, GOS <1; b) Grain size distribution plot of the partitioned area shown in **Figure 7.28(a)**.

The presence of high angle grain boundaries is also observed, which are transformed grain boundaries with increasing strain. *Figure 7.33(b)* shows the area cropped at the area oriented in

$\langle 111 \rangle$. Fine subgrains equiaxed in nature are evident from the figure. The formation of band structure and its transformation in to equiaxed has occurred due to multi directional slip. The misorientations of the subgrains are uniform and lower than 5° . *Figure 7.33(c)* shows subgrain structure evolution in the grains which are oriented in $\langle 101 \rangle$. The average grain size is found to be $1 \mu\text{m}$. The point to point misorientations are higher than the $\langle 111 \rangle$ orientation grains.

Figure 7.34 shows the EBSD results obtained from the location mentioned as D in *Figure 7.22(c)*, which is nearer to the edge. The microstructure reveals predominantly low angle grain boundaries with lamellar in nature having average grain boundary spacing nearly 3 to $4 \mu\text{m}$.

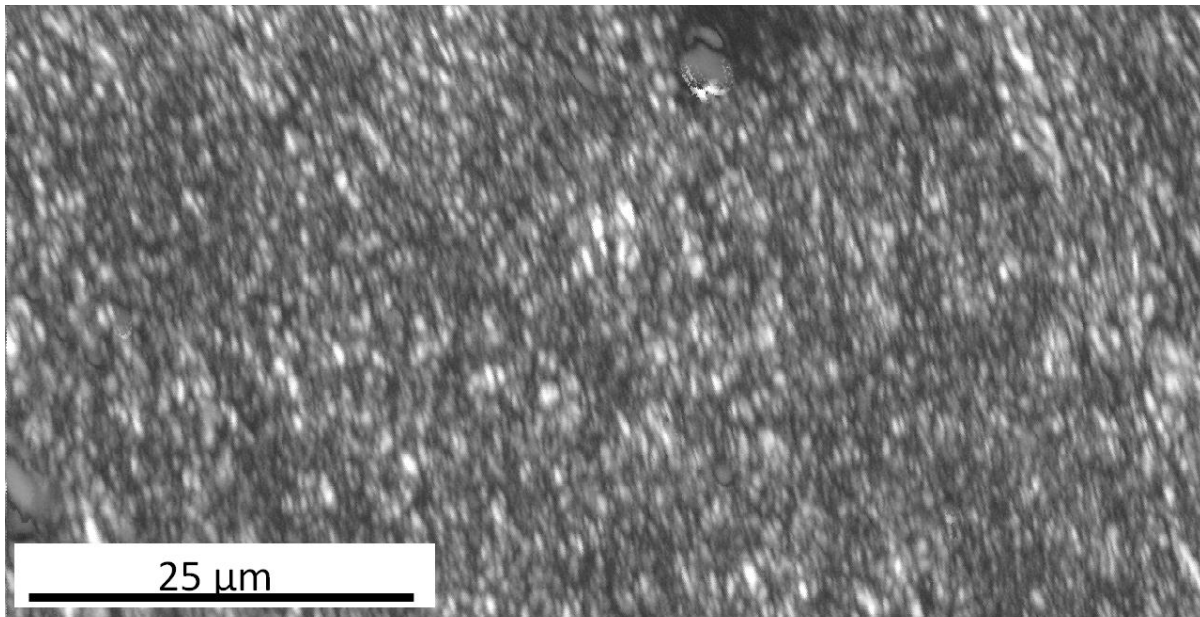


Figure 7.29: EBSD map (Image quality (IQ) map)) of 10 cycles MDF Al 6061 alloy at location B shown in Figure 7.22 (C).

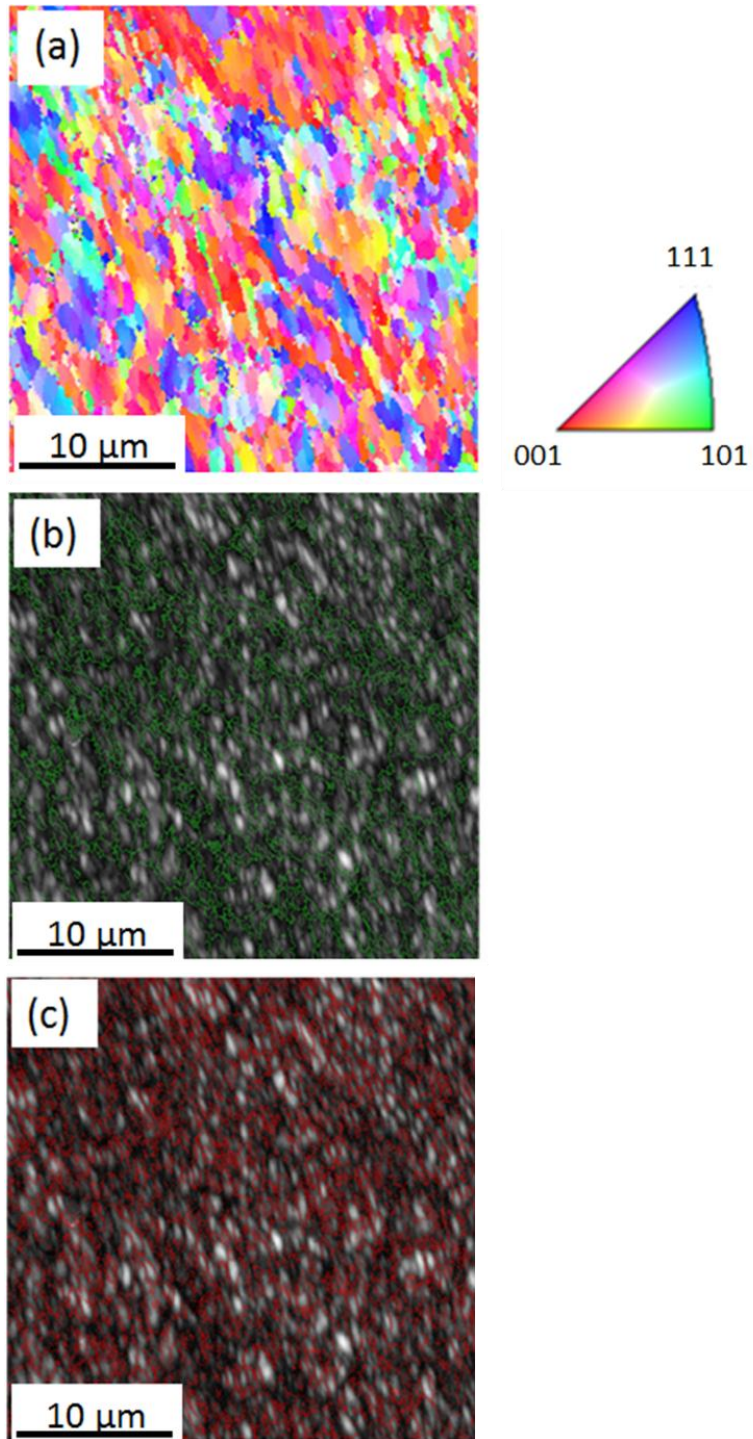


Figure 7.30: EBSD maps of cropped area from image shown in **Figure 7.29**; a) Inverse pole figure map, b) IQ map overlaid with high angle grain boundaries (green color); c) IQ map overlaid with low angle grain boundaries (red color).

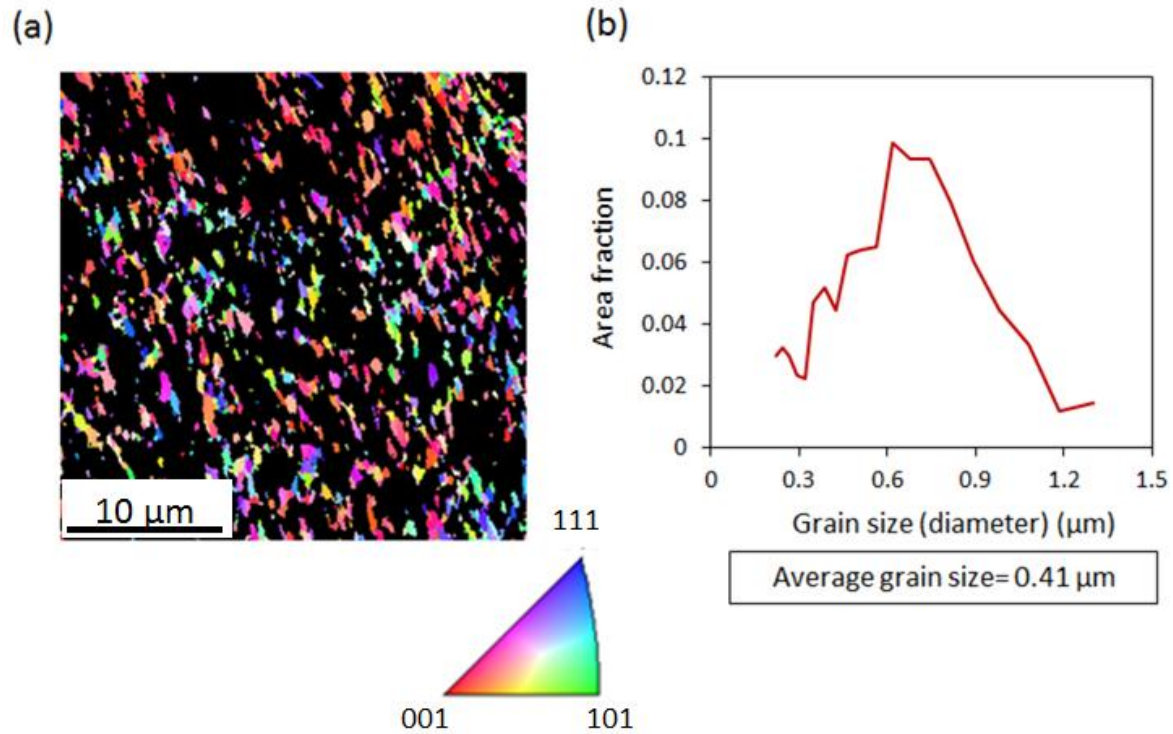


Figure 7.31: EBSD data of 10 cycles MDF Al 6061 alloy at location B; a) Dynamically recrystallized grains partitioned using criteria, $GOS < 1$; b) Grain size distribution plot of the partitioned area shown in **Figure 7.30(a)**.

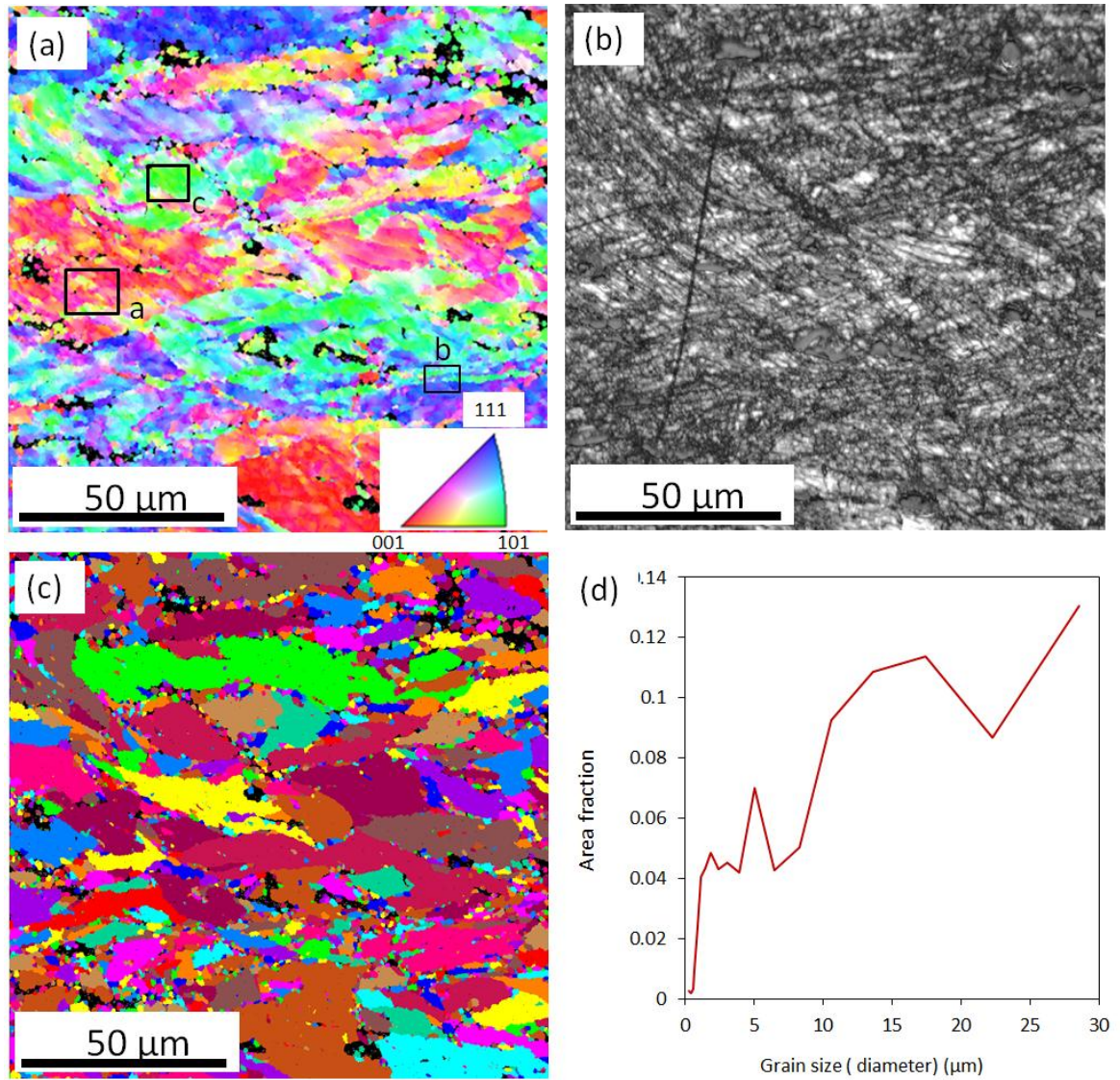


Figure 7.32: EBSD Maps of 10 cycles MDF Al 6061 alloy at location C as shown in **Figure 7.22(C)**; a) Inverse pole figure map, b) IQ map; c) Grain size map; d) Grain size distribution plot.

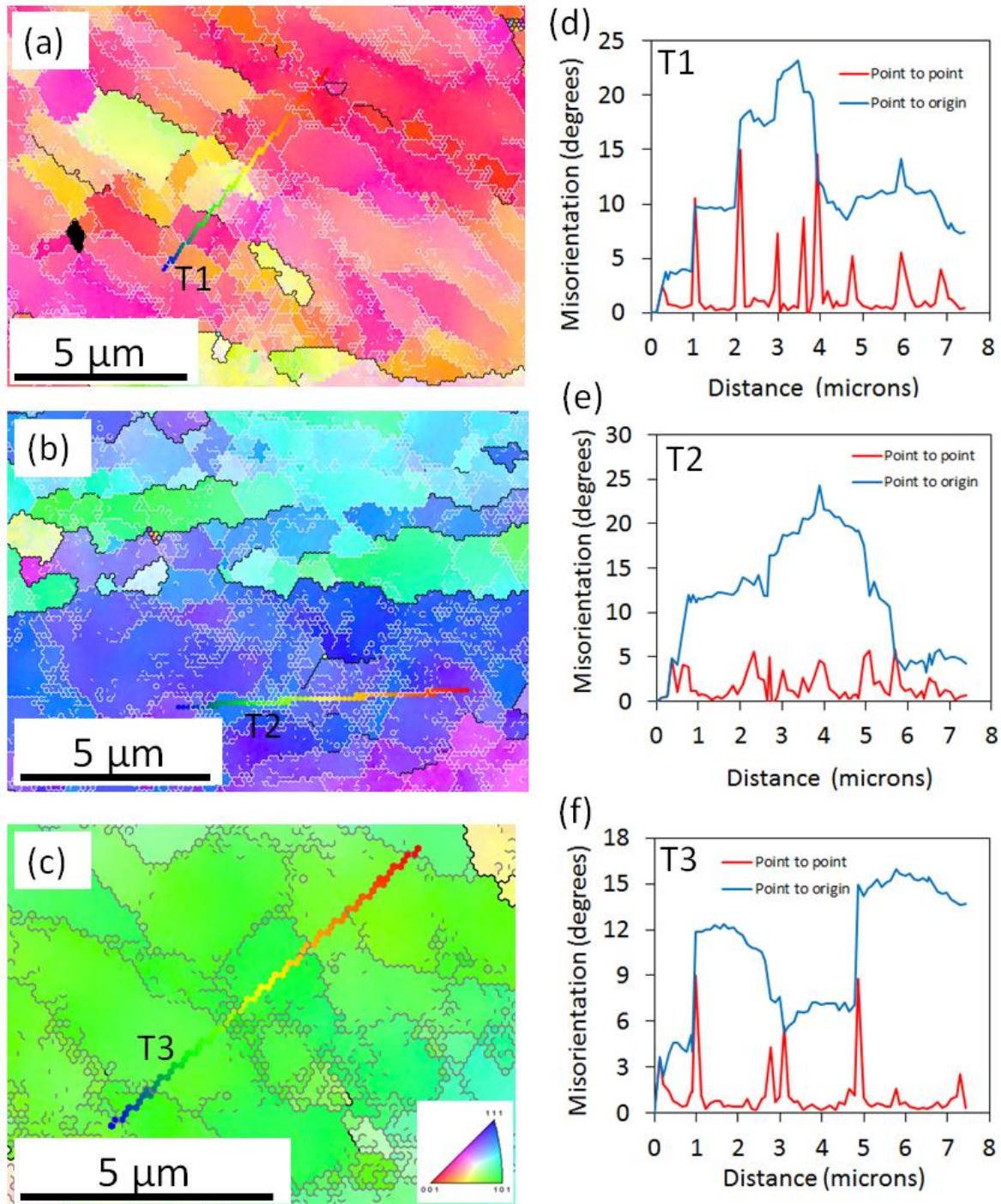


Figure 7.33: EBSD maps along with local misorientation profiles of location indicated with boxes in **Figure 7.32(a)**; a), b) and c) are inverse pole figure maps of the areas indicated in boxes a, b and c respectively, d), e), f) Misorientation profiles along the lines indicated in **Figure 7.33. a), b) and c)** respectively.

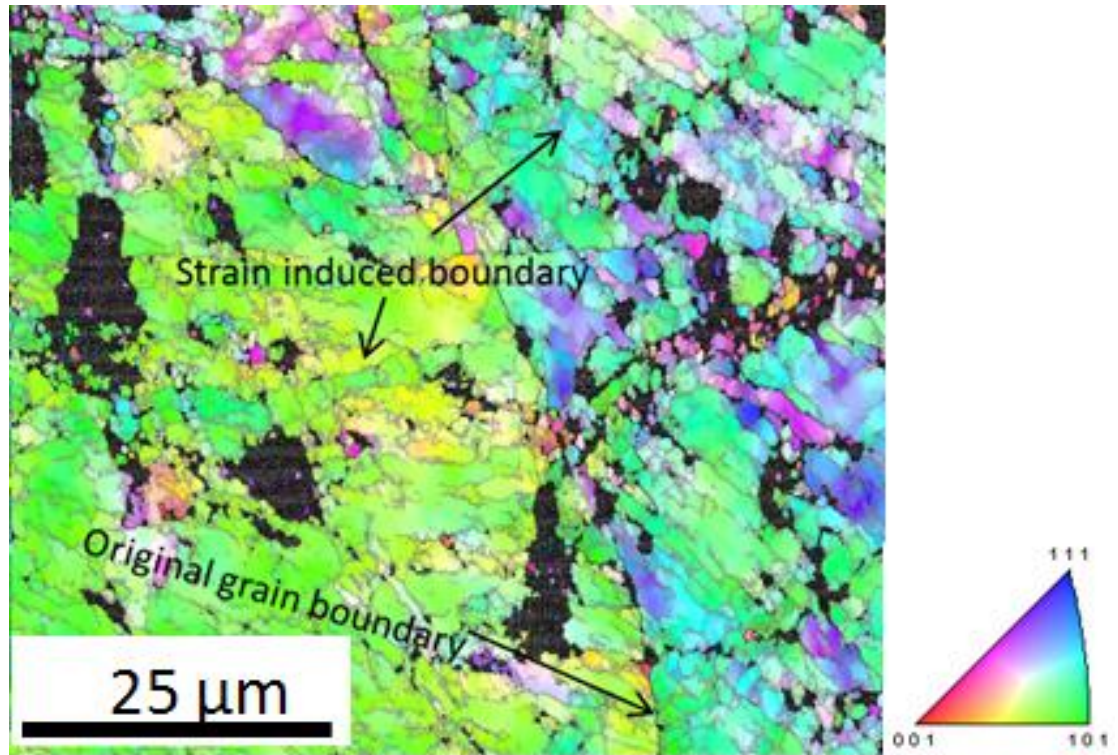


Figure 7.34: EBSD micrograph at near to edge (at location D in Figure 7.22 (C) in central plane of 10 cycles MDF sample

Misorientation Distribution

Misorientation distribution plots corresponding to the microstructure representing at three different states of MDFed sample is shown in *Figure 7.35(a)*. After MDF up to three cycles, the fraction of low angle grain boundaries (< 15 degrees) are around 92%. With increasing number of MDF cycles up to 6, there is no significant change in the fraction of LAGB. However, the fraction in the range of 5-15 °C is increased in 6 cycles MDFed sample. After 10 cycles of MDF, the fraction of LAGB has dropped to 70% and the corresponding HAGB are increased as observed from *Figure 7.35(b)*. Within 10 cycles of MDFed sample, the misorientation distribution at various locations such as A, B, C and D are shown in *Figure 7.35(b)*. By traversing vertically from center to edge, the intensity of LAGB peaks is increasing. At the edge (location D), 90% of the peaks are within the range of 1.5 to 5 degrees. At location B, the diffused population of peaks corresponding to high angle misorientation (> 15 degrees) is

observed as similar to the location 'A' (center). The volume fraction of the HAGB at 'B' is slightly lower as compared to the location 'A'. The variation in misorientation in the sample is attributed to the strain localization in the sample.

7.2.3.3 DSC studies

To investigate the state of second phase, DSC study is performed by taking the sample at the center of the sample block after forging. DSC curves with heating rate of 20 °C/min and testing range of 30 – 450 °C are shown in Figure 7.36. A thorough study of precipitation evolution that occurs in undeformed and deformed alloy at cryogenic temperature has been reported in our earlier work [269]. It was observed that deformation led to significant changes in the number and position of exothermic peaks, which are corresponding to precipitation process. The broad exothermic peak within the range of 50 to 175 °C is corresponding to cluster/G.P zone formation and the second exothermic peak corresponding to formation of β''/β' (major strengthening phase) metastable phases. It may be emphasized that the intensity of the second exothermic peak does not change with increasing strain. It is evident from the DSC thermo grams that there is no significant endothermic peak corresponding to precipitate dissolution that refers to formation of precipitates during the processing.

7.2.4 Discussions

In the present investigation, Al 6061 alloy was solution treated and water quenched followed by severely deformed through MDF at cryogenic temperature. Unlike cryorolling, the sample blocks were completely submerged in liquid nitrogen during cryoforging [276] [304]. It may be concluded from the Vickers hardness, EBSD and DSC measurements that dislocation free UFGs with high angle grain boundaries can be produced at supersaturated solid solution state by cryoforging. For Al 6061 alloy, the sufficient strain is observed as 6 or above to produce UFG grains. The sample size used in the present study is relatively bigger [305] [306]. Based on the observed Vickers hardness distribution and microstructure in 10 cycles forged material, it is

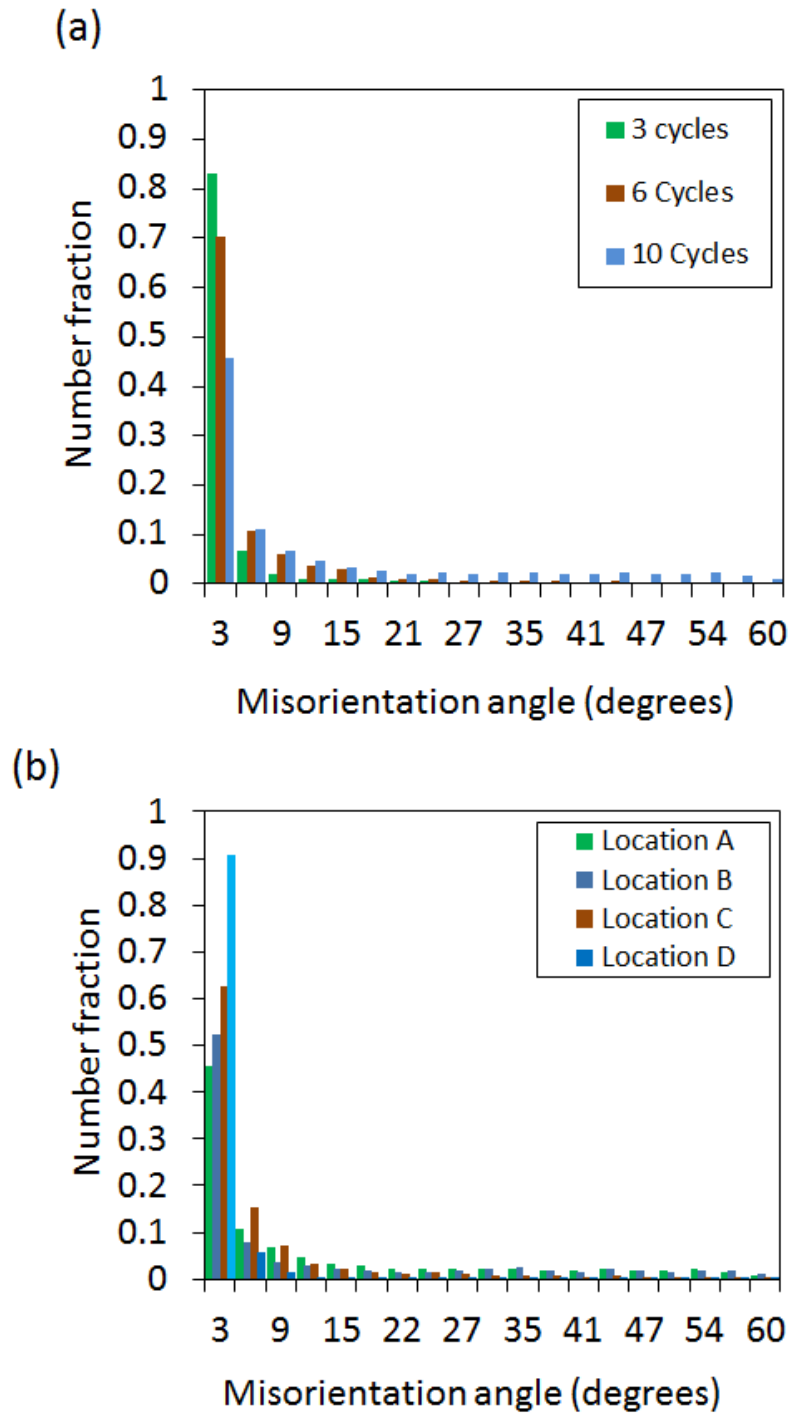


Figure 7.35: a) Misorientation plots of microstructure observed at various strain levels; b) Misorientation plots of microstructure at various locations on central plane of 10 cycles MDF sample; A,B,C and D.

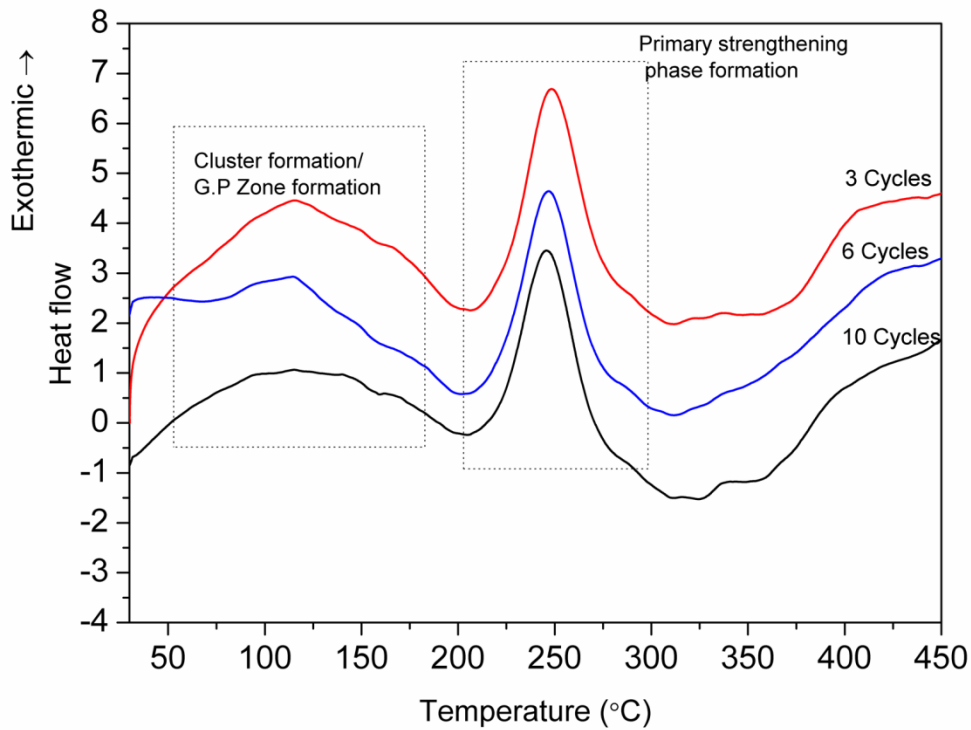


Figure 7.36: DSC curves of MDF sample after 3,6,10 MDF cycles.

reasonable to infer that with increasing number of forging cycles, the homogeneity of the microstructure is increased by spreading from center to corners. The obtained results are interesting as they facilitate to produce stable UFG structures in bulk materials with better precipitation strengthening.

There are several reports on homogeneity of microstructure in the UFG material developed through various SPD techniques [307] [308] [309]. The mode of deformation, amount of strain, stacking fault energy of the material and deformation temperature affect the microstructural homogeneity. In the present study, it is necessary to understand the evolution of microstructure with increasing strain at liquid nitrogen temperature for producing homogeneous bulk UFG material. A thorough microstructural observation through EBSD at different strain levels indicates evolution of UFG structure from coarse grained structure through grain fragmentation or subdivision by formation of MSBs during multi directional forging. With increasing deformation strain, the grain interiors were developed with MSBs. The advantage of

MDF is due to the fact that it enables the formation of MSBs in various directions [310]. The repeated deformation in multi directions led to crossing of shear bands of different directions (cross kink bands), which causes the formation of equiaxed axed grains [311].

After 3 cycles of forging, strain induced high angle grain boundaries are observed in the MSBs. From the TEM studies (previous section of this chapter), it was clear that combination of shear band structure with lamellar grain boundaries and equiaxed sub grain structure was observed [276]. At lower temperatures, the mode of deformation is primarily due to formation of MSB. It was suggested that the shear bands forms due to the instability of dislocations substructure [312]. A high stress concentration at the tip of shear bands enables them to penetrate in to neighboring grain [313]. At lower strains, the MSBs are restricted to within the grain. With increasing strain, the MSBs are penetrating through the grains as a macro shear bands.

TEM observations (previous section of this chapter (*Figure 7.5*)) shows, the formation of MSBs with 4-5 μm width consisting of several UFGs aligned along shearing direction. The average width of the UFG was found to be 0.2 μm . At higher strains, even finer (0.1 μm) UFG were observed in the shear bands. Due to repeated shear during forging, it led to increase in misorientation of the substructure boundaries in the shear bands. As reported by Korbel and Martin [313], macroscopic shear band formation involves nucleation of the microband (Generation of a first avalanche of dislocations) and its subsequent conversion into a macroscopic shear band while encountering grain boundary or if further long distance crystallographic glide is precluded.

The deformation structure that observed in 6 cycles of MDFed material (equivalent strain 3.6), shows several MSBs intersecting and forming thick band structures. The crystal orientation of these bands is completely altered with the matrix. With clear observation, it can be seen that these thick bands consists of several UFGs. The misorientation profiles across these bands (T2, T3 in *Figure 7.25(a)*) indicate significant high misorientation. The network of UFGs along these macro shear bands are attributed to the formation of cross kink MSBs during MDF. The new UFG grains are formed along the MSBs and with increasing strains, the volume fraction of MSBs has increased. It ultimately leads to spreading of UFG structure throughout the matrix. With increasing strain from 3.6 to 6, shear band structures have transformed into equiaxed UFG structure, which has spread homogeneously at the center. UFGs with GOS values lower than 1

indicates material has undergone dynamic recrystallization. The increase in the fraction of high angle grain boundaries and evolution of UFGs with GOS < 1 at the location A and B in 10 cycle's cryoforged material indicates that even at liquid nitrogen temperature, the dynamic restoration through recovery/recrystallization is significant in the Al 6061 alloy, which has high stacking fault energy.

In 10 cycles cryoforged material, the local inhomogeneity with respect to grain morphology is due to orientation difference of the matrix grains. This has been clearly seen from the microstructure observed at location C in 10 cycles forged material (*Figure 7.33*). Grains with different orientations consist of different morphology and size of cell structures. The orientation of the grains influences the misorientation of dislocation boundaries, its morphology, stored energy and dislocation densities of deformed structure as reported in the literature [198]. The microstructural observation after 10 cycles is in tandem with the hardness contour plots on the central plane. The present investigation has shown that processing of Al 6061 alloy by MDF (open die) up to 6 equivalent strain, led to formation of the UFG structure with mixture of dynamically recrystallized grains with dislocation free interiors and grains with dislocation filled at super saturated solid solution state. The dislocation free grains may influence the precipitation kinetics to realize improved tensile strength of the alloy.

7.2.4.1 Homogeneity after MDF

In the present investigation, the hardness maps and microstructural investigation through EBSD have shown the existence of structural inhomogeneity after 10 cycles of MDF (equivalent strain 6). The variation in hardness from the center to edge observed in the present work is in accordance with hardness variations reported for Al 6061 ECAPed samples [314]. The reports on SPD process (ECAP) indicates that with increasing number of passes and changing the strain path, inhomogeneity has been reduced [78] [314]. For achieving microstructural homogeneity using MDF, channel die forging and closed die forging would be better. However, open die forging is convenient to process the bulk samples at very low temperatures. Along with open die cryoforging, it is reasonable to adopt secondary process like cryorolling preceded by MDF [315], which could enhance the structural homogeneity, leading to better grain refinement in supersaturated solid solution of Al 6061 alloy.

7.2.5 Conclusions

Al 6061 alloy was successfully processed through MDF up to true strain of 6.0 at liquid nitrogen temperature (-196 °C) and the following conclusions are drawn based on the EBSD characterization, Vickers hardness measurements and DSC studies of the deformed samples.

1. Microstructural refinement was achieved through formation of MSBs during MDF of Al 6061 alloy. These bands have facilitated the formation of ultrafine grains with increasing plastic strain imparted to the samples.
2. Development of homogeneous ultrafine grain structure with high angle grain boundaries and dislocation free interiors were observed at the core and corner of the sample.
3. Dislocation free ultrafine grained structure in supersaturated solid solution was successfully achieved through MDF up to a true strain of 6. It may be mentioned that 6 is the critical strain to induce dynamically recrystallized grains in Al 6061 alloy at super saturated solid solution state through cryoforging.
4. Strain localization during forging led to structural inhomogeneity in the sample and it led to variation in microstructure from core of the sample to the edge.
5. Long range microstructural variation was due to inhomogeneous strain distribution from the sample core to the edge and the local microstructure variation was due to local strain gradients by shear band formation, presence of coarse undissolved constituent particles, and orientation of the grains.

Suggestions for Future Work

1. The present investigation has shown that, nanosized second phase precipitate particles play a significant role in retaining UFG structure by pinning down the grain boundaries. However, with increasing temperature and time, they tend to become unstable. Further investigation is required for introducing thermally stable nanoparticles and its effect on microstructural and thermal stability of UFG Al 6061 alloys.
2. It is well proved from the present study that, the dynamic ageing exhibits beneficial effect for improving mechanical properties of cryorolled Al 6061 alloy. The detailed investigation of the effect of various combinations of cryorolling followed by warm rolling temperatures with different induced deformation strain on precipitation hardenable Al alloys is required.
3. DSC studies of CR and WR materials have shown higher activation energy values for the formation of strengthening phase. A thorough investigation of the kinetics of precipitation in CR and WR materials through advanced characterization techniques such as Atom Probe Tomography (APT) is required.
4. The advantage of cryoforging for imparting high strain to the alloy at super saturated solid solution state, can be explored further to realize the maximum precipitation hardening effect in UFG Al alloy
5. A combination of cryoforging followed by rolling can be performed to obtain UFG sheets with better combination of strength and ductility.

References

1. Polmear, I.J. Light Alloys- Metallurgy of light metals. s.l.: Arnold, London, 1995.
2. Ruslan Z. Valiev, Yuri Estrin, Zenji Horita, Terence G. Langdon, Michael J. Zechetbauer, Yuntian T. Zhu. Producing bulk ultrafine-grained materials by severe plastic deformation. 4, 2006, JOM, Vol. 58, pp. 33-39.
3. Ruslan Z. Valiev, Terence G. Langdon. Principles of equal-channel angular pressing as a processing tool for grain refinement. 2006, Progress in Materials Science, Vol. 51, pp. 881–981.
4. Alexander P. Zhilyaev, Terence G. Langdon. Using high-pressure torsion for metal processing: Fundamentals and applications. 2008, Progress in Materials Science, Vol. 53, pp. 893–979.
5. Y. Beygelzimer, V. Varyukhin, S. Synkov, D. Orlov. Useful properties of twist extrusion. 2009, Materials Science and Engineering A, Vol. 503, pp. 14–17.
6. D.Orlov, Y. Beygelzimer, S.Synkov, V.Varyukhin, N.Tsuji, Z. Horita. Microstructure evolution in pure Al processed with twist extrusion.1, 2009, Materials Transactions, Vol. 50, pp. 96-100.
7. Y.Saito, N.Tsuji, H. Utsunomiya, T.Sakai, R.Hong. Ultra-fine grained bulk aluminum produced by accumulative roll-bonding (ARB) process. 9, 1998, Scripta Materialia, Vol. 39, pp. 1221-1227.
8. X. Huang, N. Tsuji, N. Hansen, Y. Minamino. Microstructural evolution during accumulative roll-bonding of commercial purity aluminum. 2003, Material Science and Engineering A, Vol. 340, pp. 265–271.
9. R.S. Mishra, Z.Y.Ma. Friction stir welding and processing. 2005, Material science and engineering R, Vol. 50, pp. 1-78.

10. Y.H. Zhao, X.Z. Liao, S. Cheng, E. Ma, Y.T. Zhu. Simultaneously increasing the ductility and strength of nanostructured alloys. 2006, *Advanced Materials*, Vol. 18, pp. 2280–2285.
11. S.K. Panigrahi, R. Jayaganthan. Effect of ageing on microstructure and mechanical properties of bulk, cryorolled, and room temperature rolled Al 7075 alloy. 2011, *Journal of Alloys Compounds*, Vol. 509, pp. 9609–9616.
12. S.K. Panigrahi, R. Jayaganthan, V. Pancholi, Manoj Gupta. A DSC study on the precipitation kinetics of cryorolled Al 6063 alloy. 2010, *Materials Chemistry and Physics*, Vol. 122, pp. 188–193.
13. Y.H. Zhao, X.Z. Liao, S. Cheng, E. Ma, Y.T. Zhu. Simultaneous increasing the ductility and strength of nanostructured alloys. 2006 *Advanced Materials*, Vol. 18, pp. 2280–2283.
14. Sheng, Y.H. Zhao, T.T. Zhu, E. Ma. Optimizing the strength and ductility of the fine structured 2024 Al alloy by nano precipitation. 2007, *Acta Materialia*, Vol. 55, pp. 5822–5832.
15. I. Gutierrez-Urrutia, M.A. Muñoz-Morris, D.G. Morris. The effect of coarse second-phase particles and fine precipitates on microstructure refinement and mechanical properties of severely deformed Al alloy. 2005, *Materials Science and Engineering A*, Vol. 394, pp. 399–410.
16. Hans J. Roven, Manping Liu, Jens C. Werenskiold. Dynamic precipitation during severe plastic deformation of an Al–Mg–Si aluminium alloy. 2008, *Materials Science and Engineering A*, Vols. 483–484, pp. 54–58.
17. I. Gutierrez-Urrutia, M.A. Muñoz-Morris, D.G. Morris. Recovery of deformation substructure and coarsening of particles on annealing severely plastically deformed Al–Mg–Si alloy and analysis of strengthening mechanisms. 2, 2006, *Journal of Materials Research*, Vol. 21, pp. 329–342.

18. J.M. García-Infanta, S. Swaminathan, C.M. Cepeda-Jiménez, T.R. McNelley. Enhanced grain refinement due to deformation-induced precipitation during ambient-temperature severe plastic deformation of an Al–7%Si alloy. 2009, *Journal of Alloys and Compounds*, Vol. 478, pp. 139–143.
19. R.Z Valiev, R.K. Islamgaliev, I.V. Alexandrov. Bulk nanostructured materials from severe plastic deformation. 2000, *Progress in material science*, Vol. 45, p. 103-189.
20. Yuntian T Zhu, Terry C Lowe, Terence G Langdon. Performance and applications of nanostructured materials produced by severe plastic deformation.8, 2004, *Scripta Materialia*, Vol. 51, pp. 825–830.
21. Gleiter, H. Nanocrystalline materials. 4, 1989, *Progress in Material Science*, Vol. 33, pp. 223-315.
22. J.Ecket, J.C. Holzer, C.E. Krill, W.L. Johnson. Reversible grain size changes in ball-milled nanocrystalline Fe-Cu alloys. 1992, *Journal of materials research*, Vol. 7, p. 1980.
23. (Ed.), C Suryanarayana. *Non-equilibrium processing of materials*. Amsterdam: Pergamon, 1999.
24. V.M. Segal, V.I. Reznikov, A.E. Drobyshevskii, V.I. Kopylov. Plastic treatment of metals by simple shear. 1, 1981, *Izv. Akad. Nauk SSSR, Ser. Met*, pp. 115-123.
25. Segal, V.M., *Metal processing by severe plastic deformation*. 5, 2006, *Russian metallurgy*, Vol. 2006, pp. 474-483.
26. Langdon, Terence G., *The principles of grain refinement in equal-channel angular pressing*. 1-2, 2007, *Materials Science and Engineering: A*, Vol. 462, pp. 3–11.
27. S. D. Terhune, D. L. Swisher, K. Oh-Ishi, Z. Horita, T. G. Langdon, T. R. McNelley. An investigation of microstructure and grain-boundary evolution during ECA pressing of pure aluminum. 7, 2002, *Metallurgical and Materials Transactions A*, Vol. 33, pp. 2173-2184.

28. C. P. CHANG, P. L. SUN, P. W. KAO. Deformation Induced Grain Boundaries in Commercially Pure Aluminium. 2000, *Acta materialia*, Vol. 48, p. 3377±3385.
29. Joon- Yeon Chang, Jong-Seo Yoon, Gyeong- Ho Kim. Development of submicron sized grain during cyclic equal channel angular pressing. 2001, *Scripta Materialia*, Vol. 45, pp. 347-354.
30. Alexandre Goloborodko, Oleg Sitdikov, Taku Sakai, Rustam Kaibyshev, Hiromi Miura. Grain Refinement in As-Cast 7475 Aluminum Alloy under Hot Equal-Channel Angular Pressing. 4, 2003, *Materials Transactions*, Vol. 44, pp. 766-774.
31. Y. Estrin, A. Vinogradov. Extreme grain refinement by severe plastic deformation: A wealth of challenging science. 2013, *Acta materialia*, Vol. 61, pp. 782-817.
32. Ho Yong Um, Eun Yoo Yoon, Dong Jun Lee, Chong Soo Lee, Lee Ju Park, Sunghak Lee, Hyoung Seop Kim. Hollow cone high-pressure torsion: Microstructure and tensile strength by unique severe plastic deformation. 2014, *Scripta Materialia*, Vol. 71, pp. 41–44.
33. Sang Heon Lee, Dong Nyung Lee. Analysis of deformation textures of asymmetrically rolled steel sheets. 2001, *International Journal of Mechanical Sciences*, Vol. 43, pp. 1997–2015.
34. Dharmendra Singh, P. Nageswara Rao, R. Jayaganthan. Effect of deformation temperature on mechanical properties of ultrafine grained Al–Mg alloys processed by rolling. 2013, *Materials & Design*, Vol. 50, pp. 646–655.
35. A. Yamamoto, Y. Tsukahara, S. Fukumoto. Effects of Wavy Roll-Forming on Textures in AZ31B Magnesium Alloy. 2008, *Materials Transactions*, Vol. 49, pp. 995 - 999.
36. K. Chandra Sekhar, B.P. Kashyap, S. Sangal. AFM Characterization of Structural Evolution and Roughness of AISI 304 Austenitic Stainless Steel under Severe Deformation by Wavy Rolling. 2013, *Advanced Materials Research*, Vol. 794, pp. 230-237.
37. Eivani, AR. Towards bulk nanostructured materials in pure shear. 2015, *Materials Letters*, Vol. 139, pp. 15–18.

38. A. Zangiabadi, M. Kazeminezhad. Development of a novel severe plastic deformation method for tubular materials: Tube Channel Pressing (TCP). 2011, *Materials Science and Engineering: A*, Vol. 528, pp. 5066–5072.
39. R.Z. Valiev, I.V. Alexandrov. Paradox of strength and ductility in metals processed by severe plastic deformation. 2002, *Journal of Materials Research* , Vol. 17.
40. Eun Jeong Kwak, Cheon Hee Bok, Min Hong Seo, Taek-Soo Kim, Hyoung Seop Kim. Processing and Mechanical Properties of Fine Grained Magnesium by Equal Channel Angular Pressing. 5, 2008, *Materials Transactions*, Vol. 49, pp. 1006 - 1010.
41. V.V.Stolyarov, Y.T. Zhu, I.V. Alexandrov, T.C. Lowe, R.Z. Valiev. . Influence of ECAP routes on the microstructure and properties of pure Ti. 2001, *Materials Science and Engineering A*, Vol. 299, p. 59.
42. Z. Horita, T. Fujinami, M. Nemoto, T.G. Langdon. Improvement of mechanical properties for Al alloys using equal channel angular pressing. 2001, *Journal of Materials Processing Technology*, Vol. 117, p. 288.
43. F.H. Froes, C. Suryanarayana, G.-H. Chen, A. Frefer G.R. Hyde. 1992, *JOM*, Vol. 5, p. 26.
44. R.Z. Valiev, T.G. Langdon. Developments in the use of ECAP processing for grain refinement. 2006, *Reviews in Advanced Material Science*, Vols. 15-26.
45. Bridgman, P. On torsion combined with compression. 1943, *Journal of applied physics*, Vol. 14, p. 273.
46. Cheng Xu, Zenji Horita, Terence G. Langdon. The evolution of homogeneity in an aluminum alloy processed using high-pressure torsion. 18, 2008, *Acta Materialia*, Vol. 56, pp. 5168–5176.

47. A.P. Zhilyaev, G.V. Nurislamova, B.K. Kim, M.D. Baro, J.A. Szpunar, T.G. Langdon. Experimental parameters influencing grain refinement and microstructural evolution during high-pressure torsion. 2003, *Acta Materialia*, Vol. 51, pp. 753–765.
48. Cheng Xu, Minoru Furukawa, Zenji Horita, Terence G. Langdon. Using ECAP to achieve grain refinement, precipitate fragmentation and high strain rate superplasticity in a spraycast aluminum alloy. 2003, *Acta Materialia*, Vol. 51, pp. 6139–6149.
49. R.Z. Valiev, R.K. Islamgaliev, I.V. Alexandrov. Bulk nanostructured materials from severe plastic deformation. 2000, *Progress in Material Science*, Vol. 45, pp. 103–189.
50. C. Kobayashi, T. Sakai, A. Belyakov, H. Miura. Ultrafine grain development in copper during multidirectional forging at 195 K. 2007, *Philos Mag Lett*, Vol. 87, pp. 751–66.
51. Somjeet Biswas, Satyam Suwas. Evolution of sub-micron grain size and weak texture in magnesium alloy Mg–3Al–0.4Mn by a modified multi-axial forging process. 2012, *Scripta Materialia*, Vol. 66, pp. 89–92.
52. H. Miura, T. Maruoka, J.J. Jonas. Microstructure and mechanical properties of multi directionally forged Mg–Al–Zn alloy. 2012, *Scripta materialia*, Vol. 66, pp. 49–51.
53. H. Miura, T. Maruoka, J.J. Jonas. Effect of ageing on microstructure and mechanical properties of a multi-directionally forged Mg–6Al–1Zn alloy. 2013, *Material Science and Engineering A*, Vol. 563, pp. 53–9.
54. H. Miura, X. Yang, T. Sakai. Evolution of ultra-fine grains in AZ31 and AZ61 Mg alloys during multi directional forging and their properties. 2008, *Material Transactions*, Vol. 49, pp. 1015–20.
55. B. Cherukuri, R. Srinivasan. Properties of AA 6061 processed by multi axial compression/forging (MAC/F). 2006, *Materials and Manufacturing Process*, Vol. 21, pp. 519–25.

56. Y. Saito, H. Utsunomiya, N. Tsuji, T. Sakai. Novel ultra-high straining process for bulk materials—development of the accumulative roll-bonding (ARB) process. 2, 1999, *Acta Materialia*, Vol. 47, pp. 579–583.
57. Dengke Yang, Pavel Cizek, Peter Hodgson, Cui'e Wen. Ultrafine equiaxed-grain Ti/Al composite produced by accumulative roll bonding. 2010, *Scripta Materialia*, Vol. 62 , pp. 321–324.
58. K. Wu, H. Chang, E. Maawad, W.M. Gan, H.G. Brokmeier, M.Y. Zheng. Microstructure and mechanical properties of the Mg/Al laminated composite fabricated by accumulative roll bonding (ARB). 2010, *Materials Science and Engineering A*, Vol. 527 , pp. 3073–3078.
59. M. Movahedi, H.R. Madaah-Hosseini, A.H. Kokabi. The influence of roll bonding parameters on the bond strength of Al-3003/Zn soldering sheets. 2008, *Materials Science and Engineering A*, Vol. 487, pp. 417–423.
60. L. Zhang, L. Meng, S.P. Zhou, F.T. Yang. Behaviors of the interface and matrix for the Ag/Cu bimetallic laminates prepared by roll bonding and diffusion annealing. 2004, *Materials Science and Engineering A*, Vol. 371, pp. 65–71.
61. S.C.V. Lima, A.D. Rollett. Length scale effects on recrystallization and texture evolution in Cu layers of a roll-bonded Cu–Nb composite. 2009, *Materials Science and Engineering A*, Vol. 520, pp. 189–196.
62. S.H.Lee, T. Sakai, Y. Saito, H.Utsunomiya, N. Tsuji. Strengthening of sheath-rolled aluminum based MMC by the ARB process. 1999, *Materials Transactions, JIM*, Vol. 40, pp. 1422-1428.
63. Vahid Yousefi Mehr, Mohammad Reza Toroghinejad, Ahmad Rezaeian. Mechanical properties and microstructure evolutions of multilayered Al–Cu composites produced by accumulative roll bonding process and subsequent annealing. 2014, *Materials Science and Engineering: A*, Vol. 601, pp. 40–47.

64. K.H. Kim, D.N. Lee. Analysis of deformation textures of asymmetrically rolled aluminum sheets. 13, 2001, *Acta Materialia*, Vol. 49, pp. 2583–2595.
65. H. JIN, D.J. LLOYD. The Tensile Response of a Fine-Grained AA5754 Alloy Produced by Asymmetric Rolling and Annealing. 2004, *Metallurgical and Materials Transactions a*, Vol. 35A, pp. 997- 1006.
66. Q.Cui, K.Ohori. 2000, *Material Science and Technology*, Grain refinement of high purity aluminum by asymmetric rolling. Vol. 16, pp. 1095-1010.
67. W.J. Kim, S.J. Yoo, H.T. Jeong, D.M. Kim, B.H. Choe, J.B. Lee. Effect of the speed ratio on grain refinement and texture development in pure Ti during differential speed rolling. 2011, *Scripta Materialia*, Vol. 64, pp. 49–52.
68. W.J. Kim, B.G. Hwang, M.J. Lee, Y.B. Park. Effect of speed-ratio on microstructure, and mechanical properties of Mg-3Al-1Zn alloy, in differential speed rolling. 34, 2011, *Journal of Alloys and Compounds*, Vol. 509, pp. 8510-8517.
69. Y.H. Ji, J.J. Park, W.J. Kim. Finite element analysis of severe deformation in Mg–3Al–1Zn sheets through differential-speed rolling with a high speed ratio. 2007, *Materials Science and Engineering: A*, Vols. 454–455, pp. 570–574.
70. H. Watanabe, T. Mukai, K. Ishikawa. Differential speed rolling of an AZ31 magnesium alloy and the resulting mechanical properties. 2004, *Journal of Materials Science*, Vol. 39, pp. 1477 – 1480.
71. Cunqiang Ma, Longgang Hou, Jishan Zhang, Linzhong Zhuang. Experimental and numerical investigations of the plastic deformation during multi-pass asymmetric and symmetric rolling of high-strength aluminum alloys. 2014, *Materials Science Forum*, Vols. 794-796, pp. 1157-1162.

72. Mitsuaki Furui, Michiyo Noguchi, Shigeoki Saji. Stored energy and recrystallization of 3004 and 5083 aluminium alloys prepared by two- directional rolling at cryogenic temperature. 5, 1999, Journal of Japan institute of Light Metals, Vol. 49, pp. 209-213.
73. Mitsuaki Furui, Chikako Sekiguchi, Takehiko Mae, Shigeoki Saji. Recovery and recrystallization of 3004 and 5083 aluminium alloys prepared by two-directional rolling at liquid nitrogen temperature. 9, 2002, Journal of Japan Institute of Light Metals, Vol. 52, pp. 403-409.
74. Mitsuaki Furui, Takayuki Kawakami, Shigeoki Saji, Tadashi Minoda, Hiroki Esaki, Hiroki Tanaka, Hideo Yoshida. Stored energy and its release behavior during recovery and recrystallization processes for aluminum alloys rolled at cryogenic temperature. 8, 2002, Journal of Japan Institute of Light metals, Vol. 52, pp. 339-345.
75. M. Noda, K. Funami, M. Kobayashi. Improvement of mechanical properties of 3004 aluminum alloy by heavy working at cryogenic temperature. 5, 2000, Journal of the Japan Institute of Metals, Vol. 64, pp. 395-398.
76. Yinimin Wang, Mingwei Chen, Fenghua Zhou, En Ma. High tensile ductility in a nanostructured metal. 2002, Nature, Vol. 31, p. 419.
77. Cheng Xu, Terence G. Langdon. Influence of a round corner die on flow homogeneity in ECA pressing. 2003, Scripta Materialia, Vol. 48, pp. 1–4.
78. Cheng Xu, Minoru Furukawa, Zenji Horita, Terence G. Langdon. The evolution of homogeneity and grain refinement during equal-channel angular pressing: A model for grain refinement in ECAP. 2005, Materials Science and Engineering A, Vol. 398, pp. 66–76.
79. Cheng Xu, Kenong Xia, Terence G. Langdon. The role of back pressure in the processing of pure aluminum by equal-channel angular pressing. 2007, Acta Materialia, Vol. 55, pp. 2351–2360.

80. Cheng Xu, Terence G. Langdon. Three-dimensional representations of hardness distributions after processing by high-pressure torsion. 2009, *Materials Science and Engineering A*, Vol. 503, pp. 71–74.
81. Cheng Xu, Kenong Xia, Terence G. Langdon. Processing of a magnesium alloy by equal-channel angular pressing using a back-pressure. 2009, *Materials Science and Engineering A*, Vol. 527, pp. 205–211.
82. Cheng Xu, Steven Schroeder, Patrick B. Berbon, Terence G. Langdon. Principles of ECAP–Conform as a continuous process for achieving grain refinement: Application to an aluminum alloy. 2010, *Acta Materialia*, Vol. 58, pp. 1379–1386.
83. Levente Balogh, Tama’s Unga’r, Yonghao Zhao, Y.T. Zhu, Zenji Horita, Cheng Xu, Terence G. Langdon. Influence of stacking-fault energy on microstructural characteristics of ultrafine-grain copper and copper–zinc alloys. 2008, *Acta Materialia*, Vol. 56, pp. 809–820.
84. S.H. Lee, Y. Saito, T. Sakai, H. Utsunomiya. Microstructures and mechanical properties of 6061 aluminum alloy processed processed by accumulative roll-bonding. 2002, *Materials Science and Engineering A*, Vol. 325, pp. 228–235.
85. W.C. Liu, M.B. Chen, H. Yuan. Evolution of microstructures in severely deformed AA 3104 aluminum alloy by multiple constrained compression. 2011, *Materials Science and Engineering A*, Vol. 528, pp. 5405–5410.
86. Majid Vashti, Hyosung Seep Kim, Ali Karim Their, Amir Moment. Inhomogeneity Through Warm Equal Channel Angular Pressing. 2013, *JMEPEG*, Vol. 22, pp. 1666–1671.
87. N. Haghdadi, A.Zarei-Hanzaki, D.Abou-Ras, M.H.Maghsoudi, A.Ghorbani. An investigation into the homogeneity of microstructure, strainpattern and hardness of pure aluminum processed by accumulative back extrusion. 2014, *Materials Science & Engineering A*, Vol. 595, pp. 179–187.

88. Wei Guo, Qudong Wang, Bing Ye, Hao Zhou. Enhanced microstructure homogeneity and mechanical properties of AZ31–Si composite by cyclic closed-die forging. 2013, *Journal of Alloys and Compounds*, Vol. 552, pp. 409–417.
89. W.M. Gan, K. Wu, M.Y. Zheng, X.J. Wang, H. Chang, H.-G. Brokmeier. Microstructure and mechanical property of the ECAPed Mg₂Si/Mg composite. 2009, *Materials Science and Engineering A*, Vol. 516, pp. 283–289.
90. Segal, V.M. *Materials processing by simple shear*. 2, 1995, *Materials Science and Engineering: A*, Vol. 197, pp. 157–164.
91. Y.Wu, I. Baker. An experimental study of equal channel angular extrusion. 4, 1997, *Scripta Materialia*, Vol. 37, pp. 437-442.
92. P.B. Prangell, C. Harris, S.M. Roberts. Finite element modelling of equal channel angular extrusion. 7, 1997, *Scripta Materialia*, Vol. 37, pp. 983-989.
93. S.L. Semiatin, D.P. Delo, E.B. Shell. The effect of material properties and tooling design on deformation and fracture during equal channel angular extrusion. 2000, *Acta materialia*, Vol. 48, pp. 1841-1851.
94. Saleh N. Alhajeri, Nong Gao, Terence G. Langdon. Hardness homogeneity on longitudinal and transverse sections of an aluminium alloy processed by ECAP.10–11, 2011, *Materials Science and Engineering: A*, Vol. 528, pp. 3833–3840.
95. Roberto B. Figueiredo, Paulo R. Cetlin, and Terence G. Langdon. Stable and Unstable Flow in Materials Processed by Equal-Channel Angular Pressing with an Emphasis on Magnesium Alloys. 2010, *Metallurgical and Materials Trans A*, Vol. 41A, pp. 778-786.
96. A.P. Zhilyaev, B.K. Kim, G.V. Nurislamova, M.D. Baro, J.A. Szpunar, T.G. Langdon. Orientation imaging microscopy of ultrafine-grained nickel. 2002, *Scripta Materialia*, Vol. 46, pp. 575–580.

97. A. Vorhauer, R. Pippan. On the homogeneity of deformation by high pressure torsion. 2004, Scripta Materialia, Vol. 51, pp. 921–925.
98. Genevois C, Deschamps A, Denquin A, Doisneau-cottignies B. Quantitative. Investigation of precipitation and mechanical behavior for AA2024 friction stir welds. (8), 2005, Acta Mater, Vol. 53, pp. 2447–58.
99. Zenji Horita, Terence G. Langdon. Microstructures and micro hardness of an aluminum alloy and pure copper after processing by high-pressure torsion. 2005, Materials Science and Engineering A, Vols. 410–411, pp. 422–425.
100. Yuri Estrin, Rimma Lapovok. Moscow, Russia: s.n., A New Paradigm of Severe Plastic Deformation: Fabrication of Hybrid Nanomaterials. 2014. XII International Conference on Nanostructured Materials (NANO 2014). Vol. Bulk Metallic Nanomaterials (oral).
101. The stored energy of cold work. A.L.Titchener, B. Bever. Progress in metal physics.
102. Ondrej Man, Libor Pantelejev, Ludvík Kunz. Study of Thermal Stability of Ultrafine-Grained Copper by means of Electron Back Scattering Diffraction. 2010, Materials Transactions, Vol. 51, pp. 209 - 213.
103. X. Molodova, G. Gottstein, M. Witting, R.J. Hellmig. Thermal stability of ECAP processed pure copper. 2007, Materials Science and Engineering A, Vols. 460–461, pp. 204–213.
104. S. Bhaumik, X. Molodova, G. Gottstein. Effect of stress on the annealing behavior of severely plastically deformed aluminum alloy 3103. 21–22, 2010, Materials Science and Engineering: A, Vol. 527, pp. 5826–5830.
105. A. Vinogradov, A. Washikita, K. Kitagawa, V.I. Kopylov. Fatigue life of fine-grain Al-Mg-Sc alloys produced by equal-channel angular pressing. 2003, Materials Science and Engineering A, Vol. 349, pp. 318-326.

106. S. V. Dobatkin, V. V. Zakharov, A. Yu. Vinogradov, K. Kitagawa, N. A. Krasil'nikov, T. D. Rostova, E. N. Bastarash. Nanocrystalline Structure Formation in Al–Mg–Sc Alloys during Severe Plastic Deformation. 2006, Russian Metallurgy (Metally), Vol. 2006, pp. 533–540.
107. E. Avtokratova, O. Sitdikov, M. Markushev, R. Mulyukov. Extraordinary high-strain rate superplasticity of severely deformed Al–Mg–Sc–Zr alloy. 2012, Materials Science and Engineering: A, Vol. 538, pp. 386–390.
108. A. Vinogradov, V. Patlan, Y. Suzuki, K. Kitagawa, V.I. Kopylov. Structure and properties of ultra-fine grain Cu–Cr–Zr alloy produced by equal-channel angular pressing. 2002, Acta Materialia, Vol. 50, pp. 1639–1651.
109. S.K. Panigrahi, D. Devanand, R. Jayaganthan. Effect of ageing on strength and ductility of ultrafine grained Al 6061 alloy. 2010, 633-634, pp. 303-309.
110. S.K. Panigrahi, R. Jayaganthan. Effect of annealing on precipitation, microstructural stability, and mechanical properties of cryorolled Al 6063 alloy. 20, 2010, Journal of Materials Science, Vol. 45, pp. 5624-5636.
111. S.K. Panigrahi, R. Jayaganthan. Influence of solutes and second phase particles on work hardening behavior of Al 6063 alloy processed by cryorolling. 7-8, 2011, Materials Science and Engineering A, Vol. 528, pp. 3147-3160.
112. H.Mughrabi, H.W. Höppel, M. Kautz, R.Z. Valiev. Annealing treatments to enhance thermal and mechanical stability of ultrafine-grained metals produced by severe plastic deformation. 10, 2003, Materials Research and Advanced Techniques, Vol. 94, pp. 1079-1083.
113. Kyung-Tae Park, Yong-Seog Kim, Jung Guk Lee, Dong Hyuk Shin. Thermal stability and mechanical properties of ultrafine grained low carbon steel. 2000, Materials Science and Engineering A, Vol. 293, pp. 165–172.

114. Ruslan Z. Valiev, Ilchat Sabirov, Alexander P. Zhilyaev, Terence G. Langdon. Bulk Nanostructured Metals for Innovative Applications. 10, 2012, Journal of Materials, JOM, Vol. 64, pp. 1134-1142.
115. I. Sabirov, M.Yu. Murashkin, R.Z. Valiev. Nanostructured aluminium alloys produced by severe plastic deformation: New horizons in development. 2013, Materials Science & Engineering A, Vol. 560, pp. 1-24.
116. <http://www.britannica.com/EBchecked/topic/369081/materials-science/32300/Materials-for-medicine>. [Online]
117. A. Vinogradov, T. Mimaki, S. Hashimoto, R. Valiev. On the Corrosion Behaviour of Ultra-fine Grain Copper.3, 1999, Scripta Materialia, Vol. 41, pp. 319–326.
118. X.X. Xu, F.L. Nie, J.X. Zhang, W. Zheng, Y.F. Zheng, C. Hu., G. Yang. Corrosion and ion release behavior of ultra-fine grained bulk pure copper fabricated by ECAP in Hanks solution as potential biomaterial for contraception. 2010, Materials Letters, Vol. 64, pp. 524–527.
119. H. Wang, Y. Estrin, Z. Zuberova. Bio-corrosion of a magnesium alloy with different processing histories. 2008, Materials Letters, Vol. 62, pp. 2476–2479.
120. B. Ratna Sunil, T.S. Sampath Kumar, Uday Chakkingal, V. Nandakumar, Mukesh Doble. Friction stir processing of magnesium–nanohydroxyapatite composites with controlled in vitro degradation behavior. 2014, Materials Science and Engineering: C, Vol. 39, pp. 315–324.
121. S. Faghihi, F. Azari, A.P. Zhilyaev, J.A. Szpunar, H. Vali, M.Tabrizian. Cellular and molecular interactions between MC3T3-E1 pre-osteoblasts and nanostructured titanium produced by high-pressure torsion. 2007, Biomaterials, Vol. 28(27), pp. 3887-3895.
122. Y.Estrin, C. Kasper, S. Diederichs, R. Lapovok. Accelerated growth of preosteoblastic cells on ultrafine grained titanium. 4, 2009, Journal of Biomedical Materials Research - Part A, Vol. 90, pp. 1239-1242.

123. R.Z. Valiev, I.P. Semenova, V.V. Latysh, H. Rack, T.C. Lowe, J. Petruzelka, L. Dluhos, D.Hrusak, J. Sochova. Nanostructured titanium for biomedical applications. 8, 2008, *Advanced Engineering Materials*, Vol. 10, pp. B15-B17+702.
124. H.Wang, Y. Estrin, H. Fu, G. Song, Z. Zuberova. The effect of pre-processing and grain structure on the bio-corrosion and fatigue resistance of magnesium alloy AZ31. 11, 2007, *Advanced Engineering Materials*, Vol. 9, pp. 967-972.
125. Y. Estrin, M. Janecek, G.I. Raab, R.Z. Valiev, A. Zi. Severe Plastic Deformation as a means of producing Ultra-Fine-Grained Net-Shaped Micro Electro-Mechanical Systems Parts. 2007, *Metallurgical and Materials Transactions A*, Vol. 38A, pp. 1906-1909.
126. Xiao Guang Qiao, Nong Gao, Zakaria Moktadir, Michael Kraft, Marco J Starink. Fabrication of MEMS components using ultrafine grained aluminium alloys. 2010, *Journal of Micromechanics and Microengineering*, Vol. 20, p. 045029.
127. X.G. Qiao, M.T. Bah, J.W. Zhang, N. Gao, Z. Moktadir, M. Kraft, M.J. Starink. Microembossing of ultrafine grained Al: microstructural analysis and finite element modelling. 2010, *Journal of micromechanics and microengineering*, Vol. 20, p. 105002.
128. Polmear, I.J. *Light Alloys: From traditional alloys to Nano crystals*. London: Butterworth, 2006.
129. Mondolfo, L.F. *Aluminium Alloys: Structure and properties*. London: Butterworths, 1976.
130. <http://www.aluminum.org/aluminum-advantage>. <http://www.aluminum.org>. [Online]
131. J.Hirsch. Automotive trends in aluminium. *Materials forum* 28, Vol. 1, pp. 15-23.
132. Aluminium in innovative light-weight car design. Hirsch, I.J. *Lightweight Vehicle Structure Conference*.
133. AMAG. *Automotive Alureport 03*. 2012.

134. Hirsch, J. Aluminium Alloy for Automotive Application. 1997, Materials Science Forum, Vol. 242.
135. <http://www.ctia.com.cn/Technology/2009/24667.html>. [Online]
136. W.F. Miao, D.E. Laughlin. Precipitation hardening in aluminum alloy 6022. 1999, Scripta Materialia, Vol. 40, pp. 873–878.
137. W.F. Miao, Laughlin D.E. Differential scanning calorimetry study of aluminum alloy 6111 with different pre-aging treatments. 2000, Journal of materials science letters, Vol. 19, pp. 201-203.
138. G.A. Edwards, K. Stiller, G.L. Dunlop, M.J. Couper. The precipitation sequence in Al–Mg–Si alloys. 11, 1998, Acta Materialia, Vol. 46, pp. 3893-3904.
139. I. Kovacs, J. Lendvai, E. Nagy. The mechanism of clustering in supersaturated solid solutions of Al-Mg₂Si alloys. 1972, Acta Metallurgica, Vol. 20, pp. 975-983.
140. D. W. Pashley, M. H. Jacobs, J. T. Vietz. The basic processes affecting two-step ageing in an Al-Mg-Si alloy. 1967, Philosophical Magazine, Vol. 16, pp. 51-76.
141. M. Murayama, K. Hono. Pre-precipitate Clusters and Precipitation Processes in Al±Mg±Si alloys. 5, 1999, Acta materialia, Vol. 47, pp. 1537-1548.
142. A. Serizawa, S. Hirosawa, T. Sato. Three dimensional atom probe characterization of nanoclusters responsible for multistep ageing behavior of an Al-Mg-Si alloy. 2008, Metallurgical and Materials Transactions A, Vol. 39A, pp. 243-251.
143. M. Torsæter, H.S. Hasting, W. Lefebvre, C.D. Marioara, J.C. Walmsley, S.J. Andersen, R. Holmestad. The influence of composition and natural aging on clustering during preageing in Al- Mg-Si alloys. 2010, Journal of Applied Physics, Vol. 108, p. 073527.

144. T. Abid, A. Boubertakh, S. Hamamda. Effect of pre-aging and maturing on the precipitation hardening of an Al–Mg–Si alloy. 2010, *Journal of Alloys and Compounds*, Vol. 490, pp. 166–169.
145. J.K Kim, H.G Jeong, S.I Hong, Y.S Kim, W.J Kim. Effect of aging treatment on heavily deformed microstructure of a 6061 aluminum alloy after equal channel angular pressing. 8, 2001, *Scripta Materialia*, Vol. 45, pp. 901–907.
146. Daisuke Terada, Yoma Kaneda, Zenji Horita, Kenji Matsuda, Shoichi Hirose, Nobuhiro Tsuji. Mechanical properties and microstructure of 6061 aluminum alloy severely deformed by ARB process and subsequently aged at low temperatures. 2014, *Materials Science and Engineering*, Vol. 63, p. 012088.
147. Gulnaz Nurislamova, Xavier Sauvage, Maxim Murashkin, Rinat Islamgaliev, Ruslan Valiev. Nanostructure and related mechanical properties of an Al–Mg–Si alloy processed by severe plastic deformation. 2008, *Philosophical Magazine Letters*, Vol. 88, pp. 459–466.
148. M. Caia, D.P Field, G.W Lorimer. A systematic comparison of static and dynamic ageing of two Al–Mg–Si alloys. 2004, *Materials Science and Engineering: A*, Vol. 373, pp. 65–71.
149. Equal-Channel Angular Pressing of Commercial Aluminum Alloys: Grain Refinement, Thermal Stability and Tensile Properties. 2000, *Metallurgical and Materials Transactions A*, Vol. 31A, pp. 691–701.
150. S.H Lee, Y. Saito, T. Sakai, H. Utsunomiya. Microstructures and mechanical properties of 6061 aluminum alloy processed by accumulative roll-bonding. 1–2, 2002, *Materials Science and Engineering: A*, Vol. 325, pp. 228–235.
151. W.J. Kim, J.Y. Wang. Microstructure of the post-ECAP aging processed 6061 Al alloys. 1–2, 2007, *Materials Science and Engineering: A*, Vol. 464, pp. 23–27.

152. Gulnaz Nurislamova, Xavier Sauvage, Maxim Murashkin. Nanostructure and related mechanical properties of an Al–Mg–Si alloy processed by severe plastic deformation. 2008, *Philosophical Magazine Letters*, Vol. 88, pp. 459–466.
153. Mohammad Reza Rezaei, Mohammed Reza Toroghinejad, Fakhreddin Ashrafizadeh. Effects of ARB and ageing processes on mechanical properties and microstructure of 6061 aluminum alloy. 2011, *Journal of Material Processing and Technology*, Vol. 211, pp. 1184–90.
154. M.H. Farshidi, M. Kazeminezhad, H. Miyamoto. Severe plastic deformation of 6061 aluminum alloy tube with pre and post heat treatments. 2013, *Materials Science and Engineering: A*, Vol. 563, pp. 60–67.
155. G. Sha, K. Tugcu, X.Z. Liao, P.W. Trimby, M.Y. Murashkin, R.Z. Valiev, S.P. Ringer. Strength, grain refinement and solute nanostructures of an Al–Mg–Si alloy (AA6060) processed by high-pressure torsion. 2014, *Acta Materialia*, Vol. 63, pp. 169-179.
156. F.J. Humphreys, M.Hatherly. *Recrystallization and Related Annealing Phenomena*. Kidlington, Oxford: Elsevier ltd, 2004.
157. Huajian Gao, Yonggang Huang. Geometrically necessary dislocation and size-dependent plasticity. 2003, *Scripta Materialia*, Vol. 48, pp. 113–118.
158. Zenji Horita, David J.Smith, Minoru Furukawa, Minoru Nemoto, Ruslan Z. Valiev, Terence G. Langdon. An investigation of grain boundaries in submicrometer-grained Al-Mg Solid solution alloys using high resolution microscopy. 1996, *Journal of material research*, Vol. 11, pp. 1880-1890.
159. A. Loucif, R.B. Figueiredo, T. Baudin, F. Brisset, R. Chemam, T.G. Langdon. Ultrafine grains and the Hall–Petch relationship in an Al–Mg–Si alloy processed by high-pressure torsion. 2012, *Material science and engineering A*, Vol. 532, pp. 139-145.

160. M. Furukawa, Z. Horita, M. Nemoto, R.Z. Valiev, T.G. Langdon. Microhardness measurements and the Hall-Petch relationship in an Al-Mg alloy with submicrometer grain size. 1996, *Acta materialia*, Vol. 44.
161. E. Nesa, B. Holmedal, E. Evangelista, K. Marthinsen. Modelling grain boundary strengthening in ultra-fine grained aluminum alloys. 2005, *Materials Science and Engineering: A*, Vols. 410–411, pp. 178–182.
162. Hall, E.O. The deformation and ageing of mild steel: III Discussion of results. 9, 1951, *Proceedings of the Physical Society. Section B*, Vol. 64, p. 747.
163. Petch, N.J. 1953, *J. Iron Steel Inst.*, Vol. 174, p. 25.
164. R.Z. Valiev, N.A. Enikeev, M.Yu. Murashkin, V.U. Kazykhanov, X. Sauvage. On the origin of the extremely high strength of ultrafine-grained Al alloys produced by severe plastic deformation. 2010, *Scripta Materialia*, Vol. 63, pp. 949–952.
165. Hall–Petch relation and boundary strengthening. Niels Hansen. 8, s.n., 2004, *Scripta Materialia*, Vol. 51, pp. 801–806.
166. K.S Kumar, H. Van Swygenhoven, S. Suresh. Mechanical behavior of nanocrystalline metals and alloys. 19, 2003, *Acta Materialia*, Vol. 51, pp. 5743–5774.
167. Oyvind Ryen, Oscar Nijs, Emma Sjolander, Bjorn Holmedal, Hans-Erik Ekstro M, Erik Nes. Strengthening Mechanisms in Solid Solution Aluminum Alloys 2006, *Metallurgical and Materials Transactions A*, Vol. 37A, p. 1999.
168. P.V. Liddicoat, X.Z. Liao, Y.H. Zhao, Y.T. Zhu, M.Y. Murashkin, E.J. Lavernia, R.Z. Valiev, S.P. Ringer. Nanostructural hierarchy increases the strength of aluminium alloys. 2010, *Nature Communications*, Vol. 1, p. 63.

169. X. Sauvage, A. Ganeev, Y. Ivanisenko, N. Enikeev, M. Murashkin, R. Valiev. Grain Boundary Segregation in UFG Alloys Processed by Severe Plastic Deformation. 2012, *Advanced Engineering Materials*.
170. G. Sha, S.P. Ringer, Z.C. Duan, T.G. Langdon. An atom probe characterisation of grain boundaries in an aluminium alloy processed by equal-channel angular pressing. 2009, *Int. J. Mater. Res.*, Vol. 100, pp. 1674–1678.
171. R.Z. Valiev, N.A. Enikeev, M.Yu. Murashkin, S.E. Alexandrov, R.V. Goldshtein. Superstrength of ultrafine-grained aluminum alloys produced by severe plastic deformation. 2010, *Dokl. Phys.*, Vol. 55 (6), p. 267.
172. Alfred Wilm and the beginnings of Duralumin. Olivier, HARDOUIN DUPARC. 2005, *Zeitschrift für Metallkunde*, Vol. 96, pp. 398-404.
173. Physikalisch-metallurgische Untersuchungen über magnesiumhaltige Aluminiumlegierungen. Wilm, Alfred. 1911, *Metallurgie : Zeitschrift für de gesamte Hüttenkunde*, Vol. 8 (8), pp. 225–227.
174. Stefan Pogatscher, Marion Werinos, Helmut Antrekowitsch, Peter J. Uggowitzer. The Role of Vacancies in the Aging of Al-Mg-Si Alloys. 2014, *Materials Science Forum*, Vols. 794-796, pp. 1008-1013.
175. I. Gutierrez-Urrutia, M.A. Munoz-Morris, D.G. Morris. The effect of coarse second-phase particles and fine precipitates on microstructure refinement and mechanical properties of severely deformed Al alloy. 2005, *Materials Science and Engineering A*, Vol. 394, pp. 399–410.
176. I. Gutierrez-Urrutia, M.A. Muñoz-Morris, D.G. Morris. Recovery of deformation substructure and coarsening of particles on annealing severely plastically deformed Al–Mg–Si alloy and

- analysis of strengthening mechanisms. 2006, *Journal of Materials Research*, Vol. 21, pp. 329-342.
177. P. Szczygiel, H.J. Roven, O. Reiso. On the effect of SPD on recycled experimental aluminium alloys: Nanostructures, particle break-up and properties. 2005, *Materials Science and Engineering A*, Vols. 410–411, pp. 261–264.
178. J.M. Garc'ia-Infanta, S. Swaminathan, A.P. Zhilyaev, F. Carreno, O.A. Ruano, T.R. McNelley. Microstructural development during equal channel angular pressing of hypoeutectic Al–Si casting alloy by different processing routes. 2008, *Materials Science and Engineering A*, Vol. 485, pp. 160–175.
179. M. Murayama, Z. Horita, K. Hono. Microstructure of Two-phase Al–1.7 at% Cu alloy Deformed by Equal-Channel Angular Pressing. 2001, *Acta materialia*, Vol. 49, pp. 21–29.
180. I. G. Brodova, I. G. Shirinkina, A. N. Petrova, O. V. Antonova, V. P. Pilyugin. Evolution of the Structure of V95 Aluminum Alloy upon High Pressure Torsion. 2011, *The Physics of Metals and Metallography*, Vol. 111, pp. 630–638.
181. D. G. Morris, I. Gutierrez-Urrutia, M.A. Munoz Morris. Analysis of Strengthening Mechanisms in a Severely Plastically-Deformed Al–Mg–Si alloy with Submicron grain size. 2007, *Journal of Material Science*, Vol. 42, pp. 1439–1443.
182. Sushanta Kumar Panigrahi, R. Jayaganthan. A Study on the Combined Treatment of Cryorolling, Short-Annealing, and Aging for the Development of Ultrafine-Grained Al 6063 Alloy with Enhanced Strength and Ductility. 2010, *Metallurgical and Materials Transactions A*, Vol. 41A, pp. 2610–2675.
183. G.J. Fan, H. Choo, P.K. Liaw, E.J. Lavernia. Plastic deformation and fracture of ultrafine-grained Al–Mg alloys with a bimodal grain size distribution. 7, 2006, *Acta Materialia*, Vol. 54, pp. 1759–1766.

184. Z. Lee, D.B. Witkin, V. Radmilovic, E.J. Lavernia, S.R. Nutt. Bimodal microstructure and deformation of cryomilled bulk nanocrystalline Al–7.5Mg alloy. 2005, *Materials Science and Engineering: A*, Vols. 410–411, pp. 462–467.
185. David Witkin, Z. Lee, R. Rodriguez, S. Nutt, E. Lavernia. Al–Mg alloy engineered with bimodal grain size for high strength and increased ductility. 4, 2003, *Scripta Materialia*, Vol. 49, pp. 297–302.
186. Zonghoon Lee, Velimir Radmilovic, Byungmin Ahn, Enrique J. Lavernia, Steven R. Nutt. Tensile Deformation and Fracture Mechanism of Bulk Bimodal Ultrafine-Grained Al-Mg Alloy. 2010, *Metallurgical and Materials Transactions A*, Vol. 41A, p. 795.
187. David Witkin, Bing Q. Han, Enrique J. Lavernia. Room-Temperature Mechanical Behavior of Cryomilled Al Alloys. 2006, *Metallurgical and Materials Transactions A*, Vol. 37A, p. 185.
188. Yong-Hao Zhao, Xiao-Zhou Liao, Sheng Cheng, En Ma, Yuntian T. Zhu. Simultaneously Increasing the Ductility and Strength of Nanostructured Alloys. 2006, *Advanced Materials*, Vol. 18, pp. 2280–2283.
189. Y.H. Zhao, X.Z. Liao, Z. Jin, R.Z. Valiev, Y.T. Zhu. Microstructures and mechanical properties of ultrafine grained 7075 Al alloy processed by ECAP and their evolutions during annealing. 15, 2004, *Acta Materialia*, Vol. 52, pp. 4589–4599.
190. W.J. Kim, C.S. Chung, D.S. Ma, S.I. Hong, H.K. Kim. Optimization of strength and ductility of 2024 Al by equal channel angular pressing (ECAP) and post-ECAP aging. 4, 2003, *Scripta Materialia*, Vol. 49, pp. 333–338.
191. S. Cheng, Y.H. Zhao, Y.T. Zhu, E. Ma. Optimizing the strength and ductility of fine structured 2024 Al alloy by nano-precipitation. 17, 2007, *Acta materialia*, Vol. 55, pp. 5822–5832.

192. G. Liu, G. J. Zhang, F. Jiang, X. D. Ding, Y. J. Sun, J. Sun & E. Ma. Nanostructured high-strength molybdenum alloys with unprecedented tensile ductility. 2013, *Nature Materials*, Vol. 12, pp. 344–350.
193. L. Jiang, J.K. Li, P. M.Cheng, G. Liu, R. H. Wang, B. A. Chen, J. Y. Zhang, J. Sun, M. X. Yang, G. Yang. Microalloying Ultrafine Grained Al Alloys with Enhanced Ductility. 2014, *Scientific reports*, Vols. 4, 3605.
194. T. Hu, K. Ma, T. D.Topping, B. Saller, A. Yousefiani, J. M. Schoenung, E. J. Lavernia. Improving the tensile ductility and uniform elongation of high-strength ultrafine-grained Al alloys by lowering the grain boundary misorientation angle. 2014, *Scripta Materialia*, Vols. 78-79, pp. 25-28.
195. Demircan Canadinc, Emre Biyikli, Thomas Niendorf, Hans Jurgen Maier. Experimental and Numerical Investigation of the Role of Grain Boundary Misorientation Angle on the Dislocation–Grain Boundary Interactions. 2011, *Advanced Engineering Materials*, Vol. 13, p. 281.
196. B.Bay, N. Hansen, D.A. Hughes, D.K. Wilsdorf. Evolution of f.c.c. deformation structures in polyslip. 1992, *Acta materialia*, Vol. 40, pp. 205-219.
197. D. A. Hughes, N. Hansen. High Angle Boundaries Formed by Grain Subdivision Mechanisms. 1997, *Acta materialia*, Vol. 45, pp. 3871-3886.
198. Q. Liu, D. Juul Jensen, N. Hansen. Effect of grain orientation on deformation structure in cold-rolled polycrystalline aluminium. 1998, *Acta Materialia*, Vol. 46, pp. 5819–5838.
199. N.Rangaraju, T. Raghuram, B.V. Krishna, K.P. Rao, P. Venugopal. Effect of cryorolling and annealing on microstructure and properties of commercially pure aluminium. 2005, *Material Science and Engineering A*, Vol. 398, pp. 246-251.

200. Y.B.Lee, D.H. Shin, K.T. Park, W.J. Nam. Effect of annealing temperature on microstructures and mechanical properties of a 5083 Al alloy deformed at cryogenic temperature. 2004, *Scripta Materialia*, Vol. 51, pp. 355-359.
201. T. Shanmugasundaram, B.S. Murty, V.S. Sarma. Development of ultrafine grained high strength Al–Cu alloy by cryorolling. 2006, *Scripta Materialia*, Vol. 54, pp. 2013–2017.
202. S.K. Panigrahi, R.Jayaganthan, V. Chawla. Effect of cryorolling on microstructure of Al–Mg–Si alloy. 2008, *Materials Letters*, Vol. 62, pp. 2626–2629.
203. N.Tsuji, Y. Ito, Y. Saito, Y. Minamino. Strength and ductility of ultrafine grained aluminum and iron produced by ARB and annealing. 2002, *Scripta Materialia*, Vol. 47, pp. 893-899.
204. Driver, J.H. Stability of nanostructured metals and alloys. 8, 2004, *Scripta Materialia*, Vol. 51, pp. 819–823.
205. R.Sh. Musalimov, R.Z. Valiev. Dilatometric analysis of aluminium alloy with submicrometre grained structure. 12, 1992, *Scripta Metallurgica et Materialia*, Vol. 27, pp. 1685–1690.
206. S.K. Panigrahi, R.Jayaganthan. Effect of annealing on thermal stability, precipitate evolution, and mechanical properties of cryorolled Al 7075 alloy. 2011, *Metallurgical and Materials Transactions A: Physical Metallurgy and Materials Science*, Vol. 42, pp. 3208-3217.
207. J. Wang, Y. Iwahashi, Z. Horita, M. Furukawa, M. Nemoto, R.Z. Valiev, T.G. Langdon. An investigation of microstructural stability in an Al–Mg alloy with submicrometer grain size. 1996, *Acta Materialia*, Vol. 44, p. 2973.
208. K. Oh-ishi, Z. Horita, D.J. Smith, and T.G. Langdon. Grain boundary structure in Al–Mg and Al–Mg–Sc alloys after equal channel angular pressing. 2001, *Journal of Materials Research*, Vol. 16, p. 583.

209. S. Lee, A. Utsunomiya, H. Akamatsu, K. Neishi, M. Furukawa, Z. Horita, T.G. Langdon. Influence of scandium and zirconium on grain stability and superplastic ductilities in ultrafine grained Al–Mg alloys. 2002, *Acta Materialia*, Vol. 50, p. 553.
210. I. Dutta, S. M. Allen. A calorimetric study of precipitation in commercial aluminium alloy. 1991, *Journal of Materials Science Letters*, Vol. 10, pp. 323-326.
211. A. Borrego, J. Ibanez, V. Lopez, M. Lieblich, G. Gonzales-Doncel. Influence of extrusion temperature on the aging behavior of 6061Al-15 vol%SiCw composites. 1996, *Scripta Materialia*, Vol. 34, pp. 471–478.
212. Y. Birol. The effect of sample preparation on the DSC analysis of 6061 alloy. 24, 2005, *Journal of Materials Science*, Vol. 40, pp. 6357-6361.
213. Y. Song, T.N. Baker. A calorimetric and metallographic study of precipitation process in AA6061 and its composites. 1995, *Material Science and Engineering A*, Vol. 201, pp. 251–260.
214. 6061 Aluminum alloy-SiC particulate composite: a comparison between aging behavior in T4 and T6 treatments. P. Appendino, C. Badini. 1991, *Material Science and Engineering A*, Vol. 135, pp. 275–279.
215. J.Y. Huang, Y.T. Zhu, H.G. Jiang, T.C. Lowe. 2001, *Acta Materialia*, Vol. 49, p. 1497.
216. D.G Morris, M.A Muñoz-Morris. Microstructure of severely deformed Al–3Mg and its evolution during annealing. 16, 2002, *Acta Materialia*, Vol. 50, pp. 4047–4060.
217. F.J. Humphreys, M. Hatherly. *Recrystallization and related annealing phenomena*. 2nd. Oxford, Pergamon Press: s.n., 2004.
218. F. J. Humphreys, P. B. Prangnell, J. R. Bowen, A. Gholinia, C. Harris. s.l.: The royal society, developing stable fine-grain microstructures by large strain deformation. 1999, *Philosophical Transactions A*, Vol. 357, pp. 1663–1681.

219. M. Ferry, N.E. Hamilton, F.J. Humphreys. Continuous and discontinuous grain coarsening in a fine-grained particle-containing Al–Sc alloy. 4, 2005, *Acta Materialia*, Vol. 53, pp. 1097–1109.
220. B.L.Ou, J.G. Yang, M.Y. Wei. Effect of Homogenization and Aging Treatment on Mechanical Properties and Stress-Corrosion Cracking of 7050 Alloys. 2007, *Metallurgical Materials Transactions A*, Vol. 38A, p. 1960.
221. Doherty, R. D. Role of interfaces in kinetics of internal shape changes. 1, 1982, *Metal Science*, Vol. 16, pp. 1-14.
222. U.G.Kang, J.C. Lee, S.W. Jeong, W.J. Nam. The improvement of strength and ductility in ultrafine grained 5052 Al alloy by cryogenic and warm rolling. 2010, *Journal of Material Science*, Vol. 45, pp. 4739-4744.
223. Gang, U.G. 2009, *Mater Trans JIM*, Vol. 50, pp. 82–86.
224. Sushanth Kumar Panigrahi, R. Jayaganthan. Development of ultrafine-grained Al 6063 alloy by cryorolling with the optimized initial heat treatment conditions. 2011, *Materials and Design*, Vol. 32, pp. 2172–2180.
225. Vaseghi Majid, Taheri Ali Karimi, Hong Sun Ig, Kim Hyoung Seop. Dynamic ageing and the mechanical response of Al–Mg–Si alloy through equal channel angular pressing. 2010, *Materials and design*, Vol. 31, pp. 4076–4082.
226. S.K. Panigrahi, R.Jayaganthan. A Comparative Study on Mechanical Properties of Al 7075 Alloy Processed by Rolling at Cryogenic Temperature and Room Temperature. 2008, *Material Science Forum*, Vol. 584, pp. 734-740.
227. S.K. Panigrahi, R.Jayaganthan. Effect of rolling temperature on microstructure and mechanical properties of 6063 Al alloy. 2008, *Material Science and Engineering A*, Vol. 492, pp. 300-305.

228. P.N. Rao, S.K. Panigrahi, R.Jayaganthan. Effect of annealing on microstructure and mechanical properties of Al 6061 alloy processed by cryorolling. 2010, Material Science and Technology, Vol. 26, pp. 371-374.
229. Ui Gu Gang, Sang Hun Lee, Won Jong Nam. The Evolution of Microstructure and Mechanical Properties of a 5052 Aluminium Alloy by the Application of Cryogenic Rolling and Warm Rolling. 2009, Materials Transactions, Vol. 50, pp. 82-86.
230. P.Nageswara rao, R.Jayaganthan. . Effects of warm rolling and ageing after cryogenic rolling on mechanical properties and microstructure of Al 6061 alloy. 2012, Materials and Design, Vol. 39, pp. 226–233.
231. D. Guo, M.Li, Y.Shi, Z.Zhang, T.Ma, H.Zhang, X. Zhang. Simultaneously enhancing the ductility and strength of cryorolled Zr via tailoring dislocation configurations. 2012, Material Science and Engineering A, Vol. 558, pp. 611-615.
232. D.Guo, M.Li, Y.Shi, Z.Zhang, T.Ma, H.Zhang, X. Zhang. High strength and ductility in multimodal-structured Zr. 2012, Materials and Design, Vol. 34, pp. 275-278.
233. F. Prados Erika, L. Sordi Vitor, Ferrante Maurizio. The effect of Al₂Cu precipitates on the microstructural evolution, tensile strength, ductility and work-hardening behaviour of a Al–4 wt. % Cu alloy processed by equal-channel angular pressing. 2013, Acta Materialia, Vol. 61, pp. 115-125.
234. Kapoor R, Sarkar A, Yogi R, Shekhawat SK, Samajdar I, Chakravartty JK. Softening of Al during multi-axial forging in a channel die. 2013, Mater Sci Eng A, Vol. 560, pp. 404–12.
235. Sixth International Conference on Aluminium Alloys. T. Petersen, K. Nord–Varhaug, E. Nes (Eds.), Vol. 2 Japan Institute of Light Metals, Toyohashi, Japan: s.n., 1998. p. 751.

236. U.G.Kang, H.J.Lee, W.J.Nam. The achievement of high strength in an Al 6061 alloy by the application of cryogenic and warm rolling. 2012, Journal of Materials science, Vol. 47, pp. 7883-7887.
237. A. Serizawa, T. Sato, M.K. Miller. Effect of cold rolling on the formation and distribution of nanoclusters during pre-aging in an Al–Mg–Si alloy. 2013, Materials Science & Engineering A, Vol. 561, pp. 492–497.
238. Katharina Teichmann, Calin D. Marioara, Sigmund J. Andersen, Knut Marthinsen. The effect of preaging deformation on the precipitation behavior of an Al-Mg-Si alloy. 2012, Metallurgical and Materials Transactions A: Physical Metallurgy and Materials Science, Vol. 43, pp. 4006-4014.
239. Doan Chau Long, Yasuya Ohmori, Kiyomichi Nakai. Effects of cold rolling on the ageing kinetics in an Al-Mg-Si based commercial alloy. 6, 2000, Materials Transactions, JIM, Vol. 41, pp. 690-695.
240. Huei-Long Lee, Wun-Hwa Lu, Sammy Lap-Ip Chan. Effect of cold rolling on the aging kinetics of Al₂O₃ 6061 Al composite by differential scanning calorimetric technique. 1991 , Scripta Metallurgica et Materiala, Vol. 25 , pp. 2165-2170.
241. S.Matsuo, T.Hirata. Studies related to ageing kinetics in Al-Mg-Si alloy. 1973, JIM, Vol. 15, pp. 1-7.
242. T. Christman, A. Needleman, S. Nutt and S.Suresh. On microstructural evolution and micromechanical modelling of deformation of a whisker-reinforced metal-matrix composite 1989, Material Science and Engineering A, Vol. 107, pp. 49-57.
243. Y. Birol. DSC analysis of the precipitation reaction in AA6005 alloy. 3, 2008, Journal of Thermal Analysis and Calorimetry, Vol. 93, pp. 977-981.

244. K. Matsuda, T. Kawabata, Y. Uetani, T. Sato, A. Kamio, S. Ikeno,. HRTEM observation of G.P.zones and metastable phase in Al-Mg-Si alloys. 2000, Materials Science Forum, Vols. 331-337, pp. 989-994.
245. H.Suzuki, M.Kanno, G.Itoh. 1980, Journal of Japan institute of light metals, Vol. 30, p. 606.
246. L. Zhen, W.D. Fei, S.B. Kang, H.W. Kim. Precipitation behaviour of Al-Mg-Si alloys with high silicon content. 1997, Journal of Materials Science, Vol. 32, pp. 1895-1902.
247. Lloyd, A.K. Guptha and D.J. Study of precipitation kinetics in a super purity Al-0.8 pct Mg-0.9 pct Si alloy using differential scanning calorimetry. 1999, Metallurgical and Material transactions A, Vol. 30A, pp. 879-883.
248. Kang, L.Zhen and S.B. DSC analyses of the precipitation behavior of two Al-Mg-Si alloys naturally aged for different times. 1998, Materials letters, Vol. 37, pp. 349-353.
249. A.K. Guptha, D.J. Lloyd, S.A Court. Precipitation hardening processes in an Al-0.4%Mg-1.3%Si-0.25%Fe aluminum alloy. 2001, Material science engineering, Vol. 301A, pp. 140-146.
250. Chang C. S. T., Banhart J. Low-Temperature Differential Scanning Calorimetry of an Al-Mg-Si Alloy. 7, 2011, Metallurgical and Materials Transactions A, Vol. 42, pp. 1960-1964.
251. Reza S. Yassar, David P.Field, Hasso Weiland. The effect of cold deformation on the kinetics of the β'' precipitates in an Al-Mg-Si alloy. August, 2005, Metallurgical and Materials Transactions A, Vol. 36A, pp. 2059-2065.
252. S.P. Chen, K.M. Mussert, S. Van Der Zwaag. Precipitation kinetics in Al 6061 and in an Al 6061 -alumina particle composite. 1998, Journal of Material Science, Vol. 33, pp. 4477-4483.

253. A.Gaber, M.A. Gaffar, M.S. Mostafa, E.F. AboZeid. Precipitation kinetics of Al-1.12 Mg₂Si-0.35 Si and Al-1.07 Mg₂Si-0.33 Cu alloys. 2007, Journal of Alloys and Compounds, Vol. 429, pp. 167-175.
254. Youcef Aouabdia, Abdelhamid Boubertakh, Smail Hamamda. Precipitation kinetics of the hardening phase in two 6061 aluminium alloys.2010, Materials letters, Vol. 64, pp. 353-356.
255. I. Dutta, D.L. Bourell. A theoretical and experimental study of aluminum alloy 6061-SiC metal matrix composite to identify the operative mechanism for accelerated aging 1989, Material Science and Engineering A, Vol. 112, pp. 67-77.
256. I. Kovacs, J. Lendvai, E. Nagy. The mechanism of clustering in supersaturated solid solutions of Al-Mg₂Si alloys .7, 1972, Acta Metallurgica, Vol. 20, pp. 975–983.
257. Y.Birol. DSC Analysis of the precipitation reactions in the alloy AA 6082- Effect of sample preparation. 1, 2006, Journal of thermal analysis and Calorimetry, Vol. 83, pp. 219-222.
258. Yucel Birol, Miroslav Karlik. The interaction of natural ageing with straining in a twin roll cast Al-Mg-Si automotive sheet. 2006, Scripta materialia, Vol. 55, pp. 625-628.
259. Birol, Yucel. Pre-straining to improve the bale hardening response of a twin-roll cast Al-Mg-Si alloy. 2005, Scripta materialia, Vol. 52, pp. 169-173.
260. J. Banhart, C. S. T. Chang, Z. Q. Liang, N.Wanderka, M. D. H. Lay, A. J. Hill. Natural Aging in Al-Mg-Si Alloys–A Process of Unexpected Complexity.2010, Advanced Engineering Materials, Vol. 12, p. 559-571.
261. M. J. Starink, L. F. Cao, and P. A. Rometsch. A model for the thermodynamics of and strengthening due to co-clusters in Al–Mg–Si-based alloys. 2012, Acta Materialia, Vol. 60, pp. 4194- 4207.
262. S. Esmaeili, D. J. Lloyd, and W. J. Poole. Modeling of precipitation hardening for the naturally aged Al-Mg-Si-Cu alloy AA6111. 2003, Acta Materialia, Vol. 51, pp. 3467- 3481.

263. S.Esmaeili, X. Wang, D.J. LLOYD, W.J.Poole. On the precipitation-Hardening behaviour of the Al-Mg-Si-Cu alloy AA611. 2003, Metallurgical and Materials Transactions A, Vol. 34A, p. 751.
264. S. Pogatscher, H. Antrekowitsch, M. Werinos, F. Moszner, S. S. A. Gerstl, M. F. Francis, W. A. Curtin, J. F. Löffler, P. J. Uggowitzer. Diffusion on Demand to Control Precipitation Aging: Application to Al-Mg-Si Alloys. 22, 2014, Physical Review Letters, Vol. 112, p. 225701.
265. I.Dutta, D.L. Bourell, Latimer. A Theoretical Investigation of Accelerated Aging in Metal-Matrix Composites. 1988, Journal of composite materials, Vol. 22, p. 829.
266. S.Suresh, T.Christman, Y.Sugimura. Accelerated aging in cast Al alloy-SiC particulate composites. 1989, Scripta metallurgica, Vol. 23, p. 1599.
267. T. Christman, S.Suresh. Microstructural development in an aluminum alloy-SiC whisker composite. 1988, Acta metallurgica, Vol. 36, p. 1691.
268. R.Jayaganthan, Sushanth Kumar Panigrahi. The effect of cryorolling strain on precipitation kinetics of Al 7075 alloy. 2008, Materials Science Forum, Vols. 584-586, pp. 911-916.
269. P.Nageswara Rao, B.Viswanadh, R. Jayaganthan. Effect of cryorolling and warm rolling on precipitation evolution in Al 6061 alloy. 12, 2014, Materials Science and Engineering: A, Vol. 606, pp. 1-10.
270. G.K. Quainoo, S.Yannacopoulos. The effect of cold work on the precipitation kinetics of AA6111 aluminum. 21, 2004, Journal of Materials Science, Vol. 39, pp. 6495-6502.
271. A. A. Vasilyev, N. L. Kuzmin, A. S. Gruzdev. Study of the formation kinetics of Metastable phases in quenched Al-Mg-Si Alloys. 8, 2011, Physics of the Solid State, Vol. 53, pp. 1658-1663.

272. Takeshi Saito, Calin D. Marioara, Jostein Røyset, Knut Marthinsen, Randi Holmestad. The effects of quench rate and pre-deformation on precipitation hardening in Al–Mg–Si alloys with different Cu amounts. 2014, *Materials Science and Engineering: A*, Vol. 609, pp. 72–79.
273. Takeshi Nagai, Kenji Matsuda, Junya Nakamura, Tokimasa Kawabata, Susumu Ikeno, Daichi Akama, Zenji Horita, Syoichi Hirosawa. Influence of HPT or rolling on age-hardening in Al–Mg–Si alloys. 2012, *Advanced Materials Research*, Vol. 409, pp. 603–606.
274. Lihong Su, Cheng Lu, Huijun Li, Guanyu Deng, Kiet Tieu. Investigation of ultrafine grained AA1050 fabricated by accumulative roll bonding. 2014, *Materials Science and Engineering: A*, Vol. 614, pp. 148–155.
275. M. Vedani, G. Angella, Paola Bassani, D. Ripamonti, A. Tuissi. DSC Analysis of Strengthening Precipitates in Ultrafine Al–Mg–Si alloys. 1, 2007, *Journal of Thermal Analysis and Calorimetry*, Vol. 87, pp. 277–284.
276. P. Nageswara rao, Dharmendra Singh, R. Jayaganthan. Mechanical properties and microstructural evolution of Al 6061 alloy processed by multidirectional forging at liquid nitrogen temperature. 2014, *Materials and Design*, Vol. 561, pp. 97–104.
277. G.I. Rosen, D. Juul Jensen, D.A. Hughes. Microstructure and local crystallography of cold rolled aluminium. 1995, *Acta Metall Mater*, Vol. 43, pp. 2563–79.
278. P.J. Hurley, F.J. Humphreys. The application of EBSD to the study of substructural development in a cold rolled single-phase aluminium alloy. 2003, *Acta Mater*, Vol. 51, pp. 1087–102.
279. F.J. Humphreys, Hatherly. *Recrystallization and related annealing phenomena*. 2nd ed. Oxford (UK): Elsevier Ltd., 2004.
280. Cottrell, A.H. *The mechanical properties of matter*. New York: Wiley, 1964.

281. V.S. Sharma, W.W. Jian, J. Wang, H. Conrad, Y.T. Zhu. Effect of rolling temperature on the evolution of defects and properties of an Al–Cu alloy. 2010, *Journal of Material Science*, Vol. 45, pp. 4846–4850.
282. A. Chatterjee, Sharma Garima, A. Sarkar, J.B. Singh, J.K. Chakravartty. A study on cryogenic temperature ECAP on the microstructure and mechanical properties of Al–Mg alloy. 2012, *Material Science and Engineering A*, Vol. 556, pp. 653–657.
283. J.B. Singh, R. Kapoor, A. Durga Prasad, J.K. Chakravartty. Comparison of microstructures and strengths of an Al–25Mg alloy subjected to severe plastic deformation at room and liquid nitrogen temperatures. 2013, *Material Science and Engineering A*, Vol. 581, pp. 26–30.
284. Y.G. Ko, D.H. Shin, K.T. Park, C.S. Lee. An analysis of the strain hardening behavior of ultra-fine grain pure titanium. 2006, *Scripta Materialia*, Vol. 54, pp. 1785–1789.
285. A.K. Padap, G.P. Chaudhari, V. Pancholi, S.K. Nath. Warm multiaxial forging of AISI 1016 steel. 2010, *Materials and Design*, Vol. 31, pp. 3816–3824.
286. P.L. Sun, C.Y. Yu, P.W. Kao, C.P. Chang. Influence of boundary characters on the tensile behavior of sub-micron-grained aluminium. 2005, *Scripta Materialia*, Vol. 52, pp. 265-269.
287. T.Hu, K.Ma, T.D. Topping, B. Saller, A. Yousefiani, J.M. Schoenung, E.J. Lavernia. Improving the tensile ductility and uniform elongation of high- strength ultrafine - grained Al alloys by lowering the grain boundary Misorientation angle. 2014, *Scripta Materialia*, Vols. 78-79, pp. 25-28.
288. V.G. Gryaznov, L.I Trusov. Size effects in micromechanics of nanocrystals. 1993, *Progress in material science*, Vol. 37, p. 128.
289. Substitutional solution hardening. Fleischer, R.L. 1963, *Acta metallurgica*, Vol. 11, pp. 203-209.

290. Oyvind Ryen, Oscar Nijs, Emma Sjolander, Bjorn Holmedal, Hans erik Ekstrom, Erik Nes. Strengthening Mechanisms in solid solution Aluminium alloys. 2006, Metallurgical and Materials Transactions A, Vol. 37A, pp. 1999-2006.
291. N. Kumar, R.S. Mishra. Additivity of strengthening mechanisms in ultrafine grained Al-Mg-Sc alloy. 2013, Material Science and Engineering A, Vol. 580, pp. 175-183.
292. American Society for Metals. s.l.: ASM metals reference, 1979. p. 127. Vol. 2.
293. Wilm, A. Physical-metallurgical experiments on aluminum alloys containing magnesium. 1911, Metallurgie, Vol. 8, p. 223.
294. Symposium on internal stress in metals and alloys, Session III Discussion, Institute of metals, London. Orowan, E. 1948, pp. 451-453.
295. Kaka Ma, Haiming Wen, Tao Hu, Troy D. Topping, Dieter Isheim, David N. Seidman, Enrique J. Lavernia, Julie M. Schoenung. Mechanical behavior and strengthening mechanisms in ultrafine grain precipitation-strengthened aluminum alloy. 2014, Acta Materialia, Vol. 62, pp. 141–155.
296. M.R.Ahmadi, B.Sonderegger, E. Povoden-Karadeniz, A. Falahati, E. Kozeschnik. Precipitate strengthening of non-spherical precipitates extended in $\langle 100 \rangle$ or $\{100\}$ direction in fcc crystals. 2014, Materials Science and Engineering: A, Vol. 590, pp. 262-266.
297. P.C. Hung, P.L. Sun, C.Y. Yu, P.W. Kao, C.P. Chang. Inhomogeneous tensile deformation in ultrafine-grained aluminum. 6, 2005, Scripta Materialia, Vol. 53, pp. 647–652.
298. Y. H. Zhao, J. F. Bingert, Y. T. Zhu, X. Z. Liao, R. Z. Valiev, Z. Horita, T. G. Langdon, Y. Z. Zhou, E. J. Lavernia. Tougher ultrafine grain Cu via high-angle grain boundaries and low dislocation density. 2008, Applied Physics Letters, Vol. 92, p. 081903.

299. R. Kapoor, N. Kumar, R.S. Mishra, C.S. Huskamp, K.K. Sankaran . Influence of fraction of high angle boundaries on the mechanical behavior of an ultrafine grained Al–Mg alloy. 20, 2010, *Materials Science and Engineering: A*, Vol. 527, pp. 5246–5254.
300. N.Kumar, R.S. Mishra, C.S. Huskamp, K.K. Sankaran. The effect of friction stir processing on the microstructure and mechanical properties of equal channel angular pressed 5052 Al alloy sheet. 2011, *Journal of Material Science*, Vol. 46, pp. 5527-5533.
301. F.Shi, S.Ye, L.Wang, S.Lu. Effect of friction on billet deformation during multi axial compressions. 2010, *Advanced Materials Research*, Vols. 143-144, pp. 879-883.
302. I. Sabirov, Y. Estrin, M.R. Barnett, I. Timokhina, P.D. Hodgson. Tensile deformation of an ultrafine grained aluminium alloy: Micro shear banding and grain boundary sliding. 2008, *Acta Materialia*, Vol. 56, pp. 2223-2230.
303. V.Segal. Severe plastic deformation: simple shear versus pure shear. 2002, *Material Science and Engineering A*, Vol. 338, pp. 331-344.
304. P. Nageswara Rao, D. Singh, R. Jayaganthan. Effect of annealing on microstructure and mechanical properties of Al 6061 alloy processed by cryorolling. 2013, *Material Science and Technology*, Vol. 39, pp. 76-82.
305. H. Miura, W. Nakamura. Microstructure and mechanical properties of Mg–8Al alloy fabricated by room-temperature multi-directional forging. 2013, *Philosophical Magazine Letters*, Vol. 93, pp. 601-607.
306. Y. Nakao, H. Miura. Nano-grain evolution in austenitic stainless steel during multi-directional forging. 2011, *Material Science and Engineering A*, Vol. 528, pp. 1310-1317.
307. Jie Xua, Mahmood Shirooyeh, Jitraporn Wongsan-Ngam, Debin Shan, Bin Guo, and Terence G. Langdon. Hardness homogeneity and micro-tensile behavior in a magnesium AZ31 alloy

- processed by equal-channel angular pressing. 2013, Material Science and Engineering A, Vol. 586, pp. 108-114.
308. Megumi Kawasaki, Terence G. Langdon. Developing hardness and microstructural homogeneity in High-Pressure Torsion. 2012, Material Science Forum, Vols. 706-709, pp. 1805-1810.
309. Chuan Ting Wang, Alan G. Fox, Terence G. Langdon. An Investigation of hardness homogeneity and microstructure in pure titanium processed by High Pressure Torsion. 2014, Material Science Forum, Vols. 783-786, pp. 2701-2706.
310. T.Sakai. Fine-grained structure evolution in BCC/FCC stainless steels under multiaxial forging conditions. 2003, Bull. Iron Steel inst. Japan, Vol. 16, p. 1288.
311. O. Sitdikov, Sakai, A. Goloborodko, H. Miura, R. Kaibyshev. Grain refinement in coarse grained 7475 Al alloy during sever hot forging. 2005, Philosophical Magazine, Vol. 85, pp. 1159-1175.
312. Richert, A. Korbel and M. Formation of shear bands during cyclic deformation of aluminium. 1985, Acta metall, Vol. 33, pp. 1971-1978.
313. A. Korbel and P. Martin. Microscopic versus macroscopic aspect of shear bands deformation. 1986, Acta Metall., Vols. 34, p. 1905.
314. Michaela Prell, Cheng Xu, Terence G. Langdon. The evolution of homogeneity on longitudinal sections during processing by ECAP. 2008, Materials Science and Engineering A, Vol. 480 , pp. 449–455.
315. Tang Liechong, Liu Chuming, Chen Zhiyong, I DaweiJ, Xiao Hongchao. Microstructures and tensile properties of Mg–Gd–Y–Zr alloy during multidirectional forging at 773K. 2013, Materials & Design, Vol. 50, pp. 587-596.

316. M. Furukawa, Z.Horita, M.Nemoto, R.Z. Valiev, T.G. Langdon. Factors Influencing the Flow and Hardness of Materials with Ultra-fine Grain Sizes. 1998, Philosophical Magazine, Vol. 78, pp. 203-215.
317. M.V. Markushev, M.Yu.Murashkin. Structure and mechanical properties of commercial Al-Mg 1560 alloy after equal-channel angular extrusion and annealing. 2004, Material Science and Engineering A, Vol. 367, pp. 234-242.
318. N.Tsuji, in: Y.T. Zhu, V.Varyukhin (Eds.). Nanostructured Materials by high pressure severe plastic deformation. s.l.: Springer, 2006. pp. 227-234.